



**University of Sheffield**  
**Department of Mechanical Engineering**

# **Novel Developments of Moiré Techniques for Industrial Applications**

**Volume I**

**Manuel Eduardo Heredia Ortiz**

**April 2004**

**Thesis Submitted for the Degree of  
Doctor of Philosophy**

To Nieves, for getting me into delicious trouble.

To my parents, who taught me the good things about being different.

Va revoir les roses. Tu comprendras que la tienne est unique au monde.

*Le Petit Prince* Antoine de Saint-Exupéry

# ABSTRACT

The family of moiré and fringe projection techniques can be used to measure the shape, orientation and deformation of arbitrary objects. These experimental techniques are easy to automate, allow remote operation, provide full-field information and are versatile, inexpensive and relatively simple. They have been applied extensively in the past, but mostly in the controlled environment of a laboratory.

There is great potential in the use of these techniques for a variety of industrial applications including quality control and process monitoring. However, this implies dealing with the adverse conditions of the factory, hangar or similar environment. In addition, these techniques will only appeal to industry if they are fast, simple, and foolproof.

The main goal of this research was to exploit recent technological advances to fulfil the requirements of industry, making these techniques easier to use and more robust, and explore the potential offered by the combination and cross-fertilization of moiré methods with techniques from different fields such as experimental stress analysis, non-destructive evaluation, and machine vision.

This research resulted in the development of a number of instruments and procedures for industrial applications based in moiré and fringe projection techniques, including:

- A handheld instrument based in the shadow moiré technique designed to assist in the detection of very small surface defects in aircraft parts, during in-service maintenance inspections;
- A multi-purpose system to measure remotely (i) the shape and deformation of three-dimensional objects by means of the fringe projection technique, and (ii) the location of the object by means of triangulation. The elements were integrated in a portable instrument, and fully automated novel algorithms were implemented to process the data;
- Finally, a novel experimental technique is proposed that uses thermal marking to measure deformation in a component, in a combination of concepts from moiré and thermography.

Experimental results obtained in a range of situations are presented in several industrial applications in the context of the aerospace industry and in bioengineering.

# ACKNOWLEDGEMENTS

I would like to express my sincere thanks to my supervisor Professor Eann A. Patterson. I have learnt a great deal from him, and not only about experimental mechanics. Working with someone you admire is a privilege.

Special thanks to Dr. Mark Pacey for his assistance with the photoelastic experiments, and for introducing me to the Sheffield Steelers. Dr. Hector Canabal, from University Complutense of Madrid, made useful suggestions on fringe pattern analysis at the start of my work, when I most needed them.

Dr. Zhifan Wang helped build an interface between the fringe projection software JOSHUA and the photoelastic software VIZION. Richard Kay produced most of the specimens, prototypes and instruments I used in this work, and Derek Hallford took beautiful photographs. They are both excellent professionals. Terry Senior and Wendy Birtwhistle also assisted in some of the projects. I am very grateful as well to Jean Edwards and Lisa Gardiner in the general office and to Jean Hoskins, assistant to Prof. Patterson. It has been very pleasant working with them.

I supported a number of undergraduate students in their final year projects on moiré techniques. David Mitchem, Tom Hughes, Jochen Krueger and Jon Matthews provided fresh viewpoints, asked difficult questions, produced valuable feedback, and generally helped me to improve the quality of my work.

This research would not have been possible without the sponsors. The research on defect detection and location of components was partly funded by the BRITE Euram program through the INDUCE project no. BE 97-4057 for NDE techniques in the aerospace industry. The work on shape correction of reflection photoelasticity was partly funded by SNECMA Moteurs. The vibration experiments of turbine blades were conducted in the facilities of SNECMA Moteurs (Villaroche, France) and Rolls Royce (Derby, UK). Finally, the research on thermal moiré was funded by the Engineering and Physical Sciences Research Council (Grant no. GR/R71542/01).

I have been fortunate to have industrial partners who helped me to keep my feet on the ground and brought on board their significant expertise. I would like to mention John Smith (BAE Systems), Michel Taroni and Philippe Brailly, (SNECMA Moteurs), Mariano Alvaro (EADS CASA), Michael Adams and Simon Johnson, (Unilever Research), Jon Lesniak and Brad Boyce (Stress Photonics), Dr. Eddie O'Brien and Dr. Richard Burguete (Airbus UK).

Thanks to my colleagues at the Experimental Stress Analysis Lab: Dr. Gaetano Burriesci, Paco Díaz, Paul Elliott, Rene J. Estrada, Sarah ‘Miss Butterfly’ Gibson, Richard Greene, Dr. James Hobbs, Dr. Mark Pacey, Dr. Giuseppe Pitarresi, ‘Mimmo’ Tripoli, and Dr. Su Juan Zhang. They all contributed in one way or another to make this thesis possible.

Thanks to my good friends in Sheffield. Paco Díaz and Leigh Brown kept my morale high by letting me beat them at squash. Dimitri Kourkoulis, Reme Carmona, and Isabelle K/Bidy are also among these special people that made my time here a very happy one.

Thanks to Maru and Edu for invading my house every summer. My parents Manolo and Maruxa opened all the opportunities for me and always supported me. I don’t even know how to start to make them justice. Finally, thanks to Nieves for making me laugh and cry and being the best thing that ever happened to me.

# NOMENCLATURE

$\alpha$	Isochromatic parameter
$\Phi$	Modulated phase, ( <i>rad</i> )
$\gamma$	Signal modulation of the fringe image
$\nu$	Poisson's ratio
$\lambda$	Wavelength of light, ( $\mu\text{m}$ )
$\rho$	Pseudocorrelation
$\rho$	Density, ( $\text{kg m}^{-3}$ )
$\xi, \psi$	CCD physical coordinates, ( <i>mm</i> )
$\alpha, \beta, \theta, \phi, \omega$	Angles, ( <i>rad</i> )
$\sigma_1, \sigma_2$	Principal stresses, ( <i>MPa</i> )
$A$	Background intensity
$A$	Area, ( $\text{m}^2$ )
$b$	Distance between camera focal point and laser source, ( <i>mm</i> )
$B$	Fringe amplitude
$Bi$	Biot number
$B_k$	Size of $k^{\text{th}}$ bin, ( <i>pixels</i> )
$C$	Specific heat, ( $\text{J kg}^{-1} \text{K}^{-1}$ )
$E$	Young's modulus, ( $\text{N m}^{-1}$ )
$e$	Efficiency coefficient
$f_c, f_p$	Effective focal distance of the camera and projector lenses, ( <i>mm</i> )
$f_{co}, f_{p0}$	Focal length of the camera and projector lenses, ( <i>mm</i> )
$h$	Film coefficient, ( $\text{W m}^{-2} \text{K}^{-1}$ )
$h, d$	Distances in optical model, ( <i>mm</i> )
$I$	Image intensity
$i, j$	Image pixel coordinates
$K$	Calibration constant, ( $\text{mm rad}^{-1}$ )

$K$	Coating's strain coefficient
$K_{xx}$	Thermal conductivity, ( $W m^{-1} K^{-1}$ )
$m$	Slope of phase map, ( $rad pixel^{-1}$ )
$m; m_p$	Camera magnification, (non-dimensional; $mm pixel^{-1}$ )
$O$	Object image
$OPL$	Optical path length, ( $mm$ )
$p$	Pitch of the reference grating, ( $mm$ )
$P$	Pitch of the reference image, ( $pixel$ )
<b>P, Q, O, S, C</b>	Points in the optical model
$p'$	Pitch of the model grating, ( $mm$ )
$Q$	Number of active pixels
$Q$	Heat, ( $W$ )
$q$	Heat flux, ( $Wm^{-2}$ )
$R$	Reference image
$R$	Thermal resistance, ( $K W^{-1}$ )
$r$	Reflectivity coefficient
$Ra$	Rayleigh number
$S$	Laser source
$t$	Thickness, ( $mm$ )
$t$	Time, ( $s$ )
$T$	Temperature, ( $K$ )
$u, v$	Components of in-plane displacement, ( $mm$ )
$U, V$	Components of in-plane displacement, ( $pixels$ )
$W\{\}$	Wrapping operator
$x, y, z$	Cartesian coordinates, ( $mm$ )

## TABLE OF CONTENTS

ABSTRACT .....	III
ACKNOWLEDGEMENTS .....	IV
NOMENCLATURE .....	VI
TABLE OF CONTENTS .....	1
CHAPTER I INTRODUCTION .....	6
I.1 The Moiré Effect.....	6
I.2 The Industrial Applications Of Moiré Techniques .....	7
I.3 Overview Of This Thesis .....	8
FIGURES OF CHAPTER I .....	10
CHAPTER II REVIEW OF THE STATE OF THE ART.....	12
II.1 Introduction.....	12
II.2 Historical Review Of Moiré Techniques .....	13
II.2.1 Major Texts And Review Papers.....	16
II.3 Basic Principles Of Moiré Techniques .....	16
II.3.1 In Plane Moiré.....	16
II.3.1.1 Geometrical Interpretation Of The Moiré Fringes .....	17
II.3.1.2 Displacement Field Approach.....	18
II.3.2 Out-Of-Plane Moiré.....	20
II.3.2.1 Shadow Moiré.....	20
II.3.2.2 Reflection Moiré .....	21
II.3.2.3 Projection Moiré .....	22
II.3.2.4 Fringe Projection.....	23
II.3.3 Other Moiré Methods .....	26
II.4 Fringe Pattern Measurement Techniques.....	27
II.4.1 Introduction .....	27
II.4.2 Intensity Methods.....	28
II.4.3 Phase Measurement Methods .....	29
II.4.4 Phase Unwrapping .....	31
II.5 Review Of Applications Of Moiré Techniques .....	32
II.5.1 Shadow Moiré.....	32
II.5.2 Projection Moiré.....	33
II.6 Critical Analysis Of The Literature.....	34
II.6.1 Specimen Gratings For In-Plane Moiré .....	34

II.6.2	<i>Simplicity And Robustness Of The Experimental Apparatus</i> .....	35
II.6.3	<i>Computational Algorithms For Fringe Analysis</i> .....	35
II.6.4	<i>Flexibility Of The System And Calibration Methods</i> .....	36
II.6.5	<i>Requirements On Surface Finish And Lighting Conditions</i> .....	36
II.7	Formal Statement Of The Problem.....	36
II.8	Objectives.....	37
FIGURES OF CHAPTER II.....		38
CHAPTER III DETECTION OF SURFACE DEFECTS.....		44
III.1	Introduction.....	44
III.2	Requirements.....	46
III.2.1	<i>Surface Defects</i> .....	46
III.2.1.1	<i>Defect Typology</i> .....	46
III.2.1.2	<i>Size Considerations</i> .....	46
III.2.2	<i>Inspection Surfaces</i> .....	48
III.2.2.1	<i>Geometry</i> .....	48
III.2.2.2	<i>Surface Finish</i> .....	48
III.2.3	<i>Operational Conditions</i> .....	48
III.3	Materials And Methods.....	49
III.3.1	<i>Description Of The Samples</i> .....	49
III.3.2	<i>Surface Profilometry</i> .....	50
III.4	Experimental Apparatus.....	51
III.4.1	<i>Technique Selection</i> .....	51
III.4.2	<i>MIDAS 1 Prototype</i> .....	53
III.4.3	<i>MIDAS 2 Prototype</i> .....	55
III.5	Experimental Results.....	56
III.5.1	<i>Surface Finish Tests</i> .....	56
III.5.2	<i>Impacts On Flat Panels</i> .....	57
III.5.3	<i>Impacts On Curved Panels</i> .....	59
III.6	Quantitative Measurement.....	60
III.6.1	<i>A Hybrid Fringe Analysis Technique</i> .....	60
III.6.2	<i>Validation</i> .....	63
III.7	Discussion.....	64
III.8	Conclusion.....	65
FIGURES OF CHAPTER III.....		66
CHAPTER IV FRINGE PROJECTION: MATERIALS AND METHODS.....		92
IV.1	Introduction.....	92
IV.2	Technique Selection.....	93
IV.3	Experimental Apparatus.....	94
IV.4	Methodology Of Use.....	95
IV.4.1	<i>General Considerations</i> .....	95
IV.4.2	<i>Set-Up Of The Optical Elements</i> .....	96

IV.4.3	Data Collection.....	97
IV.5	Algorithms Of Digital Fringe Pattern Analysis .....	97
IV.5.1	Phase Measurement Five Step Spatial Algorithm .....	98
IV.5.2	Phase Unwrapping Quality Bins Algorithm .....	100
IV.5.3	Pre-Processing Normalisation Algorithm .....	105
IV.6	System Calibration .....	106
IV.6.1	Phase To Height Conversion .....	106
IV.6.1.1	Telecentric Expression.....	106
IV.6.1.2	Perspective Correction.....	108
IV.6.1.3	Simplified Non-Telecentric Expression.....	108
IV.6.1.4	First Order Approximation .....	109
IV.6.2	Reference Alignment Procedure .....	110
IV.6.3	Manual Calibration Procedure .....	110
IV.6.4	Automatic Calibration Procedure .....	112
IV.7	Evaluation Of The Method.....	114
IV.7.1	Numerical Evaluation Of The Method.....	114
IV.7.1.1	Effect Of Slope .....	116
IV.7.1.2	Effect Of Random Noise .....	117
IV.7.1.3	Effect Of Modulation In Background And Amplitude.....	117
IV.7.1.4	Effect Of Normalization .....	119
IV.7.2	Experimental Error Analysis .....	119
IV.8	Discussion And Conclusions .....	123
FIGURES OF CHAPTER IV .....		126
CHAPTER V MEASUREMENT OF SHAPE AND DEFORMATION.....		160
V.1	Introduction.....	160
V.2	Shape Measurement Examples .....	161
V.2.1	Buddha Statue.....	161
V.2.2	Fan Blade.....	163
V.3	Shape Correction In Digital Reflection Photoelasticity .....	163
V.3.1	Experimental Apparatus .....	165
V.3.2	Experimental Procedure.....	166
V.3.3	Shape Correction Processing Algorithms.....	167
V.3.4	Experimental Evaluation Of The Technique.....	168
V.3.4.1	Preparation Of The Samples .....	168
V.3.4.2	Description Of The Test.....	170
V.3.4.3	Experimental Results .....	170
V.3.5	Case Study: Vibration Test Of A Small Compressor Blade.....	172
V.4	Deformation Measurement.....	173
V.4.1	Background: In Vivo Measurement Of Deformation In Human Skin.....	174
V.4.1.1	Mechanical Behaviour Of Soft Tissue .....	175
V.4.1.2	Experimental Tests.....	175
V.4.2	Description Of The Numerical Model .....	176
V.4.3	Methodology .....	176
V.4.4	Qualitative Results.....	177
V.4.4.1	Indentation Tests.....	177

V.4.4.2	Sliding With Indentation .....	178
V.4.5	<i>Quantitative Results</i> .....	179
V.5	Conclusion .....	181
FIGURES OF CHAPTER V .....		183
CHAPTER VI LOCATION OF COMPONENTS .....		199
VI.1	Introduction .....	199
VI.2	Background On NDE .....	200
VI.3	Requirements .....	201
VI.3.1	<i>Operating Environment</i> .....	201
VI.3.2	<i>Inspection Area</i> .....	202
VI.3.3	<i>Precision</i> .....	202
VI.3.4	<i>Other Requirements</i> .....	202
VI.4	Methodology .....	203
VI.4.1	<i>Principles Of The Light Spot Technique</i> .....	204
VI.4.2	<i>Apparatus</i> .....	205
VI.4.3	<i>Experimental Procedure</i> .....	206
VI.4.4	<i>System Calibration</i> .....	207
VI.5	Results .....	211
VI.5.1	<i>Shape And Location Measurement Of A Complex Component</i> .....	211
VI.5.2	<i>Correlation With CAD Data</i> .....	214
VI.5.3	<i>Applications</i> .....	216
VI.6	Case Studies .....	217
VI.6.1	<i>X-Ray Inspection</i> .....	217
VI.6.2	<i>Ultrasound Inspection</i> .....	219
VI.6.3	<i>Hangar</i> .....	220
VI.7	Conclusion .....	220
FIGURES OF CHAPTER VI .....		222
CHAPTER VII THERMAL MOIRÉ .....		238
VII.1	Introduction .....	238
VII.2	Aims .....	240
VII.3	Background In Thermal Techniques .....	240
VII.4	Fundamental Study .....	243
VII.4.1	<i>Loads</i> .....	244
VII.4.1.1	<i>Initial And Boundary Conditions</i> .....	245
VII.4.1.2	<i>External Load By Contact</i> .....	245
VII.4.1.3	<i>External Load By Radiation</i> .....	246
VII.4.1.4	<i>Convection</i> .....	247
VII.4.2	<i>Material Properties</i> .....	247
VII.4.3	<i>Geometry And Meshing</i> .....	248
VII.4.4	<i>Steady State Analysis</i> .....	248
VII.4.5	<i>Transient Analysis</i> .....	248
VII.4.5.1	<i>Estimation Of The Time Step</i> .....	248

VII.4.5.2	Load Steps .....	249
VII.4.6	Experimental Validation .....	250
VII.5	Experimental Apparatus .....	252
VII.5.1	Contact Prototype .....	253
VII.5.2	Projector Prototype .....	254
VII.5.2.1	Heat Source .....	255
VII.5.2.2	Condenser .....	255
VII.5.2.3	Grating .....	255
VII.5.2.4	Lens .....	256
VII.5.2.5	Efficiency .....	257
VII.5.3	Thermal Imagers .....	257
VII.6	Analysis Of Thermal Patterns .....	258
VII.7	Experimental Results .....	262
VII.7.1	Contact Prototype .....	263
VII.7.2	Projector Prototype .....	264
VII.8	Discussion And Conclusions .....	267
FIGURES OF CHAPTER VII .....		268
CHAPTER VIII DISCUSSION AND CONCLUSIONS .....		284
VIII.1	Introduction .....	284
VIII.2	General Discussion .....	284
VIII.3	Conclusions .....	288
VIII.4	Contributions To Knowledge .....	289
VIII.5	Recommendations For Future Research .....	290
REFERENCES .....		294
APPENDICES .....		301
AI	Five-Step Spatial Phase Measurement Algorithm .....	301
AI.1	Generalized Five-Step Algorithm .....	301
AI.2	Application To The Analysis Of Projected Fringes .....	302
AI.3	First Order Approximation Analysis Of The Error .....	303
AI.4	Conclusions .....	305
AII	JOSHUA Software For Fringe Pattern Analysis .....	306
AII.1	Welcome Screen And Main Menu .....	306
AII.2	File Menu .....	306
AII.3	Action Menu .....	306
AII.4	View Menu .....	308
AII.5	Help Menu .....	308
AIII	List Of Publications .....	309
AIII.1	Published Conference Papers .....	309
AIII.2	Published Papers In International Journals .....	309
AIII.3	Papers In Preparation .....	309
FIGURES OF THE APPENDICES .....		310

## CHAPTER I

# INTRODUCTION

### I.1 The Moiré Effect

Moiré is a fascinating visual effect that occurs when two fine repetitive motifs are superimposed. The limited resolution of the human eye blurs the detail of the fine patterns and creates the illusion of a coarser pattern of dark and light fringes, which is very sensitive to small differences between the motifs. This makes the moiré pattern very dynamic, changing very rapidly with a slight movement and catching the eye of the observer.

The effect is illustrated in fig. 1.1, which shows a regular array of parallel lines. An identical motif has been printed in a transparent sheet in the previous page. When one observes the figure through the transparent sheet, a moiré pattern of coarse dark fringes appears in the overlapping of the two gratings. The effect is particularly striking when seen from a distance. It can be noted that the shape and pitch of the moiré fringes change rapidly with small relative displacements or rotations of the two gratings.

Everyday examples of occurrences of the moiré effect are not difficult to find. As a matter of fact, the term *moiré* is not the name of a person, but the French name for a type of fabric, also known as watered silk, which exhibits these patterns of dark and light bands. The effect also can be seen in the overlapping of two layers of window screen, mosquito nets, or blinds made of fine fabric. When travelling by car, the effect can be seen on distant fences superimposed in the landscape.

Beyond being a curiosity, moiré has some useful applications, and can also be an issue of concern in some cases. In multicolour printing, the orientation of superimposed halftone screens must be carefully controlled to eliminate moiré effects that would ruin the result. Television presenters never wear striped clothes because they cause a distracting moiré pattern with the raster of the screen.

The moiré effect also possesses a certain aesthetical value. The famous painting from the Belgian artist René Magritte inspired fig. 1.2, which plays with the *trompe l'oeil* character of moiré. The visual effect that occurs when this figure is seen through the transparent grating in

the previous page is not strictly moiré, although shares the same principle. Slight displacements of the transparent sheet make the figure disappear and reappear.

The moiré effect can be described more rigorously as a beat pattern produced when two repetitive patterns, such as arrays of lines or dots of similar spacing, are superimposed so that one can be seen through the other. The interaction of the two patterns produces light and dark bands known as moiré fringes. The moiré fringe pattern is very sensitive to small differences between the two interacting motifs, working as an amplifier for relative displacement and deformation.

Lord Rayleigh introduced the use of this effect for high sensitivity tests in 1874. He used the moiré between two identical rulings to determine their quality, despite each grating being too fine to be resolved under a microscope.

Since then, a family of experimental techniques based on this effect has developed, which allow the measurement of shape, displacements and deformations of objects with high precision (Cloud, 1998, McKelvie, 1998).

## **I.2 The Industrial Applications Of Moiré Techniques**

The control of manufacturing processes in industry is still nowadays in many cases more the result of experience and the use of trial-and-error strategies, rather than being based on a clear understanding of the effect that changes in the processing parameters have on the quality of the finished product (*e.g.* shape and dimensional tolerances, mechanical properties, presence of residual stresses, etc.).

There are many techniques in the general field of Experimental Mechanics that can potentially provide industry with the ability to quantify the effect of these changes, which constitutes very valuable information to enable a better control of industrial processes. However, it is necessary to balance the potential advantages, such as improved quality, reduced rejects, faster set-ups etc. with a number of drawbacks, including the resulting increase in processing time, the high cost or the need for skilled labour.

The recent technological advances, particularly in the field of electronics, have made available high performance sensors and digital illumination devices, and impressive amounts of computing power at a very low cost. This is helping to incline the balance in favour of the adoption of experimental techniques in industry, a trend that will ultimately result in more efficient processes and better quality products.

The potential of moiré techniques in particular comes from their low cost and simplicity, their portability and versatility, the absence of related health and safety hazards, and the ability to provide full-field and intuitive information.

Instances where moiré techniques could potentially be applied include process monitoring and quality control, non-destructive evaluation and testing, maintenance, strain measurement, and medicine. The ability to digitise shape information has also applications in the art industry, and for special effects, creation of characters for video games, etc.

Although there are a few systems commercially available (see section II.5), the use of these methods is perhaps not as widespread as it should, partly because most of the applications described in the literature to date have been developed in the controlled environment of a laboratory.

The first objective of this research was to investigate the application of moiré techniques for the measurement of location, shape, and deformation of arbitrary objects, both in static and dynamic applications, and mainly in industrial situations. In order to do so, it was deemed necessary to develop tools and methodologies that were flexible, robust and reliable, easy to use and calibrate, and inexpensive. The recent advances in optical and computer equipment made this goal achievable.

The second objective of this research was to investigate the combination of moiré techniques with other techniques from the fields of stress analysis, non-destructive evaluation, or machine vision, in situations where two or more techniques provide complementary information about the object under study.

### **I.3 Overview Of This Thesis**

Chapter II presents a review of the state-of-the-art of moiré techniques and their industrial applications. The main limitations of current methods are exposed in a critical analysis of the literature to determine the issues that need to be addressed in order to facilitate the industrial use of moiré methods. The chapter concludes with the formal statement of the objectives of this research, which have been already outlined above.

Chapter III demonstrates the process of adapting moiré techniques from the laboratory to an industrial environment through a case study: the design of a handheld device for the detection of small surface defects in aircraft.

Chapter IV describes the elements (apparatus and algorithms) of a multipurpose system developed in this research for the measurement of location, shape and deformation of arbitrary objects in industrial situations. The chapter starts with a discussion that justifies the selection of

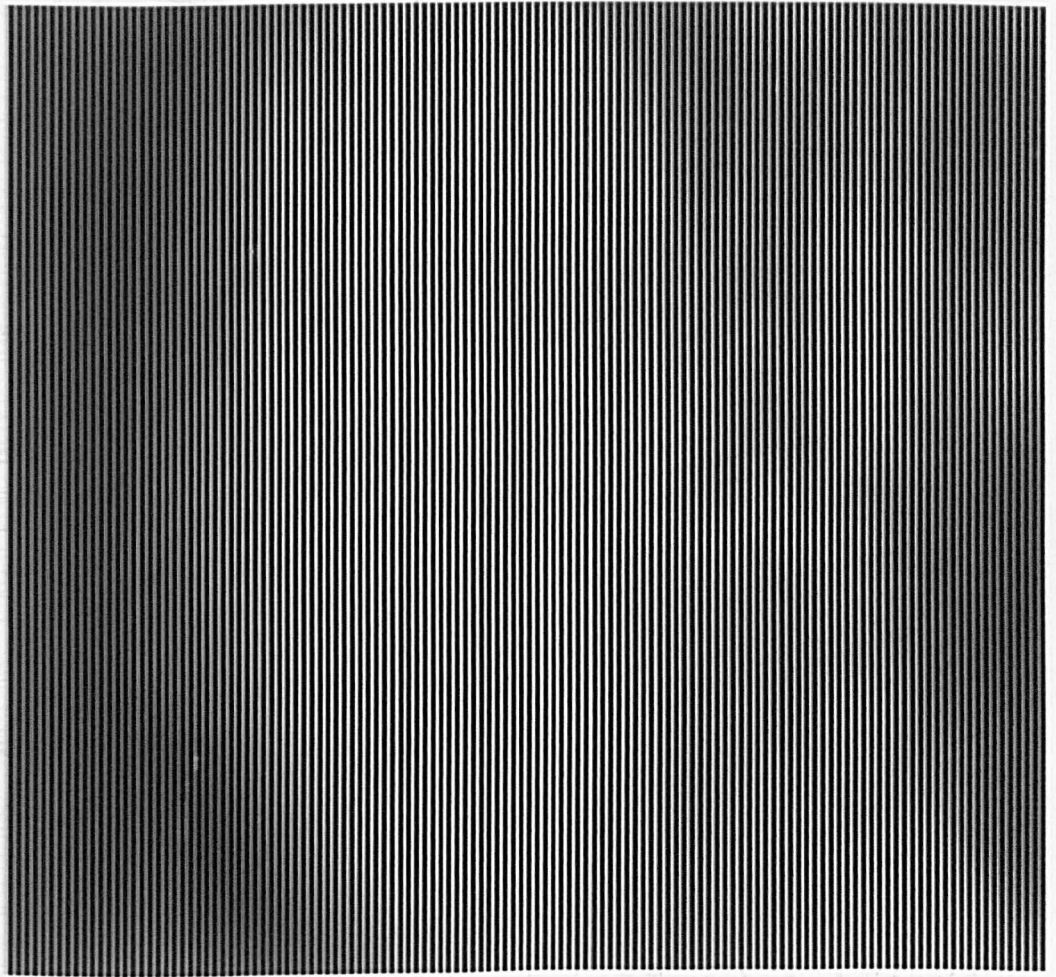
the fringe projection technique as a basis for the development of the system, describes the elements and methodology of use, and presents an assessment of the accuracy of the method.

Chapters V and VI concentrate on the diverse applications of the multipurpose system. Chapter V demonstrates the use of the system for the measurement of shape, in particular to assist reflection photoelasticity in complex aeronautical components, and also discusses an application in the field of biomechanics where the goal is the measurement of out-of-plane deformation rather than shape. Chapter VI presents some improvements to the system that allow the measurement of the location in space of objects in addition to their shape, and discusses some applications in the field of non-destructive inspection in the aerospace industry.

Finally, Chapter VII presents for the first time a new experimental technique born from the combination of moiré and infrared thermography that allows the performance of non-invasive measurements of in-plane deformation. This technique presents unique advantages over existing methods and plenty of potential for further development.

To conclude, Chapter VIII brings together the discussion of the previous chapters and rounds up the conclusion with a summary of the contributions and suggestions for further work.

The objectives of this research were achieved with a high degree of success. The outcome of this work includes several prototype systems based in moiré techniques for a number of industrial applications. Publication of the findings of this research in international scientific journals and conference proceedings has been undertaken in order to ensure a broad dissemination.



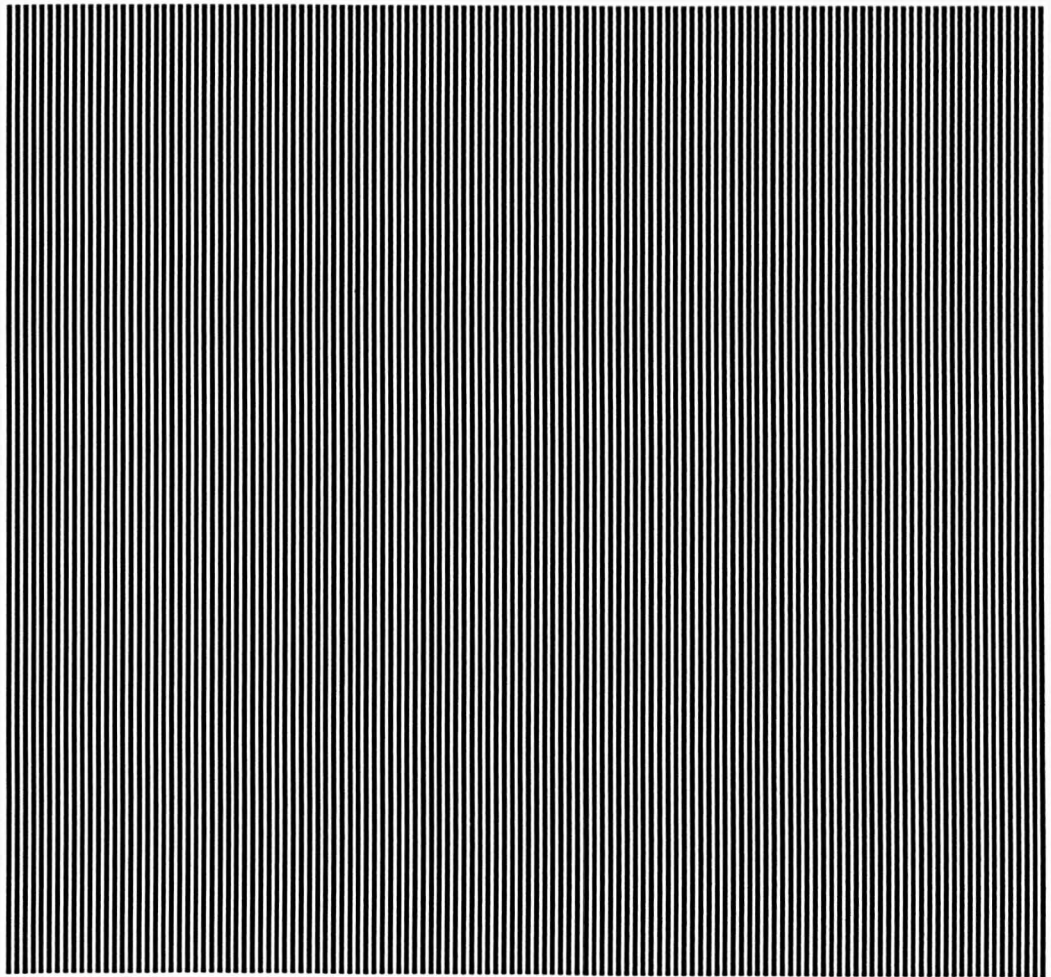


Figure 1.1: The dark bands formed when the grating printed in this page is seen through the transparent grating in the previous page are known as moiré fringes. The moiré phenomenon is caused by the beat pattern between the two gratings. It can be seen that the fringes change rapidly in response to a small misalignment of the gratings, working as an amplifier of relative displacement or deformation. This potential for high sensitivity testing has been exploited to develop a family of experimental techniques.

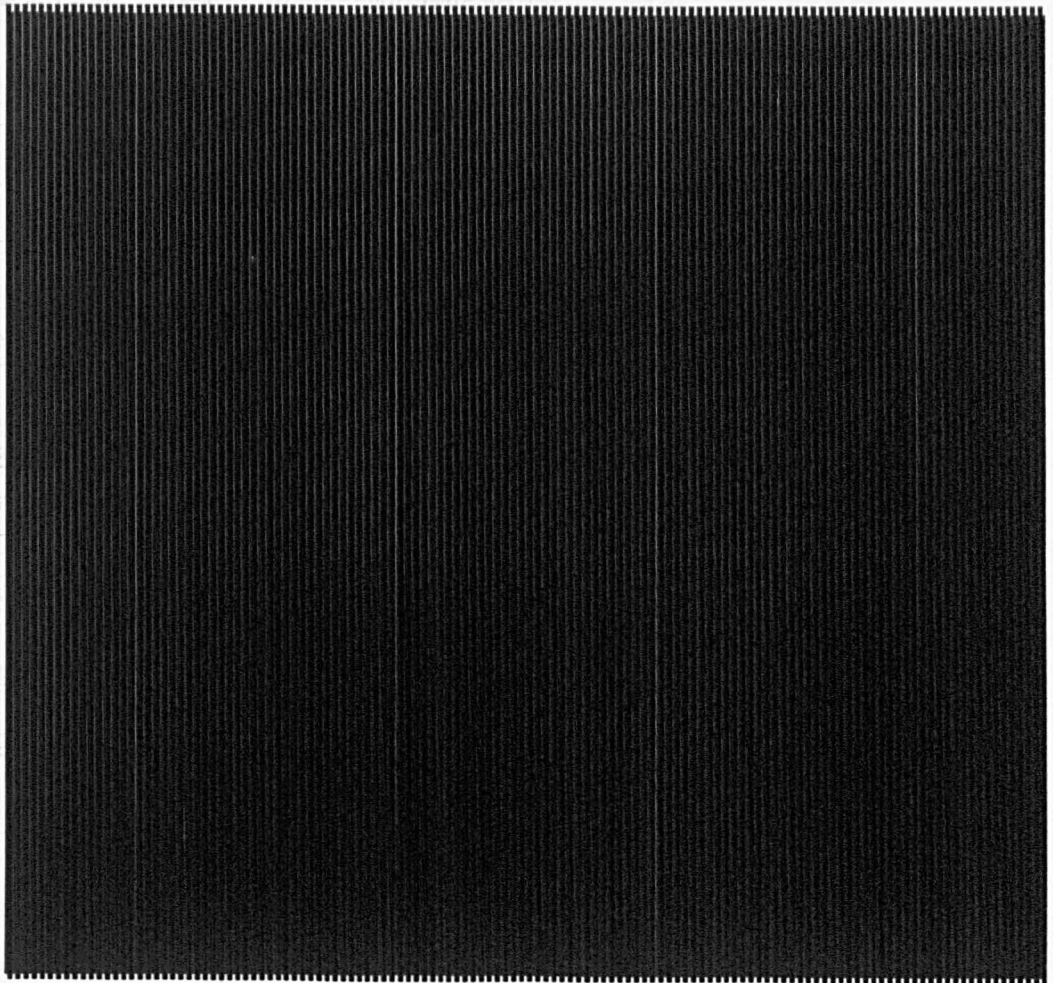
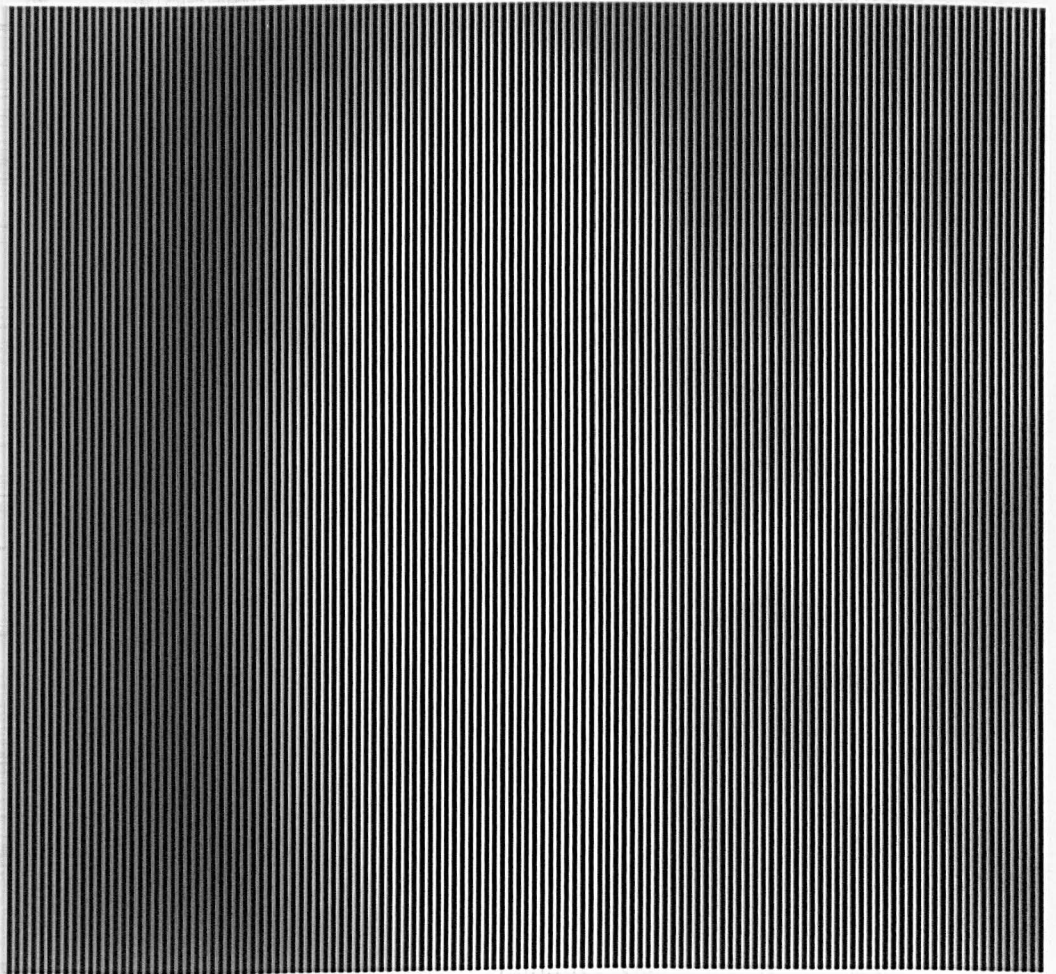


Figure 1.1: The dark bands formed when the grating printed in this page is seen through the transparent grating in the previous page are known as moiré fringes. The moiré phenomenon is caused by the beat pattern between the two gratings. It can be seen that the fringes change rapidly in response to a small misalignment of the gratings, working as an amplifier of relative displacement or deformation. This potential for high sensitivity testing has been exploited to develop a family of experimental techniques.



CHAPTER II  
REVIEW OF THE STATE OF THE ART

Fig. 1. Introduction



Figure 1.2: This figure is inspired by the famous painting from Belgium artist René Magritte. The visual effect that occurs when this figure is seen through the transparent grating in the previous page is not strictly moiré, although shares the same principle. When the transparent grating is aligned with the figure, the pipe and the lettering disappear completely. A slight displacement of the grating makes them reappear. The effect is particularly striking when seen from a distance, and is caused by the limited resolution of the human eye.

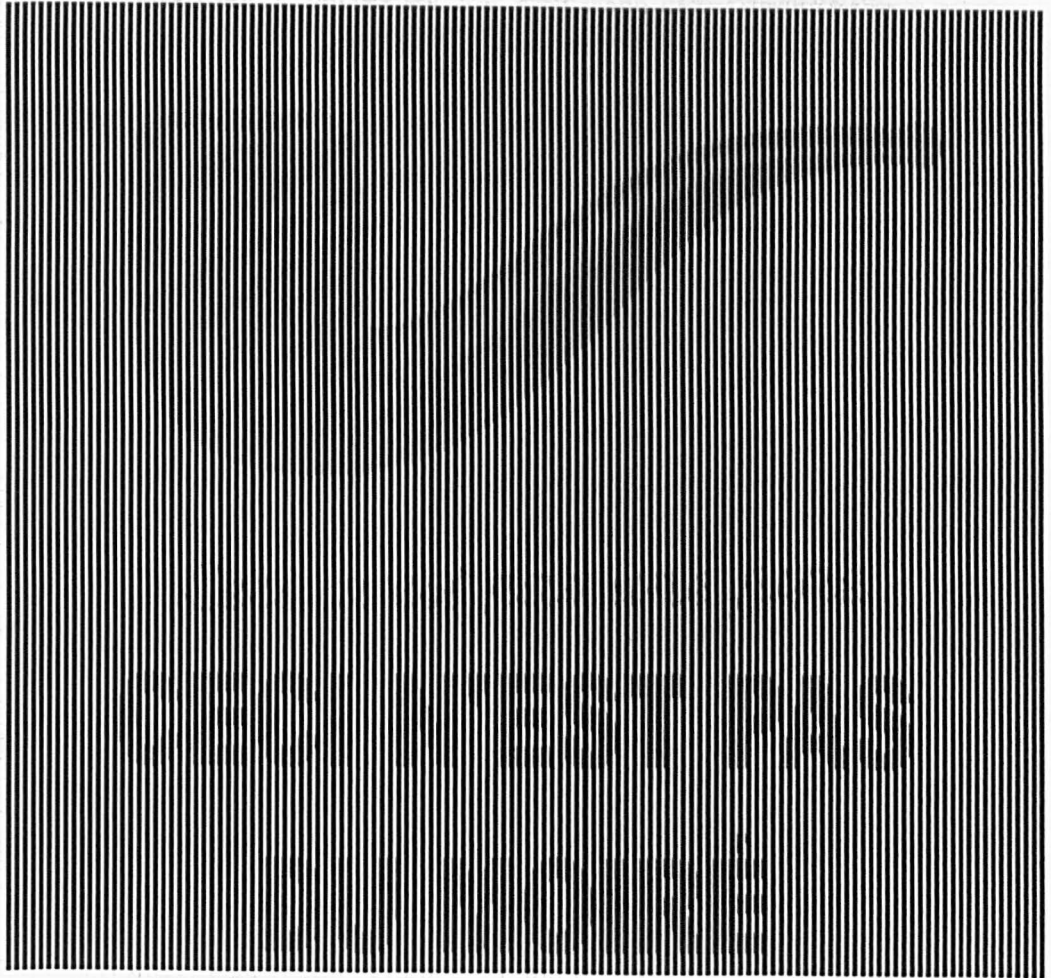


Figure 1.2: This figure is inspired by the famous painting from Belgium artist René Magritte. The visual effect that occurs when this figure is seen through the transparent grating in the previous page is not strictly moiré, although shares the same principle. When the transparent grating is aligned with the figure, the pipe and the lettering disappear completely. A slight displacement of the grating makes them reappear. The effect is particularly striking when seen from a distance, and is caused by the limited resolution of the human eye.

## CHAPTER II

# REVIEW OF THE STATE OF THE ART

### II.1 Introduction

This chapter presents a review of the literature in the field of moiré and fringe projection techniques for experimental mechanics. The subject is introduced in the following section with a historical overview of the most relevant milestones in the development of the family of moiré techniques. Interferometric methods that use coherent light, such as holography, shearography, speckle interferometry or moiré interferometry are closely related, but were considered outside the scope of this review.

Section II.3 presents the basic principles and a brief outline of the implementation for the most important members of the family. The aim is to provide a basic overview rather than a comprehensive guide to the subject, hence only the main ideas are presented, and extensive use is made of references. Moiré techniques for the measurement of in-plane displacements are described first, using both the geometrical and the displacement-field approach. Out-of-plane techniques follow, including shadow moiré, reflection moiré, projection moiré, and fringe projection, with some of the most important variants.

Section II.4 reviews the literature on the interpretation of the fringe patterns that typically result from the application of moiré methods. In the early days, the interpretation of these fringe patterns was a tedious and skilled job that had to be performed manually. The subject has greatly benefited from the revolution in computer technology in recent years, which allowed the development of digital fringe pattern analysis methods. These can be broadly classified in two groups: intensity-based methods, and phase-extraction methods. The more recent phase-extraction approach generally offers decisive advantages and has largely superseded intensity-based techniques for most applications, and will therefore be discussed in more detail.

The subject of the industrial applications of moiré techniques is explored in section II.5, with emphasis on the merits and drawbacks, the field of application and potential of each technique.

A critical analysis of the literature is presented in section II.6. The goal is identifying the main limitations that have prevented a more widespread industrial use of current moiré techniques,

preparing the field for the formal statement of the problem that motivated this research, and which is presented in section II.7. The relevance of the stated research question is discussed with reference to the literature, to conclude with a concise summary of the objectives in section II.8.

## II.2 Historical Review Of Moiré Techniques

Lord Rayleigh first described the phenomena of moiré fringes in 1874, and proposed the first practical application of the effect. He observed that it was possible to judge the quality of rulings such as halftone screens or diffraction gratings, in terms of spacing, parallelism and straightness of the lines, by comparing with a master ruling and observing the moiré fringes. This method allowed him to achieve increased sensitivity. A few years later, Righi (1887) first noticed that the movement of the moiré fringes allowed the measurement of the relative displacement of two gratings.

However, it took more than fifty years for the first systematic attempt at describing the formation of moiré fringes to appear. Tollenaar published in 1945 a paper in Dutch where he studied the relationships between the spacings and inclinations of the moiré fringes in a pattern and the geometry of the two interfering line arrays that produced the pattern. This paper was precursor of the geometrical interpretation, which is the first of two main approaches that can be found in the literature for the description of moiré patterns, and was later developed by Morse *et al.* (1960) for strain analysis applications.

The next significant advance came from Weller and Shepard (1948), who applied moiré to measure deformation on an object by looking at differences in the grating pattern before and after loading the object. This constitutes an altogether different interpretation of the moiré effect, known as the displacement-field approach, by which the moiré fringes describe the components of the relative displacement field between the two gratings. Dantu (1954) further developed this description by introducing the interpretation of moiré fringes as components of displacement for plane elasticity problems, and shortly after that Sciammarella and Durelli (1961) extended this approach into the region of large strains.

In addition, Weller and Shepard were the first to use moiré to measure out-of-plane displacements. They proposed the shadow moiré technique, where a grating placed in front of a non-flat surface is used to determine the shape of the surface behind it by looking at the moiré fringes that form between the grating and its shadow. They also suggested the first applications to measure deflections in plates and isopachics in photoelasticity. This remarkable paper passed relatively unnoticed, and the technique remained little used until the early 1950's, when the technique to produce reliable diffraction gratings was perfected.

In 1954 Ligtenberg introduced a novel technique, named reflection moiré, which allowed direct measurement of slopes and curvature of surfaces. The technique required a mirror surface on the specimen, but had the advantage of eliminating one differentiation of the experimental data. Ligtenberg presented a rigorous theory of moiré fringes for mapping slope contours in 1955. Shortly afterwards, Guild (1956, 1960) did the same for displacement measurement.

Theocaris (1964a, 1964b) used moiré to measure in-plane deformation, generating isopachics, which combined with photoelastic isochromatics allowed the separation of principal stresses. He also reported the use of the shadow moiré method to measure deflections on flexed plates, effecting the applications originally proposed by Weller and Shepard in 1948. These first applications of moiré techniques were realised in the laboratory for plate deformation problems and buckling of shells, including the analysis of torsion using Prandtl's analogy.

Rowe and Welford (1967) first proposed the projection of interference fringes for contouring objects, introducing the fringe projection technique. The method entailed projecting a fringe pattern onto an object and viewing from a different direction. In the resulting image, the deviation of the projected fringes from straight lines in the object image can be related to the surface shape. Later, Welford published in 1969 some work on a number of applications for projected fringes. Der Hovanesian and Hung (1971) proposed to generate the fringes by means of a slide projector that imaged a small transparent master grating onto the object, and effected several applications of the method for surface contouring and vibration analysis. Kethan (1975) and later Gasvik (1987) wrote in-depth mathematical treatments of the fringe projection method, and Case *et al.* (1987) described the relationship of this technique with optical triangulation. The fringe projection technique shares many of the principles and expressions of moiré techniques, but does not exploit the moiré effect.

In 1969, Brooks and Heflinger introduced the projection moiré technique for optical gauging and deformation measurement as a variation of the fringe projection technique. They placed a second grating in front of the camera, and recorded the moiré fringes resulting from the interference of the projected fringe pattern with the second grating, which they called analyser or reference grating. The technique was developed by several researchers including Idesawa *et al.* (1977), and good theoretical expositions were published by Benoit *et al.* (1975) and later Doty (1983). Projection moiré is a very similar method to fringe projection (and indeed there has been some degree of confusion in the literature) but differs from it in that achieves higher sensitivity by exploiting the moiré effect.

The general principle and theory for point source illumination and central point observation were reported in a series of papers independently published in close sequence in the 1970's by Pirodda (1969), Wasowski (1970), Meadows *et al.* (1970), Takasaki (1970) and Dykes (1971).

This generalisation opened the way to extensive application of the technique for surface contouring of large three-dimensional objects, because it dispensed with the collimating optics.

Meadows *et al.* (1970) observed that the use of finite optics produced contours of varying height, and identified configurations of the optical elements that simplified the expressions. The paper also generalized the theory to gratings with any shape of transmission function that could be described using a Fourier series, in particular the popular square wave grids.

Takasaki published two remarkable papers in 1970 and 1973, where he described his application of the shadow moiré technique to living bodies. In them, he described numerous refinements to improve practical aspects of the technique. He was the first to propose methods to remove harmonics and shadows from the moiré pattern, respectively by using a moving grating and double projection. He also formulated expressions to calibrate the fringe order when using finite optics, and to correct perspective effects. Finally, he also addressed the problem of the distinction between hills and valleys in the moiré pattern.

Dykes (1971) reported the first industrial application of shadow moiré for out-of-plane deformation of large panels in aeronautical industry.

Der Hovanesian and Hung (1971) and Gasvik (1987) developed moiré techniques for vibration analysis. Chiang (1975) proposed the use of a composite grating with two different pitches. Marasco (1975) first used a curved grating in shadow moiré. Benoit *et al.* (1975) presents a detailed mathematical treatment, theoretical review and experimental comparison of moiré and fringe projection techniques for surface contouring. Buitrago and Durelli (1978) described the effects of rotations and translations of the grating, and their effects on the sensitivity of the shadow moiré method.

Pirodda (1982) presented the basic principles and theory of shadow and projection moiré methods using purely geometrical analysis and following a unifying approach. He described the measurement of absolute shape, shape difference between an object and a master, and changes of shape. He also proposed an extensive list of applications and discussed sensitivity, reporting limits of about  $1/10(mm)$  for both shadow and projection in practical cases. By the mid 1980's elementary shadow and projection had reached a point of definite development, and Pirodda (1982) envisioned that future innovations would come from cross-fertilization with other fields, such as combinations with coherent light techniques and computerization.

Post published in 1979 advanced methods based in moiré that used coherent light to achieve very high sensitivity. Moiré interferometry uses a diffraction grating bonded to the surface of the component and a laser interferometer generating a reference grating to reveal the interference fringe patterns when the specimen is stressed. Moiré interferometry falls outside the

scope of this work, which is why only a brief note is included here despite its importance as a high sensitivity testing method. A comprehensive discussion can be found in Post *et al.* (1994).

### ***II.2.1 Major Texts And Review Papers***

Theocaris (1962, 1969) compiled excellent historical reviews of the early work in the field. Guild (1956, 1960), Theocaris (1969), and Durelli and Parks (1970) are long standing texts. Patorski (1993) is more modern and describes the theory thoroughly. Malacara (1992) and Cloud (1998) deal with optical techniques in general, but devote several chapters to describe moiré techniques. Similarly, Kobayashi (1987) and Dally and Riley (1991) include chapters on moiré techniques in the context of experimental stress analysis. In particular, the chapters in the book by Dally and Riley are a good entry point to the subject.

Review papers on moiré techniques include Post (1982), Reid (1984), Halioua and Liu (1989), and more recently, McKelvie (1998).

## **II.3 Basic Principles Of Moiré Techniques**

### ***II.3.1 In Plane Moiré***

The general concepts and nomenclature common to all moiré methods will be introduced in this section for the most intuitive case of in-plane moiré. As already mentioned, moiré patterns are formed by superposition of two regular patterns, typically known as the object or specimen pattern, and the reference or master pattern.

The most common pattern used for stress analysis is an array of parallel straight lines, which is commonly referred to as a grating. Typical values of the line density (*i.e.*, the number of lines per unit length) are between 2 and 40 lines/mm. The pitch of the grating  $p$  is the centre-to-centre distance between the grating lines, and is reciprocal of the line density. Other configurations frequently used are arrays of dots or sets of two perpendicular gratings, usually referred to as cross-gratings.

Conventional in-plane moiré uses a reference grating and an object grating. The object grating can be applied by bonding, etching, ruling, or by coating the specimen with photographic emulsion and contact printing through the reference grating. The reference grating is overlaid by mechanical or optical means in such a way that object and reference gratings are identical in the undeformed state. Upon loading, the specimen undergoes deformation and the object grating deforms with it, while the reference grating remains undeformed. The moiré pattern that results can be related to the displacement field (Dally and Riley, 1991).

Moiré fringes are produced either by rotation of the specimen grating with respect to the master grating or by changes in the pitch of the specimen grating as a result of load-induced deformations. Two alternative approaches exist in the literature to explain the formation of moiré fringes: the geometrical interpretation and the displacement-field approach. A brief summary of these two descriptions follows (see section II.2 for references).

### II.3.1.1 Geometrical Interpretation Of The Moiré Fringes

Let us assume that we superimpose a pair of gratings made of opaque bars and transparent interspaces. A section taken in the direction perpendicular to the plane of the gratings is shown in fig. 2.1 to illustrate the formation of moiré fringes. The gratings are illuminated from below with an incident light beam of uniform intensity  $I_o$ . The shadowed areas in the figure represent areas where the opaque bars in either the reference or the model gratings block the transmission of light. If both gratings are identical and aligned, as shown in fig. 2.1(a) the transmitted intensity presents a series of regular bands of intensity  $I_o$  and width one half of the pitch. The transmitted intensity is averaged over small regions of size  $d$ , which represents the smallest size that can be resolved with the viewing system, *i.e.* the area corresponding to one pixel in the CCD detector, a grain of the camera film, or the resolution of the human eye. If the system we use to view the pattern has a resolution of the same order of magnitude or larger than the pitch  $p$  of the gratings, the transmitted intensity appears as a uniform grey field of one half the intensity of the incident beam.

In fig. 2.1(b) the model is subjected to uniform deformation in the direction perpendicular to the lines of the grating, which is normally referred to as the primary direction, and as a result exhibits a deformed pitch  $p'$ . The transmission occurs now as a series of bands of different width depending on the overlap of opaque bars and interspaces of the two gratings. Maximum transmission (viewed as a brighter fringe when the light is averaged over the resolution length  $d$ ) occurs where the interspaces of the two gratings are aligned. Conversely, dark fringes appear where opaque bars in one grating are aligned with interspaces in the other.

Inspection of fig. 2.1(b) indicates that a bright fringe forms when the specimen grating undergoes a deformation in the primary direction of the grating equal to the pitch  $p$  of the master grating. On the other hand, deformation in the direction parallel to the lines (secondary direction) does not produce moiré fringes. If we number the fringes consecutively, the relative displacement  $u$  between master and model gratings in the primary direction is

$$u = Np \tag{2.1}$$

where  $N$  is the order number assigned the moiré fringe, and  $p$  is the pitch of the master grating.

Moiré fringes also form when gratings of identical pitch are rotated with respect to one another. The moiré fringes appear in a direction that bisects the obtuse angle between the lines of the gratings, as shown in fig. 2.2(a). The relationship between the angle of relative rotation  $\theta$  and the inclination of the fringes  $\phi$  is

$$\theta = 2\phi - \pi \quad (2.2)$$

If we consider an arbitrary point on the surface of the deformed specimen, rotation and change in pitch of the specimen grating occur simultaneously, producing a moiré pattern such as the one shown in fig. 2.2(b). The inclination  $\phi$  and the spacing  $\delta$  of the moiré fringes can be measured in this pattern and used to determine the pitch of the specimen grating  $p'$  in the deformed state and the angle of rotation  $\theta$  with respect to the reference grating. The expressions for  $\theta$  and  $p'$  in the general case can be found in Morse *et al.* (1960). For small rotations, those expressions reduce to

$$\begin{aligned} \theta &= \frac{p}{\delta} \\ p' &= \frac{p\delta}{p \pm \delta} \end{aligned} \quad (2.3)$$

Once  $p'$  has been obtained, the component of normal strain in the direction perpendicular to the lines of the master grating can be written as:

$$\varepsilon = \frac{p' - p}{p} \quad (2.4)$$

### II.3.1.2 Displacement Field Approach

Inspection of eq. (2.1) shows that a moiré fringe is a locus of points that exhibit the same component of displacement in the primary direction of the master grating (*i.e.* perpendicular to the lines). Although that expression was derived for uniform deformation and no rotation, the observation applies as well to the general case (Cloud, 1998).

The value of the displacement varies as a function of position in the field of view  $u=u(x, y)$ . This expression conceptually defines an imaginary surface, where the height of a point on the surface above a plane of reference would represent the component of displacement of the point in the primary direction of the master grating. The moiré fringes can be thought of as contours of this imaginary surface that represents the field of displacement.

In the practical application of the moiré method, two moiré fringe patterns are usually obtained with the specimen and master grating oriented perpendicular to the  $x$  and  $y$  axes in order to obtain the  $u$  and  $v$  components of displacement. This can be achieved placing mutually

perpendicular gratings on the two halves of a symmetric model, or by using two separate models, or by means of separate  $u$  and  $v$  master gratings to interrogate a cross-grating bonded to the specimen.

The Cartesian components of strain can be computed from the derivatives of the displacements, and therefore, moiré can be used to measure strain as well as displacement. The following equations are valid for the case of small strains, and similar expressions can be derived for the case of large strains (Dally and Riley, 1991).

$$\begin{aligned}\varepsilon_{xx} &= \frac{\partial u}{\partial x} \\ \varepsilon_{yy} &= \frac{\partial v}{\partial y} \\ \gamma_{xy} &= \frac{\partial u}{\partial y} + \frac{\partial v}{\partial x}\end{aligned}\tag{2.5}$$

Note that the out-of-plane displacement gradients  $\partial w/\partial x$  and  $\partial w/\partial y$  are normally not considered in moiré analysis of in-plane deformation fields.

The direct displacement gradients  $\partial u/\partial x$  and  $\partial v/\partial y$  are obtained from the slopes of the displacement surfaces in the primary direction of the master grating, usually with acceptable accuracy. In theory, the cross derivatives  $\partial u/\partial y$  and  $\partial v/\partial x$  could also be obtained from the slopes of the displacement surfaces in the direction parallel to the lines of the master grating. However, this is very difficult in practice when the  $u$  and  $v$  fringe patterns are obtained from separate model or master gratings, because slight misalignments produce large changes in the fringe pattern due to rotation.

Two methods have been proposed to eliminate this shear-strain error. The first method makes use of cross-gratings on the specimen and master to obtain two simultaneous displays of the  $u$  and  $v$  displacement fields, so that the contribution of any rotational misalignment to the cross derivatives is equal and opposite for the two fields and cancels in the shear-strain determination. This idea was first suggested by Weller and Shepard (1948), and developed by Post (1965), who suggested using cross gratings with different pitches to produce two distinct families of moiré fringes and prevent interweaving.

The second method is an application of the rosette concept commonly employed with strain gauges (Dally and Riley, 1991). Three model gratings are employed perpendicular to the  $x$ ,  $y$  and  $n$  axes, where  $n$  is usually  $45^\circ$  with respect to the  $x$ -axis. The three normal strains  $\varepsilon_{xx}$ ,  $\varepsilon_{yy}$ ,  $\varepsilon_n$  can be determined at every point from the direct derivatives, and from them the complete state of strain at the point can be calculated using the rosette equation.

$$\gamma_{xy} = 2\varepsilon_{45} - \varepsilon_{xx} - \varepsilon_{yy} \quad (2.6)$$

### II.3.2 Out-Of-Plane Moiré

This section describes the use of moiré techniques for the measurement of three-dimensional shape, surface orientation and out-of-plane displacement. Some of the most widely used variations of the method are described, including shadow moiré, reflection moiré, projection moiré and the fringe projection technique, which is very closely related to projection moiré although it does not strictly make use of the moiré effect.

#### II.3.2.1 Shadow Moiré

Shadow moiré is the oldest, and possibly the simplest technique that makes use of the moiré effect to measure surface shape. It was first proposed by Weller and Shepard in 1948, and developed by Theocaris (1964a, 1964b).

In the basic configuration shown in fig. 2.3(a), a master grating of pitch  $p$  is placed just in front of the object of interest, and is illuminated obliquely so that it casts a shadow onto the surface. When the object is viewed through the grating from a different direction, the interference between the grating and its shadow produces a moiré pattern that contains information about the shape of the object. There are no great requirements on the surface finish, although light coloured, matte surfaces produce the best fringe contrast.

The simplest analytical case arises when we assume that the light source  $S$  and viewer  $C$  are at infinity, (i. e. parallel illumination and viewing). This can be achieved in practice by means of collimated illumination and a camera with telecentric optics, and in many cases, it is a good approximation provided the light source and camera are located far away from the object. The grating is illuminated at incidence angle  $\alpha$  and viewed at observation angle  $\beta$ . The direction of observation is usually taken normal to the grating, or symmetrical to the illumination with respect to the normal.

The shadow of point  $P$  in the grating is cast onto point  $P'$  on the object, which is seen by the viewer superimposed with point  $Q$  in the grating. Examination of fig. 2.3(a) shows that the elongation of the shadow cast onto the object can be treated as a lateral shift of the object grating so that the following relation between height  $z$  and fringe order  $N$  can be written

$$z = \frac{Np}{\tan \alpha + \tan \beta} \quad (2.7)$$

where  $\alpha$  and  $\beta$ , are respectively the illumination and viewing angles, and  $p$  is the pitch of the master grating. A rigorous derivation of this expression can be found in the literature (e.g.

Takasaki, 1970 or Meadows *et al.* 1970). Equation (2.8) implies that the moiré fringes represent contour lines corresponding to sectioning the surface with equispaced planes parallel to the grating. The contour interval and hence the sensitivity of the method is given by

$$C = \frac{p}{\tan \alpha + \tan \beta} \quad (2.8)$$

It is difficult to illuminate large objects with collimated light, so it is also important to consider the case of diverging optics (i. e. finite illumination and viewing distances). In the most general case the fringes represent curved contour surfaces (*e.g.* Takasaki, 1970, Meadows *et al.* 1970 or Pirodda, 1982). A simplified case where these contour surfaces become planes arises when the light source **S** and viewing centre **C** lie in a plane parallel to the grating. In this case, the planes present variable spacing that increases with the fringe order as follows

$$z = \frac{Nph}{d - pN} \quad (2.9)$$

where  $d$  is the distance between **S** and **C** and  $h$  is the distance from the grating to the plane where **S** and **C** lie.

Note that if  $z/h \ll 1$  and  $p/d \ll 1$  one can write

$$z = \frac{Nph}{d} \quad (2.10)$$

which yields again equispaced contour planes. Equation (2.11) can also be derived from eq. (2.8) by noting that when **S** and **C** are at a finite distance  $h$  from the plane of the grating, the angles  $\alpha$  and  $\beta$  change for every point in the surface, but assuming  $z \ll h$  the expression  $\tan \alpha + \tan \beta$  is approximately constant and equal to  $d/h$ .

This technique can be employed to determine absolute shape, or to monitor out-of-plane deformation. However, it is necessary to determine the displacement of at least one point (i. e. assign the zero order fringe) either from theoretical considerations or by another experimental method, so that the displacements of all other points on the surface can be referred to this point.

The main limitations of this technique are that the grating needs to be at least the same size of the object of interest, and must be kept very close to the surface to prevent diffraction effects.

### II.3.2.2 Reflection Moiré

The reflection moiré method for mapping slope contours was first introduced in 1954 by Ligtenberg. The technique was later developed by various other researchers including Bradley (1959) and Kao and Chiang (1982).

The basic experimental arrangement is shown in fig. 2.3(b). The specimen must have a polished surface to act as a mirror. A large master grating is placed at a distance  $h$ . The camera is set up behind a hole in the centre of the grating, and focused on the virtual image of the grating reflected on the surface of the object. A first image is collected of the unloaded object, so that the reflected image of point  $Q$  in the grating is seen at point  $P$  on the object. The object is deformed so that point  $P$  in the specimen moves to  $P'$ , and because the curvature has changed, the image reflected corresponds now to point  $Q'$  in the grating. A second exposure is taken, producing a moiré pattern in the double-exposure image, where the fringe order can be related to the slope of the specimen plate as follows (Cloud, 1998):

$$\theta_x = \frac{Np}{2h} \quad (2.11)$$

This technique allows direct measurement of slopes and curvature of surfaces, therefore eliminating one differentiation of the experimental data in the determination of strain, but is very limited in that it can only be applied to specimens with a mirror-like surface finish.

### II.3.2.3 Projection Moiré

In contrast with the shadow technique described in the previous section, the projection moiré method introduced by Brooks and Hellfinger (1969) requires two different gratings. In the simplest configuration a grating is imaged on the surface of the specimen by means of a projecting lens, and another grating is placed in front of the viewer. Alternatively, the projected fringes can be produced by interference of coherent light.

Shadow and projection moiré differ in their application, but are theoretically very similar and can be studied using a unified approach (Pirodda, 1982). In-depth mathematical treatments of projection moiré including both infinite and finite optics, and with emphasis on the differences compared to shadow moiré and the limitations imposed by optical systems have been published by Benoit *et al.* (1975) and Doty (1983).

Figure 2.4(a) shows the basic configuration of projection moiré. A virtual plane has been defined for convenience in front of the surface. Provided that (i) the projected and analyser grating are matched and (ii) the reference plane is chosen parallel to the projected grating, there is a perfect equivalence between this system and the shadow moiré configuration described in the previous section, as can be seen by comparing figures 2.3(a) and 2.4(a).

Projection moiré is useful for remote and/or large objects, and the resulting fringe pattern is easier to process automatically by introducing shifts in the analyser grating as discussed in section II.4.3. Projection moiré normally requires finer gratings than shadow, but also much smaller in size.

There are two geometries of projection moiré, as shown in fig. 2.5(a). The parallel optical axes configuration (e.g. Idesawa *et al.*, 1977) results in planar contours but it is awkward to build practically, requiring a large distance so that the projected grating falls in the field of view of the camera. On the other hand, the crossed optical axes configuration (e.g. Doty, 1983) is simpler to attain, but produces non-planar contours. It has also been suggested the use of gratings with variable pitch to obtain plane contours with the crossed axes configuration (Pirodda, 1982), although this severely limits the flexibility of the method.

The double projection technique is a variation in which two gratings are projected onto the surface from two different illumination angles, generating a moiré pattern onto the object that can be directly observed without the need for an analyser. (e.g. Cabaj *et al.*, 1974, Halioua *et al.*, 1983). Other advantages of this configuration over the single projector scheme are that it can produce shadowless moiré fringes and allows normal viewing of the surface without loss of sensitivity. On the other hand, it requires accurate alignment of the two fringe projectors, and the additive moiré pattern obtained with this technique has poorer contrast than the multiplicative moiré formed in shadow and single projection moiré (Doty, 1983). A schematic of the double projector configuration is presented in fig. 2.5(b).

#### **II.3.2.4 Fringe Projection**

The fringe projection technique for surface topography, pioneered by Rowe and Welford (1967), also entails projecting a grating onto an object and viewing it from a different direction, much like in single projection moiré. Indeed, both methods can be described by a single theory and the fundamental expressions are very similar. The main difference is that the shape information is measured directly from an image of the projected fringes instead of viewing through an analyser grating to produce a moiré pattern. The projected fringes represent inclined sections of the surface, so that the surface contours can be obtained by subtracting a reference plane (Malacara, 1992). Out-of-plane displacements and changes in shape can also be measured by subtracting the surface contours of the object in the initial state (*i.e.* the reference surface) from those of the final state (*i.e.* the object surface).

Such differential measurements of shape can also be achieved easily by using double exposure photography to superimpose two images of the fringes projected onto the specimen in the initial state (*i.e.* the reference image) and the final state (*i.e.* the object image). The interference of the two images yields moiré fringes that correspond with contours of out-of-plane displacement. This variation of the technique can be used as well to measure absolute shape if a flat plate is used as reference, in which case the fringes represent depth contours. The double exposure technique takes advantage of the moiré effect, albeit without an analyser grating, and is somewhere between projection moiré and fringe projection.

An alternative is the 'Fourier transform profilometry' (FTP) technique, introduced in 1983 by Takeda and Mutoh, in which the reference and object images of the projected fringes are combined and processed directly in the computer without generating interference moiré fringes.

The methods that use the moiré effect provide higher sensitivity, because only the moiré pattern and not the grating lines need to be resolved by the camera, thus finer gratings can be used. However fringe projection has the advantage that the optics are less complicated and there is no need for accurate matching of the projecting and viewing gratings, providing a very convenient technique for contouring relatively coarse objects.

In the following, the mathematical expressions of fringe projection will be described in some detail, considering both the telecentric (*i.e.* viewing and observation at infinity) and non-telecentric cases. A schematic diagram of the elements in a typical fringe projection system is shown in fig. 2.6. A master grating  $G$  (top left) is projected using the projector lens  $E'_p-E_p$  onto the object of interest (bottom). A camera (top centre) is used to view and record images of the fringe pattern projected onto the object.

The optical axes of the projector ( $E'_p-E_p$ ) and the camera ( $E'_c-E_c$ ) lie on the plane of the figure and intersect at a point  $O$  near the object surface. The coordinate system  $xyz$  was chosen with origin in  $O$ ,  $z$  on the camera axis (positive towards the camera),  $x$  on the plane of the figure, and  $y$  normal to the plane of the figure. A fictitious reference plane  $R$  was defined at  $z=0$ .

The optical elements are positioned so that  $E_c$  and  $E_p$  (respectively the centres of the pupils of the camera and projector) are located at the same distance  $h$  from the reference plane, and separated from each other a distance  $d$ . The camera lens  $E'_c-E_c$  images the reference plane  $R$  onto the sensor plane  $S$ .

The lines of the master grating  $G$  are parallel to the  $y$ -axis. An image of the grating is formed by the projector lens on the image plane, which is perpendicular to the projector axis and passes through the origin  $O$ . The pitch of the fringes projected on this plane,  $p$  can be calculated from the pitch of the master grating,  $P$  and the position of the centre of projection.

When  $E_p$  is at infinity (telecentric projector, denoted by  $E_\infty$  in the figure) the image of the grating projected onto the reference plane  $R$  ( $z(x, y)=0$ ) is a regular pattern of frequency  $f=1/p=\cos\alpha/p_o$ . If, for the sake of simplicity, we assume that the transmission function of the grating is sinusoidal, the intensity distribution of the image seen by the camera would be

$$I(x, y) = \frac{1}{2} (1 + \cos(2\pi fx)) \quad (2.12)$$

However, if  $E_p$  is at a finite distance, then the image of the grating will be distorted and the pitch will vary with  $x$ . Note that a ray through a point  $A$  on the image plane cuts the reference

plane  $R$  at point  $\mathbf{B}$  in the telecentric case. However, in the non-telecentric case, the ray will cut at point  $\mathbf{C}$ . The intensity distribution of the camera image can be written in this case as

$$I(x, y) = \cos(2\pi f(x + s_o(x))) \quad (2.13)$$

where

$$s_o(x) = \overline{\mathbf{BC}} \quad (2.14)$$

Note that  $s_o(x)$  is a function of  $x$ , and is positive when  $\mathbf{B}$  is to the left of  $\mathbf{C}$ , as in the figure. For convenience, we express eq. (2.13) as a spatially phase-modulated signal

$$I(x, y) = \cos(2\pi f x + \Phi_o(x)) \quad (2.15)$$

where

$$\Phi_o(x) = 2\pi f s_o(x) = 2\pi f \overline{\mathbf{BC}} \quad (2.16)$$

This implies that the optical configuration shown in fig. 2.6 yields non-planar contours unless telecentric (collimating) optics are used.

For an arbitrary surface described by the function  $z=z(x, y)$ , the ray  $\mathbf{E}_p\text{-}\mathbf{A}$  hits the surface at point  $\mathbf{H}$ , which will be seen as point  $\mathbf{D}$  in the reference plane when observed from the viewpoint  $\mathbf{E}_c$ . Hence, the deformed grating will be seen as

$$I(x, y) = A(x, y) + B(x, y) \cos(2\pi f(x + s(x))) \quad (2.17)$$

where  $A(x, y)$  and  $B(x, y)$  are respectively background and modulation terms that models an arbitrary distribution of reflectivity on the object surface. Again, we can write the expression above as a spatially phase-modulated signal

$$I(x, y) = A(x, y) + B(x, y) \cos(2\pi f x + \Phi(x)) \quad (2.18)$$

and

$$\Phi(x) = 2\pi f s(x) = 2\pi f \overline{\mathbf{BD}} \quad (2.19)$$

Note that  $\mathbf{E}_p\mathbf{H}\mathbf{E}_c$  and  $\mathbf{CHD}$  are similar triangles, hence

$$\overline{\mathbf{CD}} = \frac{zd}{h-z} \quad (2.20)$$

and

$$\overline{\mathbf{CD}} = \overline{\mathbf{BD}} - \overline{\mathbf{BC}} = \frac{\Phi(x)}{2\pi f} - \frac{\Phi_o(x)}{2\pi f} = \frac{\Delta\Phi(x)}{2\pi f} = \frac{zd}{h-z} \quad (2.21)$$

Rearranging this expression we obtain

$$z = \frac{h\Delta\Phi}{\Delta\Phi - 2\pi fd} \quad (2.22)$$

and substituting  $f$

$$z = \frac{\left(\frac{\Delta\Phi}{2\pi}\right)ph}{d - \left(\frac{\Delta\Phi}{2\pi}\right)p} \quad (2.23)$$

Note that eq. (2.23) is perfectly equivalent to eq. (2.10), the formula derived for shadow moiré in classical texts such as Meadows *et al.* (1970) or Takasaki (1970), except that  $\Delta\Phi/2\pi$  takes the place of the fringe order number  $N$ . Equation (2.23) provides an interpretation of the modulated phase  $\Phi$  as a generalization of the fringe order number to the continuum domain. Also, the description provided by eq. (2.17) of the fringe pattern as a phase-modulated signal is the basis for the phase measurement techniques for fringe analysis that will be discussed in section II.4.3. These methods combine a reference and an object image to extract the phase terms and calculate the phase difference  $\Delta\Phi$ , and then apply eq. (2.23) to obtain surface height.

The previous derivation is not valid for the differential measurement of out-of-plane displacements between two non-flat surfaces, since the reference plane terms do not cancel out when we subtract two instances of eq. (2.23). Therefore the measurement of out-of-plane displacements between two non-flat surfaces requires combining each of the two surfaces with a reference plane to calculate two separate maps of phase difference, and then subtracting the depth maps calculated with eq. (2.23).

The following simplification of eq. (2.23) is valid when  $z/h \ll 1$  and  $p/d \ll 1$ , and yields equispaced planar contours

$$z = \frac{hp}{d} \frac{\Delta\Phi}{2\pi} \quad (2.24)$$

With this expression, equivalent to eq. (2.10), it is possible to perform differential measurements by directly combining the two images without the need for a flat reference.

### II.3.3 Other Moiré Methods

A range of techniques to enhance the sensitivity of moiré methods has been proposed in the literature. For instance, mechanical sharpening of the fringes can be achieved by using particular combinations of reference and model gratings with different widths of bars and

spacings, called complementary gratings. (Dally and Riley, 1991). Also, diffraction methods have been used for sharpening and multiplication of the moiré fringes in order to increase the sensitivity (Guild, 1956). The use of a slotted mask inside the camera lens has also been proposed to tune the response of the camera, preserving a high resolution at the spatial frequency of the grating over an increased depth of field (Forno, 1988).

Moiré can also be used to obtain derivatives of data encoded in fringe patterns. For instance, the moiré fringes between two superimposed maps of isochromatics obtained with photoelasticity represent the locus of constant change in maximum shear stress with load. Similarly, shifting two patterns of the same load yield the partial space derivatives in the direction of the shift. This subject has been explored extensively (*e.g.* Parks and Durelli, 1966, Post 1965), but has lost part of its appeal with the advent of computers and digital image processing methods.

## **II.4 Fringe Pattern Measurement Techniques**

### ***II.4.1 Introduction***

Many full-field methods in experimental mechanics, including moiré, interferometry, photoelasticity, etc., encode the information about the physical property they measure in a fringe pattern. In the early days, specialist technicians would carefully track the fringes and assign fringe order numbers to extract the information. This was a laborious and time-consuming process, and imposed a serious limitation for the routine use of these techniques.

The situation changed as increasingly powerful computers became widely available, opening the way for fully automated methods of fringe pattern analysis. The field has been very active over the past thirty years, with most methods originating to assist a particular application. Towards the mid 1980's these techniques gradually coalesced into a subject in its own right, which reached a plateau of development in the early 1990's. A good review of digital fringe pattern measurement techniques can be found in Malacara (1992), and the book by Robinson and Reid (1993) constitutes a comprehensive guide to the subject.

There are two main approaches to digital fringe pattern analysis. Intensity-based methods measure fringe patterns on the basis of the image intensity distribution alone, by means of image-processing and pattern-recognition procedures. Phase-extraction methods are a more modern alternative which rely on the measurement of the phase of the fringes and present some advantages over intensity methods. This group can be further subdivided in temporal and spatial phase-measurement methods. In the former, a series of intensity images are recorded over time, and combined to extract the phase information. Spatial phase measurement methods record all the phase information simultaneously, and are therefore well suited to deal with measurements conducted in unfavourable conditions or involving transient events.

The pioneering work on computerization applied to moiré is due to Idesawa *et al.* (1977). Their 'scanning moiré method' was an intensity-based method that allowed the automatic analysis of fringe patterns by finding the fringe centres. Cline *et al.* (1982) and Yagatai and Idesawa (1982) among others also made contributions to this approach.

The 'phase-locked moiré method' by Moore and Truax (1979) was the first application of heterodyne interferometry (*i.e.* point-by-point temporal phase measurement) to moiré. Temporal phase measurement methods for moiré fringes were further developed by Perrin and Thomas (1979), Shagam (1980), and Reid (1984) among others.

Spatial phase measurement was first introduced in projected fringes by Indebetouw (1978) and further developed by Takeda *et al.* (1982), Takeda and Mutoh (1983) and Srivanasan *et al.* (1984, 1985). The 'Fourier transform profilometry' (FTP) technique introduced in 1983 by Takeda and Mutoh remains one of the most popular to date. Roddier and Roddier (1987) further developed the Fourier analysis of fringe patterns for a more general case.

#### **II.4.2 Intensity Methods**

The early attempts at digital analysis of fringe patterns were mainly intensity-based methods (Idesawa *et al.* 1977, Cline *et al.* 1982, Yagatai and Idesawa, 1982). These methods work by locating the fringe centres, which represent surface contours, and assigning fringe order numbers. Fractional fringe order numbers at points between fringe centres must be obtained by interpolation.

Intensity based methods present several shortcomings:

- The data is available only at the fringe centres, therefore interpolation using a polynomial fitting is required to extract data at an arbitrary point in the field of view.
- The sign of the fringe order is undetermined, thus additional information is needed to distinguish between hills and valleys.
- These techniques are very sensitive to noise in the input data.
- Assigning fringe order numbers is a very difficult task to automate without a priori knowledge of the result, and often needs to be done interactively

Despite these drawbacks, intensity methods remain in use for some specialized applications (*e.g.* Cardenas *et al.*, 1994). Sometimes phase measurement methods are not viable, for instance for the analysis of fringe patterns retrieved from photographic records, or obtained in situations where it is impractical to introduce a carrier (*e.g.* some time average holographic and speckle interferographic techniques). These techniques are also useful when the measurement is repetitive and there is a priori knowledge of the result, so that a simple and efficient intensity

method can be designed. For instance Der Hovanesian *et al.* (1972) used this approach to design a quality control system based on projection moiré with a pass/no pass type output.

The basic procedure involves three main steps:

1. Pre-processing of the images to reduce the effect of noise, to which intensity methods are very sensitive. Pre-processing normally involves a combination of histogram adjustment to improve fringe contrast, and filtering or smoothing to reduce noise. Median filtering is sometimes used to remove spike noise while preserving fine detail.
2. Detecting the fringe centre lines. The first of two main strategies is to convert the grey level image into a binary image by choosing an appropriate threshold, and then apply image-processing operations such as erosion and thinning to reduce the fringes to their centre lines. The main difficulty lies in choosing the right threshold for a general case. A second approach is to work directly in the grey level image to find the locus of the fringe maxima (or minima), either by scanning the whole image or by tracking fringes one by one. Grey-level based methods tend to be more sensitive to noise but can be more precise. Polynomial curve fitting of the skeletonized image is also normally required with either approach.
3. Assigning fringe order numbers, either interactively (Yagatai and Idesawa, 1982) or automatically (Cline *et al.* 1984). In both cases some a priori knowledge is required to determine the sign (*i.e.* to distinguish hills from valleys in the contour map) and the zero order fringe.

If data is required at points that do not coincide with the fringe centres, it is necessary to perform two-dimensional interpolation using for instance a least squares fitting or bi-cubic splines.

### II.4.3 Phase Measurement Methods

Phase-extraction methods constitute a more recent approach to the problem of digital fringe analysis. These methods aim to extract the modulated phase that contains the information encoded in the fringe pattern. This approach is based on the mathematical description of the intensity distribution  $I$  of a fringe pattern introduced in section II.3.2.4.

$$I(x, y) = A(x, y) + B(x, y) \cos(2\pi fx + \Phi(x, y)) \quad (2.25)$$

Where  $A$  and  $B$  respectively account for the variation of background illumination and fringe modulation,  $f$  is the carrier frequency, and the modulated phase  $\Phi$  is the term related to the physical property encoded in the fringe pattern. The goal of phase-extraction techniques is to measure the modulated phase  $\Phi$  of a fringe pattern.

Phase-measurement techniques have a number of advantages over intensity-based methods. They provide full-field data and higher (sub-fringe) sensitivity, and eliminate the need for interpolation. They also provide better immunity to noise and automatic distinction between hills and valleys, overcoming the problems associated with intensity-based fringe analysis. They do not require the assignment of fringe numbers, and it is easier to design fully automated methods without a priori knowledge of the result. In addition, they are free from errors due to spurious fringes caused by higher order harmonics.

Phase measurement methods can be classified in two main groups, depending on the procedure they use to introduce the phase carrier (Huntley, 1998).

Temporal phase-shifting techniques introduce known constant shifts to the phase content of the whole fringe pattern. These phase shifts are normally achieved by means of a suitable device, known as a phase shifter, that applies a controlled tilt or displacement to the master grating. These techniques combine a set of phase-shifted images recorded over a period of time to calculate the phase, providing excellent accuracy. They are also very easy to automate. The main shortcomings from the point of view of industrial applications are the need for very exact mechanical displacements and calibration of the shifter, and the fact that data collection takes place over a period of time, which makes these techniques very sensitive to vibration and generally unsuitable for transient applications.

In contrast, a second group of techniques known as spatial phase shifting allow the collection of all data at the same time. The phase can be processed in the spatial domain, using convolution, or in the frequency domain, using the Fourier transform (FT), the latter being probably the most popular method for fringe analysis at present. The main disadvantages of spatial phase extraction methods are that the computations are normally very involved, and there is a loss of resolution in the direction of the phase shift because the calculated phase is averaged over a fringe period. In addition, spatial methods have difficulty dealing with discontinuous patterns, such as those resulting from the measurement of shapes with negatives or steps.

Up to now, the trend was generally favourable to the development of devices based in temporal phase-measurement, and in fact almost all commercially available systems are based in this technology. This is mainly because long processing times and low-resolution recording devices hindered the development of spatial phase-measurement methods. However, these barriers are disappearing as computer processing power and sensor array sizes continue growing exponentially, and the trend is likely to change, because the limitations of temporal phase-measurement with respect to transient events and sensitivity to vibration are more difficult to overcome.

#### ***II.4.4 Phase Unwrapping***

The need for phase unwrapping arises from the fact that the phase is not a physical, measurable signal in itself, but a property of a measurable signal, which in this case is the intensity distribution of the fringe pattern. The phase is a property related to the spatial or temporal wavelength of the intensity map, and thus influences the intensity map only through phase principal values, that is, only those values that lie between  $\pm\pi$  radians.

Although the phase cannot be directly measured, it is possible to extract the phase principal values by performing mathematical operations on the intensity maps. The principal values are commonly referred to as wrapped phase in this context. The wrapping operator  $W\{\}$  is a non-linear operator that can be defined as follows

$$W\{\Phi\} = \Phi + 2\pi L \quad (2.26)$$

where  $L$  is an integer function that forces  $-\pi < W\{\Phi\} \leq \pi$ .

The unwrapping problem is concerned with obtaining an estimate of the continuous phase map  $\Phi$ , associated to the physical property of interest, from the discontinuous wrapped phase  $W\{\Phi\}$  that can be calculated by means of any of the phase-extraction methods mentioned in the previous section.

The phase values are typically obtained from an arctangent operation, and therefore appear wrapped within the range  $(-\pi, \pi)$ , with  $2\pi$  discontinuities at the end of the periods. A simple approach to the problem is to detect these jumps and add appropriate multiples of  $2\pi$  to the wrapped phase until it is made continuous. However, the implementation of this simple method in reality can be problematic even in the 1-D case, due to the presence of noise and singularities that may create false jumps. Since the signals are treated in the discrete domain, a low sampling frequency may also cause the failure of the unwrapping algorithm due to aliasing. In two or more dimensions, all these effects make the unwrapping process path-dependent.

A number of algorithms have been developed to perform phase unwrapping in two dimensions. Research on this field is very active (e. g. reviews by Malacara, 1992, Judge and Bryanston-Cross, 1994, or Huntley, 1998), the leading authority probably being Ghiglia and Pritt, 1998.

Unwrapping algorithms can be broadly classified in two groups. Path-following algorithms fundamentally use local operations at pixel level to determine the unwrapping path. The Goldstein algorithm, the quality-guided methods, the mask-cut algorithms, and Flynn's minimum discontinuity technique fit in this group. A second type of algorithm uses a global approach to the problem, seeking to minimize some measure of the difference of gradients

between the wrapped and unwrapped phase. This group includes the minimum  $L^p$  -norm, the least squares, the Fourier transform (FT), and the multi-grid algorithms.

Ghiglia and Pritt (1998) provided references, a detailed description, and software implementations of each of these state-of-the-art unwrapping algorithms, and also presented a ranking of the algorithms using memory requirements, computation time and grade of success as criteria to characterize their performance. The FT and Goldstein algorithms proved to be the fastest, but not very reliable, and at the other end of the scale Flynn's and  $L^p$ -norm were found to be very robust but extremely time consuming. The quality-guided algorithm scored third in terms of reliability and memory requirements, and fourth in speed, and can be considered good trade-off.

## II.5 Review Of Applications Of Moiré Techniques

### II.5.1 Shadow Moiré

The first applications of the shadow moiré method were largely restricted to the laboratory, and in the field of experimental mechanics. They included plate deformation problems, buckling of shells and torsion with Prandtl's analogy (Weller and Shepard, 1948, Theocaris, 1964a, 1964b, and Pirodda, 1969).

Some early industrial applications were reported in the aeronautical industry for the out-of-plane deformation of large panels *ca.* 2(m) in size, using shadow moiré, (Dykes, 1971, and also Vestergren and Knutson, 1978). Performance requirements were not very strict, and therefore the techniques were used in their simplest form.

Pirodda, (1982) suggested the potential to apply moiré to dimensional metrology, and on-line inspection of mechanical parts, by comparing with a master by differential contouring.

There have been diverse industrial applications of shadow moiré, including:

- Dimensional control of large parabolic reflectors for microwave radiation (Takasaki, 1982).
- Study of vibrations using the time-averaged method (Reid, 1984).
- Contouring of impact craters (Andrews, 1982).
- Measuring the shape of tyre sidewalls (Weissman, 1990).
- Measuring the thickness of water films beneath an aquaplaning tyre (Browne, 1982).

In addition, the shadow moiré method has found considerable application in medicine, for human body measurement in orthopaedics (Ikeda and Terada, 1981) and to monitor chiropractic adjustments (Brand and Gizoni, 1982). The shadow moiré method has been widely used in

Japan for early detection of scoliosis among school children, and Canada has adopted a nation-wide screening for a spinal deformity in five-year-old children (Pekelsky, 1986). Also, morphometric studies of the feet have been reported with the shadow moiré technique (Soares *et al.* 1982). Dirck and Decraemer (1991) used shadow moiré to study the deformation in the tympanic membrane under static pressure load conditions.

A range of new methods have lately been developed to enhance the standard shadow moiré method. Wang *et al.* (1998) recently proposed a novel technique for the interpretation of fringe patterns based in frequency shifting, as opposed to the more commonly used phase-shifting method. Also Arai & Yokozeki (1999) suggested a procedure to improve the accuracy of the method, by considering the influence of the harmonics caused by the master grating in the moiré profile.

A method for the measurement of the transient deformation in a material under impact was developed using high speed photography and shadow moiré by Kokidko *et al.*, (1997), which provides knowledge of the entire deformation field and its time history for the material under study.

The shadow moiré technique has also found application for the measurement of surface topography and warping due to thermal stresses in printed circuit boards (Stiteler and Ume, 1997, Ume, 1998).

More recently, the shadow moiré technique has been successfully applied in an industrial environment to monitor buckling modes of failure and high-speed impact tests of aircraft parts (Burguete, 2002).

### ***II.5.2 Projection Moiré***

One of the first industrial applications of projection moiré was the study of vibration and shape deformation of turbine blades by means of differential double exposure (Dessus and Leblanc, 1975). Also, this method is very useful for differential studies of mechanical elements by comparing them with a master. The use of an analyser grating, which corresponds to the master, enables the detection of dimensional errors during the production process (Pirodda, 1982). The same author also suggested the potential of projection moiré for large scale remote testing, such as load testing of building structures in civil engineering and architecture, monument surveying, and even aerial land mapping. The technique is in principle only limited by the illumination power available.

The projection moiré method is also suitable for the quality control of components from the car, aircraft and ship building industry, specially in cases with high requirements of tolerance and parts resulting from manufacturing processes difficult to control such as high temperature

forming, welding, powder moulding, etc. However, literature on this field seems relatively scarce (e.g. Der Hovanesian *et al.*, 1972)

Video techniques have extended the application of projection moiré to the field of automation and the automation of technological processes, like CNC machining (Harding and Tait, 1986). The study of small deformation and changes in shape in objects with significant profile depth and measuring highly curved structures have been investigated by Harding *et al.*, 1988.

Projection moiré topography is also an important tool in medical and biological studies since it matches well the requirements both in sensitivity and accuracy (Bauman and Herron, 1989). A projection moiré system for the detection of surface defects in panels has also been recently patented (Boehnlein, 1994).

Kim *et al.* (1999) and Sciammarella *et al.* (2001) have developed automatic shape measurement methods for the sake of reverse engineering, based respectively on projection moiré with phase-shifting fringe analysis and fringe projection. The measuring range and resolution can be adjusted to suit the application, by varying the pitch of the moiré gratings. These systems are significantly faster than coordinate measurement machines (CMM) and can achieve comparable accuracies in the micrometer range.

There are some instances of shape measurement systems based on projection moiré, which are commercially available for some applications. The Triform (Wicks & Wilson Ltd.) range of scanners, based in the work by Reid *et al.* (1984), are used in medicine and as a training aid by athletes, to monitor changes in body shape. Oreb *et al.* (1992) developed an optical surface profiler for the minting industry at CSIRO (Australia). Both systems are relatively bulky and heavy, in order to provide the stability required by the use of temporal phase stepping techniques for the analysis of the fringe patterns.

## **II.6 Critical Analysis Of The Literature**

This section attempts to highlight, by direct reference to the literature review presented in the previous sections, the main reasons that explain the somewhat limited adoption of existing moiré methods for routine industrial use, and the main areas that require development to address this issue.

### ***II.6.1 Specimen Gratings For In-Plane Moiré***

The main disadvantage of in-plane moiré is the effort and skill required in the preparation of the specimen grating. Also, all the methods described in the literature are invasive, in that the grating must be bonded, etched, printed etc. onto the object. In many cases this would permanently damage the specimen. In other cases this is simply not practical. There is a need for

a non-invasive technique to generate specimen gratings for the measurement of in-plane displacements.

Instances of potential applications of such technique could be found in the glass, plastics, paper, textile industries, as well as in biological sciences, to perform *in vivo* tests.

### ***II.6.2 Simplicity And Robustness Of The Experimental Apparatus***

Most of the experimental apparatus described in the literature requires assembly on an optical bench, in order to isolate the equipment from vibrations and also to allow precise positioning of the optical elements to calculate the calibration parameters.

There is a need for a simple, inexpensive instrument, made of standard components, and robust so that it can stand vibration and work in adverse conditions. Most of the hardware designed for temporal phase extraction and phase unwrapping methods of analysis fall outside this category. These instruments incorporate piezoelectric actuators and delicate mechanisms to generate phase shifts by displacing elements of the optics with sub-micrometer precision. The purpose-made optical assemblies add to the cost and complexity of the instruments and decrease their robustness.

### ***II.6.3 Computational Algorithms For Fringe Analysis***

Industrial applications require a highly automated algorithm that can be operated by a non-specialist for the processing of the fringe patterns. Most intensity-based methods are inadequate because they require user intervention to aid the fringe tracking and numbering in any other than very simple cases.

Temporal phase stepping algorithms are very accurate and fast but require collection of data over a period of time, and are therefore ill suited to situations in which the equipment cannot be isolated from vibrations or the object of interest is moving, as is often the case in industrial applications.

Spatial algorithms can deal with this problem but are computationally very involved, to the point that in many cases it has been necessary to implement them in hardware to achieve acceptable processing times. This is becoming increasingly less of a concern in view of the exponential growth experienced by available computer power over the last years.

Probably one of the most popular fringe analysis methods today is the Fourier transform method (Takeda, 1983). However, this method presents one major drawback in the fact that frequency leakage results in major errors that are difficult to identify by a non-specialist. This method requires very careful implementation and the design of filter windows is difficult to automate.

Spatial methods that process the data in the spatial domain appear particularly promising because they have only been limited up until now by the resolution of the detector. However, the size of standard CCD detectors has continuously increased in the last few years, opening the way for this type of solution, in a similar case to what is happening to digital image correlation algorithms. This approach has been recently followed by a number of researchers, and the field remains very active (*e.g.* Shough *et al.* 1990, Chan and Bryanston-Cross, 1995, Sutton *et al.* 2001).

#### ***II.6.4 Flexibility Of The System And Calibration Methods***

A consequence of the requirement for flexibility and portability of the instrument is that it is no longer possible to guarantee that the optical elements remain in a fixed, known configuration (*e.g.* attached to an optical bench). It is therefore necessary to develop simple procedures to quickly calibrate the system without the need for long set-up times.

#### ***II.6.5 Requirements On Surface Finish And Lighting Conditions***

Moiré techniques in general work in the visible light spectrum and rely on the interference of light to create the fringe images. In shadow, projection moiré and fringe projection the surface of the object should ideally be clear and matte, to enhance the contrast of the fringes. The presence of other light sources may reduce the contrast and impair the visibility. A dark colour, an uneven surface finish, the presence of marking or other artefacts, all may cause problems. In industrial situations it is not always possible to control these factors, and there is a need for methods to deal with poor quality images.

Image processing techniques to enhance the images may be one way of solving this problem, as well as improving the fringe processing algorithms to make them less sensitive to these effects. Alternatively, it has been suggested that since the surface emissivity and transmittance have spectral dependence, the use of the infrared spectrum of light may extend the applicability of these methods to dark (high emissivity) surfaces and translucent or transparent bodies (high transmittance).

### **II.7 Formal Statement Of The Problem**

Moiré techniques are very versatile and relatively simple to implement. However, most of the applications described in the literature have been developed in the controlled environment of a laboratory. In order to apply these techniques in an industrial environment, it is necessary to develop tools and methodologies that are robust and reliable, simple to use, easy to calibrate, and inexpensive.

The recent advances in illumination devices (LCD projectors), image acquisition devices (CCD detectors) and computer equipment for image processing, open the way for new developments of these techniques. There is also significant scope for the combination of moiré techniques with other techniques for experimental stress analysis and non-destructive evaluation, in situations where two or more techniques provide complementary information about the object under study.

The aims of this research can be summarized as follows

- To develop the tools and procedures required for the fabrication of flexible, robust and low cost systems based on moiré techniques for the measurement of location, shape, and deformation of arbitrary objects, in both static and transient situations, and with the focus placed on industrial applications.
- To explore the combination of moiré techniques with other techniques from the fields of stress analysis (*e.g.* photoelasticity), non-destructive evaluation (*e.g.* infrared thermography), or machine vision (*e.g.* laser triangulation).

## **II.8 Objectives**

The general aim of this research can be reformulated into four measurable objectives

1. To design, build and test new experimental apparatus that is more portable, robust, and simpler to use, and to provide it with the flexibility required to perform measurements under a wide range of conditions, addressing the limitations discussed in sections II.6.2 and II.6.4.
2. To design new computational algorithms for fringe analysis to make it a faster, more reliable, and fully-automated process so that it can be conducted by a non-specialist, and to deal with the issues discussed in sections II.6.3 and II.6.5.
3. To conceive a simple and foolproof methodology for the calibration of the system, the data collection and the interpretation of results, which addresses the issues described in II.6.4.
4. To develop a new experimental technique for strain measurement, based on a combination of concepts from moiré techniques and thermography, to overcome the limitations of the existing technology described in sections II.6.1 and II.6.5.

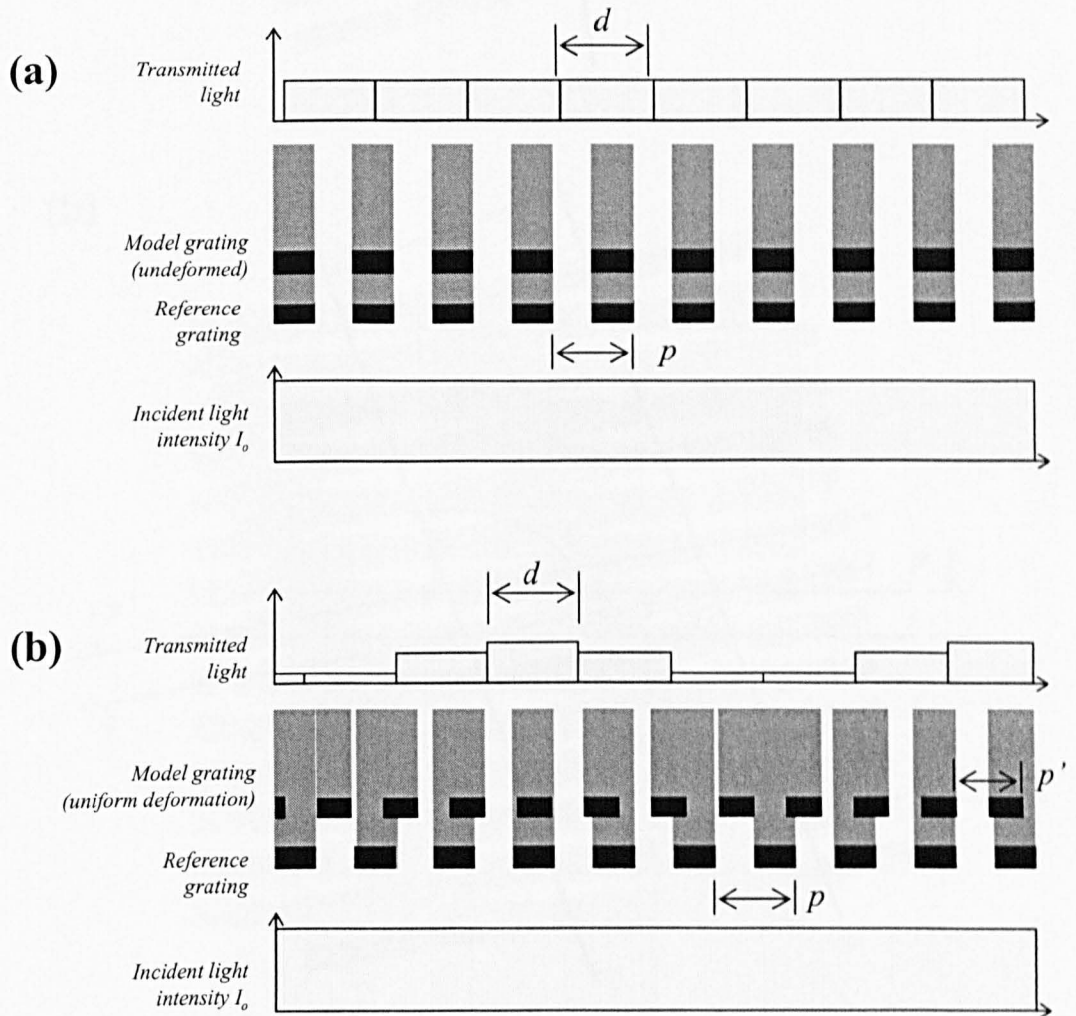


Figure 2.1: Geometrical interpretation of the formation of moiré fringes. (a) Transmission of the light through a pair of identical reference and model gratings made of transparent and opaque bars that run perpendicular to the plane of the figure (b) Formation of moiré fringes when the model grating undergoes uniform deformation in the horizontal direction.

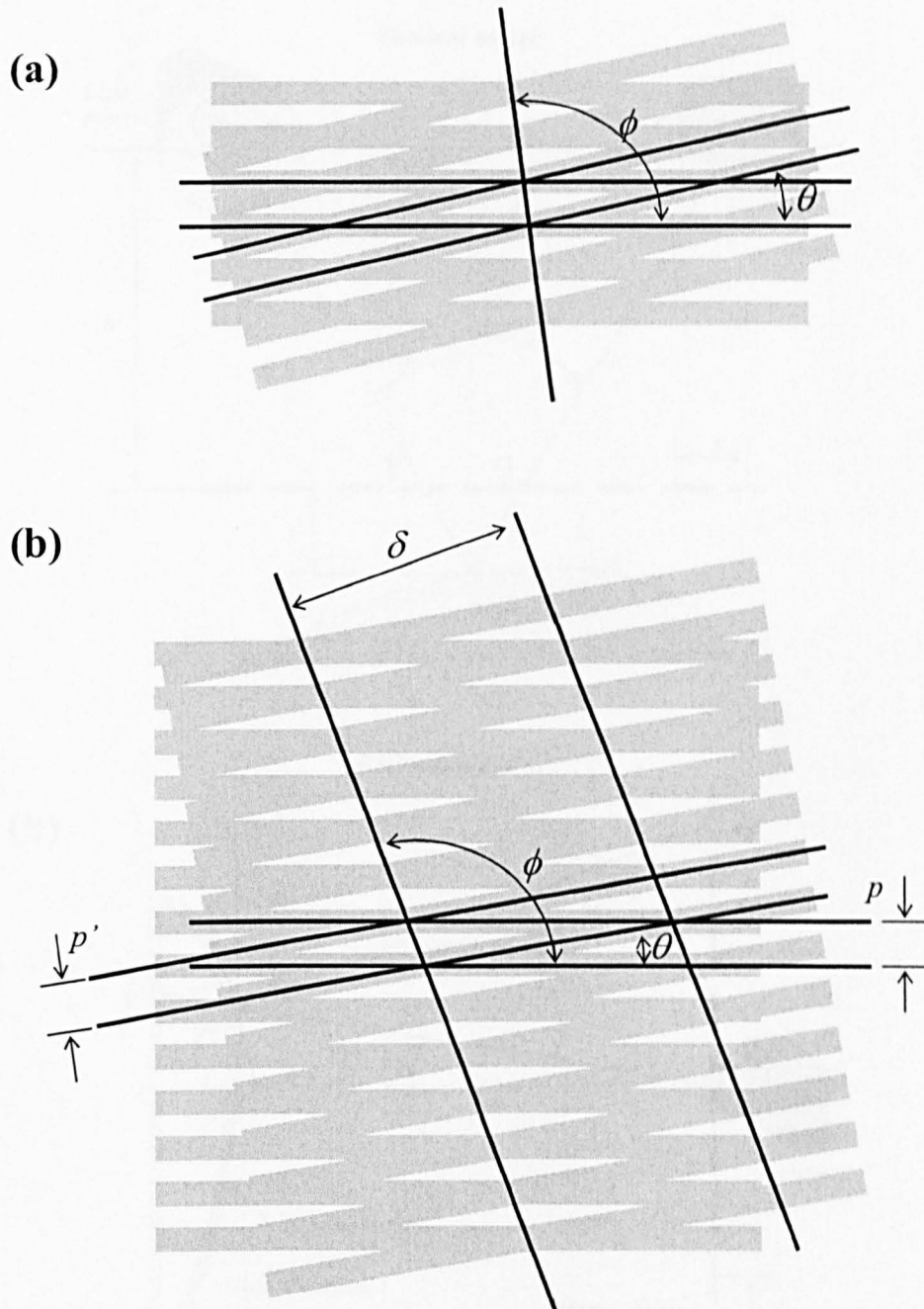


Figure 2.2: Geometrical interpretation of the formation of moiré fringes. (a) Formation of moiré fringes due to rotation. (b) Combined rotation and deformation of the model grating. The superposition of a reference grating of pitch  $p$  and a model grating of pitch  $p'$ , rotated an angle  $\phi$  with respect to the reference, yields a pattern of moiré fringes with a spacing  $\delta$  and orientation  $\theta$ .

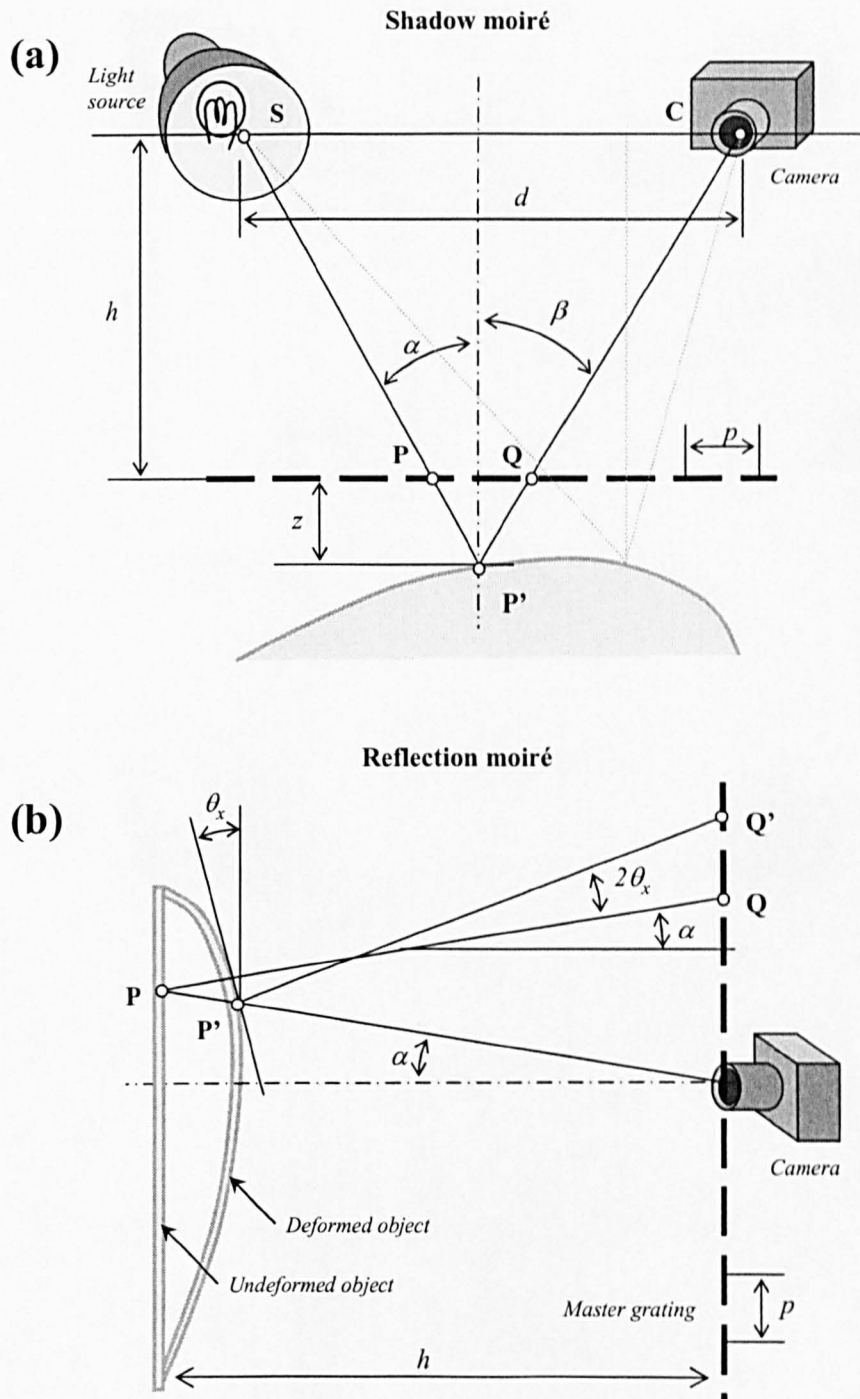


Figure 2.3: (a) Shadow moiré basic configuration (b) Reflection moiré basic configuration

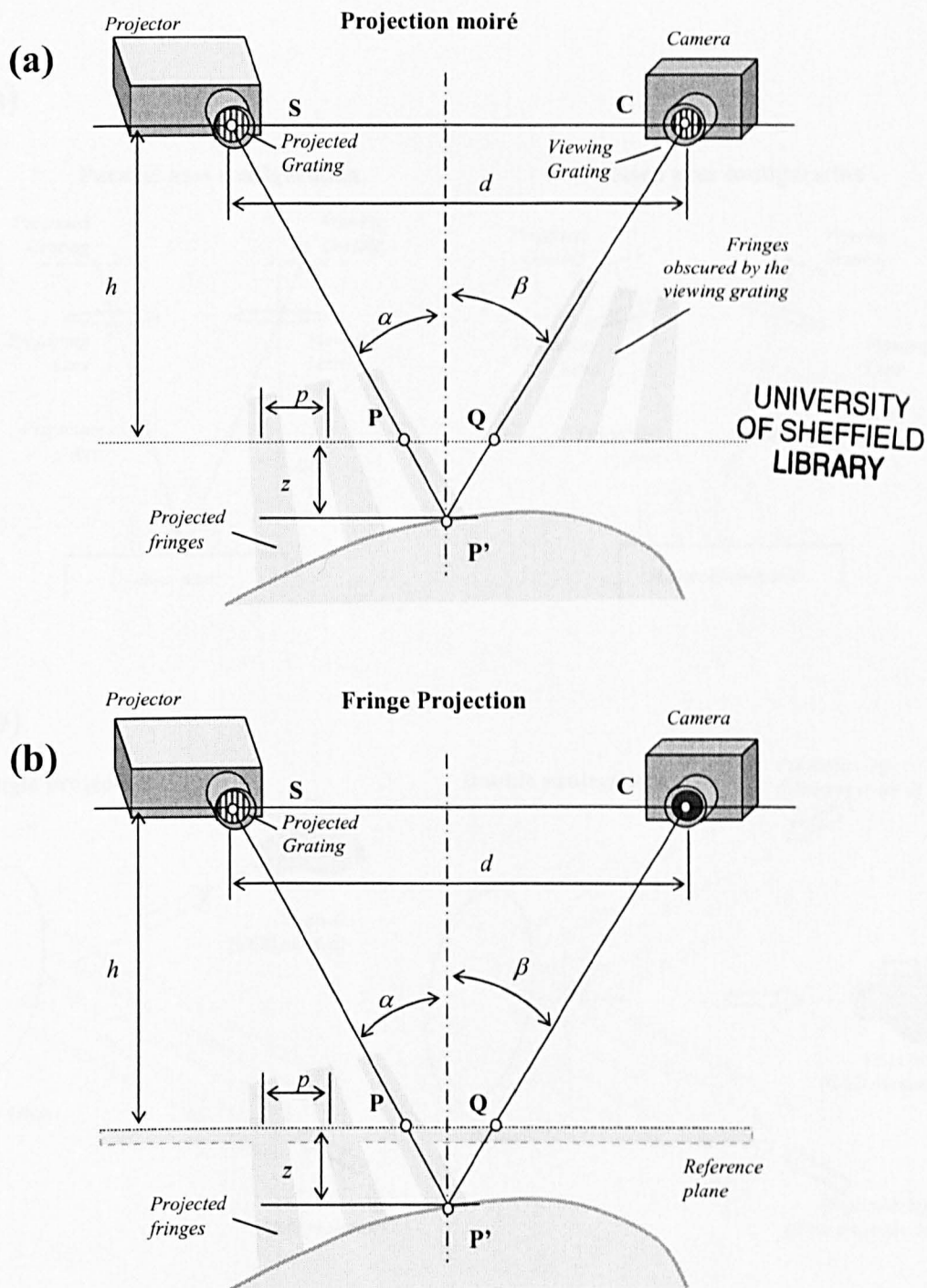
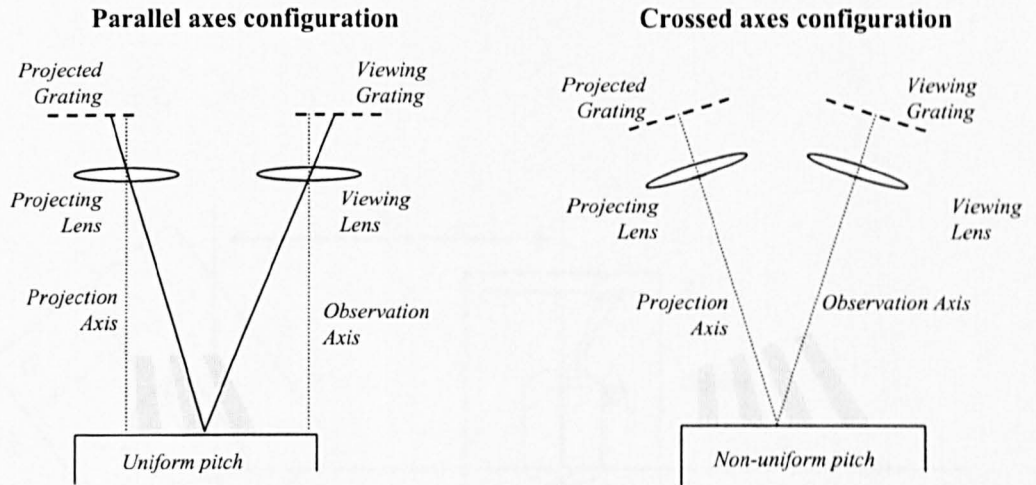


Figure 2.4: (a) Basic configuration of projection moiré. Note the parallelism with the shadow technique in fig. 2.3(a). (b) Basic configuration of fringe projection, which only differs from (a) in that it does not use a viewing grating. An image of the fringes projected on a reference plane may be superimposed with the object image by means of double-exposure photography to produce moiré fringes.

(a)



(b)

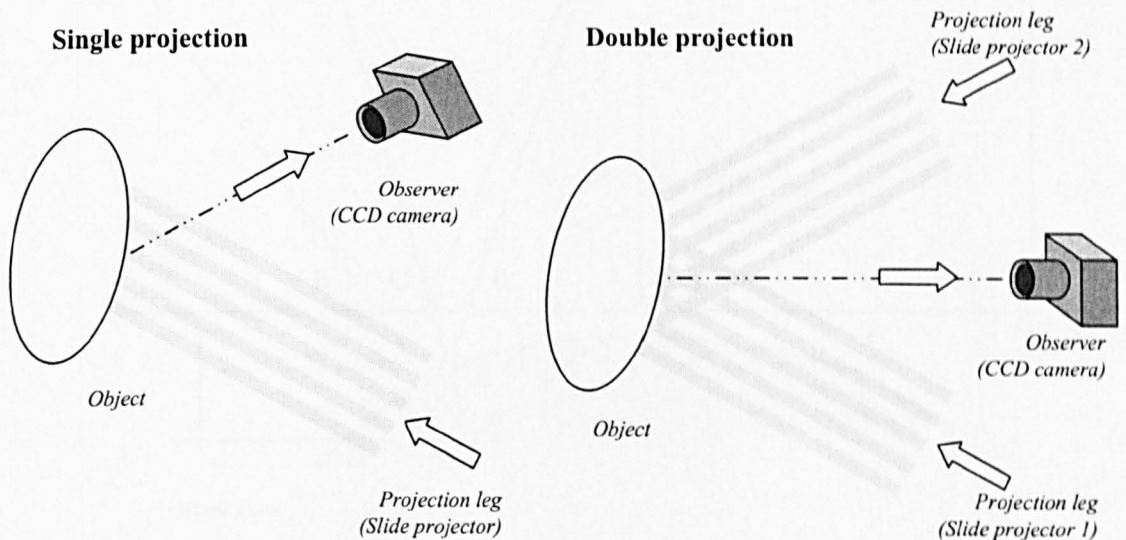


Figure 2.5: (a) Parallel axes and crossed axes configurations of the projection moiré and fringe projection techniques. The latter is easier to build but the contours are curved because the projected and the analyser gratings are not parallel. (b) A simple projection moiré or fringe projection configuration versus the double projection configuration.

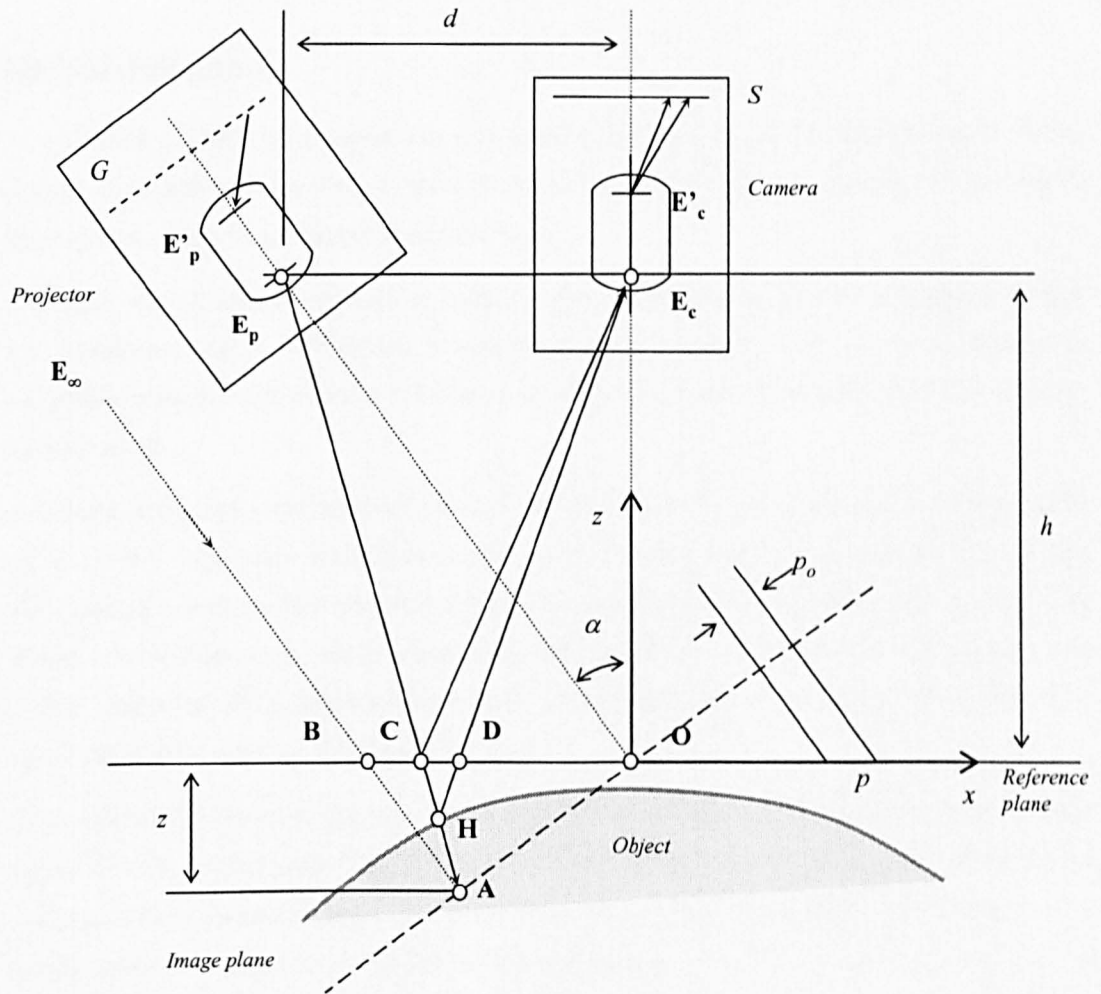


Figure 2.6: Schematic of the optical configuration for the fringe projection technique.

## CHAPTER III

# DETECTION OF SURFACE DEFECTS

### III.1 Introduction

This chapter presents the development of a handheld device for the detection of small surface defects in aircraft as a simple case study that illustrates the process of adapting moiré methods from the laboratory to an industrial environment.

The outer skin of aircraft, exposed to wear and tear and accidental damage during their service life, undergoes regular inspections in search of surface defects, such as impact damage in composite panels or corrosion in metallic parts, which may compromise the structural integrity of the aircraft.

In-service inspections are frequently carried out in less than ideal conditions, as illustrated in fig. 3.1. Very large areas need to be inspected, often with severe time constraints. As a result, the intensive use of conventional non-destructive evaluation (NDE) methods such as ultrasonic waves or eddy currents is usually impractical and expensive. A common practice is to carry out a visual inspection of the entire structure, and restrict the use of conventional NDE techniques to areas where there is visual evidence of damage.

The visibility threshold is the size of the smallest defect that can be detected by the means available with a sufficiently high degree of confidence. The size of surface defects is usually defined as the maximum vertical deviation from the nominal shape (depth if the defect is an impact crater, or height if the defect is a protuberance). A common accepted value for the visibility threshold in unaided visual inspection is  $300(\mu m)$ . When a defect larger than the threshold size is found, an in-depth inspection and possibly a repair of the component is necessary.

The underlying assumption is that defects below the visibility threshold will not pose a significant risk to the structural or functional integrity of the component. In other words, the structure must be designed to cope with any defects that could pass unnoticed during inspection.

The main drawback of this approach is the low reliability of unaided visual inspection. The method is prone to human error, hence the large value of  $300(\mu m)$  for the visibility threshold. This imposes severe constraints on design. A reduction of the visibility threshold will allow the design of lighter and therefore cheaper structures without compromising safety.

A research project was carried out in this context and within the frame of the Brite/Euram Project BE 97 – 4057 INDUCE (Advanced Integral NDE Concepts for Unified Life Cycle), under Sub-Task 4.2.1 on '3D Moiré For External Defects Inspection Applicability'. The main objective of the project was the development of a non-destructive technique based on moiré methods to aid in the detection and monitoring of surface defects such as impact damage under the visibility threshold (BVID) in composites; and of corrosion on the surface and under lap-joints in metallic parts, during in-service inspections of aeronautical structures. The partners directly involved in this task were EADS-CASA and Universidad Complutense de Madrid (UCM) in Spain, and BAe Systems and the University of Sheffield in the United Kingdom. In the following we will refer to this piece of work as a case study that exemplifies well the process of adapting moiré methods from the laboratory to an industrial environment.

The project requirements specified that the new technique should lower the visibility threshold down to  $50(\mu m)$ . Quantitative assessment of these defects may then be carried out using conventional NDE methods. The new technique ought to allow the performance of fast, reliable and cost-effective inspections. It was of prime importance to retain the speed, cost-efficiency and simplicity of unaided visual inspection, while significantly increasing the reliability and sensitivity.

Two deliverables were planned in the original project description: a simple, qualitative device for manual inspection, and an instrumented device for quantitative computer-aided inspection. An initial prototype of the manual device was presented in November 1999 by the author. This prototype was optimised during the following three months, and a second version equipped with a flexible grating was built and tested. The second version of the instrument, presented to partners of the project in April 2000, allowed manual inspection of curved surfaces according to the project requirements.

At this point in the project, a proposal for broadening the original scope of the task in order to avoid duplication of effort between partners of the consortium was presented and subsequently accepted. This entailed the introduction of a new related application, which will be discussed in detail in Chapter VI. As a result of the shift in objectives, EADS-CASA and UCM continued to develop the second deliverable (the instrumented device for quantitative computer-aided inspection), while BAe Systems and University of Sheffield switched their attention to the new application.

The following section presents a summary of the project requirements, as described by EADS-CASA in an internal report of the consortium (INDUCE CR-2210-CASA-02). Subsequent sections of this chapter describe the work carried out by the author for the INDUCE project on behalf of the University of Sheffield, including the design and construction of laboratory prototypes, experimental tests, validation and discussion of the results.

The automatic technique for defect measurement described in section III.6 was developed by the author outside the INDUCE project as a means to validate the results.

## **III.2 Requirements**

### ***III.2.1 Surface Defects***

#### **III.2.1.1 Defect Typology**

The scope of this research includes two different types of surface defects typically found during in-service inspections of aeronautical structures:

- Barely visible impact damage under the visibility threshold on composite panels. Carbon fibre composite materials are becoming increasingly popular for the manufacture of aeronautical structures such as wings, horizontal tail planes, or control surfaces. These large surfaces are exposed to in-service accidental damage due to the impacts of hailstones, birds, tools dropped during maintenance work, or stone debris during landing and take off. These impacts can damage the fibres of the composite, cause delamination or initiate a crack, potentially compromising the structural integrity of the component. It is not uncommon that the outer face of a damaged panel would only show a small impact crater, even when the panel has undergone extensive damage.
- Corrosion of metallic parts. Corrosion plays a major role in the structural integrity of metallic structures. Superficial corrosion can be easily monitored using visual inspection, but there are situations when the corroded surface is hidden, such as under lap joints, which are extensively used in aircraft. In these situations, the accumulation of corroded material under the lap causes a small protuberance in the surface. The ability to detect these protuberances would provide a tool for the early diagnosis of corrosion.

#### **III.2.1.2 Size Considerations**

The defects within the scope of this project were associated with deviations from the nominal shape of the surface, indentations in the case of impact craters on composites and protuberances related to corrosion on metals. The main requirements of the inspection device are summarised in Table III-1.

The vertical resolution of the technique gives an indication of the size of the smallest vertical deviation that can be detected in the surface under inspection, and determines the visibility threshold. The initial requirement on vertical resolution was set to  $50(\mu\text{m})$ , which represents a six-fold reduction of the visibility threshold when compared with the technology previously available.

<i>Parameter</i>	<i>Requirement</i>
<i>Vertical resolution</i>	<i>50 <math>\mu\text{m}</math> or better</i>
<i>Indication area</i>	<i><math>\approx 8 \text{ mm}^2</math></i>
<i>Area inspected in a single frame</i>	<i>At least <math>62500 \text{ mm}^2</math></i>
<i>Lateral resolution</i>	<i>300 <math>\mu\text{m}</math> or better</i>
<i>Admissible curvature of the inspected surface</i>	<i>Curvature radius <math>\geq 1500 \text{ mm}</math></i>

**Table III-1: Main requirements**

The indication area can be defined as the area of the minimum detectable defect. The area of a  $50(\mu\text{m})$  indentation produced using a  $25(\text{mm})$  hemi-spherical indenter (*i.e.* approximately  $8\text{mm}^2$ ) was used as an estimation of the typical indication area to ensure that the requirements on indication area and vertical resolution were consistent.

In order to cope effectively with the large dimensions of real aircraft parts the instrument should be capable of covering a reasonably large inspection area in a single frame. An area of  $62500(\text{mm}^2)$  was considered sufficient to obtain an adequate inspection speed. This corresponds to a square area of  $25$  by  $25(\text{cm})$ , although there was no restriction on the shape of the inspection area for the manual device. In the case of the instrumented device however, the recommendation was that the selected shape should optimise the use of the CCD detector array.

A requirement on the lateral resolution was also specified for the instrumented device planned as a second deliverable, which was eventually developed by other partners. Based on a typical commercially available  $800 \times 600(\text{pixels})$  CCD device and the estimated value of the inspection area ( $62500\text{mm}^2$ ), a value of about  $300 \mu\text{m}$  should be obtainable, which equals to around 60 pixels to describe the indication area ( $8\text{mm}^2$ ).

### ***III.2.2 Inspection Surfaces***

#### **III.2.2.1 Geometry**

The main interest was focused on large aeronautical parts, which generally present a smooth surface, with either flat or gently curved shape. However, the presence of fasteners, rivets or other common elements must also be taken into account.

The original project specifications covered only flat or cylindrical shapes, and the minimum radius of curvature was specified at 1500(*mm*) for the most unfavourable case. Both these conditions were considered reasonable for the majority of large parts in commercial aircraft. It was also stipulated that inspection would take place on the convex side of the component, as is typically the case for most parts during in-service inspections.

Some aircraft parts, such as leading edges and many components of military aircraft, fell outside this category because they present smaller radii of curvature and/or a more complex geometry (e. g. curvature in more than one direction).

#### **III.2.2.2 Surface Finish**

Aircraft components are typically painted and/or treated according to the particular use of the aircraft, and therefore the inspection technique should cope with a variety of surface finishes. There is an influence of the surface colour on the detection capability of the technique. Ideal conditions correspond to a matt light colour that improves the contrast of the fringes. Three cases were considered during the tests:

- White or light grey colours are common finishes that can be considered as a favourable case.
- During the assembling stage components are coated with primer. This primer may be light green or beige and corresponds to a neutral situation.
- Dark liveries (e. g. dark blue corporate colours of certain airlines, or black sometimes used by military aircraft) represent a challenge due to poor fringe contrast, and were considered an unfavourable situation.

### ***III.2.3 Operational Conditions***

In-service inspections are carried out under routine maintenance conditions (see fig. 3.1), which can be summarised as follows:

- Limited access, requiring the use of platforms;
- Imperfect cleaning (dirt or grease on components);

- Inspection may be performed either outdoors or inside a hangar, thus poor lighting and inclement weather must be taken into account;
- Other maintenance operations take place simultaneously on the aircraft.

The design of the inspection device had to account for the above factors, and also incorporate the following points:

- Possibility of autonomous operation with batteries;
- The inspection device should be safe and easy to operate;
- The device should allow detection of defects in real-time. Quantitative assessment however could be performed offline.
- Possibility of full control of the inspection device by one operator alone, hence maximum simplicity, and minimum size and weight.

### III.3 Materials And Methods

#### III.3.1 Description Of The Samples

The three samples shown in fig. 3.2 were provided by BAe Systems for use in this project. These carbon fibre composite panels had calibrated indentations produced by dropping a ball bearing to simulate impact damage below the visibility threshold.

Figure 3.2(a) shows a flat composite plate (sample S1), 2(mm) thick and 145×300(mm) in dimensions. Three different surface finishes were applied to the specimen as shown in fig. 3.3(a), to evaluate the performance of the technique on the different cases defined in the requirements. From left to right in the image, the surface of the sample was painted in black (*i.e.* an extreme instance of the unfavourable case), medium grey (*i.e.* neutral case) and light grey (favourable case). Two indentations by ball bearing impact were produced in each one of the three areas of the sample. Figure 3.3(b) shows an ultrasound scan of the panel, also provided by BAe Systems, in which the dark areas reveal the location of the impacts.

Sample S2, shown in fig. 3.2(b), was also a flat carbon fibre plate. The dimensions of this second specimen were 700×500(mm) and 4(mm) in thickness. It was coated in medium grey paint, (*i.e.* neutral case) which provided adequate fringe contrast. The specimen had five calibrated indentations produced by ball bearing impacts. The location of each defect in the panel and the energy of the impacts are indicated in fig. 3.4. Close-up photography of the impact craters gives an indication of how difficult is the visual detection of such defects even in optimal conditions.

Finally, Figure 3.2 (c) shows a curved carbon fibre panel. This specimen was a real component from the outer skin of the Eurofighter Typhoon aircraft (sample S3), which was tested by special request of BAe Systems. The surface of the specimen was uncoated and had a number of calibrated indentations distributed over the outer surface and indicated by chalk marks, as shown in the top left detail of fig. 3.2.

### ***III.3.2 Surface Profilometry***

It was expected that the depth of the impact craters would increase with the energy of the impact, but the actual geometry and size of a particular defect is affected by any inhomogeneities present in the composite material. A profiling device (Surtronic 3+, Taylor Hobson Precision, UK) was used in this research to provide independent quantitative measurements of the impact defects, in order to validate the inspection technique under development.

A profilometer works by drawing a diamond stylus across the surface and measuring its vertical displacement as a function of position, as shown diagrammatically in fig. 3.5(a). A ruby skid riding on the surface itself is used as a reference for these measurements, which facilitates set-up and reduces the effects of vibration.

The stylus and the skid move together in the measurement direction but are independent in their vertical movement. An inductive transducer detects vertical movement of the stylus relative to the skid with a resolution of  $0.01(\mu m)$  over a gauge range of  $300(\mu m)$ , and converts it to an electrical signal. The profile data were downloaded onto a PC and processed using commercial software (Talyprofile for Windows v2.0.6, Digital Surf, UK).

The elements typically used to describe surface texture are roughness (short wavelength imperfections), waviness (longer wavelength deviations) and form (general shape of the surface), as illustrated in fig. 3.5(a).

The profilometer is mainly intended for the analysis of surface roughness. The skid has a large radius to prevent movement in and out of the roughness characteristics of the surface, which the diamond stylus, with a tip radius of  $5\mu m$ , follows closely. Hence, the skid acts as a mechanical filter for any undulations of the surface with a wavelength longer than its diameter of  $4.6(mm)$ , as illustrated in fig. 3.5(b).

The procedure had to be adapted to perform measurements of the impact craters, because they typically have a diameter in the same order of magnitude as the ruby skid. Normally, the measurement is performed in a direction aligned with the axis of the pickup; see fig. 3.5(b). In order to prevent mechanical filtering of the crater shape, a  $0.55(mm)$  thick steel feeler gauge was attached to the surface of the sample close to the impact, and the pickup was mounted at 90

degrees angle from the measurement direction. Hence the pickup slid over the flat surface of the feeler gauge, instead of the actual surface of the sample, as shown in fig. 3.5(c)

The measurements were performed in each case across the diameter of the impact crater, using a traverse length of 16(mm), a speed of 1(mm/s), a sampling length of 2.5(mm), and setting the vertical range to 300( $\mu\text{m}$ ).

The technique presented some limitations in this application, mainly due to the fact that the instrument had not been primarily designed for this purpose

- Some data sets appeared tilted and had to be corrected in the software. This could be due to a misalignment between the pickup arm trajectory and the feeler gage used as datum, so that the distance between the sensor and the contact point of the arm and the gage varies linearly during the measurement.
- The accuracy of the measurement of the impact size (*i.e.* the maximum depth of the defect) depended on the skill of the operator in aligning the device so that the scan trajectory included the deepest point of the impact crater. The defect size was defined as the maximum depth of at least three measurements in each case.

## **III.4 Experimental Apparatus**

### ***III.4.1 Technique Selection***

The range of experimental techniques available for shape and out-of-plane deformation measurement include retroreflection, profilometry, triangulation, speckle interferometry, shearography, holography, digital image correlation, moiré and fringe projection techniques. The requirement in this case was for a fast, simple, inexpensive technique, with a potential for a wide application field.

The D-Sight system (LMI Technologies Inc., Delta, British Columbia, Canada) is a portable system based on an optical double-pass retroreflection technique that allows detection of indents with depths in the range of 0.01 to 0.05(mm). This technology however does not allow defect measurement, requires a thin liquid film known as highlighter (e.g. turpentine) to work in non-specular surfaces, needs shielding from environmental light, and has difficulties dealing with surface roughness and curvature in the direction of observation (Heida and Bruinsma, 1998).

Point-scanning techniques such as profilometry and triangulation were ruled out due to speed considerations. Although profilometry was used in this project to validate the results, it is impractical for in-service inspections. Interferometry, shearography and holography present a narrow range of conditions for applicability, with difficult set-ups and comparatively high costs. Fringe projection and digital image correlation are limited in terms of resolution, and require

processing of the input images to produce the height maps which complicates the development of a real-time inspecting device.

In contrast, shadow moiré and projection moiré seemed both strong candidates for this application. Table III-2 summarises the comparison of the two techniques. Projection moiré is non-contacting and potentially able to cope with a wider range of surface shapes, including concave. The main drawback was the relative complexity of the apparatus required. The technique required a camera and a monitor to view the fringe pattern even in the manual device, and a somewhat delicate mechanism for the precise alignment and tilt of the analyser grating. On the other hand, shadow moiré provided high sensitivity and a real-time image using extremely simple and inexpensive apparatus. Its main drawbacks were the need for a large grating and the difficulty of maintaining grating to surface contact.

	<i>Shadow</i>	<i>Projection</i>
<b>Grating pitch</b>	<i>Requires a large grating, but it can be relatively coarse</i>	<i>Uses a smaller grating, but must be very fine.</i>
<b>Apparatus</b>	<i>Very simple, inexpensive and robust</i>	<i>Higher cost and requires precise positioning of viewing grating</i>
<b>Contact</b>	<i>Needs contact with surface: difficult to achieve and not desirable.</i>	<i>Non-contact method: applicable even to concave surfaces.</i>
<b>Qualitative information</b>	<i>Provides a live fringe pattern with just the master grating. Good for manual inspection.</i>	<i>Requires a camera and a monitor to observe the fringe pattern.</i>
<b>Quantitative information</b>	<i>Automated fringe pattern analysis is complex.</i>	<i>Easy to implement reliable phase extraction.</i>

**Table III-2: Technique selection**

Based on its simplicity, robustness and low cost, it seemed preferable to develop the shadow moiré technique for this application, and deal with the issue of designing a grating that could adapt to the curved surfaces of aerospace components.

Similar applications have been investigated in the past by several researchers. Scotese and Huang (1988) developed a small manual device based on shadow moiré for the detection of low energy impact damage on composite panels. Burguete and O'Brien (2001) used a similar principle to develop a 'moiréscope' for the quality control of cold-expanded holes in metallic aircraft components. Both these devices use flat gratings and as a result are limited to small inspection areas when dealing with curved surfaces. Marasco (1975) first suggested the use of curved gratings, but the practical difficulties of manufacturing such gratings have so far prevented the adoption of this approach.

Two prototype devices for Moiré Inspection of Defects on Aircraft Skin (MIDAS) were designed, built and tested during this study, and are described in the following sections.

### III.4.2 MIDAS 1 Prototype

In the basic shadow moiré configuration shown in fig. 3.6(a), a grid of pitch  $p$  is placed at a distance  $d$  from the object of interest. Light projected from the illumination point **S** casts a shadow of the grating over the object. Seen from the observation point **C**, the grating and its shadow interfere producing a moiré pattern from which information about the shape of the object can be extracted. The following expression was introduced in section II.3.2.1:

$$z = CN = \frac{p}{\tan \alpha + \tan \beta} N \quad (3.1)$$

where  $z$  is the vertical deviation of the surface with respect to the grating,  $N$  is the fringe order number and  $C$  is the contour interval or calibration constant of a given system configuration, which was defined in section II.3.2.1 as a function of the illumination and viewing angles  $\alpha$  and  $\beta$ , and the grating pitch  $p$ . The contour interval determines the sensitivity of the technique (*i.e.* the number of fringes per millimetre of vertical deviation). Note that the sensitivity can be increased by reducing the pitch of the grating  $p$ , or increasing the illumination and observation angles  $\alpha$  and  $\beta$ . Good quality gratings with pitches of *ca.* 10-12(mm) can be printed using a professional plotter. A practical limit for the illumination angle  $\beta$  is the angle of total reflection of the material of the grating.

The design of an inspection device for this application presented a number of challenges due to conflicting requirements of sensitivity, compactness and ease of interpretation of the results.

For instance, normal observation ( $\alpha=0$ ) was preferred, in spite of the relative loss of sensitivity with respect to using a large viewing angle, in order to avoid distortion in the images, which makes interpretation more difficult.

On the other hand, the distance  $g$  between the grating and the surface of the object must remain in the same order of magnitude than the pitch of the grating  $p$  to avoid blurring of the moiré pattern. Coarser gratings were therefore preferred because they relaxed this restriction, and also they were easier to manufacture. The use of a large illumination angle was therefore necessary to achieve the sensitivity required by this application.

Another constraint of the method discussed in section II.3.2.1, is that the moiré fringes in the shadow moiré technique represent equispaced plane contours of the surface only if the light source **S** and the viewer **C** lie on a plane parallel to the grating situated at a distance  $h$  above it.

From the point of view of the illumination, this distance  $h$  should be small, particularly if large illumination angles were used. Otherwise the light source would be placed very far way, conflicting with the requirement to keep the device compact. However, if the camera is too close to the object, it would be necessary to use a wide-angle camera lens to view the full inspection area, which would introduce undesirable distortions in the images.

The solution proposed in the first prototype consisted of (i) incorporating a mirror to fold the light path, and (ii) using a miniature CCD camera equipped with a relatively short focal length camera lens of  $4.5(mm)$ , so as to cover the full inspection area. With this arrangement, the light source was located at point S' in the diagram of fig. 3.6(a), achieving the desired combination of normal viewing direction, a large illumination angle, a relative coarse grating and maintaining a reduced overall size of the device so that it could be controlled by a single operator.

Figure 3.6(b) shows a drawing of the MIDAS I prototype with all the main elements. The aim of this instrument was to prove the concepts that would be later developed into the two planned deliverables of the project, namely (i) a qualitative device for manual inspection, and (ii) an instrumented device for quantitative measurement. Table III-3 summarizes the specifications of the MIDAS I prototype.

<i>Technique</i>	<i>Shadow moiré</i>
<i>Inspection area</i>	<i>638cm<sup>2</sup> (290x220mm). Limited to flat surfaces.</i>
<i>Vertical resolution</i>	<i>Up to 40 fringes/ mm (min defect ~2 fringes)</i>
<i>Lateral resolution</i>	<i>~4 pixels/mm</i>
<i>Grating</i>	<i>10lines/mm acetate mounted on a rigid frame. Durable, low cost</i>
<i>Light Source</i>	<i>300W linear halogen-tungsten lamp</i>
<i>Recording device</i>	<i>CCD colour miniature camera with a 4.5mm lens</i>

**Table III-3: MIDAS I prototype**

The prototype included a mount for a miniature CCD camera that allowed registering images for later processing. Figure 3.7 shows an example of typical images recorded using the MIDAS I prototype. The images were taken on sample S1, on the clear finish region indicated in the figure, which gives good contrast for the shadow moiré pattern. The moiré pattern in fig. 3.7(a) was generated using a conventional glass grating with a line density of  $300(\text{lines}/\text{inch})$  i.e. approx.  $12(\text{lines}/\text{mm})$ . Two impact defects are clearly visible in the field of view of the image. Figure 3.7(b) shows an image of the same area using a flexible grating printed on acetate film, with a line density of  $10(\text{lines}/\text{mm})$ . The acetate film provided less contrast, and produced a certain amount of glare. In addition, small inaccuracies in the printing process produced uneven

spacing of the lines of the grating, resulting in faint dark fringes in the direction of the lines of the grating, as shown in fig. 3.7(b). Despite these drawbacks, the acetate gratings proved adequate for the application, in that the defects were clearly visible in fig. 3.7(b). Note that the higher fringe order in (a) is due to the higher line density of the glass grating. However, acetate gratings presented a number of important advantages over conventional glass gratings in this application. They are very light, durable, and inexpensive, but most crucially, acetate gratings are flexible, providing the potential to adapt to curved surfaces.

The acetate grating was fastened to a rigid frame, which was attached to the main u-shaped frame of the device using a spring system to maintain good contact between the grating and the inspection surface.

### III.4.3 MIDAS 2 Prototype

The original MIDAS 1 prototype was tested with the aim of identifying areas for potential design improvements. The results of these tests suggested a number of design changes that were implemented in a new version of the instrument, MIDAS 2. See Table III-4 for a comparison between the main features of the two prototypes and figures 3.8 and 3.9 respectively for concept diagrams and actual photographs of the second version of the instrument. In the second prototype the focus was decidedly on creating a manual instrument for qualitative inspection.

	<i>M.I.D.A.S. 2</i>	<i>M.I.D.A.S. 1</i>
<b>Technique</b>	<i>Shadow Moiré</i>	<i>Shadow Moiré</i>
<b>Inspection Area</b>	<i>740 cm<sup>2</sup>. Flat and curved surfaces</i>	<i>638 cm<sup>2</sup>. Flat surfaces</i>
<b>Light Source</b>	<i>500W linear halogen-tungsten</i>	<i>300W linear halogen-tungsten</i>
<b>Grating</b>	<i>Acetate 10 lines/mm on flexible frame</i>	<i>Acetate 10 lines/mm on rigid frame</i>
<b>Resolution</b>	<i>50 μm ~2 fringes</i>	<i>50 μm ~2 fringes</i>
	<i>4pix/mm</i>	<i>4pix/mm</i>

**Table III-4: Comparison MIDAS 1 vs. MIDAS 2**

During the testing of the MIDAS 1 device it was found that the use of a mirror reduced the intensity of light and hence the contrast of the resulting moiré pattern. With the focus on obtaining good qualitative results rather than accurate quantitative measurements, the limitation on the size of the instrument remained as a priority, but it was not considered necessary that the light source and viewer remained in a plane parallel to the grating. Direct illumination was used to improve the contrast and enhance image quality, and the light source was mounted on a

rotating arm that allowed adjusting the illumination angle. In addition, a more powerful 500(W) light source was installed in the device.

The frame was completely re-designed to reduce the weight and overall dimensions. The system for grid attachment also went through a series of changes in concept, in an attempt to make an instrument that could adapt to convex curved geometries. In the final design the edges of a flexible grid were fastened to a pair of cylinders mounted on the arms of a scissor frame. Figure 3.9(b) shows the prototype in use on a curved panel. The operator applied pressure on the frame, which in turn opened the scissor frame, stretching the grating against the surface of the sample. This concept also allowed the frame to be folded during transport and storage. The size of the inspection area was also increased in the new prototype. The prototype included the miniature CCD camera to record images of the fringe pattern, despite the fact that its main intended use was for manual inspection.

## **III.5 Experimental Results**

### ***III.5.1 Surface Finish Tests***

The ability of the proposed technique to cope with different surface finishes was evaluated in experimental tests using sample S1.

Figure 3.10 shows typical results obtained on a surface with favourable finish. The image in fig. 3.10(a) is a close-up photograph of the light grey region of sample S1. A long exposure and oblique illumination were used to emphasize the surface's texture so that the two impact craters, labelled W1 and W2, can be distinguished in the image. The surface profilometry technique described in section III.3.2 was used to measure the profile of the impact craters across a horizontal middle line of the impacts in the direction West-East as indicated in the figure. The profiles are shown in figures 3.10(b) and (c), where the shaded areas highlight the impact craters. Due to the limitations described in section III.3.2, the accuracy of the measurements of maximum depth was estimated as  $10(\mu m)$ . The measurements of diameter, made on the graphical representation of the profile, were accurate to approximately  $0.2(mm)$ .

This study was repeated for the impacts in the regions of neutral finish (medium grey paint) and unfavourable finish (black paint) and the results are shown respectively in figures 3.11 and 3.12. Note the decrease in visibility of the defects with a darker surface finish.

The results of the study are summarised in Table III-5. Most of the indentations on sample S1 were in the limit of the visibility threshold requirement for the new technique, with the exception of defects W1 and B2, which were slightly above, and defect B1, which fell below that limit.

Figures 3.13(a) and (b) show two typical images collected during inspection with the first prototype of the device (MIDAS 1) respectively on the medium grey (neutral finish) and light grey (favourable finish) regions of sample S1 as indicated in the diagram. Four impact defects are clearly evident in the patterns, showing at least one circular dark moiré fringe. The image on the right shows defects W1 and W2 in the light grey area, and has better fringe contrast and definition than the image on the left, showing defects G1 and G2 in the medium grey region. The images were collected with the miniature CCD camera mounted on the device. The operator of the device can see a similar view directly by observing the component through the grating.

<i>Defect</i>	<i>Surface Finish</i>	<i>Depth (<math>\mu\text{m}</math>)</i>	<i>Diameter (mm)</i>
<i>W1</i>	<i>Favourable</i>	<i>60</i>	<i>6.8</i>
<i>W2</i>	<i>Favourable</i>	<i>47</i>	<i>7.2</i>
<i>G1</i>	<i>Neutral</i>	<i>47</i>	<i>6.0</i>
<i>G2</i>	<i>Neutral</i>	<i>53</i>	<i>5.0</i>
<i>B1</i>	<i>Unfavourable</i>	<i>32</i>	<i>4.2</i>
<i>B2</i>	<i>Unfavourable</i>	<i>65</i>	<i>8.4</i>

**Table III-5: Impact defects on sample S1**

The method however failed to produce adequate results in the region of sample S1 painted in black. The black finish absorbed all the illumination, preventing the formation of moiré patterns with sufficient contrast.

### ***III.5.2 Impacts On Flat Panels***

A second set of experimental tests was performed to evaluate the capability of the technique to provide reliable information about the size of the defects. Sample 2, a flat carbon fibre panel with five calibrated defects produced by ball bearing impact, was used in these tests (see fig. 3.4). The panel was painted in medium grey, considered a neutral situation.

Figure 3.14 shows moiré images of the five calibrated impact defects. The images were collected with the miniature camera mounted on the second prototype device (MIDAS 2). The higher image quality of these images when compared with fig. 3.13, taken on a similar surface finish with the first prototype MIDAS 1 can be attributed to the improvements of the illumination system on the MIDAS 2 device. It can be observed that the good contrast of these images provides excellent defect visibility.

However the benefits of the proposed technique can be fully appreciated when compared with unaided visual inspection. A close-up photograph and a moiré image are shown side by side for each of the five defects in figures 3.15 to 3.19, to emphasize the enhancement of the visibility provided by the moiré device. Note that the moiré images can be seen in real time by the operator of the device directly on the surface of the inspected component, by simply switching on the light source and looking through the grating, without the need for a camera or a monitor.

It was found that the technique was sensitive to small particles of dirt and air bubbles trapped beneath the acetate grating, which produce extraneous moiré fringes. However, these artefacts are easy to discern from real surface defects because the defects remain stationary when the device is moved.

The device proved to be sensitive to other features of the surface as well. For instance, the internal structure of real aircraft components (e.g. ribs, changes in panel thickness) produces slight surface deviations, which can be detected by the device. This ability to trace the internal structure of assembled components using a non-invasive technique could be potentially useful during in-service inspection.

It was observed that the number of fringes increased with the energy of the impact, suggesting that the technique could provide a good indication of defect size. Figures 3.15 to 3.19 show profiles along (c) the horizontal and (d) the vertical middle line of the impact craters, measured using the surface profilometry technique previously described. The results are summarised in Table III-6.

<i>Impact Energy (Joules)</i>	<i>Profilometry</i>		<i>MIDAS 2 (manual analysis)</i>	
	<i>Depth (<math>\mu\text{m}</math>)</i>	<i>Diameter (mm)</i>	<i>Max. Fringe order Number (N)</i>	<i>Depth (<math>\mu\text{m}</math>) <math>z=75.3 N</math></i>
5	36	4.5	0.5	38
9	61	5.9	0.5	38
14	71	7.1	1.0	75
18	96	6.8	1.0	75
22	115	6.2	1.5	113

**Table III-6: Impact defects on sample S2**

Despite the fact that in the MIDAS 2 device the source and the viewer are not in the same plane of the grating (and indeed, if the component is curved the grating would not even be flat), acceptable quantitative measurements of shape could still be obtained by application of eq. (3.1) provided that (i) only a small area (a few square millimetres) is analysed, so that viewer and

source can be assumed at infinity, and (ii) the area is near the centre of the image (in the intersection of the illumination and viewing axes), so that the calibration constant can be estimated from eq. (3.1).

In this case, the viewing angle was  $\alpha=0(\text{rad})$ , the grating pitch  $p=100(\mu\text{m})$  and the illumination angle  $\beta=0.92(\text{rad})$  (approx.  $53^\circ$ ). Substitution in eq. (3.1) yielded a fringe constant  $C=75.3(\mu\text{m})$ , so that the vertical deviation  $z$  of the surface can be estimated from the fringe order  $N$  as  $z=75.3N(\mu\text{m})$ . Manual fringe order measurement was considered accurate up to  $0.5(\text{fringes})$ , which corresponds to an accuracy of approximately  $40(\mu\text{m})$  in the depth measurements with moiré.

Table III-6 shows discrepancies between the two techniques as high as  $23(\mu\text{m})$  in the worst case, but the measurements obtained with moiré were qualitatively adequate, showing the increase in defect size with impact energy and providing a quick estimate of the size, which was already beyond the original requirement for the manual device of merely enabling the detection.

However, in section III.6 the author will present a technique for the automatic measurement of defects that allowed the technique to be taken one step further, improving the accuracy and providing full-field information of the defect geometry.

### ***III.5.3 Impacts On Curved Panels***

Only cylindrical components with low curvatures, *i.e.* radius  $>1500(\text{mm})$ , were initially considered within the scope of this project. However, a special request was made from BAE Systems to investigate an application related to the EF-2000 Eurofighter Typhoon aircraft, which included a component outside these requirements. The side panel situated below the cockpit of the aircraft (sample S3), is prone to impact damage by several pieces of equipment, including the helmet, that hang from the flight suit of the pilot when boarding and alighting the aircraft. This carbon fibre panel presented curvature in two directions, with radii of curvature significantly tighter than those considered in the original project requirements.

A view of the curved panel is shown in fig. 3.20(a). The central area was primed to cover the marks that indicated the location of the defects in the panel (see the detail of fig. 3.2(c)). Figure 3.20(b) shows the device in use inspecting the panel. Despite the high curvature of the surface, the flexible grating was able to adapt very closely to the shape of the panel, providing useful moiré patterns in the majority of the field of view. An image of the operator's view during the inspection is shown in fig. 3.20(c). The image was taken from the miniature CCD camera using the  $4.5(\text{mm})$  lens to cover the full inspection area highlighted in fig. 3.20(a). Two defects corresponding to impacts of 5 and 6(J) appear on the field of view of the image as indicated. Despite the low energy of the impacts -compare with the 5(J) impact in sample S2- the defects

are readily observable. The large area of the inspection device allows a very fast inspection of the full component with high reliability.

### III.6 Quantitative Measurement

The experimental results reported in section III.5 demonstrated the suitability of the prototype device for the detection of surface defects down to  $50(\mu m)$  in size, in flat and curved components, either with favourable or neutral surface finish. The prototype also fulfilled the project requirements for a manual qualitative device in terms of portability, ease of use and ruggedness. At this point, the University of Sheffield and BAe Systems shifted objectives within the INDUCE project, and the development of a computer-aided quantitative device was undertaken by UCM and EADS-CASA.

However it appeared to the author that the proposed moiré technique offered the potential for higher accuracy and a more comprehensive quantitative assessment of the defects than that described in the previous sections, and this potential could be exploited by means of a digital technique for the analysis of the fringe patterns. This section describes an automatic fringe processing technique developed by the author outside the INDUCE project. The technique is a hybrid between intensity-based and phase measurement fringe analysis methods.

#### III.6.1 A Hybrid Fringe Analysis Technique

The discussion presented in section II.4 described a number of advantages of phase measurement methods over intensity-based methods. However, the introduction of a suitable phase carrier presented some difficulties in this application.

- Temporal methods would require phase-shifting the pattern *e.g.* by controlling the distance between the grating and the object. However this solution would complicate the apparatus, and require the collection of several snapshots.
- Spatial methods would imply introducing a spatial phase carrier, *e.g.* by tilting the grating. However, visual detection of the defects in the resulting moiré pattern is much less intuitive than in the pattern without carrier.

Neither of these solutions was really practical in this application. Ideally it should be possible to perform the measurement from a single snapshot of the fringe pattern.

We can mathematically describe the moiré patterns as follows

$$I(x, y) = A(x, y) + B(x, y) \cos(\Phi(x, y)) \quad (3.2)$$

Where  $A$  and  $B$  are slow-varying background and amplitude modulation terms and  $\Phi$  is a phase term that can be related to the surface height relative to the grating. Note that the loci of

maximum intensity (*i.e.* the bright moiré fringes in the image) correspond to even integer multiples of  $\pi$ , *i.e.*  $\Phi=(2N)\pi$ , or  $N=\Phi/2\pi$ , which substituted in eq. (3.1) yields

$$z = CN = C \frac{\Phi}{2\pi} = C^* \Phi \quad (3.3)$$

where  $C$  is the calibration constant or contour interval previously defined. It is proposed to extract the depth information from the moiré pattern by direct application of expressions 3.2 and 3.3. The steps involved are:

1. Remove the  $A$  and  $B$  terms from the intensity profile by means of image-processing operations. This involves filtering low frequency terms and re-scaling the intensity image to the range  $[-1, 1]$ . The method used in this research for this normalisation of the fringe pattern will be described in section IV.5.3.

$$I \xrightarrow{\text{normalisation}} I_1 = \cos \Phi \quad (3.4)$$

2. Calculate the inverse cosine of the resulting values. The values resulting from the arcos operation appear wrapped in the range  $[0, \pi]$ , with some peculiarities that will be described below.

$$\arccos(\cos \Phi) = W_C \{ \Phi \} \quad (3.5)$$

3. Unwrap the data to recover the phase

$$W_C \{ \Phi \} \xrightarrow{\text{unwrapping}} \Phi \quad (3.6)$$

4. Apply the calibration constant  $C^*$  to calculate  $z$ , see eq. (3.3).

It must be noted that the wrapped phase maps obtained from the arccos operation in step 3 of the method differ from those described in section II.4.4 (obtained from the arctan). The arctan function wraps the data by ‘stepping’ it, producing multiple-of- $\pi$  discontinuities in the data that are relatively easy to detect. In contrast, the arcos function wraps the data by ‘folding’ it, or applying symmetry about the horizontal axis, *i.e.* changing the sign of the first derivative. As a result the cos-wrapped data is continuous but presents discontinuities in the first derivative.

Unwrapping this type of data by looking for the discontinuities in the first derivative is extremely difficult, because (i) the value of the wrapping discontinuities in the first derivative is variable, and (ii) the first derivative of discrete data is typically very noisy. The author has not found evidence in the literature of any previous attempts to address this problem.

The approach proposed here is based in the appreciation that the cos-wrapped phase data can be transformed into quasi-tan-wrapped phase data by subtracting  $\pi/2$  from the phase map, and then

changing the sign of the cos-wrapped phase in alternate periods. Figure 3.21(a) represents a function  $\Phi$  that has been (a.1) tan-wrapped and (a.2) cos-wrapped. The first derivative of the cos-wrapped data (a.3) is also shown to illustrate that the value of the discontinuities depends on the slope of  $\Phi$  at the end of the period. The two wrapped phase functions differ in (i) the location of the ends of period, given by  $\Phi = \pi(N - 1/2)$  in the tan-wrapped phase and by  $\Phi = \pi N$  in the cos-wrapped phase, (ii) a  $\pi/2$ -multiple offset between the two functions, and (iii) a sign reversal of the cos-wrapped phase in alternate periods. Note that the ends of the periods of the cos-wrapped phase,  $\Phi = \pi N$ , coincide with the peaks and troughs of the intensity image.

In view of the above observations, the following method is proposed to accomplish the unwrapping of cos-wrapped data (*i.e.* step 3 of the method for fringe analysis):

- 3.a. Use an intensity-based technique on the image to locate the crests of both the dark fringes and the bright fringes in the image. A variation of the skeletonizing technique for fringe tracking proposed by Yagatai and Idesawa (1982) was used in this research. The fringe crests define the limits of regions where the cos-wrapped data changes sign.
- 3.b. Subtract  $\pi/2$  from the phase map. Identify in the image one of the two possible sets of alternate regions delimited by the fringe crests and multiply the cos-wrapped data by  $-1$ . This step requires user intervention to determine the overall sign of the map (*i.e.* whether the defect is an indentation or a protuberance).
- 3.c. The resulting phase map is quasi-tan-wrapped in the range  $[-\pi/2, \pi/2]$ , see the discontinuous line in fig. 3.21(a.2), and can be unwrapped using any of the automatic techniques found in the literature. The particular method used in this research will be described in detail in section IV.5.2.

Figure 3.21(b) shows the steps of the method in a simulated 1-D example. The plot (b.1) shows the original phase function. A typical intensity distribution of the corresponding moiré pattern was generated artificially, including noise and modulation of the background intensity and amplitude, see plot (b.2). The first step of the method is the normalisation of the moiré image to eliminate the noise and modulation, and re-scale the intensity range to  $[-1, 1]$ , as shown in plot (b.3). The cos-wrapped (b.4) phase is calculated in step 2. Fringe centres are found in the input image (b.2) using intensity-based analysis to determine the regions for sign change, in order to transform the phase in (b.4) into the quasi-tan-wrapped phase in (b.5). This map is unwrapped using a conventional unwrapping algorithm to yield a continuous phase map (b.6), identical to the original phase function shown in (b.1). Note that phase is proportional to surface depth by application of eq. (3.3).

Figures 3.22 and 3.23 illustrate the procedure with real data, in this case corresponding to the 18(J) defect in sample S2. The original image 3.22(a) was cropped for convenience to the small area shown in 3.22(b) containing the defect. This image was normalised to remove the noise and fringe modulation, yielding the map in 3.22(c), and then re-scaled to the  $[-1, 1]$  range.

The skeletonizing technique mentioned in step 3.a to detect the fringe centres requires an iterative algorithm. Initially the loci of intensity minima shown in fig. 3.22(d) were determined by testing each pixel in the image to determine whether it satisfies the conditions of a local peak. Each pixel was compared with other pixels in its  $5 \times 5$  neighbourhood along four directions (horizontal, vertical, and two diagonals), and awarded one point for each direction in which the condition was satisfied. Next, an iterative loop starts with the pixels that have two or more points, and successively applies binary dilation and erosion to the skeleton, retaining only the pixels newly found in each iteration that have at least one point, as shown in the sequence of images in fig. 3.22(f). The fringe centres in (g) were determined applying a binary thinning operation to the last skeleton. The same procedure was applied separately to determine the fringe maxima in the image, as shown in fig. 3.22(e), and to calculate the fringe centres using the iterative algorithm.

Both sets of fringe centres (corresponding to dark and light fringes) can then be combined as shown in fig. 3.23(a), and used to define the regions of change in sign, shown in fig. 3.23(b). Figure 3.23(c) shows the detected fringe centres superimposed to the original moiré image. The profile of cos-wrapped phase along the middle horizontal line of the image is shown in fig. 3.23(d). Note how the fringe centres were used to locate the ends of periods. The corresponding profiles of the tan-wrapped phase, obtained by changing the sign in the second period, and the unwrapped phase are also shown in the plot. The resulting unwrapped phase map is presented in fig. 3.23(e). This map was calibrated to yield surface depth. A three dimensional representation of the surface map is shown in fig. 3.23(f)

### III.6.2 Validation

The technique described in the previous section was applied to the measurement of the five calibrated indentations of sample S2, and the results compared with the measurements performed using the surface profilometry technique, and also the manual fringe counting.

Figure 3.24 shows the phase maps corresponding to the five defects, and fig. 3.25 three-dimensional representations of calibrated surface maps. The calibration constant  $C^* = 11.99 (\mu\text{m}/\text{rad})$  was calculated using eq. (3.3) with the value of  $C$  reported in section III.5.2. The results are summarised in Table III-7.

Finally, fig. 3.26 shows a graph comparing the measurements obtained using profilometry with the results of the automatic measurement technique, and the manual interpretation of the moiré patterns. When plotted against the impact energy, the results of profilometry and the automatic method show a definite monotonically increasing trend, and are also in excellent agreement with each other (within  $5\mu m$ ). The manual results are less accurate, but nevertheless provide an adequate quick estimate of the value.

<i>Impact Energy (Joules)</i>	<i>Profilometry</i>		<i>MIDAS 2 (automatic)</i>	
	<i>Depth (<math>\mu m</math>)</i>	<i>Diameter (mm)</i>	<i>Phase (rad)</i>	<i>Depth (<math>\mu m</math>) <math>z=11.99 \cdot \Phi</math></i>
5	36	4.5	3.5	41
9	61	5.9	5.3	63
14	71	7.1	6.1	74
18	96	6.8	7.8	94
22	115	6.2	9.3	112

Table III-7: Automatic measurement of defects

### III.7 Discussion

The surface finish tests performed on sample S1 using the MIDAS I prototype proved that the technique could be used for detecting defects in the limit of the requirements, up to  $50(\mu m)$  deep, both in favourable and neutral situations. In these cases the moiré images proved to be a very convenient means for detection, providing a clear indication of the location of the defect that facilitated reliable detection. However, the technique did not produce usable results when used on a black surface, considered an extreme case of unfavourable conditions in the project requirements.

The enhancement in visibility provided by the new technique can be fully appreciated when comparing the moiré images shown in figures 3.15 to 3.19, where the defects are clearly evident, with the corresponding close-up pictures of the same defects taken in optimal conditions. The device was demonstrated successfully both in flat and curved samples. A camera lens with a short focal length ( $4.5mm$  in this research) was used to collect images of the whole inspection area and facilitate the detection of defects, see e.g. fig. 3.20(c).

The results of the tests performed on sample S2 using the MIDAS II showed that the technique can be used not only to assist in the detection of defects under the visibility threshold, but also to perform measurements of their size. The calibration constant of the device in a given

configuration can be calculated from eq. (3.1) and used to obtain a quick estimate of defect size by manually counting the fringes. It is also possible to lock the light source arm in the device, fixing the illumination angle to define a pass/no pass criterion.

The automatic fringe processing technique described in the previous section can be used to perform quantitative measurements on close-up images such as the ones shown in fig. 3.14, which were collected using a 12.5(mm) camera lens, and with the device aligned to situate the defect in the centre of the inspection area.

The quantitative measurements of defect depth obtained with this technique have been validated with surface profiles of the defects measured independently with a profilometer, obtaining very good agreement between both techniques. The graph in fig. 3.26 shows a good positive correlation between impact energy and defect depth, with some non-linearities which were attributed to inhomogeneities in the composite material.

### **III.8 Conclusion**

The detection of surface damage during in-service inspections of aircraft has been considered in this chapter to introduce the subject of industrial applications of moiré techniques. Following preliminary studies, the shadow moiré configuration was preferred to the projection moiré configuration mainly due to its simplicity. A prototype device was designed, built and tested. The results of these tests were used to refine the design and develop a second prototype that complied with the project requirements for a manual instrument for the qualitative inspection of flat and curved panels. Defects with a diameter of less than 5(mm) and a depth smaller than the target size of 50( $\mu\text{m}$ ) were successfully detected in an inspection area of 740( $\text{cm}^2$ ). Moreover, a technique for the automatic analysis of the moiré images recorded with the device has been described, which combines concepts from intensity-based and phase extraction fringe analysis. The quantitative measurements obtained with the automatic technique were in good agreement (within 5 $\mu\text{m}$ ) with independent measurements of the defects obtained by means of surface profilometry.

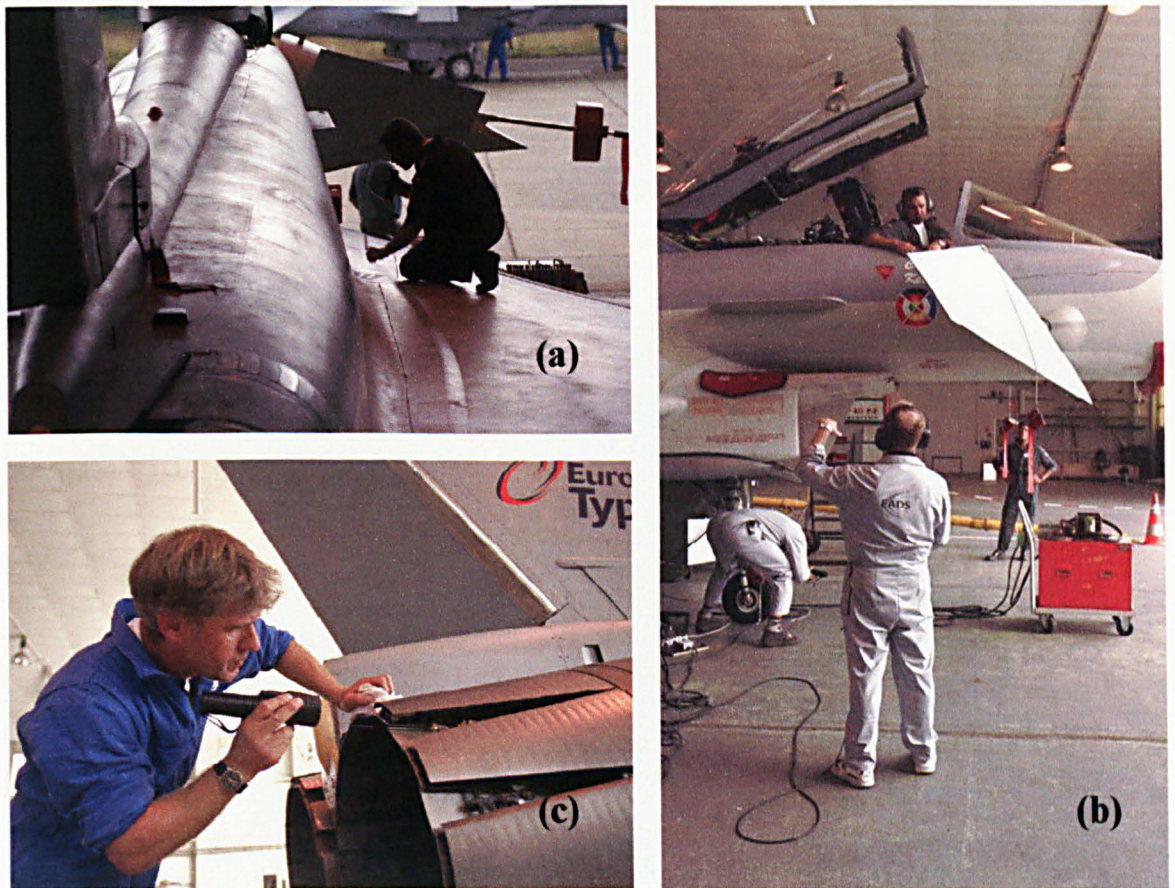


Figure 3.1: In-service inspection of aeronautical structures. (a) Inspections are carried out under routine maintenance conditions, with limited access and poor lighting conditions. The structures typically involve very large inspection areas. (b) Several maintenance operations take place simultaneously on the aircraft due to the time restrictions. (c) Unaided visual inspection is usually performed in search for defects such as impact damage and corrosion. In regions where there is visual evidence of damage, an in-depth assessment of the integrity of the component can be performed using conventional NDE techniques. (Source of images: <http://www.eurofighter.com>)

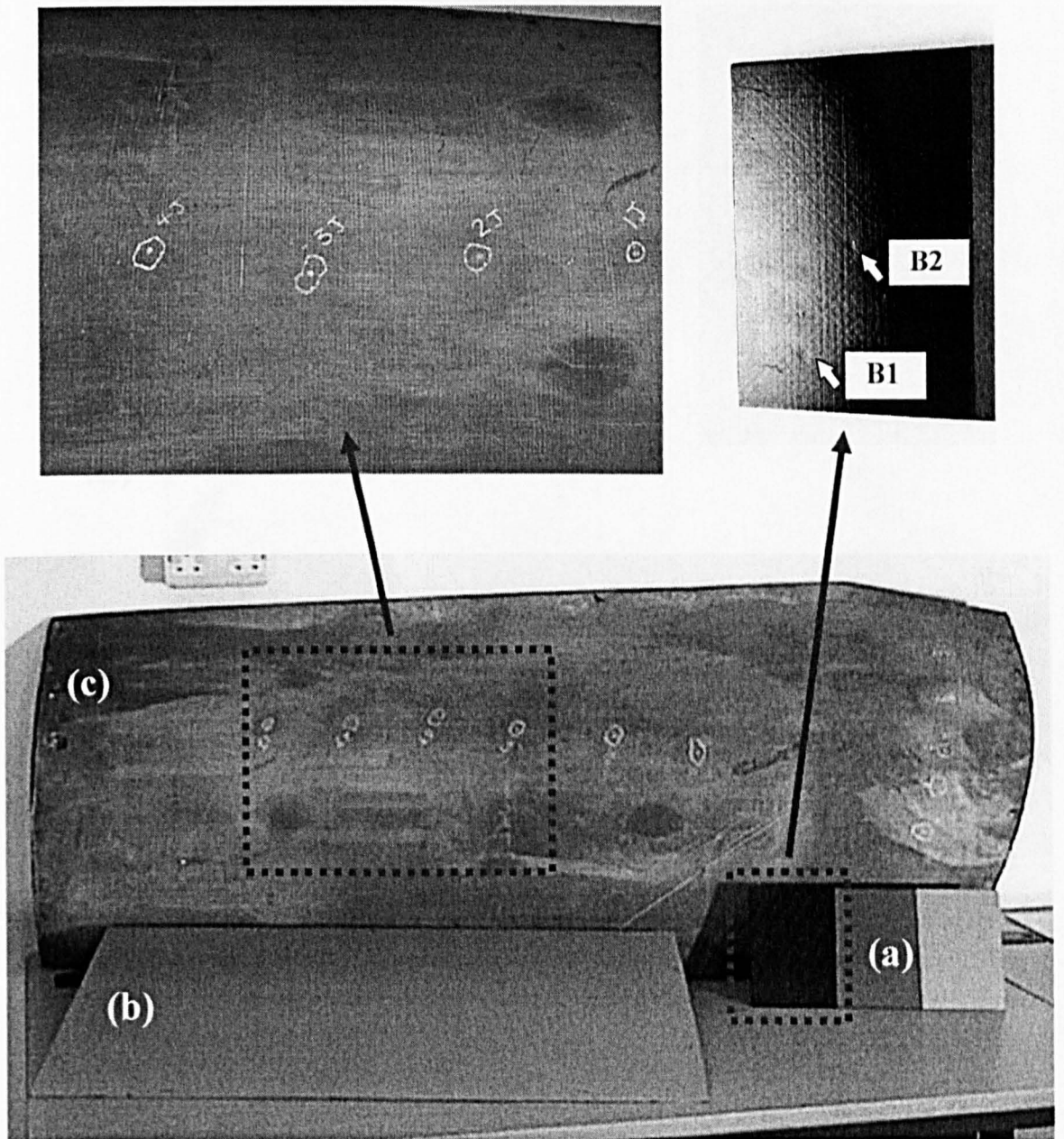


Figure 3.2: Impact damage samples courtesy of British Aerospace. (a) Sample S1: Flat composite panel with three different surface finishes. Dimensions are  $145 \times 300$ (mm) and  $2$ (mm) thickness (b) Sample S2: Flat carbon fibre sample with five calibrated indentations. Dimensions are  $700 \times 500$ (mm) and  $4$ (mm) thickness (c) Sample S3: Curved carbon fibre panel, approx. dimensions  $1300 \times 550$ (mm), from the Eurofighter Typhoon aircraft. This panel, located below the cockpit side, is prone to impact damage as the pilot boards and alights the airplane. A request was made by BAe Systems to test this component, which otherwise fell outside the original project requirements.

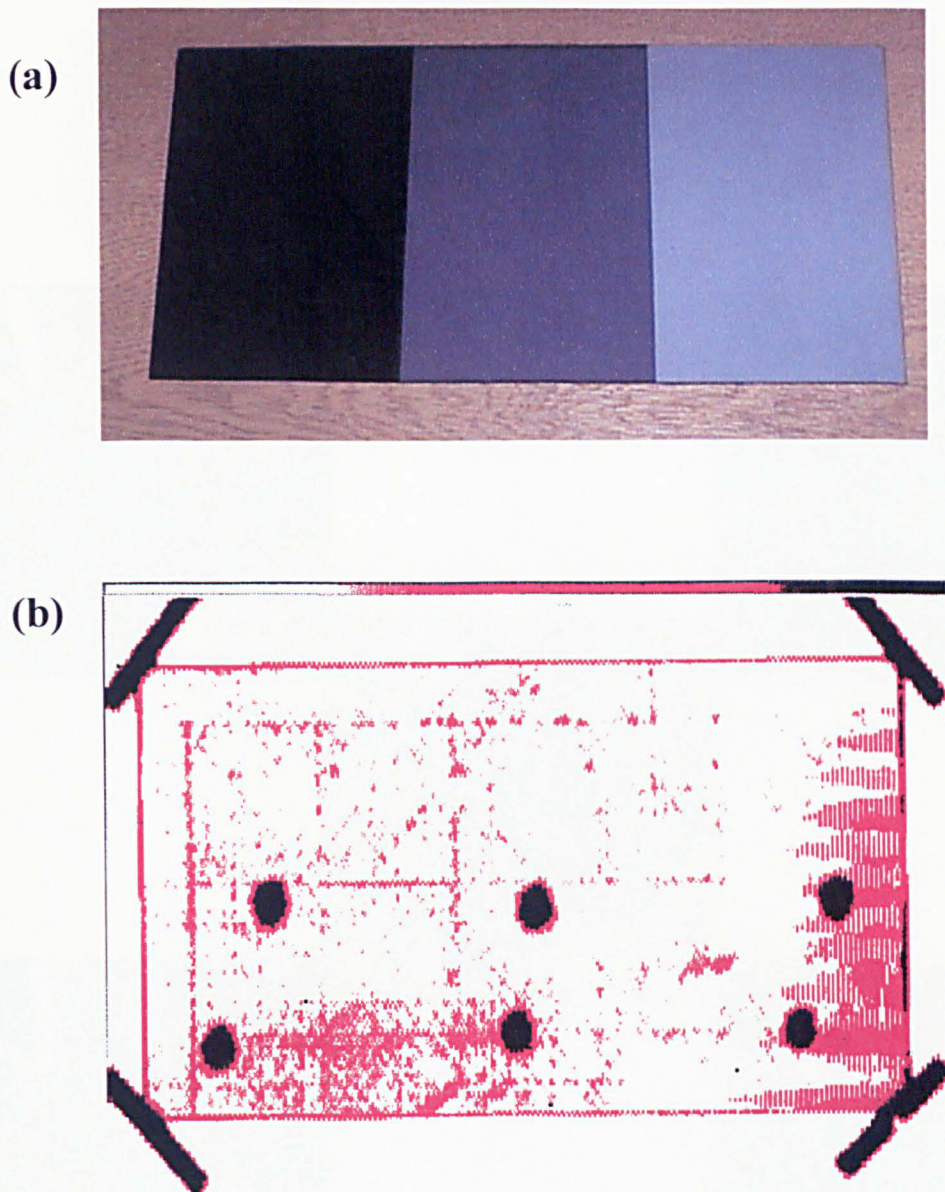


Figure 3.3: (a) View of Sample S1, which presents three different surface finishes: dark, medium and clear. Two impacts by ball bearing were produced in each region to research the effect of surface finish in the detectability of the defects. (b) This ultrasound scan of the panel S1 reveals the location of the impacts on the panel. The ultrasound test was performed by BAe Systems personnel.

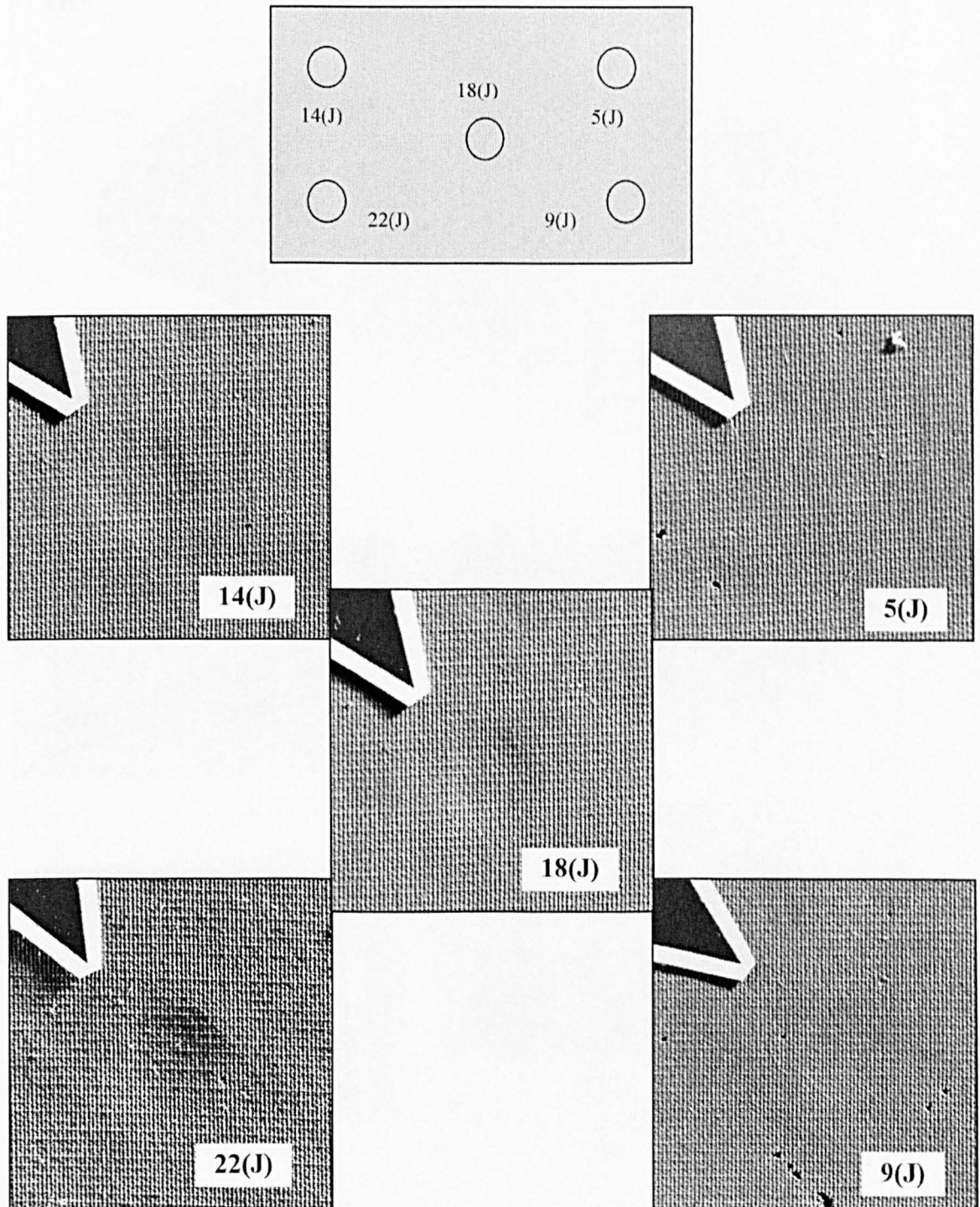


Figure 3.4: Close-up photography of five impact defects on sample S2. The defects were created by dropping a ball bearing and are labelled according to the energy of the impact, from 5 to 22(J). As expected, the depth of the defects increases with the energy of the impact. Images by D. Hallford.

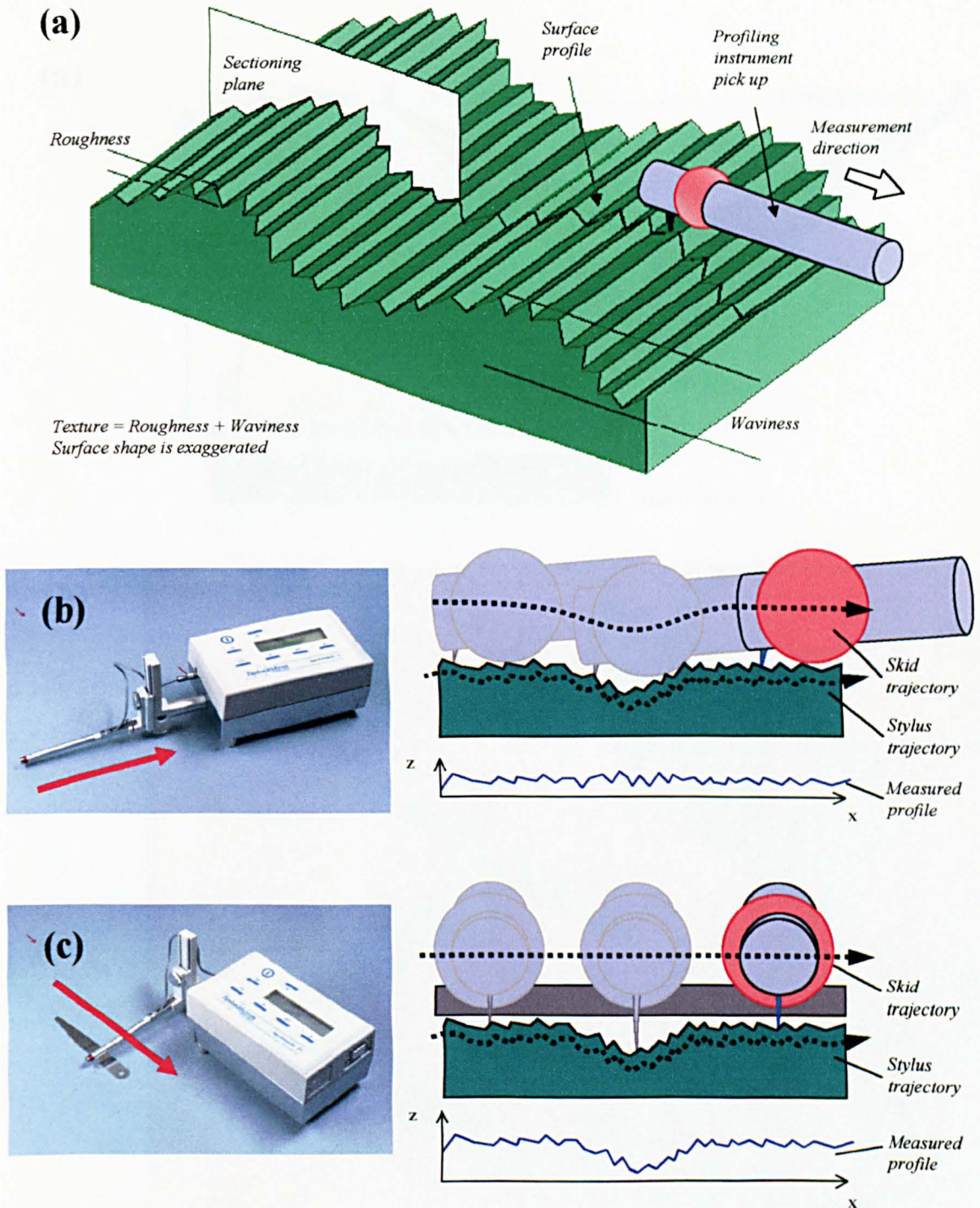


Figure 3.5: Profilometry tests. (a) The profilometer draws a diamond stylus across the surface of an object and registers its vertical movement relative to a ruby skid riding the surface. (b) This arrangement measures the surface roughness but smooths out the surface waviness, including the shape of the impact craters (c) Alternative arrangement used to measure the craters. The pickup slides over a nominally flat surface, with the direction of the measurement perpendicular to the pickup axis.

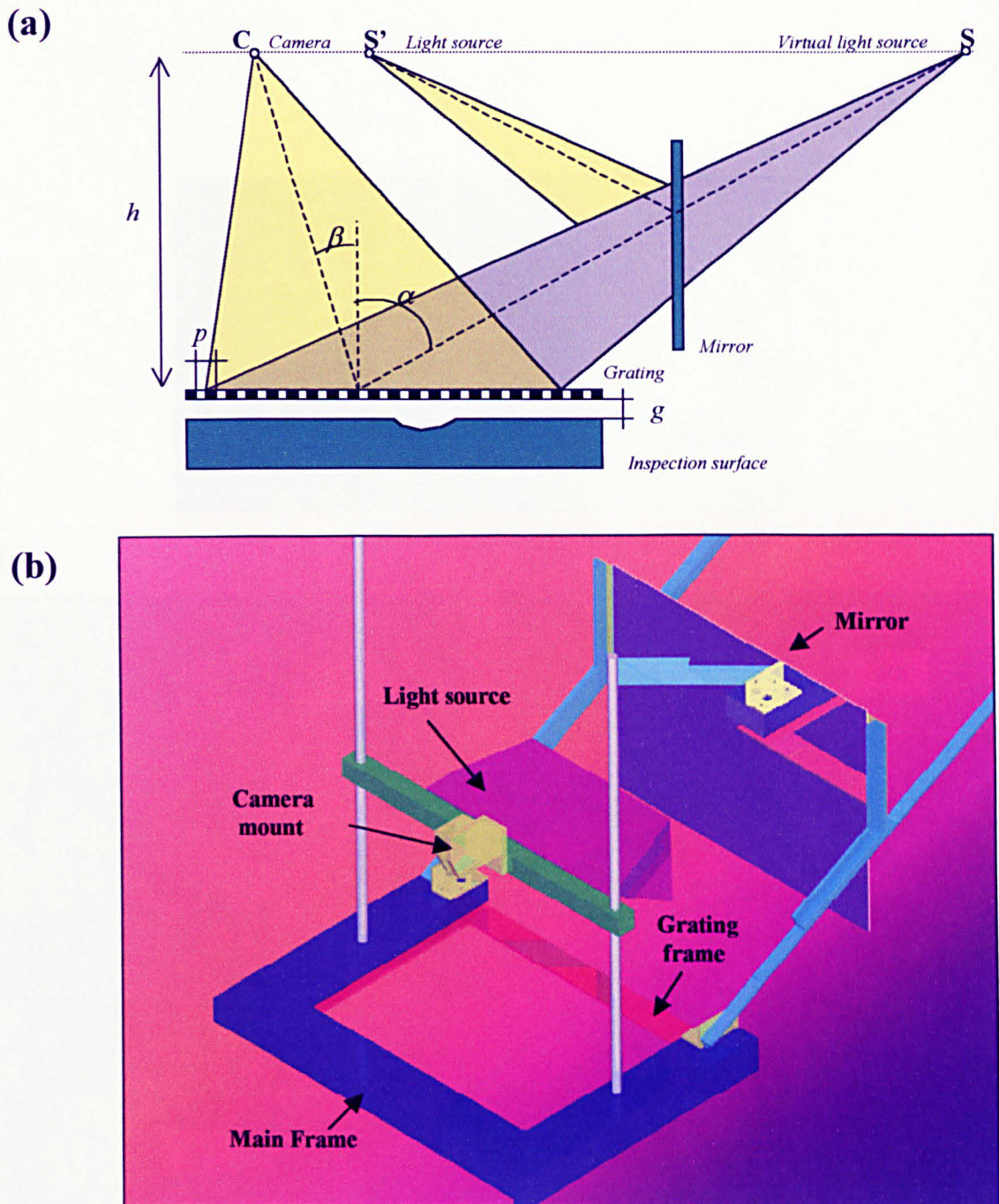


Figure 3.6: (a) Schematic of the shadow moiré configuration. The sensitivity of the technique depends on the illumination and viewing angles ( $\alpha$ ,  $\beta$ ), and on the grating pitch  $p$ . The use of fine gratings is limited in that the distance  $g$  between the grating and the object must be in the same order of magnitude as the grating pitch  $p$  to prevent diffraction effects. The light source can be placed at point S' by using a mirror. (b) Drawing of the MIDAS 1 prototype, which used a mirror to fold the light path and keep the instrument compact with a large illumination angle for improved sensitivity. A flexible grating was attached to a rigid frame mounted with a spring system to maintain close contact with the inspection surface.

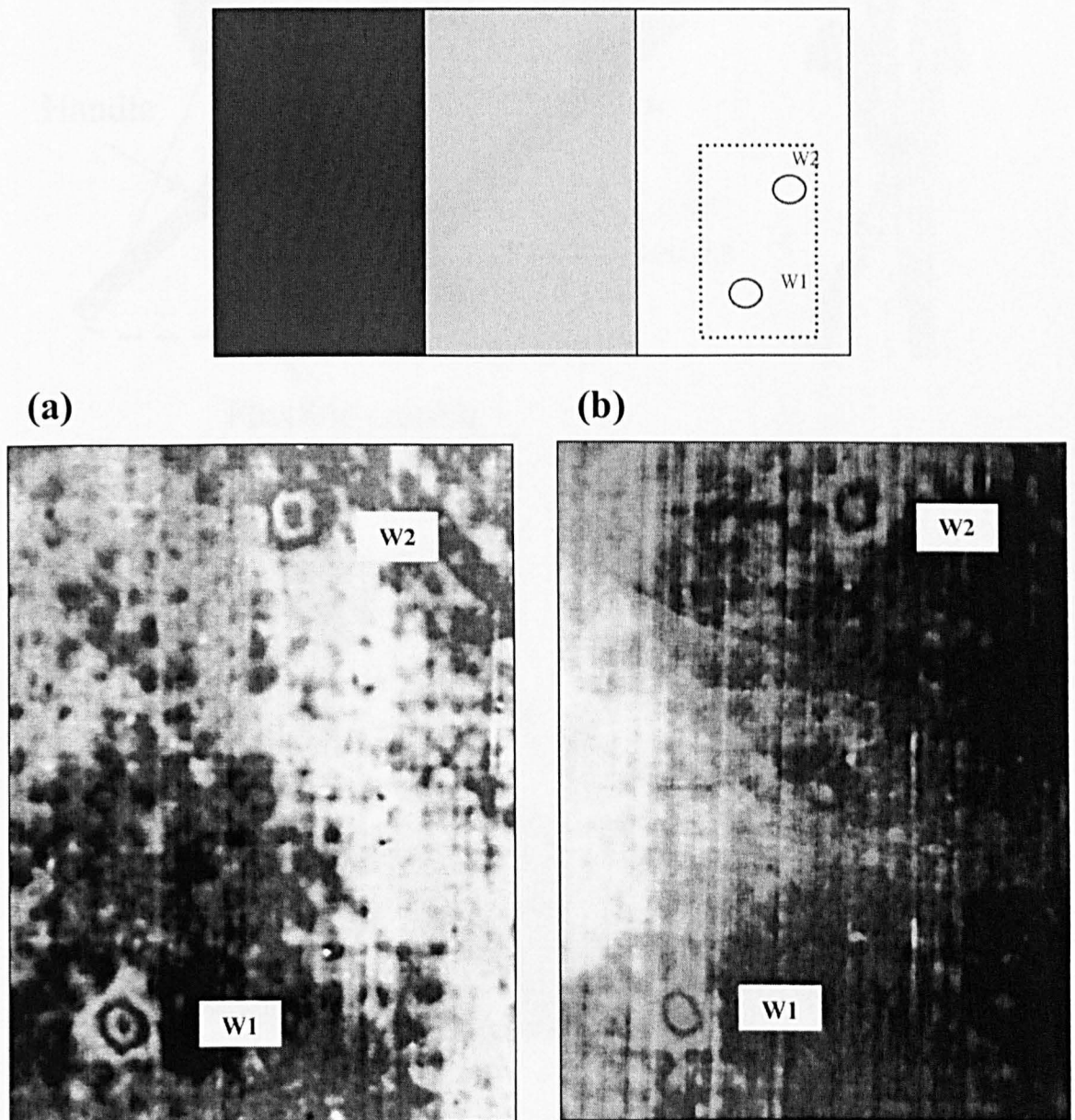
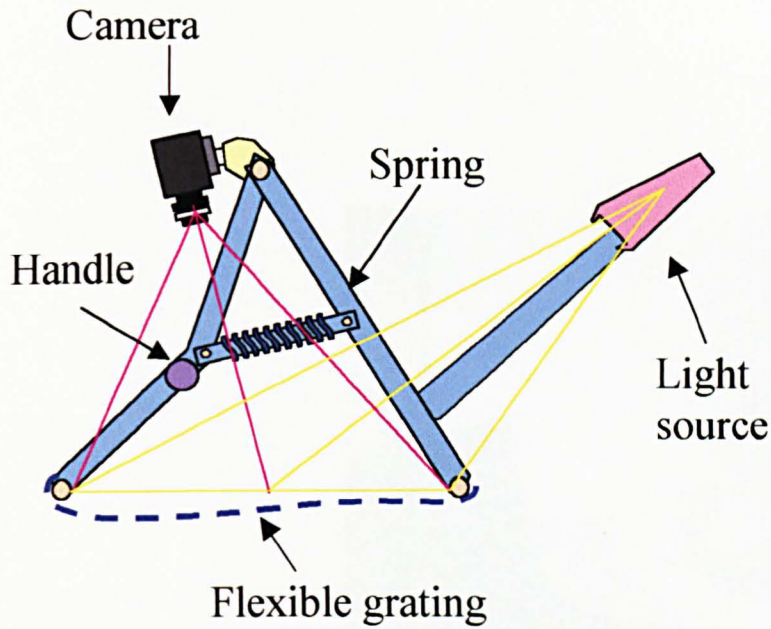
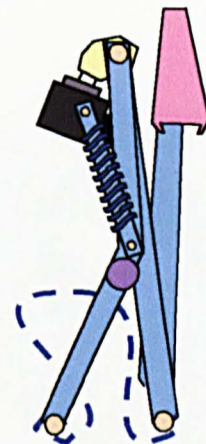


Figure 3.7: Moiré patterns on defects W1 and W2 (light grey area of sample S1) were collected using (a) a conventional glass grating with a line density of  $300(\text{lines}/\text{inch})$  (ca.  $12\text{lines}/\text{mm}$ ) and (b) a flexible grating printed on acetate film, with a line density of  $10(\text{lines}/\text{mm})$ . The film grating provides less contrast, and small non-uniformities in the line spacing result in a faint vertical line pattern. The higher fringe order in (a) is due to the higher density of the glass grating. Despite all this, the defects are clearly visible in both images.

**(a) Working position**



**(b) Travel position**



**(c) In operation**

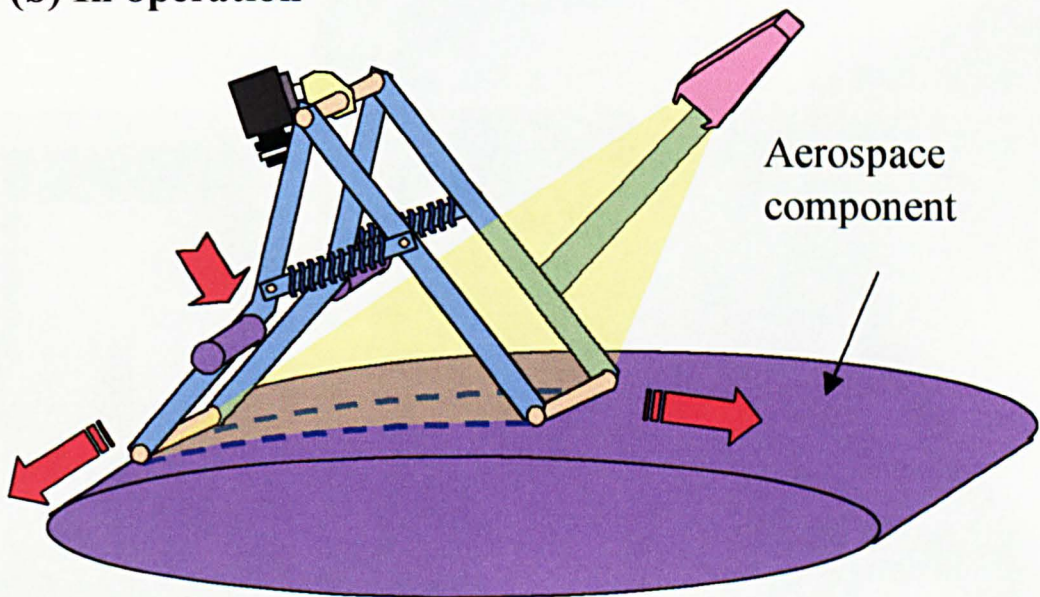


Figure 3.8: MIDAS 2 prototype shown in (a) working position, (b) in travelling/storage position and (c) in operation. The combined action of the operator pressing on the handle and the spring system help open the arms of the device. This action stretches the flexible grating which adapts to the shape of the component being inspected

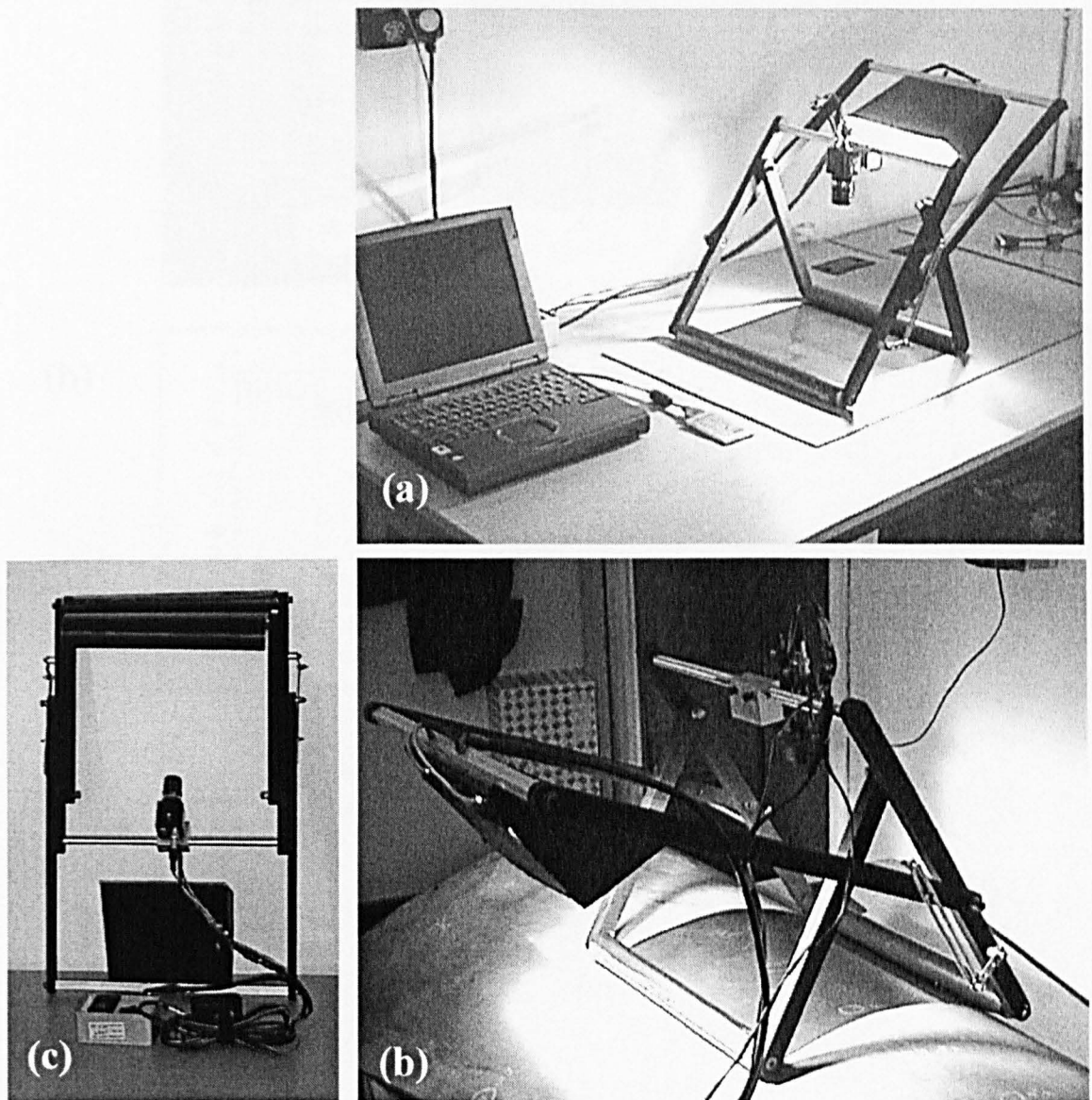


Figure 3.9: (a) The finished MIDAS II prototype system including a CCD camera and video card for collection of data. (b) The prototype in use to inspect a curved composite panel (Sample 3S). The panel belongs to the Eurofighter Typhoon aircraft. It is readily seen that the flexible grating adapts tightly to the surface of the panel. (c) The device folded for transport and/or storage.

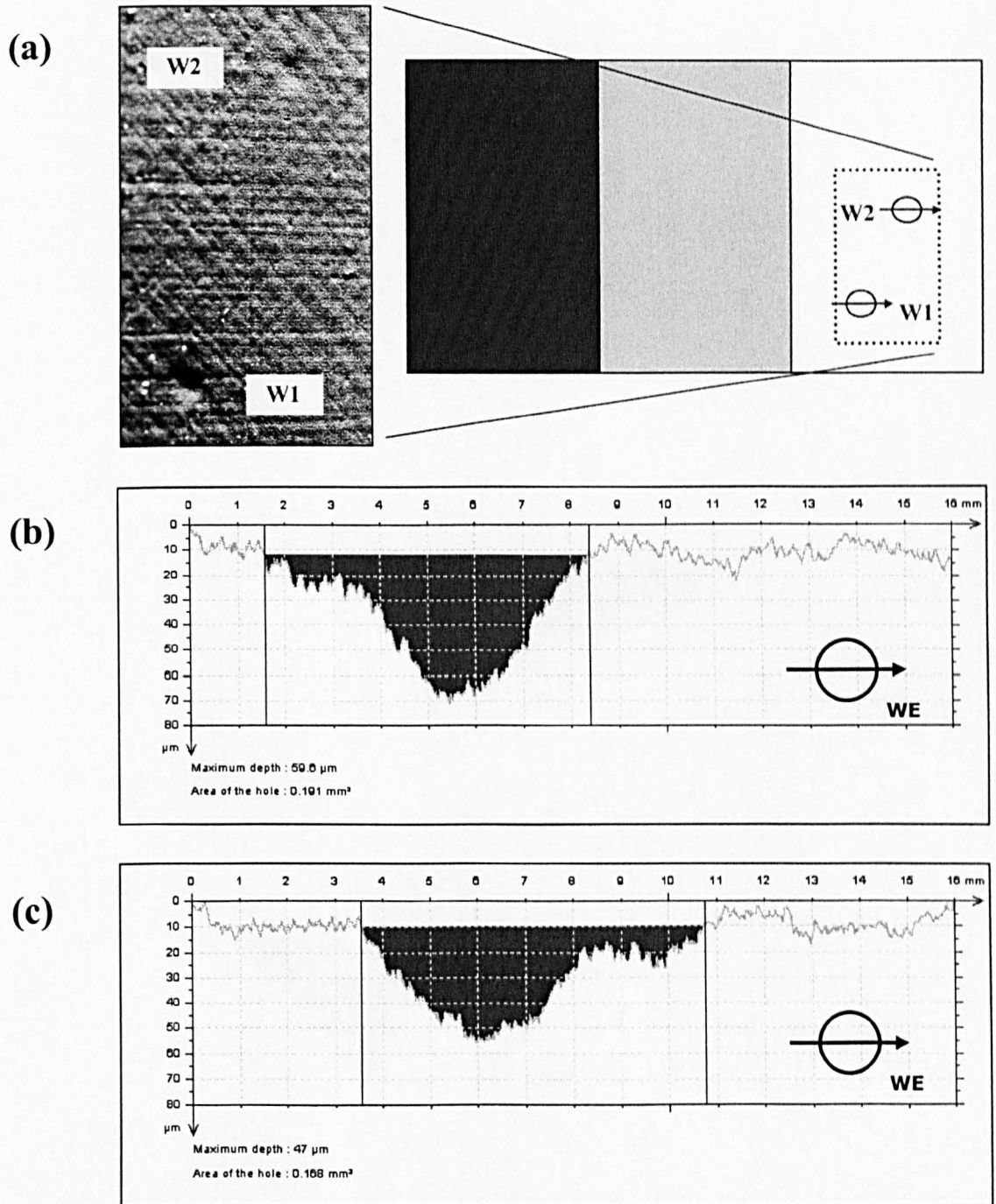


Figure 3.10: Impacts on the area of sample S1 painted light grey. (a) Close up photography and a diagram showing the location of the damaged area in the sample. (b) Profile across horizontal middle line of impact W1, direction WE. Approximate depth 60( $\mu\text{m}$ ), diameter 6.8(mm) (c) Profile across horizontal middle line of impact W2, direction WE. Approximate depth 47( $\mu\text{m}$ ), diameter 7.2(mm). Shaded areas in the profiles highlight the impact craters.

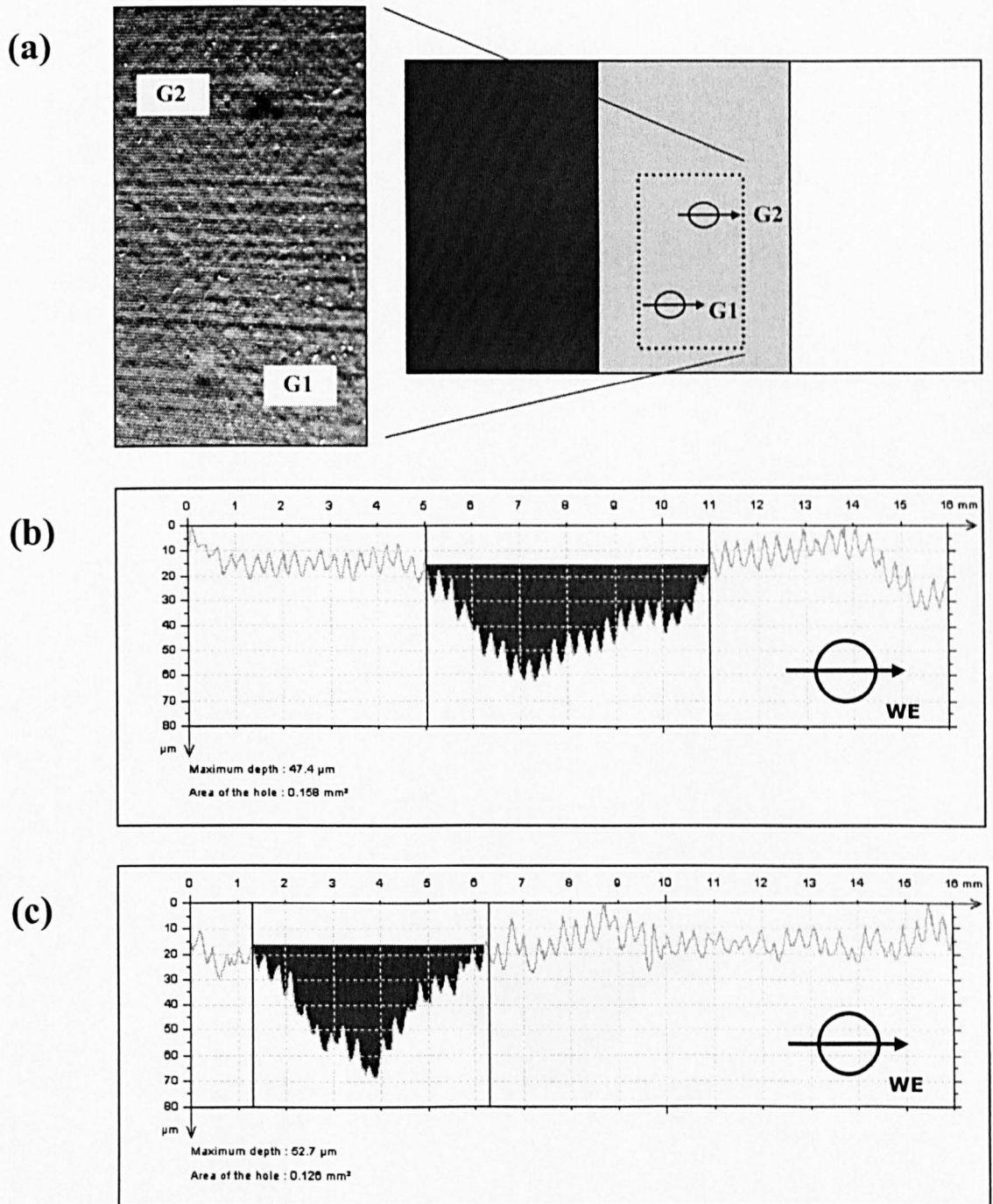


Figure 3.11: Impacts on the area of sample S1 painted medium grey. (a) Close up photography and a diagram showing the location of the damaged area in the sample. (b) Profile across middle line of impact G1, direction WE. Approximate depth  $47(\mu\text{m})$ , diameter  $6.0(\text{mm})$  (c) Profile across middle line of impact G2, direction WE. Approximate depth  $53(\mu\text{m})$ , diameter  $5.0(\text{mm})$ . Shaded areas in the profiles highlight the impact craters. Note the change in roughness compared with the light grey area, due to the different surface finish.

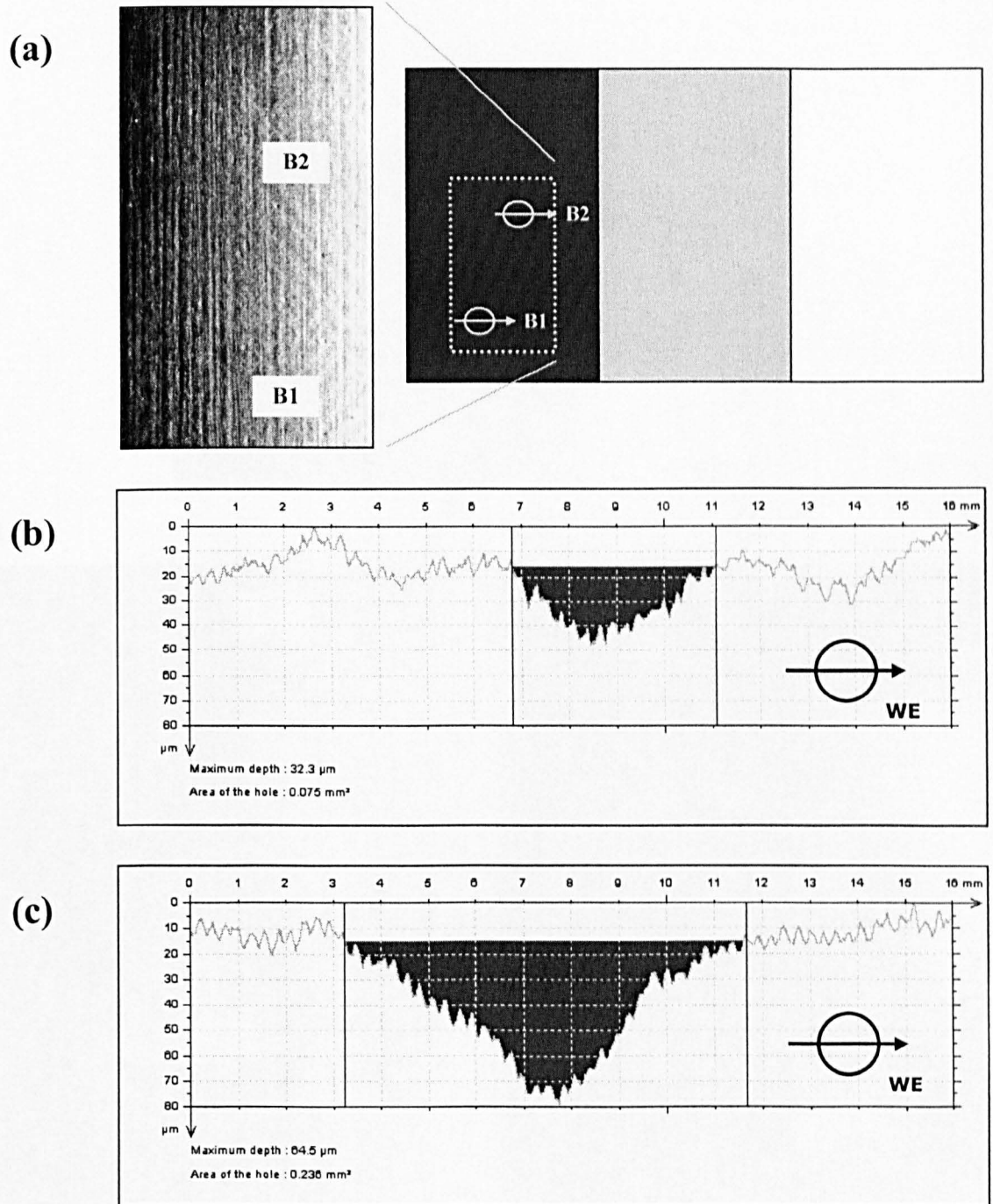


Figure 3.12: Impacts on the area of sample S1 painted black. (a) Close up photography and a diagram showing the location of the damaged area in the sample. (b) Profile across middle line of impact B1, direction WE. Approximate depth 32( $\mu\text{m}$ ), diameter 4.2(mm). Note this defect was below the visibility threshold requirement of 50( $\mu\text{m}$ ). (c) Profile across middle line of impact B2, direction WE. Approximate depth 64( $\mu\text{m}$ ), diameter 8.4(mm). Shaded areas in the profiles highlight the impact craters

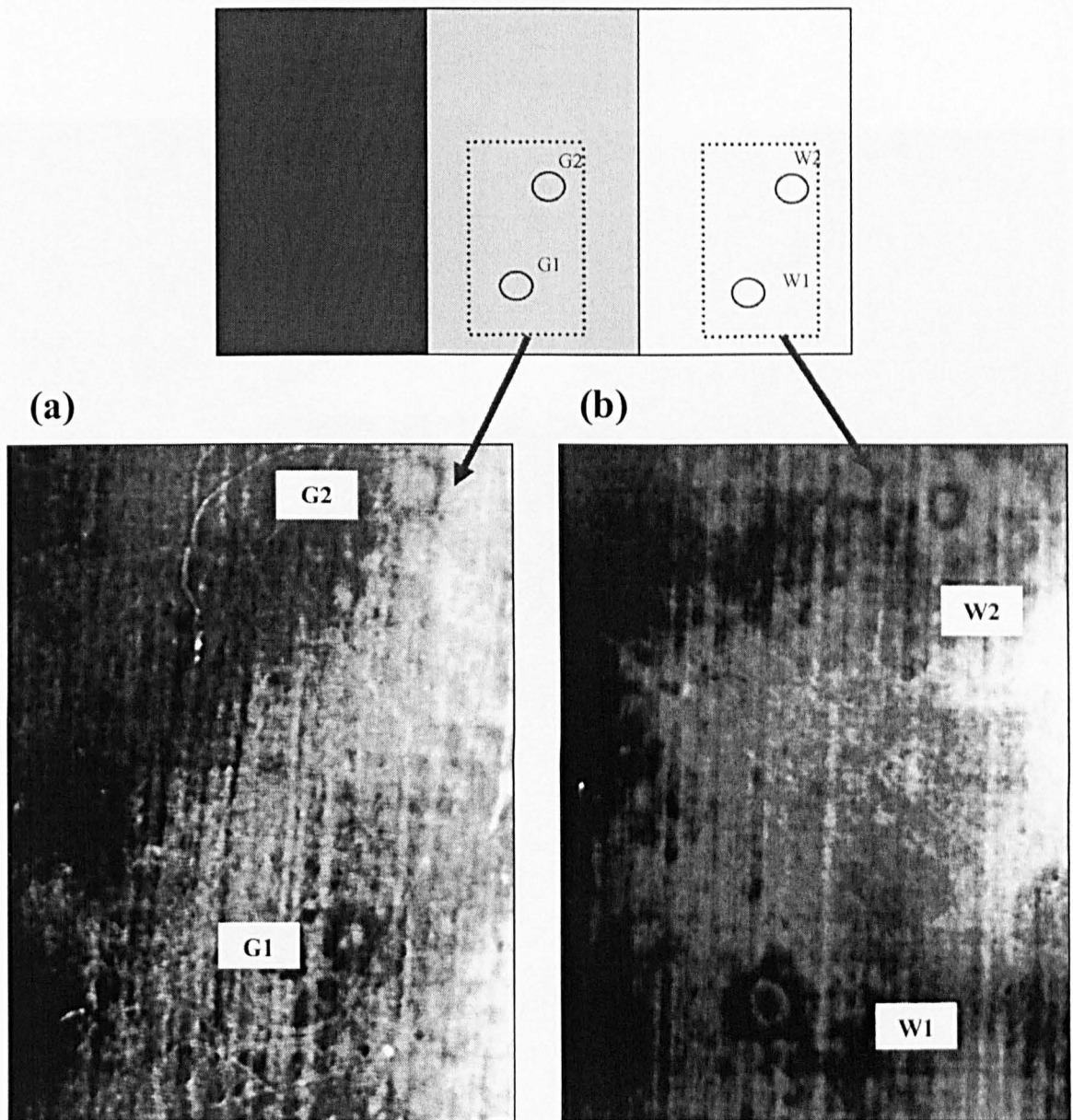


Figure 3.13: Study of the effect of surface finish on the visibility of moiré patterns (a) defects G1 and G2, on medium grey coloured area, considered neutral situation. The fringes present low contrast but the defects are still readily observable. (b) View of defects W1 and W2. The light coloured matte finish is favourable, improving the visibility. Images were collected with the first prototype of the device MIDAS 1.

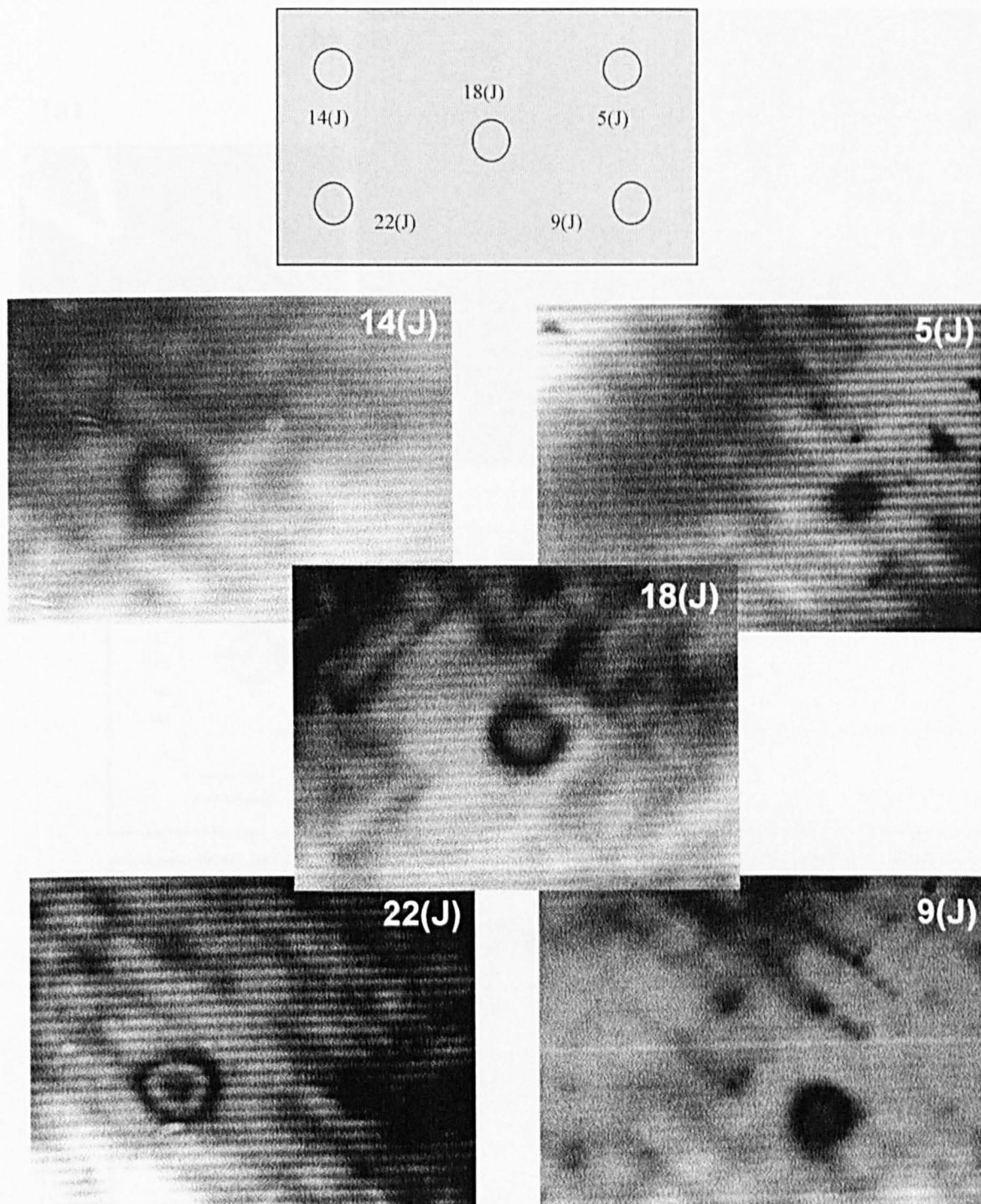


Figure 3.14: Moiré maps of the five impact defects on sample S2. The images were collected using the CCD camera mounted on the instrument MIDAS 2. The defects were created by ball bearing impact, the impact energy ranging from 5 to 22(J) as indicated in the labels. As expected, the depth of the defects and hence the number of fringes in the resulting moiré pattern increased with the energy of the impact.

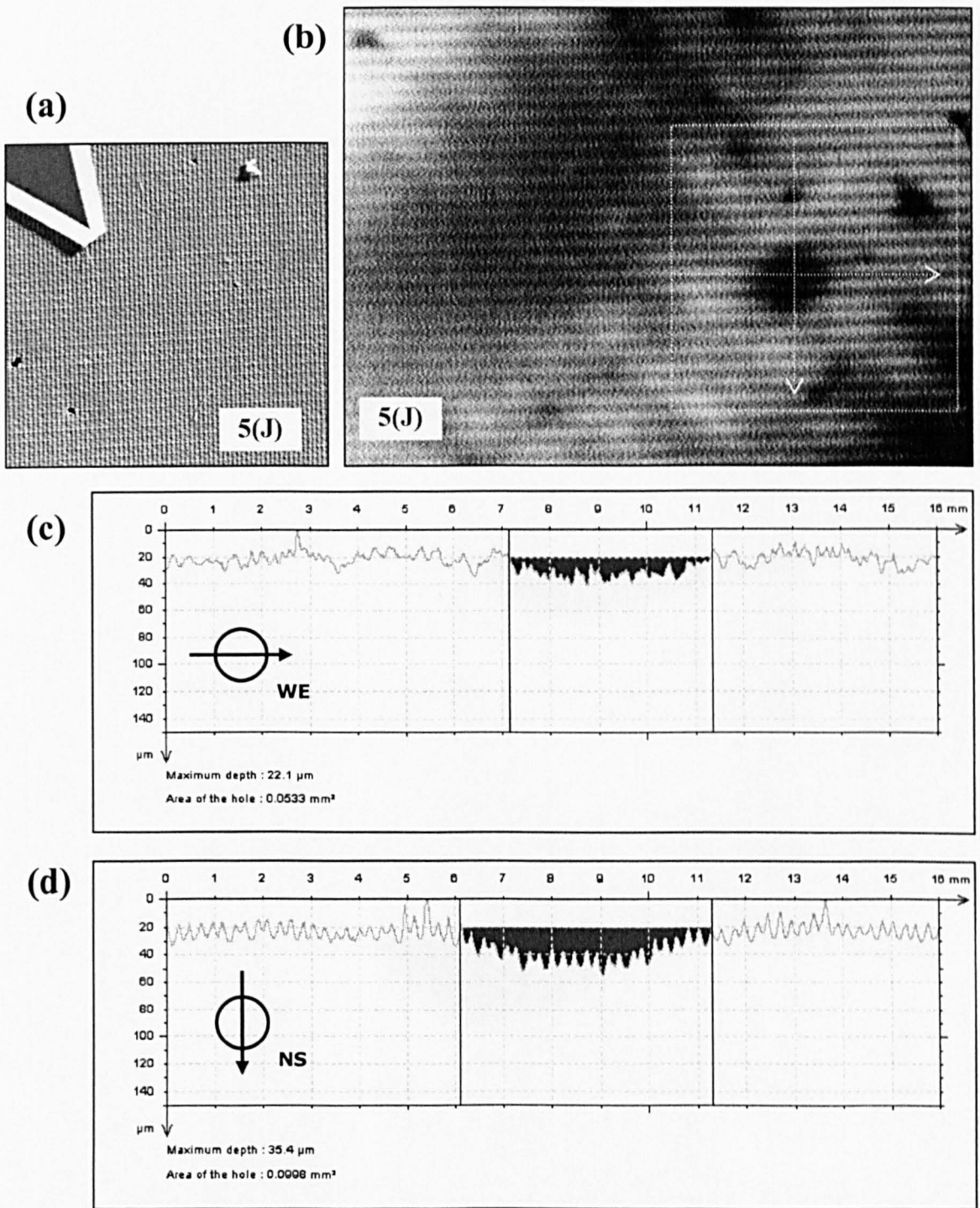


Figure 3.15: Impact 5(J) on sample S2 (a) close up photography (b) moiré photography (c) Surface profile across the horizontal middle line of the crater, scan direction WE. (d) Idem across vertical middle line, direction NS. Shaded areas in the profiles highlight the impact crater.

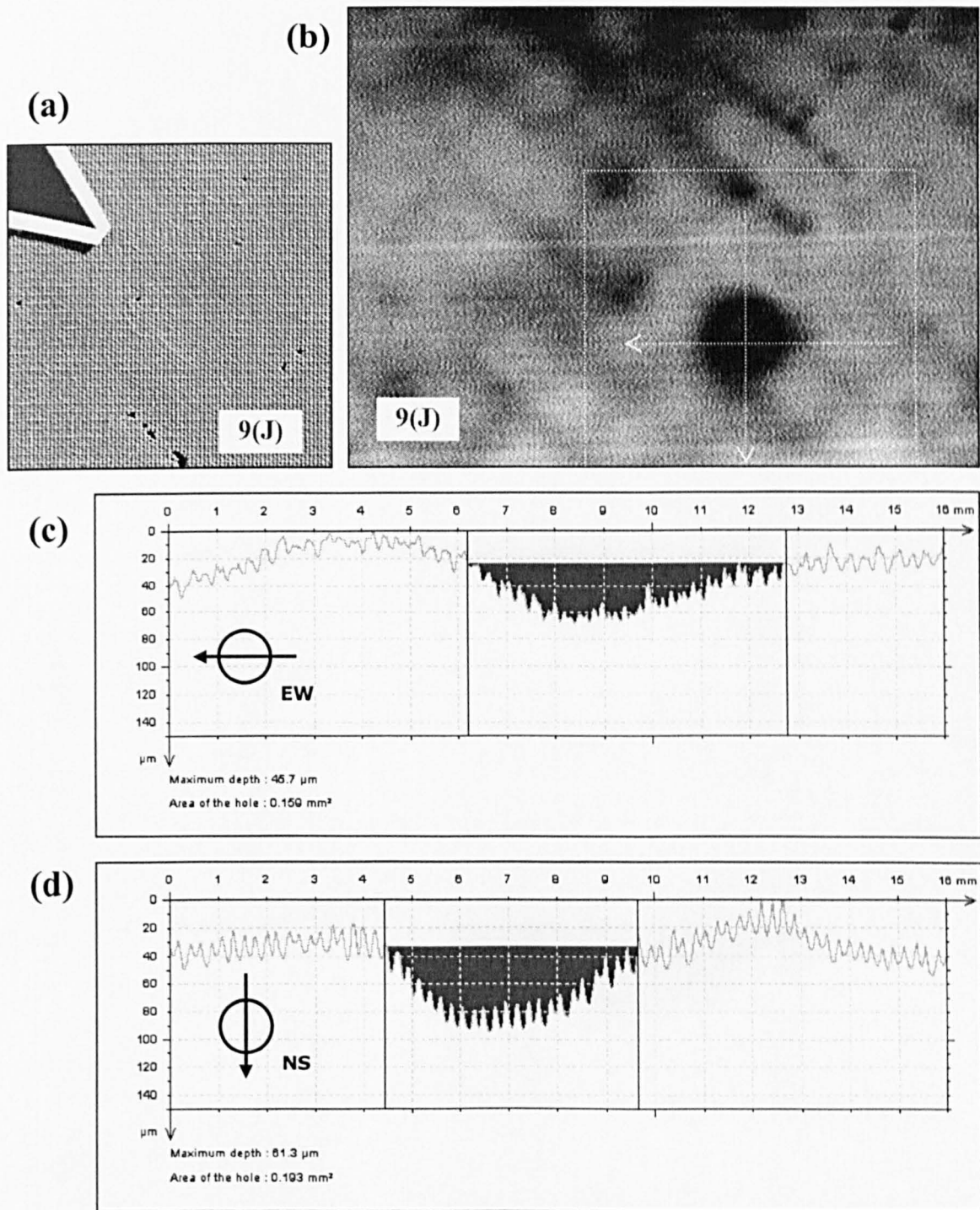


Figure 3.16: Impact 9(J) on sample S2 (a) close up photography (b) moiré photography (c) Surface profile across the horizontal middle line of the crater, scan direction EW. (d) Idem across vertical middle line, direction NS. Shaded areas in the profiles highlight the impact crater.

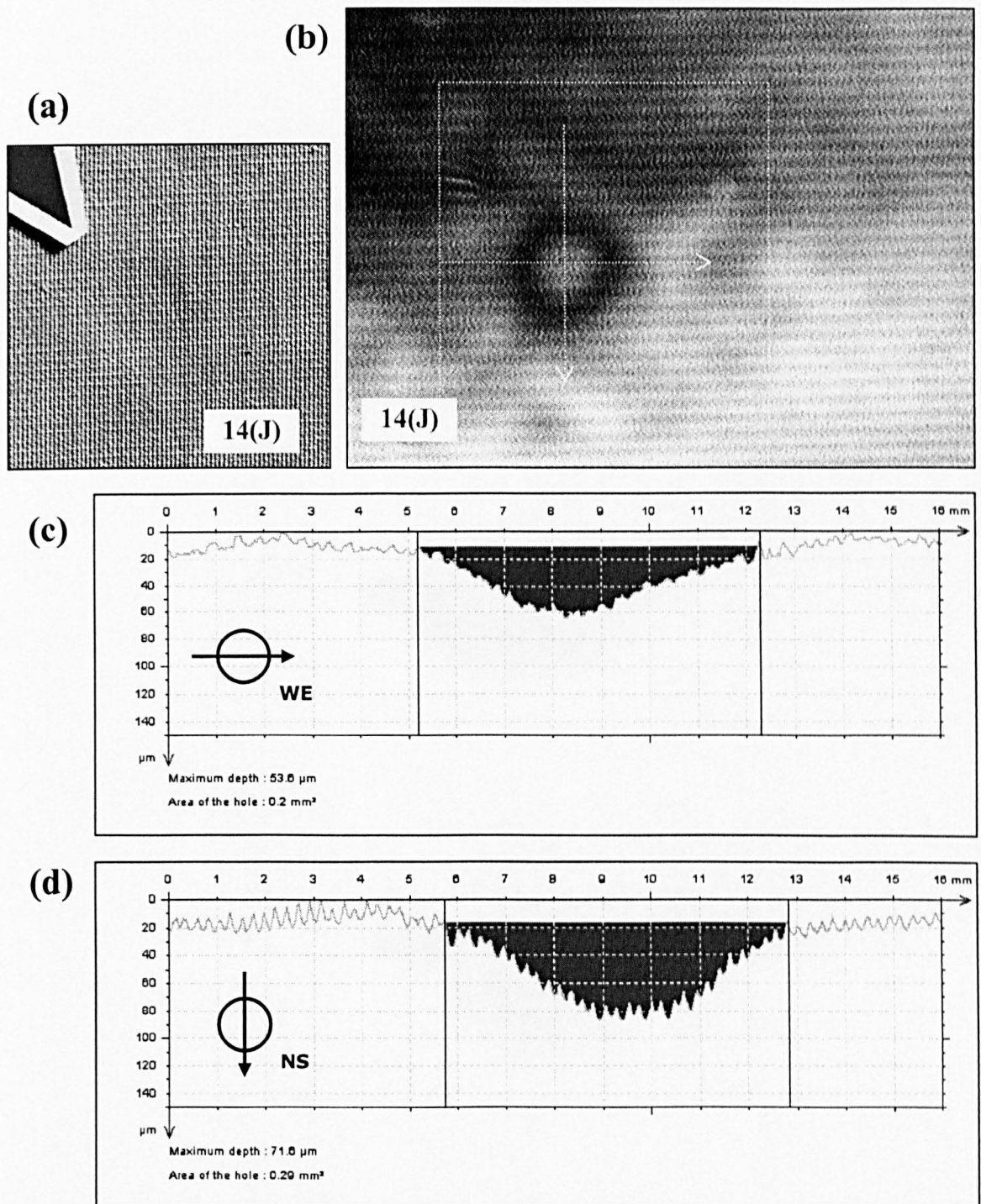


Figure 3.17: Impact 14(J) on sample S2 (a) close up photography (b) moiré photography (c) Surface profile across the horizontal middle line of the crater, scan direction WE. (d) Idem across vertical middle line, direction NS. Shaded areas in the profiles highlight the impact crater.

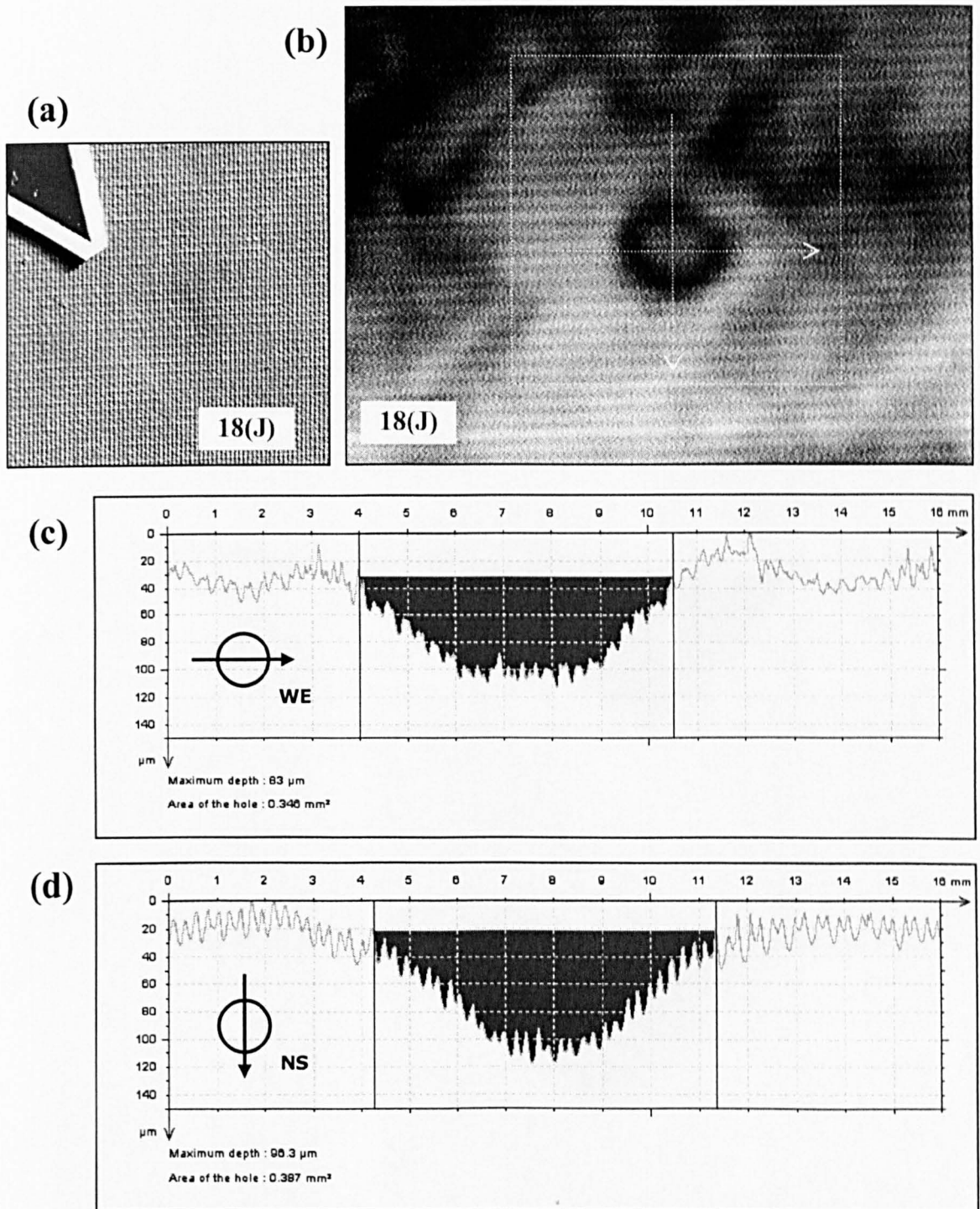


Figure 3.18: Impact 18(J) on sample S2 (a) close up photography (b) moiré photography (c) Surface profile across the horizontal middle line of the crater, scan direction WE. (d) Idem across vertical middle line, direction NS. Shaded areas in the profiles highlight the impact crater.

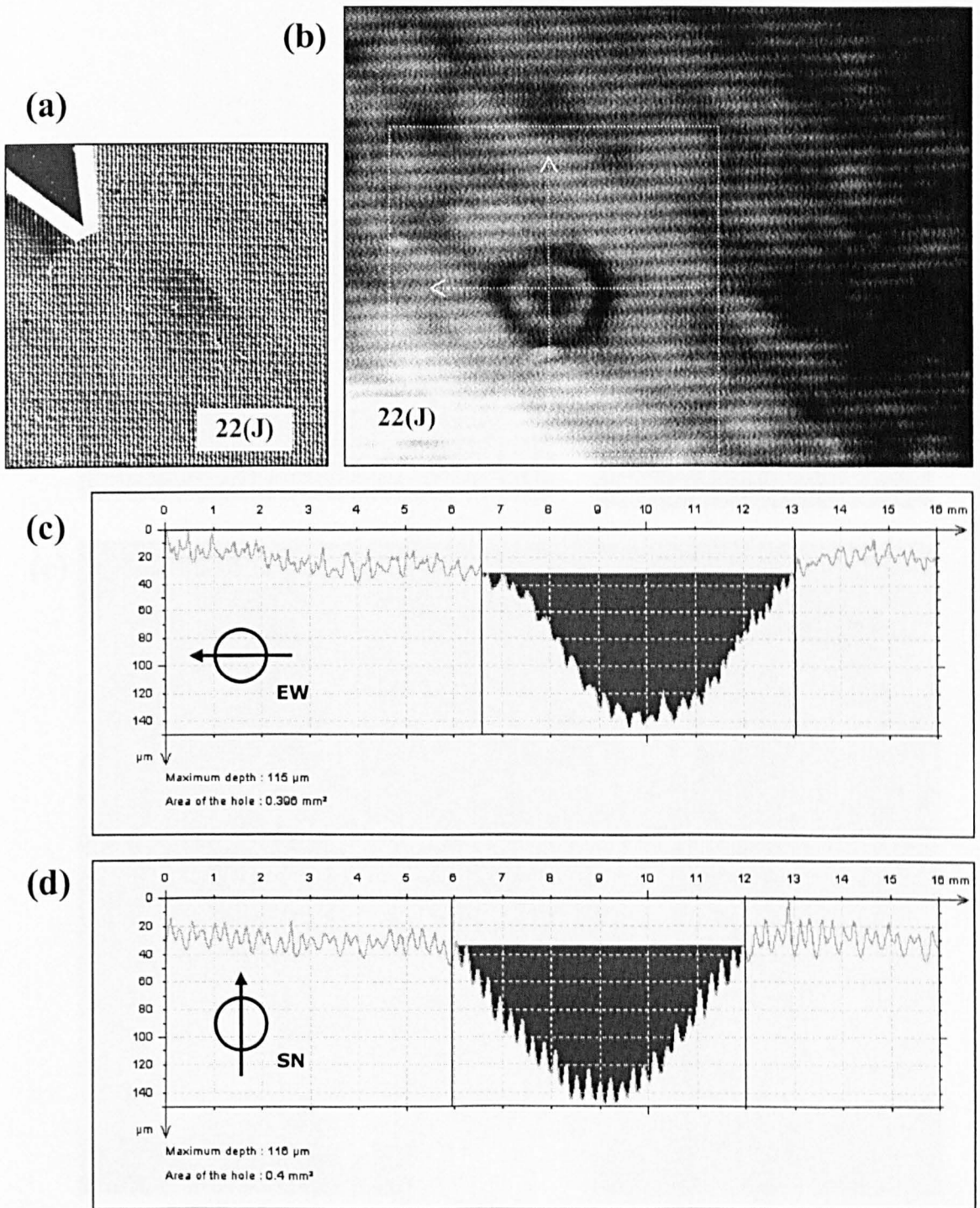


Figure 3.19: Impact 22(J) on sample S2 (a) close up photography (b) moiré photography (c) Surface profile across the horizontal middle line of the crater, scan direction EW. (d) Idem across vertical middle line, direction SN. Shaded areas in the profiles highlight the impact crater.

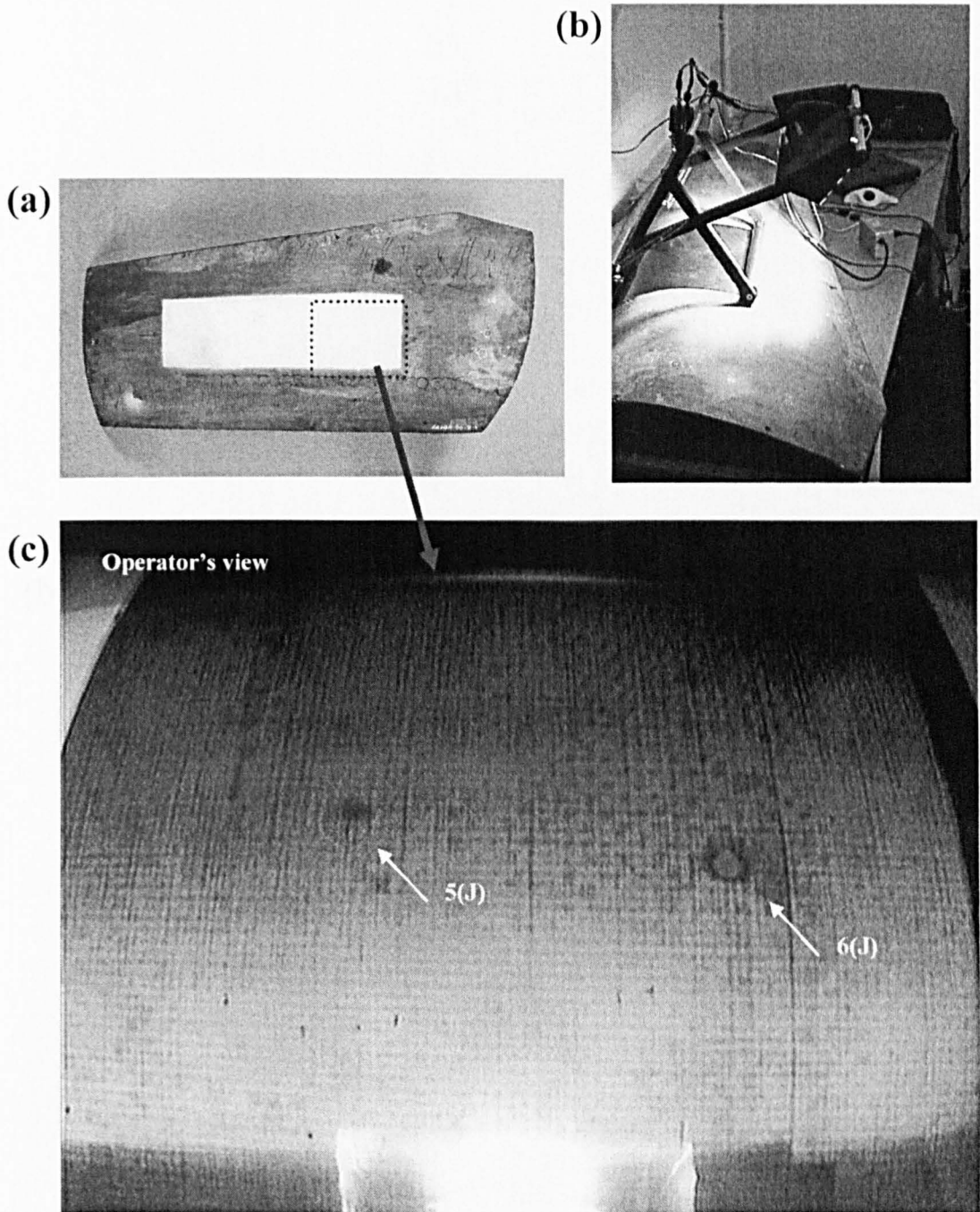


Figure 3.20: Detection of impact damage on the side panel of the EF-2000 Eurofighter Typhoon aircraft using MIDAS 2. (a) View of the curved composite panel (sample S3). The inspection area has been highlighted. (b) Inspecting the panel with the MIDAS 2 system. (c) Image of the operator's view taken from the camera mounted on the device. The area been inspected is highlighted in (a). The two impact craters that appear on the field of view correspond to impacts of 5 and 6(J) respectively.

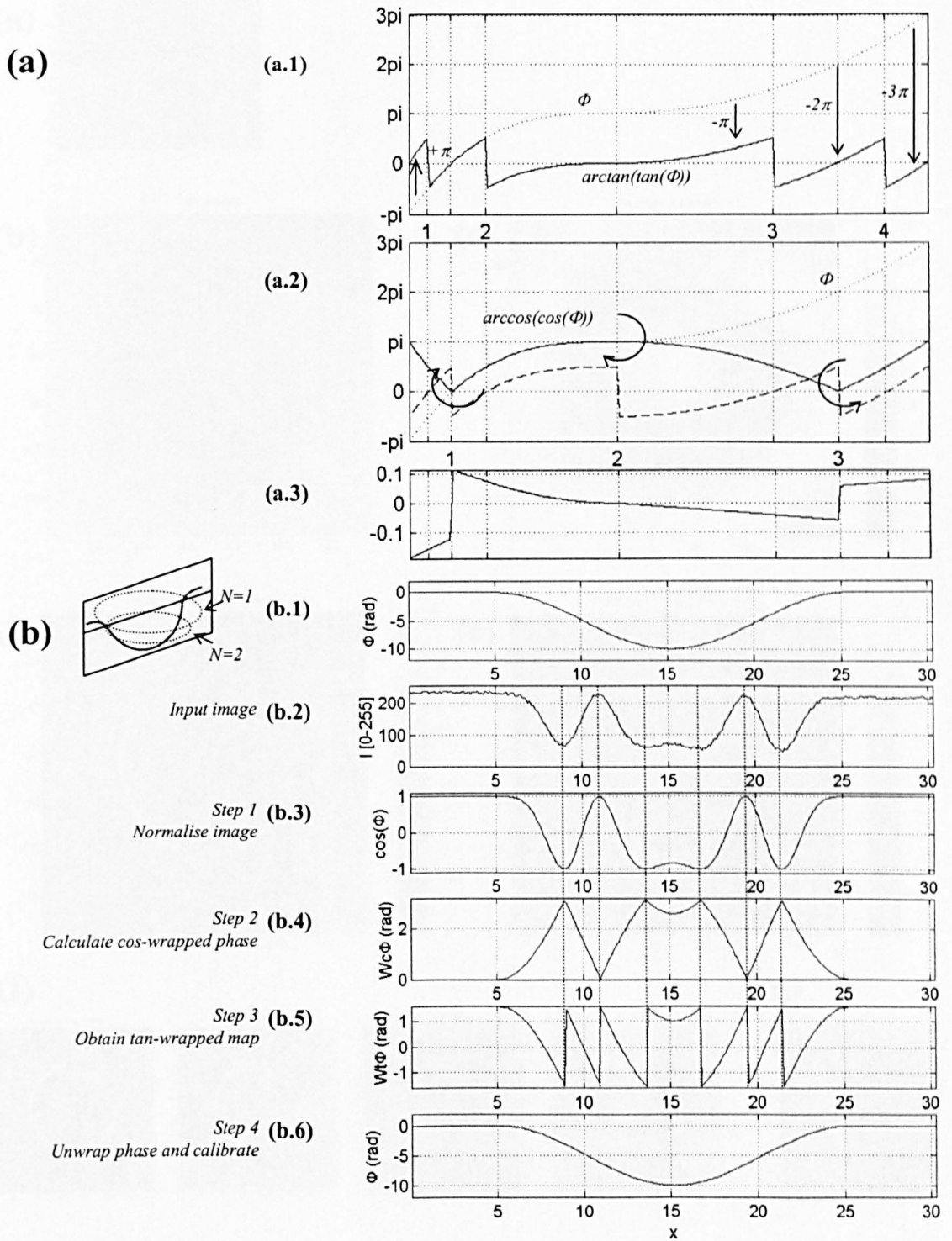


Figure 3.21: (a) Cos-wrapping versus tan-wrapping of phase data (b) Steps of the hybrid method for automatic measurement of fringe patterns, illustrated with a numerical example that simulates a surface defect. Note that the ends of the seven periods defined by the fringe crests in the moiré image 2 coincide with the discontinuities in the wrapped phase data in 4 and 5. The cos-wrapped phase in 4 was converted into tan-wrapped phase by subtracting  $\pi/2$  radians and multiplying by  $-1$  periods 1,3,5, and 7. The resulting quasi-tan-wrapped phase can be easily unwrapped by removing the  $\pi$  discontinuities at the ends of periods, and calibrated to produce a measurement of the depth.

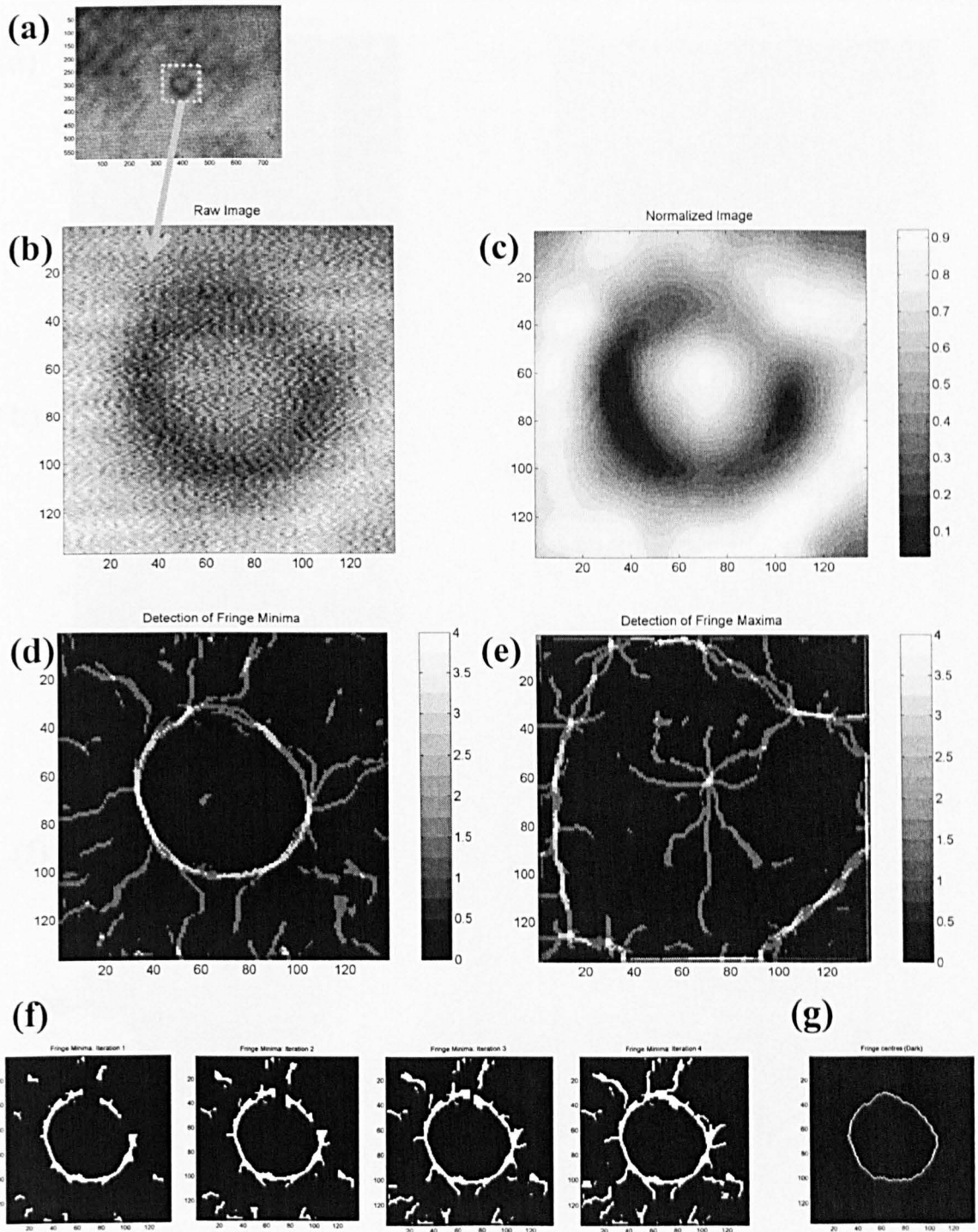


Figure 3.22: Automatic measurement of impact craters. (a) Moiré fringe pattern for the 18(*J*) impact. (b) Detail of the defect area extracted from the rest of the image. (c) Normalised image. (d) Pixels that satisfy the fringe minima condition (e) idem. for fringe maxima (f) Four iterations of the algorithm to skeletonize the locus of fringe minima shown in (d). (g) Measured fringe centre after thinning. This corresponds to the fringe minima (centre of the dark fringes). The same process is performed to reduce the image shown in (e).

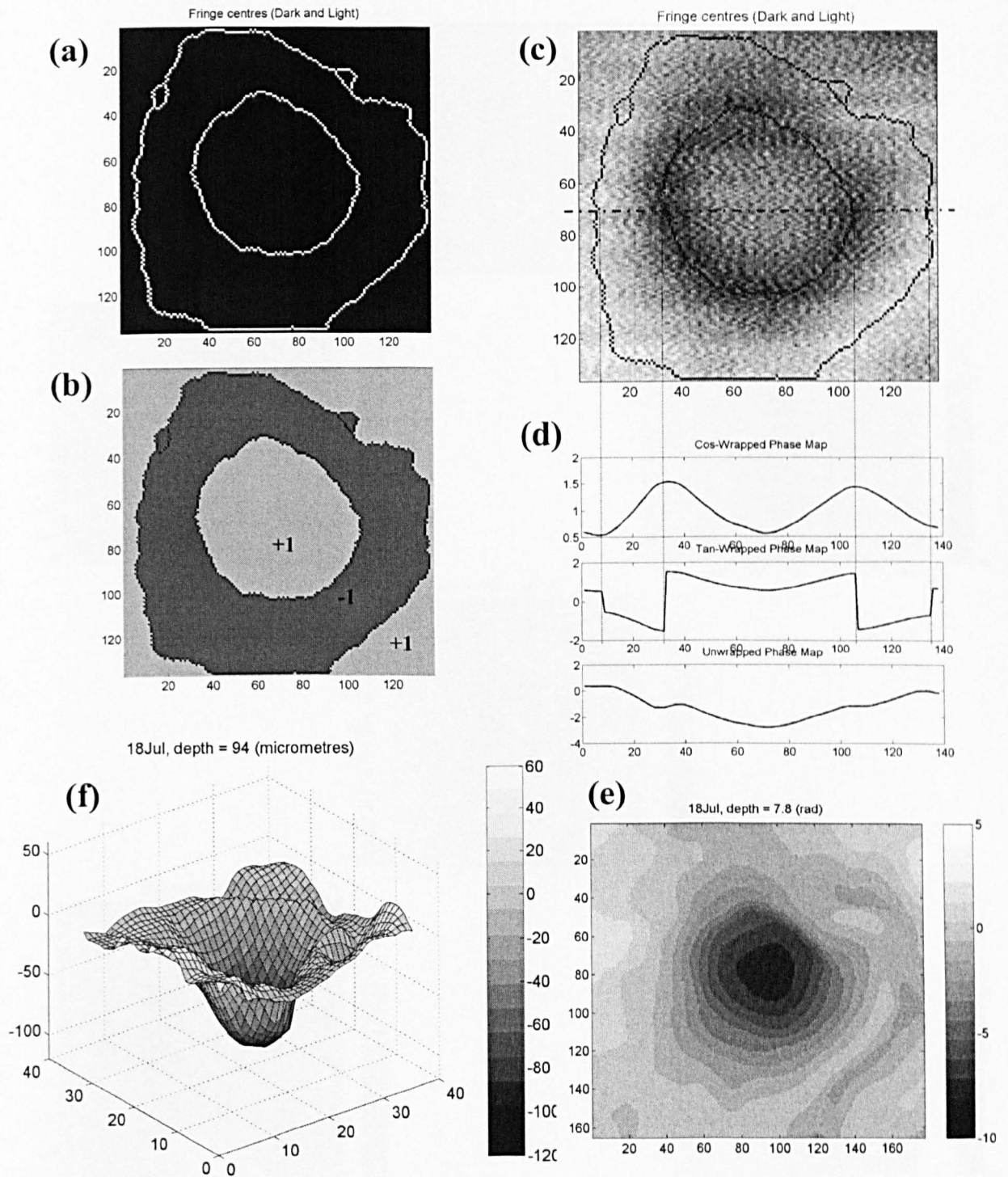


Figure 3.23: Automatic measurement of impact craters. (a) Final result from the fringe centre detection algorithm, including both the loci of minima (dark fringe centres) and maxima (bright fringe centres). (b) The regions of sign change of the cos-wrapped phase with respect to the tan-wrapped phase, defined in the image by the fringe centres. (c) The fringe centres superimposed on the fringe pattern. (d) Profiles along the middle row of the cos-wrapped phase map, the tan-wrapped phase resulting from the sign inversion, and the corresponding unwrapped phase. (d) Unwrapped phase map (e) Calibrated depth map. (f) 3D surface plot of the depth map.

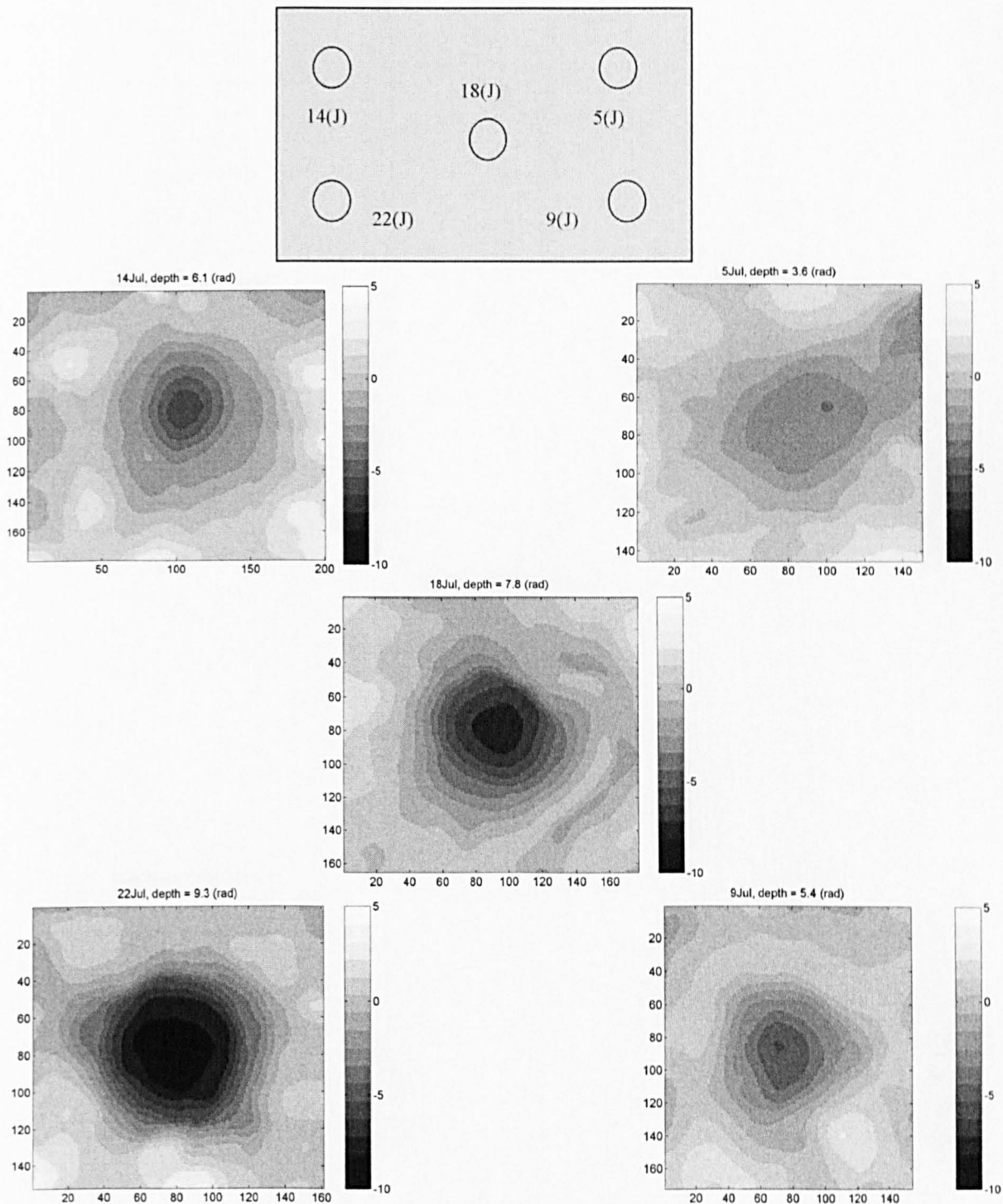


Figure 3.24: Phase maps corresponding to the five calibrated impact craters on sample S2. The units are pixels on the axes and radians on the greyscale. The magnification of the images is approx.  $0.074(mm/pixel)$ .

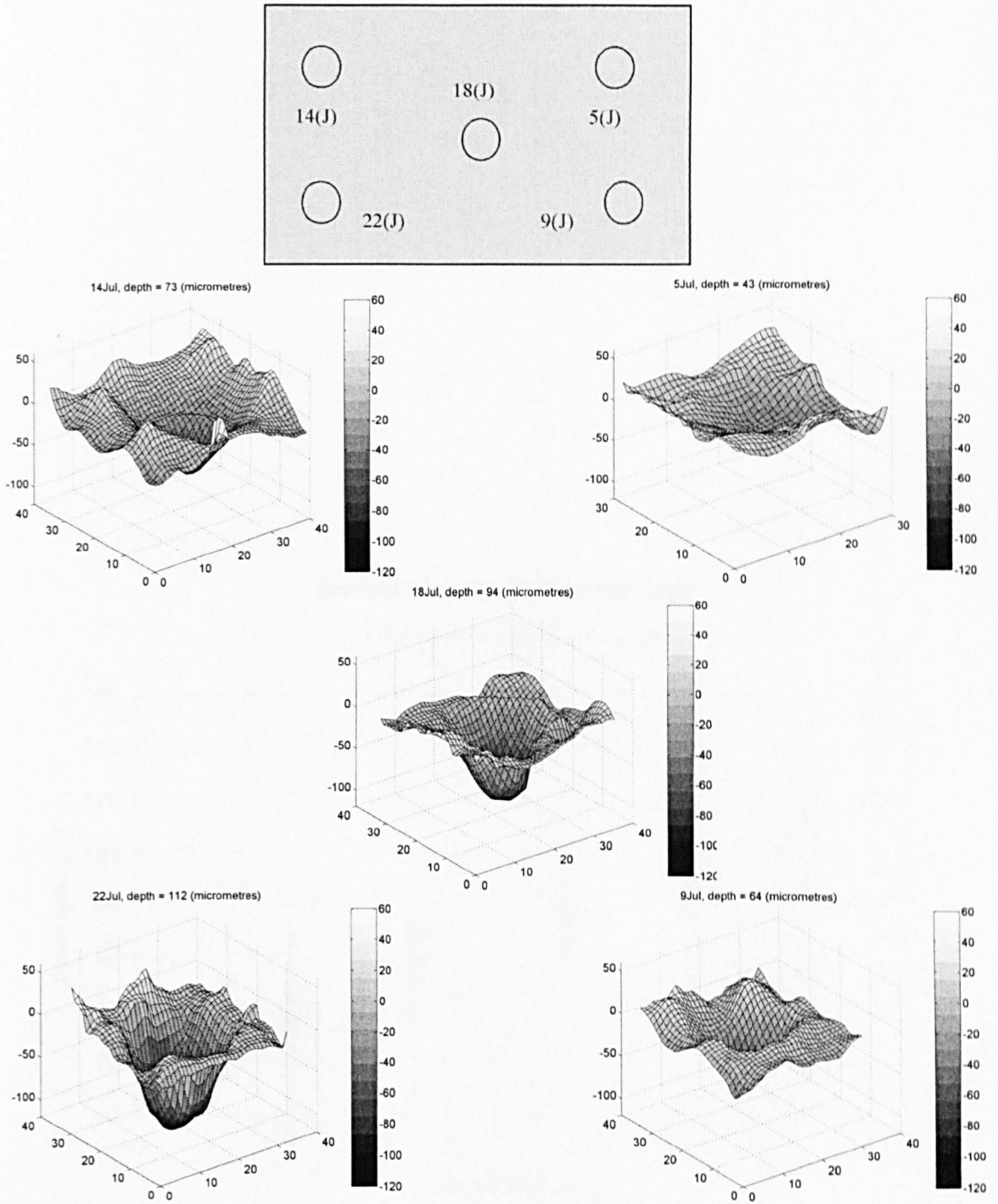


Figure 3.25: Depth maps corresponding to the five calibrated impact craters on sample S2. The units are pixels on the axes and micrometers on the greyscale. The magnification of the images is approx.  $0.074(mm/pixel)$ .

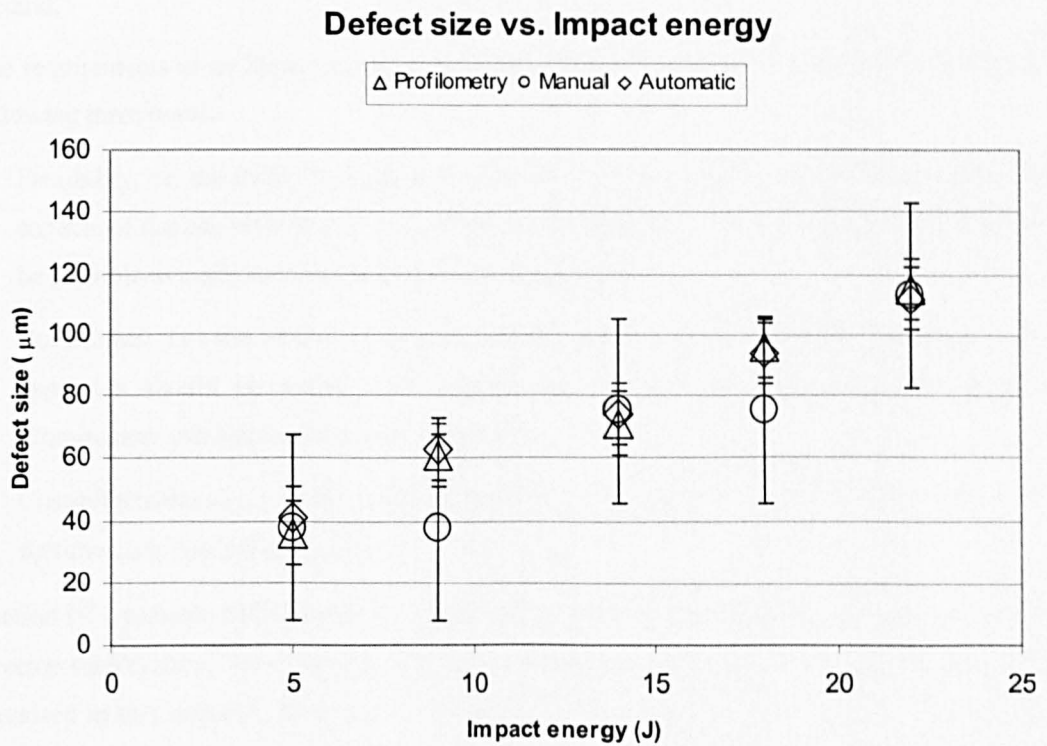


Figure 3.26: Comparison of the values of maximum depth measured using profilometry and the shadow moiré technique by means of automatic phase measurement and also by manually estimating the fringe order, for the five impact defects on sample S2. The results of profilometry and moiré are in good agreement, particularly when the automatic measurement technique is used.

## CHAPTER IV

# FRINGE PROJECTION: MATERIALS AND METHODS

### IV.1 Introduction

One of the primary goals of this research was the development of a general-purpose instrument for the measurement of shape and deformation in industrial applications, based on the moiré method.

The requirements of an ideal measurement system for industrial use can be summarised in the following three points:

- Flexibility, *i.e.* the ability to adapt to a wide range of applications. The technique should be capable of dealing with objects in a variety of sizes, shapes and surface finish, and it should be possible to easily modify the sensitivity of the system.
- Robustness, *i.e.* the ability to provide reliable results in unfavourable conditions. The apparatus should be simple and rugged, and the technique should cope with poor illumination, vibrations, and space constraints.
- Cost-effectiveness, *i.e.* inexpensive equipment, easy operation by a non-specialist, short set-up times, and low maintenance.

Section IV.2 presents the rationale that guided the selection of the fringe projection technique to develop such system. The following sections concentrate on the different elements of the system proposed in this research. Section IV.3 describes a portable and flexible prototype instrument. The methodology of use is discussed in section IV.4. Section IV.5 describes a set of novel algorithms for fast and reliable data processing. The calibration of the system is discussed in section IV.6, and section IV.7 reports on the validation of the method in a series of numerical and experimental tests. Finally, the last section of the chapter is dedicated to the discussion of the results of the validation tests and some concluding remarks.

The system presented in this chapter was used in the majority of the applications considered in this thesis, specifically those described in Chapter V, and also in the work on location of

components reported in Chapter VI. The latter required a few modifications to the instrument and procedures, which will be described there in detail.

In contrast, the new experimental technique for strain analysis proposed in Chapter VII employs a different set of experimental apparatus and procedures, which will be described in a section devoted to materials and methods in that chapter.

## **IV.2 Technique Selection**

The first step in the development of the measurement system was the selection of the most appropriate moiré technique among the existing methods for out-of-plane displacement measurement. It has been discussed that in-plane moiré techniques suffer from a number of shortcomings that make their routine application in industry difficult. Existing technologies for the preparation of specimen gratings (*e.g.* etching or bonding) require a great deal of skill and effort, and in most cases cause permanent damage to the sample. This issue will be further discussed in Chapter VII, where a novel technique is proposed to overcome this limitation.

The reflection moiré technique was discarded at an early stage because it requires a polished surface in the specimen, which narrows significantly the range of situations in which it can be applied.

The shadow moiré technique can provide high sensitivity measurements using simple apparatus, and can cope with a variety of surface finishes. This technique can indeed be successfully adapted to a particular industrial application, as demonstrated in Chapter III. However, the flexibility of this method is somehow limited when compared with the techniques that use projected fringes. A large grating must be fabricated and set-up close to the surface of the object, which adds to the cost and preparation time, especially for large objects with a complex three-dimensional shape.

The flexibility of the techniques based in projected fringes (*i.e.* fringe projection and projection moiré) makes them perhaps the best suited to build a general-purpose system. These methods can cope with objects in a wide range of sizes and arbitrary shapes. Their sensitivity range can be easily adjusted by several orders of magnitude, by changing the pitch of the projected fringes and/or the angles of projection and observation. Also, their requirements in terms of surface finish are not strict.

The main advantage of fringe projection over projection moiré is that the former uses very simple, robust and inexpensive apparatus that can be built with off-the-shelf components. In contrast, the latter requires delicate mechanisms for the precise alignment of the projecting and viewing gratings, increasing the cost and the complexity, and reducing the robustness of the apparatus.

On the other hand, the main drawback of fringe projection is a loss in sensitivity with respect to projection moiré. In the latter, the moiré effect works as a motion amplifier, and generally provides higher sensitivity because vertical displacements translate into larger lateral shifts of the moiré fringe pattern compared with those of the projected fringes. However, the sensitivity that can be achieved with fringe projection is sufficient for the majority of industrial applications. For instance Sciammarella *et al.* (2001) recently proposed a fringe projection system as an alternative to coordinate measurement machines (CMM) for high precision contouring of gear teeth, reporting accuracies in the micrometer range.

The arguments presented in this section seemed to suggest that the fringe projection technique had a high potential to fulfil the desired requirements of flexibility, robustness and cost. The remainder of this chapter describes the development of a measurement system based on fringe projection that attempts to address these requirements.

### IV.3 Experimental Apparatus

The prototype instrument developed for this research is shown in fig. 4.1. The instrument allows the generation of a set of projected fringes onto the surface of the object, and the recording of images of the resulting fringe pattern for processing.

The projector was designed by Dr. M. Pacey and Dr. J. Carazo Alvarez and built in-house using a 300(W) halogen-tungsten lamp as a light source. Two cooling fans and a cold mirror were used to reduce the heat output. The light is projected through a glass grating (Edmund Scientific precision Ronchi rulings) with line frequencies ranging from 100 to 250(*inch*<sup>-1</sup>). The projector has a standard fitting for C-mount lenses. The grating image was focused onto the surface of the object using a 12.5-75(*mm*) zoom TV lens.

A CCD camera (Panasonic WV BP100) was used to record digital images of up to 574×768 pixels. A 12.5-75(*mm*) zoom TV lens was used to image small objects, and a wide-angle 4.5(*mm*) lens for larger objects. A commercial frame grabber (MRT Video PCMCIA card) was used to connect the camera to the PC computer used for data processing (Toshiba Satellite 1700 laptop, 500(MHz) processor and 128(Mb) of RAM memory). In some of the work, the video output from the camera was displayed on a video monitor for convenience (Panasonic WV 5340), although live preview images can be seen directly on the PC using the frame-grabber software.

The instrument sat on a tripod fitted with a set of off-the-shelf components (Manfrotto). This arrangement provided a light and portable, yet stable frame that allowed great flexibility to modify the configuration of the elements according to the requirements of the application (*e.g.* object size, required sensitivity, space constraints etc.).

A pan/tilt tripod head allowed three-axis movement, controlled by separate locking handles, of the instrument as a whole. The optical elements of the system were attached using a quick-release system to the horizontal bar mounted on the tripod head, as shown in fig. 4.1. The quick-release system comprised hexagonal plates bolted to each optical element, and adaptors mounted with grips onto the horizontal bar. This system allowed easy adjustment of the relative distance and the orientation of the elements and could be securely locked in place. Two custom elements made of aluminium were added to the assembly: a counterweight to balance the instrument and a special adjustable mount for the camera with a spirit level.

The alignment procedure used a 5(mW) red laser diode to produce a bright light spot. A commercial laser module (NVG Inc. M660-5) was used, which comprises the diode, a focusing lens and batteries in a 15×46.5(mm) casing.

The alignment laser was attached to the camera and its beam aligned with the optical axis of the camera using the procedure described in section IV.6.2. A special mount was designed for the module to allow for fine adjustments of the beam direction.

## IV.4 Methodology Of Use

### IV.4.1 General Considerations

The fringe projection technique combines two images of the fringes projected respectively onto a reference surface (*i.e.* the reference image) and an object surface (*i.e.* the object image), to measure the relative out-of-plane displacement between the two surfaces at each point in the field of view of the camera. A general description of the technique and a derivation of the main mathematical expressions were presented in section II.3.2.4.

The absolute shape of an object can be measured with this technique by using a flat plate as the reference surface and the object itself as the object surface. Similarly, the out-of-plane deformation of a specimen can be measured by using the initial, unloaded state of the specimen as the reference surface, and the specimen in the final deformed state as the object surface. Other configurations are possible, for instance comparing a specimen with a master for quality control applications. In all cases, it is assumed that there are no intervening changes in the optical arrangement during the collection of the two images.

The sensitivity of the technique is controlled by the configuration of the elements, specifically by the pitch  $p$  of the lines projected on the reference plane, and the angle between the optical axes of the camera and the projector  $\theta$ . These two parameters determine the *contour spacing*, *i.e.* the value of the out-of-plane displacement that produces a variation of one in the fringe

order. The sensitivity of the technique can be increased by increasing the angle  $\theta$  and reducing the pitch  $p$ .

Modern phase measurement fringe pattern analysis methods provide accurate fractional fringe orders down to 1/100, but generally require a minimum number of pixels per fringe to adequately describe the intensity profile. As a result of this, the sensitivity is ultimately limited by the lateral resolution of the viewing system, which determines the minimum pitch  $p$  that can be used.

The following sections describe the methodology for the set-up of the system and the data collection, using a simple example to illustrate the procedure. Figure 4.2(a) shows an image of an arts and crafts mask, made of thin moulded plastic sheet; with approximate dimensions 280×230×55mm. The mask provides a nice example with which the technique can be demonstrated.

#### ***IV.4.2 Set-Up Of The Optical Elements***

This section describes step by step the general procedure for the set-up of the instrument. A sequence of images, see fig. 4.3, was collected with the camera of the instrument during the set-up for the collection of shape data in the example of the mask, in order to illustrate each step of the procedure.

1. Set-up the tripod with the instrument. Provided the space constraints specific to the application allow it, it is preferable to place the instrument far away from the object (a distance at least one order of magnitude larger than the size of the object), so that the telecentric hypothesis can be applied. Select the distance between camera and projector depending on the required sensitivity. The combination of a fine grating and a small angle generally produces better results than larger angles and coarser gratings for a given level of sensitivity. In the example, the distance  $h$  from the object to the camera was 1630(mm) and the projector was located at a distance  $d=490(mm)$  to the right of the camera, as shown in fig. 4.2(b).
2. Align the camera with the object of interest, see fig. 4.3(a)
3. Align the optical axes of the camera and the projector so that they intersect at point O situated approximately on the reference plane in the centre of the image. A simple procedure that offers reasonable accuracy is to zoom out the camera lens, and zoom in the projector to obtain a relatively small circle of light in the image. Modify the orientation of the projector so that the circle of light is at the centre of the field of view, as shown in fig. 4.3(b).
4. Set the zoom level of the camera lens to view the area of interest, see fig. 4.3(c).

5. Place the grating in the projector, and open the aperture of the lens. Focus the fringes on the surface of the object, as shown in fig. 4.3(d).
6. Set the zoom level of the projector by monitoring the size of the fringes in the TV screen, fig. 4.3(e). Estimate approximately 8 to 10(*pixels/fringe*) in relatively flat areas, and a minimum of 4(*pixels/fringe*) in areas with steep slopes facing away from the projector, where the fringes seen by the camera appear closer together.
7. Perform fine adjustments of the zoom and focus of the camera lens. The zoom needs to be set first because it affects the focusing point. Increase the aperture of the camera lens as shown in fig. 4.3(f) to reduce the depth of focus of the camera and facilitate precise focusing.
8. Gradually reduce the aperture just by the amount necessary to remove glare or overexposure, as shown in fig. 4.3(g) so as to make full use of the intensity range of the camera sensor.
9. Defocus the projector slightly to obtain a sinusoidal intensity profile in the projected fringes. Figure 4.3(h) shows the final result.

#### **IV.4.3 Data Collection**

The set-up procedure described in the previous section prepares the system for the collection of good quality fringe images. The fringe projection method requires at least an object image and a reference. Typically the set-up was carried out using the object, which would normally have more pronounced surface features, and therefore the object image, shown in fig 4.4(a) would normally be collected in the first place.

Several alternatives exist for the collection of the reference image. The reference surface would typically be a flat plate, see fig 4.4(b). When possible, the object may be removed and a flat reference plate clamped in its place perpendicular to the camera. Alternatively, if it is not practical to move the object, the reference plate may be placed directly in front of it. It is also feasible to collect the reference image later, in a different location, provided the configuration of the optical elements in the system is not disturbed during the collection of the two images. Section IV.6.2 describes a method for the precise alignment of the reference plate perpendicular to the camera axis. A calibration image may also be required for the automatic system calibration described in detail in section IV.6.4.

### **IV.5 Algorithms Of Digital Fringe Pattern Analysis**

The depth information was extracted by digitally processing the reference and object images, using the processing algorithm whose main steps are summarised in the flowchart presented in

fig. 4.5. The first step is the extraction of the phase information from the images, by means of the spatial phase-stepping algorithm described in section IV.5.1. This algorithm yields a modulo  $2\pi$  phase map (*i.e.* wrapped in the  $[-2\pi, 2\pi]$  interval), which must be further processed to obtain the continuous phase. An example of a wrapped phase map is shown in fig. 4.4(c) The unwrapping algorithm described in section IV.5.2 removes the discontinuities in the wrapped phase map following a scanning path calculated by means of quality maps of the images, such as the one shown in fig. 4.4(d). The effect of pre-processing the input images to improve the accuracy of the phase extraction step, and to reduce the errors of the unwrapping procedure are discussed in section IV.5.3. Finally, the depth information can be obtained from the unwrapped phase map using one of the calibration methods described in section IV.6.

The algorithms of fringe pattern analysis developed within this research have been implemented in the software package JOSHUA. More details on the software can be found in Appendix AII.

#### ***IV.5.1 Phase Measurement Five Step Spatial Algorithm***

Some attempts have been made by different authors to devise an algorithm that can be used on a single image, like the spatial phase-shifting techniques, with the simplicity of the calculations associated to temporal phase shifting. Some of the most successful attempts have been spatial phase measurement methods, which perform all the processing in the spatial domain, for instance the four step algorithms by Shough *et al.* (1990) and Chan and Bryanston-Cross (1995), or the Hilbert transform algorithm proposed by Sutton *et al.* (2001).

A novel technique, related to these spatial carrier phase-stepping methods is proposed here, which can be used to measure the phase from a single image with a very low computational burden. Figure 4.6 shows a flowchart that summarises the main steps of the proposed phase-extraction algorithm. The full derivation of the expressions and an analysis of the conditions of application of this algorithm are detailed in Appendix AI.

Assuming vertical orientation of the fringes in the reference image, as shown in fig. 4.4(b), the intensity distribution of the digitised image collected by the CCD camera can be mathematically described as follows:

$$I(i, j) = A(i, j) + B(i, j) \cos(2\pi f j + \Phi(i, j)) \quad (4.1)$$

where  $(i, j)$  are the pixel coordinates in the image,  $A$  and  $B$  are the background illumination and fringe modulation terms respectively,  $f$  is the carrier frequency, which is related to the pitch  $p$  of the fringes in the image (measured in pixels), and the modulated phase  $\Phi$  encodes the information related to the surface shape. Note that eq. (4.1) is a discretized version of eq. (2.17), which was introduced in section II.3.2.4. Note as well that the pixel coordinates are defined following the usual convention in image processing: the origin is located at the top left corner of

the image, the  $i$  coordinate describes the row number and increases from top to bottom, and the  $j$  coordinate gives the column number, and increases towards the right of the image.

The algorithm computes two separate maps of phase estimators for the reference and object images using the following expression

$$\Phi^* = \arctan\left(\frac{2(I_2 - I_4)}{2I_3 - I_5 - I_1}\right) \quad (4.2)$$

where the numeral subscripts denote shifts of the image in the direction perpendicular to the fringes (rows of the array following the convention described above).

The shifts are integer fractions of the pitch  $p$  of the reference image, as indicated below

$$\begin{aligned} I_1 &= I(i, j - \text{int}(p/2)) \\ I_2 &= I(i, j - \text{int}(p/4)) \\ I_3 &= I(i, j) \\ I_4 &= I(i, j + \text{int}(p/4)) \\ I_5 &= I(i, j + \text{int}(p/2)) \end{aligned} \quad (4.3)$$

Note that  $p$  represents the pitch of the reference image when the above expressions are applied to the object as well as when they are applied to the reference. The pitch can be calculated from the 1-D FFT of a row of the reference image, by removing the DC component and locating the first peak. In practice, this process is repeated for a set of evenly distributed rows, and an average value of  $p$  is calculated, to increase the robustness of the calculation (e.g. to account for noise, areas that contain background, etc.).

The phase difference between the reference and object image can be obtained by subtracting the estimators calculated for the reference and the object.

$$\Delta\Phi^* = \Phi^*_O - \Phi^*_R \quad (4.4)$$

The phase estimator defined in eq. (4.2) was derived from the self-calibrating five-bucket algorithm of temporal phase shifting proposed by Hariharan *et al.* (1987).

The analysis in Appendix AI concluded that the proposed estimators are accurate provided (i) the background and amplitude terms vary slowly relative to the phase carrier, and (ii) the modulated phase also varies slowly relative to the phase carrier.

Condition (i) is not met in some situations, such as objects that present sudden changes in the surface colour, markings etc., in which the background and/or amplitude modulation terms vary

rapidly. The techniques for pre-processing and normalization of images described in section IV.5.3 can be used in such cases to remove these terms.

Condition (ii) is required because the error of the algorithm increases with the relative difference in pitch between the reference and the object images. The accuracy of the method is reduced in surfaces that present discontinuities or very pronounced slopes. However, a good approximation can be achieved in most practical cases by selecting a pitch of the projected lines smaller than the size of the features of interest in the surface, so that the modulated phase is relatively constant for the five points sampled by the algorithm.

Conditions (i) and (ii) are not exclusive of the method proposed here. They in fact apply to all phase extraction algorithms, both temporal and spatial. In particular, the resolution of spatial methods is reduced in the direction of the phase carrier (*i.e.* perpendicular to the fringes) because the calculated phase is averaged over the sampling points.

The analysis in Appendix A1 proved that the error due to variation of the modulated phase is equivalent to a phase shift error. There is abundant literature on the influence of phase shift error on the measured phase, specifically for temporal algorithms. For instance Creath (1986) conducted a thorough comparison, and Malacara (1992) also contains a good review. One of the main conclusions of these studies was that the Hariharan algorithm minimised the error in the phase measurement due to phase shift error, and was also the less sensitive to noise. This result can be extrapolated to the spatial algorithms by means of the analogy described in Appendix A1, and it can be concluded that the proposed algorithm is expected to produce more accurate results for a wider range of surface shapes (*e.g.* with stronger slopes) than existing spatial phase measurement methods based on four-step algorithms, such as those proposed by Shough *et al.* (1990) and Chan and Bryanston-Cross (1995).

### ***IV.5.2 Phase Unwrapping Quality Bins Algorithm***

Given that the signs of the numerator and denominator in eq. (4.2) are known, it is possible to apply the four-quadrant arc tangent operator to compute the phase estimators, which as a result appear *wrapped* within the interval  $[-\pi, \pi]$ , and present  $2\pi$  discontinuities at the end of the periods. It follows that the phase difference map defined in eq. (4.4) will appear *wrapped* in the interval  $[-2\pi, 2\pi]$ , with  $2\pi$  and  $4\pi$  discontinuities at the end of the periods.

In section II.4.4 we introduced the term unwrapping, which consists of detecting the jumps and adding appropriate multiples of  $\pi$  until a continuous phase map is obtained. We mentioned also that the presence of noise and/or aliasing in real two-dimensional images may corrupt the phase, and these errors may propagate through the image during the unwrapping process making it path-dependent. We also introduced the two main categories of unwrapping algorithms: path-

following algorithms which determine the unwrapping path by means of local operations at pixel level, and global algorithms, which minimize some global measure of the difference of gradients between the wrapped and unwrapped phase.

The author used the results of a study by Ghiglia and Pitt (1998) as a guide in the selection of a suitable unwrapping algorithm. They compared eight state-of-the-art algorithms in terms of memory requirements, computation time and grade of success, finding that path-following algorithms tend in general to be faster, but can cause propagation of errors, while global algorithms sometimes provide better results but tend to be very slow. Based on the results of this study, the author considered that the quality-guided algorithm offered the best trade-off between performance and speed for the present study.

Quality guided algorithms are a conceptually very simple. They use some measure of the reliability of the wrapped phase data, in the form of a quality map, to select an unwrapping path. The goal is to process the regions where the phase data is more reliable first, in order to prevent the propagation of errors from regions where the phase information is corrupted to the rest of the image. The simplest implementation of the algorithm generates a mask to protect pixels with unreliable phase data, which are avoided by the unwrapping process. A more refined version of this algorithm maintains a sorted list of all the pixels to actually perform the unwrapping in strict order of decreasing quality (Ghiglia and Pritt, 1998), which computationally is very demanding.

A variation of the quality-guided unwrapping was developed for this study to improve the speed of execution while maintaining a good level of reliability. This novel implementation is based on partial pre-sorting of the pixels into a number of categories or bins according to their quality values.

A measure of the quality is needed to guide the unwrapping algorithm. Figure 4.6(a) shows a diagram of the two alternative techniques proposed to compute the quality map.

The first possibility is using the modulation of the sinusoidal signal in the image, which can be defined rearranging eq. (4.1) as follows

$$I(i, j) = A(i, j)(1 + \gamma(i, j) \cos(2\pi f_j + \Phi(i, j))) \quad (4.5)$$

therefore

$$\gamma(i, j) = \frac{B(i, j)}{A(i, j)} \quad (4.6)$$

The signal modulation can be expressed in terms of the lateral shifts of the image  $I_1, \dots, I_5$ , defined in eq. (4.3), by adapting an analogous expression proposed by Hariharan *et al.* (1987) for their temporal phase shifting algorithm.

$$\gamma = \frac{3\sqrt{4(I_4 - I_2)^2 + (I_1 + I_5 - 2I_3)^2}}{2(I_1 + I_2 + 2I_3 + I_4 + I_5)} \quad (4.7)$$

This expression is consistent with the phase estimators proposed in eq. 4.2, thus it can be used to determine confidence in the calculated phase value. It can be applied separately to the reference and the object images, and the results combined to obtain the quality map  $\gamma(i, j)$  of the phase difference, by multiplying the values pixel by pixel.

$$\gamma(i, j) = \gamma_R(i, j) \cdot \gamma_O(i, j) \quad (4.8)$$

An alternative approach for the generation of a quality map is to calculate the pseudo-correlation of the map of wrapped phase differences defined by eq. (4.4), by direct application of the following expression (Ghiglia and Pritt, 1998).

$$\rho(i, j) = \frac{\sqrt{(\sum \cos \Delta\Phi)^2 + (\sum \sin \Delta\Phi)^2}}{k^2} \quad (4.9)$$

where the sums are evaluated over the  $k \times k$  neighbourhood of pixel  $(i, j)$ . This expression also provides an adequate measure of quality.

Often there are regions of the image that contain background or regions that are not of interest. In such cases it is generally beneficial to exclude these areas from the unwrapping path, to avoid the propagation of any phase errors in them to other regions. This is done using a *mask*, which is a binary image with ones inside the region of interest and zeros outside it. It can be created manually in the software by selecting areas using the mouse, or automatically, by thresholding the quality map, since background areas of the image that do not contain fringes tend to present very low signal modulation. Before the unwrapping, the quality map is multiplied by the mask to set the quality value of the background regions to zero.

Figure 4.8 summarises the main steps of the unwrapping algorithm in a flowchart. First, four bins are defined associated to the image. The size of the  $k^{\text{th}}$  bin is calculated using the following empirical expression

$$B_k = Q \left( \frac{k}{4} \right)^d - \sum_{i=0}^{k-1} B_i \quad (4.10)$$

where  $Q$  is the total number of non-masked pixels in the image and  $d$  is an integer parameter that control of the distribution of the pixels in the bins. For  $d=1$  all the bins are the same size,

and as  $d$  increases more pixels are passed to the higher quality bins, so that the bins containing the lower quality pixels are smaller than those containing the higher quality pixels. This was found to reduce the effect of corrupted phase in most cases. The bins that will store higher quality pixels are assigned a higher priority level.

A histogram analysis of the quality map allows the automatic selection of the three quality thresholds  $T_k$  used to sort the pixels into the four *bins* according to their quality values. The thresholds are selected so that the number of pixels assigned to the  $k^{\text{th}}$  bin (*i.e.* with quality values between  $T_k$  and  $T_{k+1}$ ) approximately coincides with the size  $B_k$  calculated in eq. (4.10).

The algorithm assigns three tags to each pixel in the image: *wrapped/unwrapped*, *active/inactive*, and *unexplored/explored*. All pixels are initially set to *wrapped*, *inactive*, and *unexplored*. The unwrapping procedure starts at the pixel with the highest quality level. The algorithm declares this pixel *active* and *unwrapped* and starts the iterative procedure described by the flowchart in fig. 4.7. The main loop of the iterative algorithm consists of four steps as follows

1. The neighbours of the active pixel are unwrapped if appropriate, by adding the multiple of  $2\pi$  that makes the phase continuous with respect to the active pixel.
2. The quality value of each of the neighbour pixels is compared with the thresholds defined at the beginning, in order to assign each neighbour to the appropriate bin. Any pixels that may have been marked as unwrapped in a previous iteration are skipped in this step.
3. The neighbour pixels are marked as unwrapped, and the active pixel is declared inactive and explored.
4. The algorithm searches the bins for the next pixel that will be set active to continue with the algorithm. The bins are searched until a pixel is found, starting from the highest priority bin (the one that stores top quality pixels) and moving onto the lower priority bins only when the previous ones are empty. The bins use an efficient first-in-first-out architecture (*i.e.* the pixels are retrieved from the bins in the order the algorithm has encountered them), for speed of computation. The first pixel found in the bins is set active and the procedure is repeated until all the bins are empty (*i.e.* all the image has been unwrapped). Note that at any given point the bins store those pixels that have already been unwrapped but not yet explored, *i.e.* the pixels in the edge of the unwrapped region of the image.

A small image  $5 \times 5$  pixels in size was used as a simple example to illustrate the operation of the unwrapping algorithm. The pixels are numbered consecutively for convenience. A representation of the quality map is shown in fig. 4.8(a), where each pixel has been assigned to one of the four quality bins, and colour-coded in the image for clarity.

The first six steps of the algorithm in this example are diagrammatically represented in fig. 4.8(b). Each frame in the figure represents the situation in the image and the bins just at the end of each iteration. Let us assume that the first iteration starts at pixel 12, which is declared *active* and *unwrapped*. The four neighbours of pixel 12, (*i.e.* pixels 13, 7, 11, and 17) are unwrapped by adding the appropriate multiple of  $\pi$  to make the phase continuous with respect to pixel 12. The pixels are marked *unwrapped* and queued in the corresponding quality bin as shown in the figure. Pixel 12 is deactivated and marked *explored*, and the algorithm searches the bins to prepare for the second iteration. In this case, pixel 7 is found in the first bin and it becomes the *active* pixel for iteration 2.

In the second iteration, those neighbours of pixel 7 which had not been previously processed (*i.e.* 8, 2, and 6) are *unwrapped* and queued in the appropriate bin according to their quality level. This time, the first bin is found empty, so the algorithm moves on to a lower priority bin, where it finds three pixels. The pixels are always retrieved from the bins in the same order they were stored, which avoids the need to re-sort the list each time a new pixel enters the bin and hence improves the computational efficiency of the procedure. In this case, pixel 13 is declared *active* because it was the first to enter bin 2, even though pixels 17 or 8 may have a higher quality level. The rest of the iterations follow the same principles. The sequence of iterations in fig. 4.8(b) show the unwrapped region as it spreads through the image avoiding pockets of lower quality pixels.

Figure 4.9 shows a similar diagrammatic representation of the unwrapping procedure, applied this time to a real example. The quality bins in fig. 4.9(a) were generated by thresholding the histogram of the quality map in fig. 4.4(d) to obtain four bins with sizes  $B_k$  as defined by eq. 4.8. Figure 4.9(b) presents twelve snapshots taken during the unwrapping of the phase map in 4.4(c). Comparison of the evolution of the unwrapped area; shaded in green in the sequence of images; with the quality bins in (a) reveals that the unwrapping algorithm processes the high quality pixels first, then progressively moves on to pixels in lower quality regions. The resulting unwrapped phase map is shown in fig. 4.10(a). Figure 4.10(b) shows the depth map of the surface, obtained by applying a telecentric calibration as discussed in section IV.6.1.1.

The unwrapping algorithm is very fast and robust. The total processing time for the unwrapping of the image in this example, which was  $768 \times 574$  pixels in size, was 1.04(s) in a PC (500MHz Celeron processor, 128Mb RAM, running Windows ME OS), which is several orders of magnitude lower than the values the reported for other algorithms in the literature, *e.g.* Ghiglia and Pritt (1998). Note that processing times are strongly affected by the specifications of the computer and the operating system, and Ghiglia and Pritt tested the algorithms in mainframe computers running a UNIX type OS, therefore direct comparison of results is difficult.

### IV.5.3 Pre-Processing Normalisation Algorithm

It has been discussed in section IV.5.1 that the phase extraction algorithm requires the background illumination and fringe modulation terms, respectively  $A$  and  $B$  in eq. (4.1), to be uniform or at least to vary slowly when compared with the frequency of the projected fringes. There are however many practical situations in which one or both of these terms may change abruptly. This may occur due to inadequate illumination, *e.g.* uneven distribution of light, shadows, bright ambient light conditions or multiple light sources, etc. They may also be due to features of the surface finish of the object, such as the presence of markings, stains, a glossy finish that produces glare, or colour changes in the surface. Illumination can be easily controlled in the laboratory, and problems with the surface finish can sometimes be solved with adequate preparation of the sample (*e.g.* painting). However, these factors need to be dealt with in industrial situations where the above options are not feasible.

In addition to that, digital images are susceptible to random electronic noise, which affect the accuracy of the measurement. Again, in the laboratory, and if the object is stationary, the effect of random noise can be reduced by averaging several snapshots. This is however not practical if there are time restrictions, it is difficult in the presence of vibrations, and definitely not possible in transient applications.

A normalization technique based on image processing techniques was used in this research to reduce the effect of noise and modulation of the background and amplitude terms in fringe images collected in unfavourable conditions.

1. Divide the intensity map  $I$  in  $M_k \times N_k$  blocks. The block size should be larger than the pitch so as not to distort the signal, but sufficiently small to follow the variation of the amplitude and background terms. An empirical expression that provided good results in practice was  $\{M_k, N_k\} = \min(1.5p, \{M, N\}/60)$ , where  $p$  is the pitch of the fringes and  $M, N$  the image size.
2. Estimate the background term  $A^*$ : (i) calculate the average of each block, to estimate the background term at its centre, and (ii) fit a smooth polynomial function through the calculated values to extrapolate them and generate a smooth map of the background the same size of the original image, *i.e.*  $A^* = \text{extrapolate}(\text{mean}(\text{blocks}(I)))$ .
3. Estimate the modulation term  $B^*$ : (i) subtract the calculated background map  $A^*$  from the original intensity map  $I$ , (ii) calculate the difference between the minimum and maximum value of each block, and (iii) extrapolate as above to yield a smooth map of modulation, *i.e.*  $B^* = \text{extrapolate}(\text{max}(\text{blocks}(I-A^*)) - \text{min}(\text{blocks}(I-A^*)))$ .
4. Compute the normalized image by removing the two terms previously calculated from the original intensity map, *i.e.*  $NI = (I - A^*) / B^*$

5. Re-scale the normalised image to the desired range of intensity (typically 0-255).
6. Apply a smoothing filter to remove noise from the image, usually either the median or the mean filter.

The map of background illumination in the fringe image can be obtained experimentally in static applications, by removing the grating from the projector and collecting an extra image of the object illuminated by the projector. This background image can be subtracted from the fringe image prior to the normalisation. The advantage is that it is possible to follow sudden variations in modulation without distorting the signal. The technique is useful to remove shadows and deal with objects whose surface presents sudden changes in reflectivity, colour etc., in situations where it is not desirable or possible to prepare the surface. Figure 4.11 shows an example of the effect of normalization in the fringe pattern.

The normalisation algorithm described here has been successfully used throughout this research for a number of purposes, including the work on surface defect measurement reported in Chapter III and also in the analysis of dot patterns reported in Chapter VII.

An evaluation of the effect of this normalization algorithm on errors in the measured phase due to noise and modulation of the fringe pattern is presented in section IV.7.1.3.

## **IV.6 System Calibration**

### ***IV.6.1 Phase To Height Conversion***

The fringe processing technique described above yields a map of modulated phase difference  $\Delta\Phi$ , which encodes the information pertaining to the shape of the object. Several expressions have been proposed in the literature to calculate the surface depth from this phase map, some of which were discussed in section II.3.2.4. Four cases of increasing accuracy were considered in this research and are described in this section.

#### **IV.6.1.1 Telecentric Expression**

A common hypothesis is to assume that the grating is projected onto the object using a device that keeps the pitch constant in space and that observation is parallel to the optical axis everywhere. Such a device would require the use of collimating lenses, which is impractical for most real applications. However, this is a simple method that provides good results in many cases of practical interest, when the camera and projector are located at a distance from the object at least one order of magnitude larger than the size of the object, so that they can be considered to be at infinity.

This is usually known as the telecentric case, or the zero order approximation to the conversion from phase to height, and implies that the measured phase difference is proportional to the surface depth (Pirodda, 1982), *i.e.*

$$z = K\Delta\Phi \quad (4.11)$$

The calibration constant  $K$  depends of the pitch of the projected fringes  $p$ , and the distances from the camera to the projector and to the object, respectively  $h$  and  $d$

$$K = \frac{hp}{2\pi d} \quad (4.12)$$

Distances in the image are scaled by the magnification factor  $m$  of the camera, which can be defined as

$$m = \frac{L}{n \cdot L_{pix}} \quad (4.13)$$

where  $L$  is a distance measured in the plane of the object,  $n$  is the corresponding length measured in pixels on the image, and  $L_{pix}$  is the size of one element of the camera sensor.

Figure 4.12(a) shows a simplified model of the observation system, where it can be seen that the camera magnification is also equivalent to the ratio between the distance camera-object  $h$  and the effective focal length of the camera lens  $f_c$ . This, combined with the basic lens formula allows the derivation of an alternative expression for the magnification in terms of the nominal focal length of the camera lens  $f_{c0}$

$$\begin{aligned} \frac{1}{h} + \frac{1}{f_c} &= \frac{1}{f_{c0}} \\ m = \frac{h}{f_c} &= \frac{h - f_{c0}}{f_{c0}} \end{aligned} \quad (4.14)$$

Frequently it is more useful to express the magnification factor in millimetres per pixel, in order to convert distances in pixels in the image into distances in millimetres in the object. For this purpose we define  $m_p$  (*mm/pixel*) as

$$m_p = \frac{L}{n} = mL_{pix} \quad (4.15)$$

As a consequence of the telecentric hypothesis the magnification factor is constant everywhere in the field of view of the camera. Therefore the conversion between pixel number  $(i, j)$  and Cartesian coordinates in the object  $(x', y')$  is

$$\begin{aligned}x' &= m_p(j - N/2) \\ y' &= -m_p(i - M/2)\end{aligned}\tag{4.16}$$

which assumes the origin of the Cartesian coordinates in the camera axis, and the usual convention for pixel coordinates previously described (*i.e.* origin in top-left corner, row number  $i$  increasing towards the bottom and column number  $j$  increasing towards the right).

#### IV.6.1.2 Perspective Correction

When the viewer is at infinity, the observation can be modelled as an orthogonal projection of the real world onto the camera plane. However, when the viewing distance is finite, the observation corresponds to a central projection of the real world onto the image plane, as shown in fig. 4.12(b).

As a result of the observation not being orthogonal, the magnification factor, which is constant in telecentric observation, becomes a function of the distance to the camera, so that points closer to the camera appear shifted towards the edges of the image. Perspective correction can be accomplished using expressions to correct the coordinates  $(x', y')$  calculated from eq. (4.16) and obtain the true  $(x, y)$  coordinates of a point given the distance  $z$  from the reference plane and the distance  $h$  from the camera to the object along the optical axis. (*e.g.* Takasaki, 1973).

$$\begin{aligned}x &= x' \left(1 - \frac{z}{h}\right) \\ y &= y' \left(1 - \frac{z}{h}\right)\end{aligned}\tag{4.17}$$

#### IV.6.1.3 Simplified Non-Telecentric Expression

There are situations in which the telecentric hypothesis no longer holds because both the camera and projector need to be placed close to the object due to space restrictions. The following expression was derived in section II.3.2.4, and can be used to compute surface depth from the phase difference for the non-telecentric case, assuming that camera and projector centres lie on a parallel to the reference plane

$$z = \frac{\left(\frac{\Delta\Phi}{2\pi}\right)ph}{d^* - \left(\frac{\Delta\Phi}{2\pi}\right)p}\tag{4.18}$$

where  $h$  is the distance from the object to the camera,  $d^*$  is the distance between the camera and the projector assuming that they lie in a plane parallel to the reference plane, and  $p$  is the pitch of the projected fringes.

This expression assumes ideal models of the optics (*i.e.* thin lenses with no aberrations) and the camera (*e.g.* pinhole camera model, neglect misalignments of the image CCD), which are acceptable approximations for most real applications. Also the derivation assumed a grating with a sinusoidal transmission function, but can be generalised for any shape that can be expanded in a Fourier series (*e.g.* Meadows *et al.*, 1970).

As discussed in section II.3.2.4, it should be noted that the non-telecentric expression is not linear in  $\Phi$  and therefore the reference surface should always be a flat plane parallel to the camera sensor. In other words, differential measurements of displacement in initially non-flat objects should be obtained by (i) combining in turn each object image of the specimen in the initial and final state with a flat reference to obtain two phase difference maps, (ii) separately obtaining the depth map of the initial and final states by applying eq. (4.18) twice, and (iii) subtracting the depth maps to obtain the map of differential displacement. This procedure is designed to cancel out the effect of non-planar contours inherent to the technique when a non-telecentric configuration of the elements is used.

#### IV.6.1.4 First Order Approximation

In addition to the above considerations, if no assumptions are made about the position of the camera and projector with respect to the object, the expressions become increasingly complex. Kethan (1975) proposed the following expression, which takes into account only first order terms.

$$z = \frac{\Phi p}{2\pi \sin \theta} \left\{ \left( 1 - \frac{\Phi p}{2\pi s \tan \theta} \right) - \frac{x}{s \sin \theta} \left( \frac{s}{h} \cos \theta - \cos 2\theta \right) \right\} \quad (4.19)$$

where  $s$  is the distance from the object to the projector,  $\theta$  is the angle between the projector and camera axes and  $h$  is the camera distance.

This approach consists of the successive application of (i) eq. (4.19) with the uncorrected  $x'$  to obtain an estimation of height  $z'$ , followed by (ii) the perspective correction given by eq. (4.17) with  $z'$  to obtain  $(x, y)$ , which finally can be used to (iii) recalculate  $z$  in eq. (4.19).

It should be noted that once again this expression is not linear in  $\Phi$  and therefore the discussion made for the simplified non-telecentric case is also pertinent here. A flat reference is always required for this expression and the same sequential procedure can be applied for the measurement of displacements in initially non-flat surfaces.

### **IV.6.2 Reference Alignment Procedure**

This section describes a procedure to align the reference plate perpendicular to the viewing axis of the camera, by making use of a laser source mounted on the camera. The alignment laser produces a beam of light parallel to the optical axis of the camera. A small flat target with glossy finish was temporarily attached to the reference plate in order to reflect the light spot produced by the laser. The orientation of the card was adjusted so that the reflected beam was aimed back at the laser source to ensure the correct alignment, as shown in figures 4.13 (a) and (b). The reference plate was clamped in position, and the target removed.

The reference alignment procedure assumes that the laser beam is parallel to the camera axis. However, a significant misalignment was found between the laser beam and the casing of the diode, and therefore the laser beam required alignment before it could be used to align the reference plate. Note that the alignment of the laser described below only needs to be performed once, unless the laser direction is accidentally disturbed.

The laser mount was provided with adjustment screws to control the beam direction. The alignment target shown in fig. 4.13(c) was positioned far away from the camera. The camera was zoomed in and aimed so that the larger concentric circles in the target are centred in the image and the vertical and horizontal lines are aligned to the image edges. The laser light spot was aimed at the small target using the adjustment screws in the mount. After the laser beam has been aligned, the module can be locked in position and used subsequently, without further adjustment.

### **IV.6.3 Manual Calibration Procedure**

The expressions introduced in section IV.6.1 for the calculation of the height  $z$  of the object surface in terms of the measured phase difference  $\Delta\Phi$  involve a number of parameters of the optical configuration of the fringe projection system. This section describes a procedure to perform a manual calibration of the instrument from direct measurements of magnitudes such as distances and angles. A detailed diagram of the fringe projection system is shown in fig. 4.14(a).

The telecentric and non-telecentric expressions, respectively equations (4.12) and (4.18), involve three parameters: (i) the distance  $h$  between the camera centre  $C$  and the origin  $O$ ; (ii) the distance  $d^*$  between the camera and projection centres  $C$  and  $P$ , assuming both lie on a plane parallel to the reference plane; and (iii) the pitch  $p$  of the fringes projected on the reference plane  $R$ .

In addition, the first order approximation in eq. (4.19) requires two more parameters: (iv) the angle  $\theta$  between the camera and projection axes, and (v) the distance  $s$  from the object to the centre of projection (distance  $OP$ ).

Equation (4.16) is also necessary to transform pixel coordinates in the image into real distances, and involves another parameter: (vi) the camera magnification  $m_p$ .

The main difficulty is that the distances  $h$ ,  $s$  and  $d^*$  have been defined in terms of points **C** and **P**, used so far to describe the location of the camera and projector. However, points **C** and **P** are only elements of a simplified model of the optics, (camera and projector typically use complex multipart zoom lenses). These points in the model do not correspond to a physical reference that could be used to perform direct measurements of the magnitudes  $h$ ,  $s$  and  $d^*$ , which therefore must be obtained indirectly.

The master grating, located at the image plane of the projector, is easy to access and can be used as a physical reference, so that the distance  $s'$  between **O** and **G** can be measured directly. In the camera, point **I'** is defined as the intersection of the camera axis with the plane containing the front face of the lens mount, as shown in fig. 4.14(b). By construction, the image plane of the camera containing the CCD sensor, is situated at a fixed distance  $b$  (12.5mm for cameras with a standard CS-mount, and 17.526mm for C-mounts) measured along the camera axis. It is possible to measure the distance from the origin **O** to point **I'**, and add  $b$  to obtain the distance  $h'$  between **O** and **I**.

The calculation of the calibration parameters  $h$ ,  $s$ , and  $d^*$  assumes that the following magnitudes are known:

- Distances  $s'$  and  $h'$  were measured in this study using steel measuring tape, which provided measurements accurate to a few millimetres, although other means more accurate may be used if required by the application. An alternative method based in laser triangulation for the automatic measurement of  $h'$  is proposed in Chapter VI.
- Similarly, the angle  $\theta$  can be measured with the shadow method proposed by Kethan (1975). An alternative to the direct measurement is to calculate  $\theta$  from  $s'$ ,  $h'$ , and  $d'$  by application of the cosine theorem.

$$\theta = \arccos\left(\frac{s'^2 + h'^2 - d'^2}{2s'h'}\right) \quad (4.20)$$

In the latter case, the distance  $d''$  is easier to measure and a reasonable estimate of  $d'$  for this purpose. However, the value of  $d'$  as a function of  $b$ ,  $s'$ ,  $h'$  and  $d''$  is relatively simple to calculate using basic trigonometry if needed.

- The pitch of the projected lines  $p$  was measured directly on the reference plate. The accuracy can be improved by averaging over a set of 10 or 20 lines.

- The pitch  $g$  of the master grating was calculated as the inverse of the nominal line density (e.g. in a 100 lines/mm grating  $g=0.01\text{mm}$ ).
- $f_{c0}$  is the nominal focal length of a fixed lens or the zoom setting of a zoom lens.
- The camera magnification  $m_p$  can be calculated by obtaining  $m$  in eq. (4.14) and scaling by the sensor size  $L_{pix}$ , see eq. (4.15), which can usually be obtained from the manufacturer of the camera. Alternatively,  $m_p$  can be obtained by direct application of eq. (4.15) as the ratio between a real distance measured on the reference plane and the corresponding measurement on the image in pixels.

First it is necessary to calculate the effective focal distance of the camera  $f_c$ , and the distance  $h$

$$f_c = h'/2 - \sqrt{\left(\frac{h'}{2}\right)^2 - h' f_{c0}}$$

$$h = h' - f_c \quad (4.21)$$

Finally, it is possible to obtain  $d^*$  for the telecentric and non-telecentric expressions. For the first order expression, it is still necessary to calculate first the effective focal distance of the projector  $f_p$  to obtain  $s$  and  $d$ .

*Telecentric or non-telecentric expressions*

$$d^* = h \tan \theta$$

*First order expression*

$$\begin{cases} f_p = \frac{s' g}{p \cos \theta + g} \\ s = s' - f_p \\ d = \sqrt{h^2 + s^2 - 2sh \cos \theta} \end{cases} \quad (4.22)$$

#### IV.6.4 Automatic Calibration Procedure

The manual calibration routine described in the previous section is relatively complex and time-consuming. A simple automatic calibration procedure was developed to increase the flexibility and ease of use of the system. This method allows a direct calculation of the calibration constant  $K$  and camera magnification  $m_p$  required for system calibration in the telecentric case by analysing a surface of known geometry, as it eliminates the need for making direct measurements of the parameters.

The method collects and analyses a reference image of a flat plate perpendicular to the camera axis, and an object image with a calibration cone attached to the reference plate. The cone was chosen as the calibration shape because of its simple geometry, which is easy to manufacture and to describe mathematically with only two parameters (*i.e.* the height and the radius). A

range of calibration cones of different dimensions was used in this research, manufactured in aluminium for the smaller sizes, and in wood for the larger sizes (see Table IV-1). Cones 1-4 are shown in fig. 4.15(a).

<i>Cone</i>	<i>Height</i>	<i>Radius</i>	<i>Material</i>
1	6.3	12.5	Aluminium
2	12.0	25.3	Aluminium
3	16.7	35	Aluminium
4	48.0	76.0	Wood
5	140.0	150.0	Wood

**Table IV-1: Calibration cones.**

The automatic procedure only requires the collection of an extra image in addition to the object and reference images. After the reference plate is aligned and clamped in position, and the reference image is collected, a suitable calibration cone is attached to the reference plate and a calibration image recorded. The size of the cone should approximately match the features of interest in the specimen. The reference image of the example used in this chapter was presented in fig. 4.4(b), and the calibration image can be seen in fig. 4.15(b).

The fringe processing algorithms were applied to the reference and calibration images to extract and unwrap the modulated phase map. The resulting phase map, shown in fig. 4.15(c), was processed using pattern recognition techniques to automatically locate the apex and edges of the cone. User input of the real dimensions of the calibration cone (height and diameter), allows calculation of the calibration constant  $K$  as the ratio between the height of the cone in millimetres and the value of the phase at the apex of the cone in the unwrapped phase map. Similarly, the magnification factor  $m_p$  can be calculated as the ratio between the diameter of the real cone in millimetres and the diameter in pixels of the cone edge detected in the image. These constants are valid for a given optical configuration of the system, and must be re-calculated if any of the parameters are modified (*e.g.* the distance and orientation of the elements, or the focus and zoom setting of the lenses).

A procedure was designed to increase the accuracy of the calculated  $K$  and  $m_p$  and to improve the reliability with noisy data. An artificial height map of the same size of the input images was generated using the real dimensions and the detected position of the cone. A least-squares fit with  $K$  and  $m_p$  as parameters was performed between the calculated phase map and this idealised surface. This procedure uses information from a cloud of data points distributed throughout the field of view, providing a more robust algorithm.

Figure 4.15(d) illustrates the least-squares fit with an example. The data points, represented in the figure by stars (\*), were fitted to the artificially generated cone, represented in the figure by the grid. Figure 4.15(e) shows profiles of the nominal  $z$ , the uncalibrated phase, and the measured  $z$  resulting from the application of the calibration constants  $K$  and  $m_p$  to the phase map.

The nominal height can be plotted versus the measured phase to evaluate the suitability of a phase-to-height conversion expression for a particular set of data. For instance, fig. 4.15(f) shows a strong linear trend, suggesting that the telecentric approximation was adequate in this example.

The values of  $K$  and  $m_p$  calculated with the automatic calibration procedure can also be used to obtain the remaining parameters needed for the non-telecentric expressions. The method assumes that the projector and camera lie in a plane parallel to the reference and requires only one extra measurement of the distance  $h$ . This measurement can be performed as indicated in the previous section, *i.e.* obtaining  $h'$  and  $f_{c0}$  and then applying eq. (4.21). Alternatively, it is possible to use the automatic method developed for component location, which will be described in Chapter VI.

The pitch  $p$  in pixels was measured in the reference image as described in section IV.5.1, and scaled by the magnification factor to obtain the value in millimetres. Finally, eq. (4.12) can be rearranged to obtain  $\theta$  and  $d^*$ .

$$\begin{aligned} \frac{2\pi K}{p} &= \frac{h}{d^*} = \tan \theta \\ \theta &= \arctan\left(\frac{2\pi K}{p}\right) \\ d^* &= \frac{h}{\tan \theta} \end{aligned} \tag{4.23}$$

The results of tests to evaluate and compare the manual and automatic calibration techniques are reported and discussed in section IV.7.2.

## IV.7 Evaluation Of The Method

### IV.7.1 Numerical Evaluation Of The Method

A set of tests was performed using artificially generated data to evaluate the accuracy of the phase measurement procedure described in section IV.5 and to quantify the main sources of error.

In the following analysis, the magnitude of the error that can be attributed to a particular source will be estimated in terms of error in the measured phase, therefore expressed in *radians*. Note that the accuracy of the shape measurements made with the system can be quickly estimated multiplying these values by the calibration constant  $K(mm/rad)$  for each particular optical configuration of the system.

A simple numerical example is considered first to isolate the error inherent to the phase measurement algorithms from any other sources present in real experiments and to illustrate the procedure followed during the tests.

An ideal reference image was generated artificially by application of eq. (4.1) and is shown in fig. 4.16(a). The image represents a set of fringes projected onto a flat reference plane, and assumes projection and viewing at infinity. Hence, the modulated phase term of the reference  $\Phi_R=0$  (see details in section II.3.2.4). The pitch  $p$  of the fringes was set to 16 pixels. The image size was  $256 \times 256$  (pixels), and the intensity range  $[0,255]$  with uniform background and amplitude terms. Mathematically,

$$I_R(i, j) = 128 + 128 \cos\left(\frac{2\pi}{16} j\right) \quad i, j = 1, \dots, 256 \quad (4.24)$$

An ideal object image was also generated similarly by introducing a ramp of modulated phase with a slope of  $0.1(rad/pixels)$ , *i.e.* making the modulated phase term of the object  $\Phi_O=0.1j$ . The resulting image, shown in fig. 4.16(b), can be written as

$$I_O(i, j) = 128 + 128 \cos\left(\frac{2\pi}{16} j + mj\right) \quad i, j = 1, \dots, 256 \quad (4.25)$$

with  $m=0.1(rad/pixel)$ .

Note all the rows of these ideal images are exactly identical, and therefore it is sufficient to study a one-dimensional profile along a horizontal line in the images. The intensity profiles of the object and reference images are shown in fig.4.16(c). Figure 4.16(d) shows a profile of the wrapped phase map, obtained after processing the two input images with the phase-extraction algorithm described in section IV.5.1, *i.e.* expressions (4.2) to (4.4). The unwrapped phase shown in fig. 4.16(e) was calculated with the algorithm described in section IV.5.2.

The phase map thus calculated can be compared with the ramp originally introduced to generate the object image, and the discrepancy can be used to evaluate errors inherent to the algorithms, because other sources of error have been eliminated from the test. A profile of the error, calculated subtracting the original phase ramp from the measured profile is shown in fig. 4.16(f).

Inspection of the error profile allows the distinction between two separate effects: (i) a periodic error with twice the spatial frequency of the fringe pattern in the object image and uniform amplitude, and (ii) two bands near the edges of the image affected by a relatively large amount of error. The width of these bands is one half the pitch of the reference.

These two effects can be explained if we observe that the phase at a point  $(i, j)$  in the image is calculated using the intensities of five pixels in the vicinity  $(i, j-p/2), \dots, (i, j+p/2)$ .

- The periodic error is due to the fact that  $\Phi$  is not constant along the set of five pixels sampled by the algorithm. Analytical expressions of this error in first order approximation have been derived in Appendix AI. A numerical evaluation of this effect is discussed in the next section.
- The second effect can be explained if we observe that in the above-mentioned bands, some of the pixels needed to calculate the phase would fall outside the image. The algorithm arbitrarily assigns a zero intensity value to these pixels outside the image in order to generate a phase map of the same size as the input images. However, the calculated phase values in these bands are meaningless.

#### IV.7.1.1 Effect Of Slope

An extensive set of numerical tests was performed to evaluate the error as a function of the slope of the phase ramp. Figure 4.17(a) shows a set of six phase ramps generated artificially with slopes  $m = \pm 0.1, \pm 0.2, \pm 0.3$  (*rad/pixel*). Substituting these values of  $m$  into eq. (4.25) generated the set of object images shown in fig. 4.17 (b). These object images were combined with the reference in fig. 4.16(a). The analysis in Appendix AI predicted a limit of  $2\pi/p$  (*rad/pixel*) to the maximum value of the slope that the algorithm can deal with. The pitch  $p$  of the reference was 16 pixels in this case, and therefore the above values of  $m$  correspond respectively to  $\pm 25\%$ ,  $\pm 51\%$  and  $\pm 76\%$  of the limit.

The procedure explained in the previous section yielded the maps of measured phase shown in fig. 4.17(c). Figure 4.17(d) shows error maps calculated subtracting the nominal phase maps in fig. 4.17(a) from the measured phase maps in 4.17(c). Observation of the error maps in comparison with the corresponding object images confirmed the predictions obtained analytically in Appendix AI, *i.e.* (i) that the pitch of the error function is half that of the object images, and (ii) that the amplitude of the error increases with the slope of the phase ramp.

Figure 4.18(a) shows profiles along the horizontal middle line of the measured phase, superimposed on the nominal value for the six images in fig. 4.17. Each profile is labelled with the value of the slope normalized with the maximum value of  $2\pi/p$ . Figures 4.18 (b) and (c) show profiles of the error, respectively for the negative and positive slopes.

A summary of the results of this set of numerical tests is shown in fig 4.19, where the mean and standard deviation of the error maps have been plotted against the normalized slope. The mean error is very close to zero and shows no significant trend. In contrast, the standard deviation is approximately proportional to the square of the slope. However, for values of the slope within 80% of the limits, the standard deviation remains below 0.3(rad).

#### IV.7.1.2 Effect Of Random Noise

The effect of random noise in the calculated phase was evaluated numerically through a set of tests with simulated data. Modified versions of the object and reference images in fig. 4.16, with added random noise of increasing amplitude, were artificially generated using the following expression:

$$I_{noise}(i, j) = I(i, j) + P \text{rand}[-128, 128] \quad i, j = 1, \dots, 256 \quad (4.26)$$

where  $P$  is the percentage level of noise, *i.e.* the ratio between the amplitudes of the signal and the added noise in the image.

Figure 4.20(a) shows object images with 5%, 10%, 30% and 60% added noise, and corresponding profiles along the horizontal middle line. Figure 4.20(b) shows the error maps in the calculated phase resulting from processing pairs of reference and object images with the same level of added noise. Observation of the images and profiles across the horizontal middle line show that the effect in the phase is randomly distributed noise of increasing amplitude. Note that for 60% noise, the presence of noise began to corrupt the phase information and produced unwrapping errors in some areas of the measured phase map. Figure 4.21 shows histogram plots of the error maps, which illustrate the increase in the dispersion of the calculated values as the noise level increase as well as the onset of unwrapping errors for the case of 60% noise.

Figure 4.21 summarizes the results of the tests in a graph of mean error, standard deviation and maximum error in the measured phase map versus percentage error in the input images. The mean error was found to be approximately zero as expected. The standard deviation increases with the noise level following a linear trend, as does the maximum error. However, beyond 50% noise the unwrapping started to fail causing a sudden increase in the maximum error.

Noise levels for images collected experimentally generally fall below 40% even in unfavourable conditions. Thus a typical value of random error due to noise can be estimated at 0.2(rad).

#### IV.7.1.3 Effect Of Modulation In Background And Amplitude

The phase measurement algorithm described in section IV.5.1 assumed that the fringe pattern intensity distribution had constant background and amplitude terms (respectively  $A$  and  $B$  in eq.

4.1). A separate set of numerical tests was conducted to evaluate the errors on the measured phase associated with non-uniformities in the background and amplitude of the fringe pattern.

A specially designed modulation map  $\psi(i, j)$  with the same dimensions as the fringe pattern was used in these tests and is shown in fig. 4.22(a). Each row of the modulation map is a sinusoidal function of pitch  $p_m$ , which increases linearly with the row number. Thus, each row of the image is affected by a different modulation frequency, which allows testing the effect of a range of frequencies in a single test.

This modulation map was applied to the object image shown in fig. 4.16(b), in turn to the background term  $A$ , the amplitude term  $B$ , and simultaneously to both of them to generate the object images shown in fig. 4.22(b), (c) and (d). The profiles shown above each of the images in the figure show the intensity profile along a horizontal line. Note that for this row, the modulation frequency is approximately one order of magnitude lower than the frequency of the fringe pattern.

Reference images were generated similarly, based on the reference in fig. 4.16(a), and combined with the object images as in the previous tests to extract the phase. Figures 4.22(e), (f) and (g) show profiles of the error map in the measured phase along a set of different rows in each of the three cases considered ( $A$  only,  $B$  only and both  $A$  and  $B$ ). Each profile corresponds to a different modulation frequency.

The three cases show periodic errors that tend to the behaviour predicted in section IV.7.1.1 for low modulation frequencies (profiles at the top of the graphs), increase slowly for medium frequencies and rise sharply for high modulation frequencies in the same order of magnitude or higher than that of the reference image (bottom of the graphs).

The results are summarised in the graphs of fig. 4.23, showing (a) the maximum error and (b) the standard deviation versus the normalised pitch of the modulation function for the three cases. In order to evaluate the effect of modulation, these graphs should be compared with the error obtained for a 10% phase ramp with uniform background and amplitude, calculated as described in section IV.7.1.1. The values in that case were  $0.08(rad)$  for the maximum error and  $0.034(rad)$  for the standard deviation.

It can be noted that for large values of the pitch of the modulation function ( $p_m > 3p$ ) the error in the three cases remains very small and tends asymptotically to the values calculated for the ideal case. Below that, the error increases rapidly, with peak values of about  $0.6(rad)$  for the maximum error and  $0.3(rad)$  for the standard deviation at  $p_m = p/2$  in the worst case of simultaneous modulation of  $A$  and  $B$ .

The results show that the proposed five-step algorithm presents low sensitivity to non-uniformities in the background intensity and the amplitude of the fringe pattern, yielding small errors provided that the pitch of the modulation is at least three times the pitch of the reference image.

In most practical cases, the error due to modulation can be considered negligible. Localized errors however, which may be as high as  $0.8(rad)$ , can arise in sudden non-uniformities of the colour or reflectivity of the surface, e.g. changes of material, stains, edges of paint, etc.

#### IV.7.1.4 Effect Of Normalization

The effect of the normalization algorithm proposed in section IV.5.3 on the phase error due to (i) random noise and (ii) modulation of background and fringe amplitude was also evaluated numerically.

The normalization algorithm was applied to the artificial images with added noise described in section IV.7.1.2, and the normalized images were processed to calculate the error. An example is shown in fig. 4.24(a). The image on the right is the result of normalising the image with 60% random noise shown on the left. A summary of the results is shown in fig 4.24(b). Comparison of this graph with the equivalent graph for raw images, shown in fig. 4.21(b), reveals a dramatic reduction of the error due to random noise when the normalization algorithm is applied. For a typical image with noise levels below 40%, the error would be reduced from an estimated  $0.2(rad)$  for the raw images, to  $0.08(rad)$  if the images are normalized.

Similarly, the modulated images shown in fig. 4.22(b), (c) and (d) where normalised as illustrated in fig. 4.25(a) and processed again as described in section IV.7.1.3 to yield the results summarised in fig. 4.25(b). Comparison of this graph with the one in fig. 4.23(b) shows that the normalisation only has a small effect. This effect is beneficial for  $p_m < 6p$ . In contrast, for low frequency modulation the normalisation actually increases the error in the measured phase by a small amount.

#### IV.7.2 Experimental Error Analysis

Experimental evaluation of the system was carried out in a series of tests with a flat plate. The plate was fastened to the calibrated rotation table shown in fig. 4.26(a), which allows rotations about the vertical axis with  $1/60$  degrees of accuracy. The plate was aligned to ensure perpendicular viewing using the procedure described in section IV.6.2, and clamped in position, setting the scale of the rotating table to 0 degrees. The fringe projection system was set-up to collect images as described in section IV.4.2. Figure 4.26(b) shows a scaled diagram of the optical configuration. The parameters of the system were calculated as described in section

IV.6.3. The results are summarised in columns (1) and (2) of Table IV-2. The configuration of the optical components remained unchanged during the experiments.

Parameter	Manual Calibration		Automatic Calibration	
	(1) Measuring $\theta$	(2) Measuring $d'$	(3) Calib1.moi	(4) Calib2.moi
$h$ (mm)	877	877	877	877
$d$ (mm)	-248	-235	-	-
$d^*$ (mm)	-227	-216	-219	-222
$s$ (mm)	963	963	904	905
$\theta$ (rad)	-0.2531	-0.2417	-0.2451	-0.248
$p$ (mm)	3.33	3.33	3.275	3.294
$K$ (mm/rad)	-2.0537	-2.1518	-2.0839	-2.0702
$m_p$ (mm/pixel)	0.4175	0.4163	0.40936	0.41176

Table IV-2: Calibration parameters

With this configuration of the system, an image of the flat plate aligned perpendicular to the camera was collected to use as reference. A calibration cone of  $H=16.7(mm)$ ,  $R=35(mm)$  was attached to the plate and a second image was recorded for the automatic calibration procedure described in section IV.6.4. This process was repeated to collect a second calibration set (reference and calibration cone) to evaluate the repeatability of the technique. All images were  $256 \times 256(pixels)$  in size.

The two calibration sets were processed using JOSHUA to obtain the values of the calibration constant  $K$  and magnification factor  $m_p$ . The apex and edge positions were calculated using the automatic routine implemented in the software. The remaining parameters were also calculated as described in section IV.6.4, and are shown in columns (3) and (4) of Table IV-2.

The orientation of the flat plate was subsequently modified with the help of the rotating table, from  $-50$  to  $0$  and from  $0$  to  $50(degrees)$  at  $10(degrees)$  intervals, resulting in a set of twelve object images. The angle  $\alpha$  was measured from the  $x$ -axis with the sign convention illustrated in fig. 4.26(c).

The twelve object images were combined with the reference and processed using JOSHUA, to generate the phase maps. Each phase map was calibrated in turn using the four different sets of calibration parameters shown in Table IV-2, and the four different calibration expressions discussed in section IV.6.1, *i.e.* (i) telecentric without perspective correction, (ii) telecentric with correction, (iii) non-telecentric with correction, and (iv) first order approximation with

correction. This yielded 16 different height maps representing the measured surface profile of the flat plate for each of the twelve different positions of the plate.

A 200×200pixels square region was selected from the centre of the each surface maps to conduct the error analysis. This was done to discard the edges of the plate that were visible in some of the images.

The results of this series of tests are summarised in figures 4.27 – 4.30, which correspond respectively to the four sets of calibration parameters: manual calibration with direct measurement of  $\theta$  (fig. 4.27) and with  $\theta$  calculated from a measurement of  $d'$  (fig. 4.28), and automatic calibration in JOSHUA using the calibration sets *calib1* (fig. 4.29) and *calib2* (fig. 4.30).

In each of the figures, plot (a) shows the measured surface profiles along the horizontal middle line of the images for the plate at  $\pm 10$ ,  $\pm 30$  and  $\pm 50$ (degrees) rotation. The graph compares the nominal position (dotted line) and the results obtained using the four calibration expressions with the set of calibration parameters considered in each case.

The residuals were calculated as the discrepancy between the measured and the nominal profile. It was assumed that errors in the measurement system caused this discrepancy. Plot (b) shows profiles of the residuals along the middle line of the image for each position of the plate and each calibration expression.

In order to isolate the effect of different error sources, the residuals maps were averaged in the  $y$  direction, which allowed the separation of the random errors due to noise from systematic errors of the measurement system (Wykes *et al.*, 1995). Plot (c) in each of the figures shows the averaged residuals, which contain only the systematic error. Observation of the pattern of the residuals allowed the identification of two separate effects, namely (i) a smooth curvature due to the effect of finite optics, and (ii) a ripple due to estimation errors of the phase extraction algorithm.

The first type of systematic error, which can be attributed to the effect of finite optics, tends to increase with the inclination of the surface as expected. In general, this was the largest source of error, although the four calibration expressions yielded different results.

- The telecentric expression provided a simple approximation, with acceptable quality for the optical configuration under study. This expression should be sufficient in most cases unless space restrictions require that the instrument is located too close to the object or high accuracy is required. In addition, this is the only expression that does not require the measurement of the distance  $h$ .

- The application of perspective correction to the height map calculated with the telecentric expression did not produce good results. This correction did improve the accuracy in some cases, but actually magnified the error in others, depending on the orientation of the surface. A possible explanation is that this expression only takes into account the effect of finite optics in the camera and not in the projector.
- The same can be said for the non-telecentric expression with perspective correction, which produced the worst results of the four cases. This expression assumes that the camera and the projector lie in a plane parallel to the reference and proved very sensitive to small variations.
- The best results corresponded to the first order expression with perspective correction. This expression corrects for finite optics in the camera and the projector, and does not make assumptions about the configuration. This expression reduced significantly the curvature in the measured profile due to finite optics and produced very accurate measurements.

The second type of systematic error identified in these tests is periodic and varies cyclically with the period of the projected grating as predicted analytically in Appendix A1 and in the numerical tests of section IV.7.1.1. This error can be attributed to the phase extraction algorithm, and was not affected by the calibration expression used. The experimental observations were in good agreement with the predictions.

The results obtained with the four sets of calibration constants were qualitatively very similar. However, it should be noted that the first order expression produced marginally better results with the manual calibration sets compared with the automatic calibrations. This can be explained because the automatic method uses  $d^*$  as an estimate of  $d$  to reduce the number of measurements, introducing some inaccuracies.

In order to characterize the accuracy of the technique at measuring surface orientation, the best plane in the least-squares sense was fitted to each height map and the angle extracted from its horizontal slope. The discrepancy between this value and the reading in the scale of the rotation table was attributed to errors in the technique.

Figures 4.31 – 4.34 (a) show plots of the error in the measured angle versus the angle of rotation of the plate. The telecentric and non-telecentric expressions provided very similar results because the perspective correction is approximately symmetric. These expressions tend to overestimate the value of the surface orientation. The first order expression yielded in general better results.

The set of calibration parameters considered in each case did have a stronger influence. The method is very sensitive to errors in the calibration, which can lead to overestimation or

underestimation of the surface orientation. The manual calibrations (columns (1) and (2) of Table IV-2, see figures 4.31 and 4.32) provided results respectively above and below the expected values, which suggest that the calibration constants were inaccurately estimated. The automatic calibration (columns (3) and (4), figures 4.33 and 4.34) yielded better results, with higher repeatability and accuracies better than  $\pm 1$  degree. In addition, the automatic calibration is simpler and requires fewer measurements.

The maximum and standard deviation was calculated for the residual maps to quantify the error. Figures 4.31 – 4.34 (b) show plots of standard deviation (solid line) and maximum error (dotted line) versus the inclination angle of the plate, for the four calibration expressions and each of the calibration sets considered. In the telecentric and non-telecentric expressions, the error increases very rapidly with the inclination of the surface (standard deviation up to 3(mm), max. error  $>6$ (mm) in some cases). In contrast, the error remains at low levels in the first order expression because it corrects finite optics effects (standard deviation  $< 0.5$ (mm), max. error  $< 1.5$ (mm) in manual or  $< 2$ (mm) in automatic calibration). These values compare well with the results of numerical tests, which predicted accuracies of the phase measurement in the region of 0.4(rad) for a typical case (surface inclination  $< 80\%$  max., noise level  $< 40\%$ , modulation  $p_m > 4p$ ). This corresponds to  $\pm 0.8$ (mm) error in the shape measurement with the optical configuration of this example ( $K \cong 2$ mm/rad), which shows very good agreement between experimental tests and numerical simulations.

The four calibration sets produced similar results in the telecentric expression without correction. The automatic calibrations performed better in the telecentric and non-telecentric expressions with correction, probably due to a more accurate estimation of the calibration constants. The first order expression though produced slightly better results with the manual calibrations due to the approximations made in the automatic method.

## IV.8 Discussion And Conclusions

A technique based on fringe projection has been introduced that allows full-field automatic measurement of the surface shape of arbitrary 3-D objects. The experimental apparatus and processing algorithms have been described in detail. The methodology of use of the system including set-up, data collection and system calibration has also been described and illustrated with a real example.

A novel phase-extraction method for the analysis of the fringe pattern has been introduced. This method can be applied to a single image and is therefore suitable for the study of transient effects, and at the same time, it is computationally very simple. An expression to estimate the

quality of the phase maps, and a fast quality-guided unwrapping algorithm have also been described for use in conjunction with the fringe analysis algorithm.

A number of expressions for phase to height conversion have been presented which consider both infinite and finite optics. Numerical and experimental evaluations of these expressions were conducted to investigate the conditions of applicability of the technique, identify the main sources of random and systematic error and estimate the accuracy of the measurements.

Three main sources of errors have been identified and evaluated:

- (i) Random errors, either (a) constant with time, due for instance to dust in the grating, or non-uniformities in the illumination or the reflectivity of the surface, or (b) variable with time due mainly to electronic noise. The effect of random errors has been evaluated in numerical tests. In most cases it is possible to achieve noise levels below 40% and long wavelength ( $>4\mu$ ) modulation of the background and amplitude, so the random error remains typically below  $0.2(\text{rad})$ . Pre-processing of the images with the proposed normalization algorithms could reduce random errors down to  $0.08(\text{rad})$  in a typical case.
- (ii) Systematic errors that vary cyclically with the fringe spacing. These errors are inherent to the phase extraction algorithm, and can be modelled as errors in the phase step (e.g. non-uniform phase, or rounding of the pitch  $p$ ). An expression to quantify these errors has been derived analytically and the results confirmed in numerical and experimental tests. The error increases with the inclination of the measured surface. A typical value of the error for a phase ramp with 80% of maximum slope is  $0.3(\text{rad})$ .
- (iii) Systematic errors that do not vary cyclically, such as curvature of the surface contours due to finite optics. This effect depends strongly on the calibration expression and was studied in experimental tests. The telecentric approximation is simple to use and produced acceptable results in most cases. The first order approximation with perspective correction corrects the effect of finite optics and is recommended to achieve higher accuracy, or if the instrument must be placed close to the object. Other expressions were tested, which only improved results in some cases depending on the orientation of the surface, and are not recommended.

The minimum pitch required in the input images in order to determine the phase correctly was  $4(\text{pixels/fringe})$ . Also, there is a limit to the maximum phase ramp that can be measured accurately due to systematic errors. This limits the maximum inclination of the surfaces that can be measured, depending on the configuration of the optical apparatus. In particular, the accuracy of the method is reduced near sharp edges and surface discontinuities.

The tests also demonstrated a good performance of the automatic calibration procedure compared with the manual. The automatic method has comparable accuracy, higher repeatability, and is much faster and simpler to implement. The procedure uses an additional image, does not require performing any measurements in the zero order expression, and only requires one distance for the other cases.

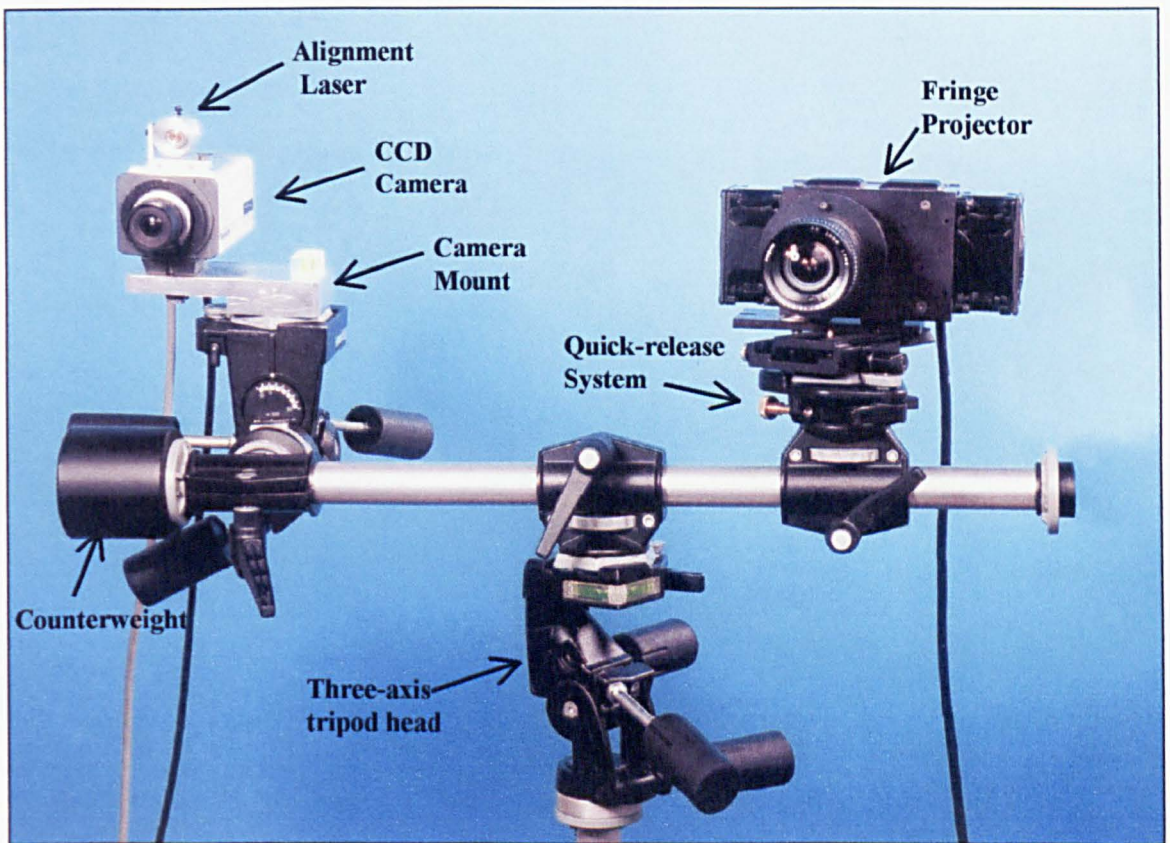


Figure 4.1: Experimental Apparatus. Ronchi gratings, projected using a specially designed light source, are used to generate a fringe pattern on the object. Images of the projected fringes are collected by means of a CCD camera. A laser was used for the alignment of the instrument.

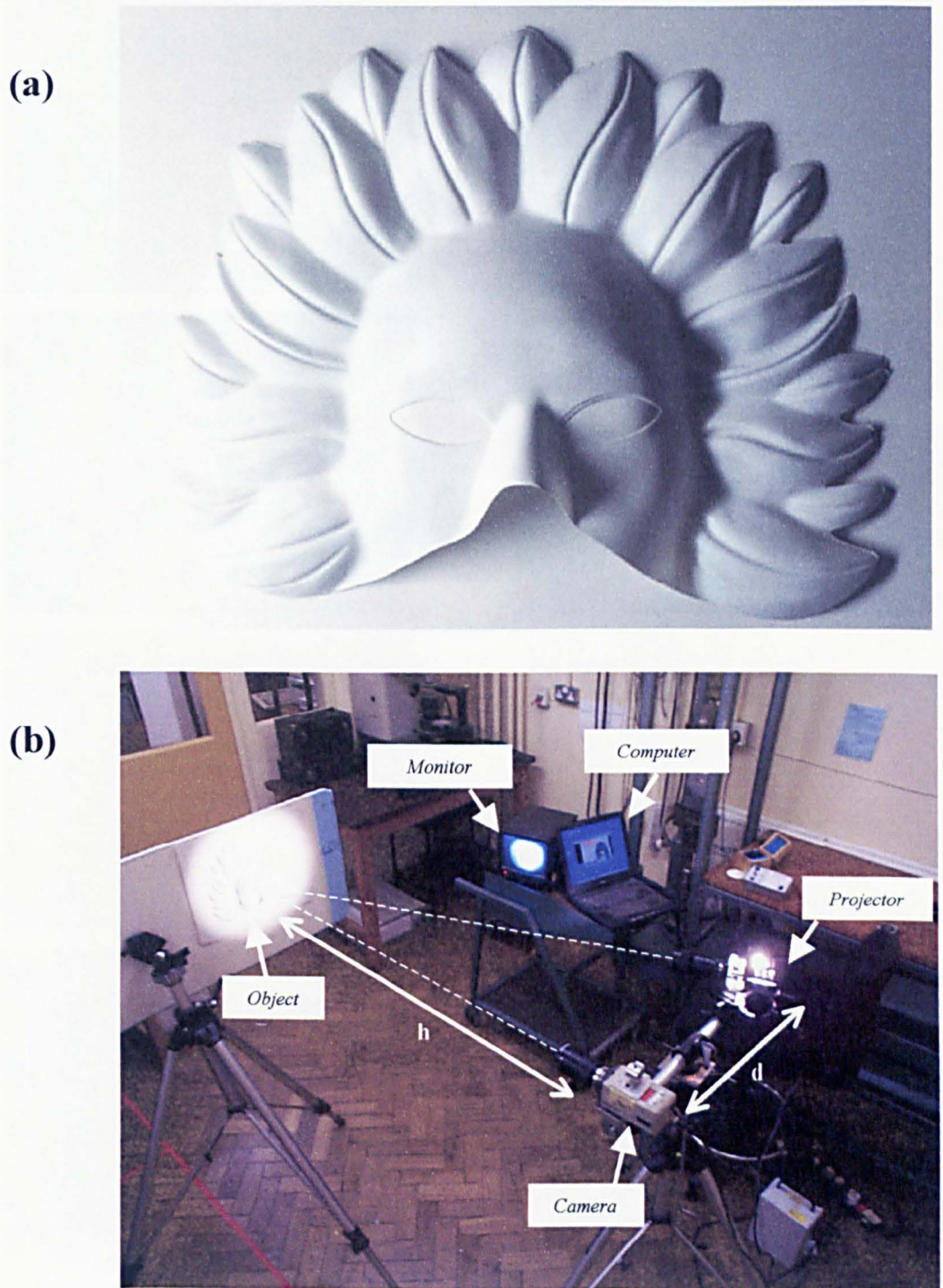


Figure 4.2: A simple example to illustrate the methodology of use of the system. (a) The figure shows a mask made of thin moulded plastic sheet, used as the object in this example. The mask fits approximately in a volume 280mm wide, 230mm high, and 55mm deep. (b) Experimental set-up showing the different elements of the system. The distance  $h$  from the object to the camera was 1630mm and the projector was located 490mm to the right of the camera, as shown in the figure.

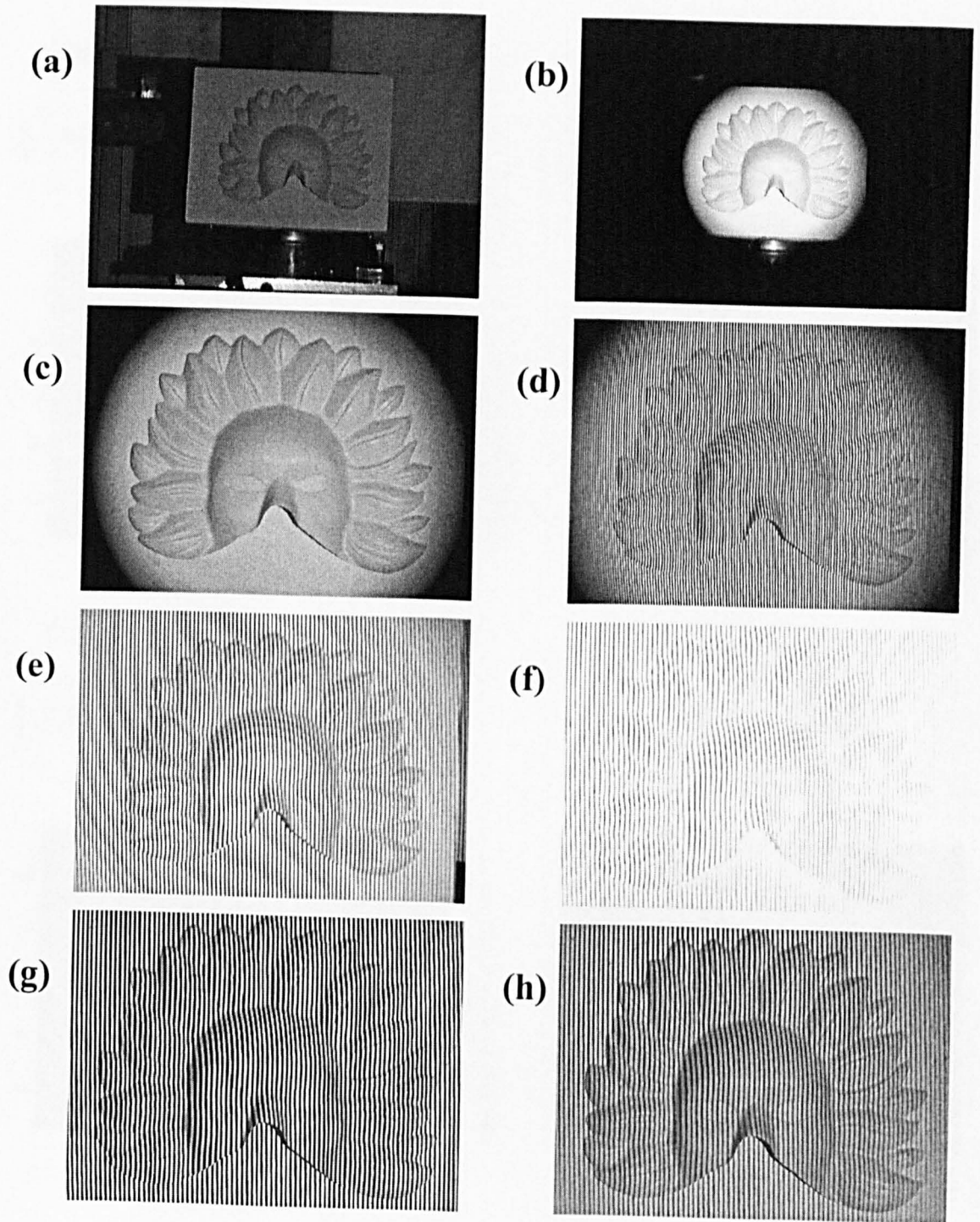


Figure 4.3: Sequence of images collected during the set-up of the elements to illustrate the steps of the procedure. (a) Alignment of camera and object (b) Alignment of the projector (c) Zoom adjustment of the camera lens (d) Selection of the grating (e) Fine adjustments of the grating pitch using the projector lens zoom to yield approximately 8 pixels/mm (f) Fine adjustments of the camera zoom and focus with the aperture open (g) Reducing the aperture of the camera lens to eliminate glare (h) Slight de-focusing of the projector lens to obtain a quasi-sinusoidal intensity profile in the projected fringes.

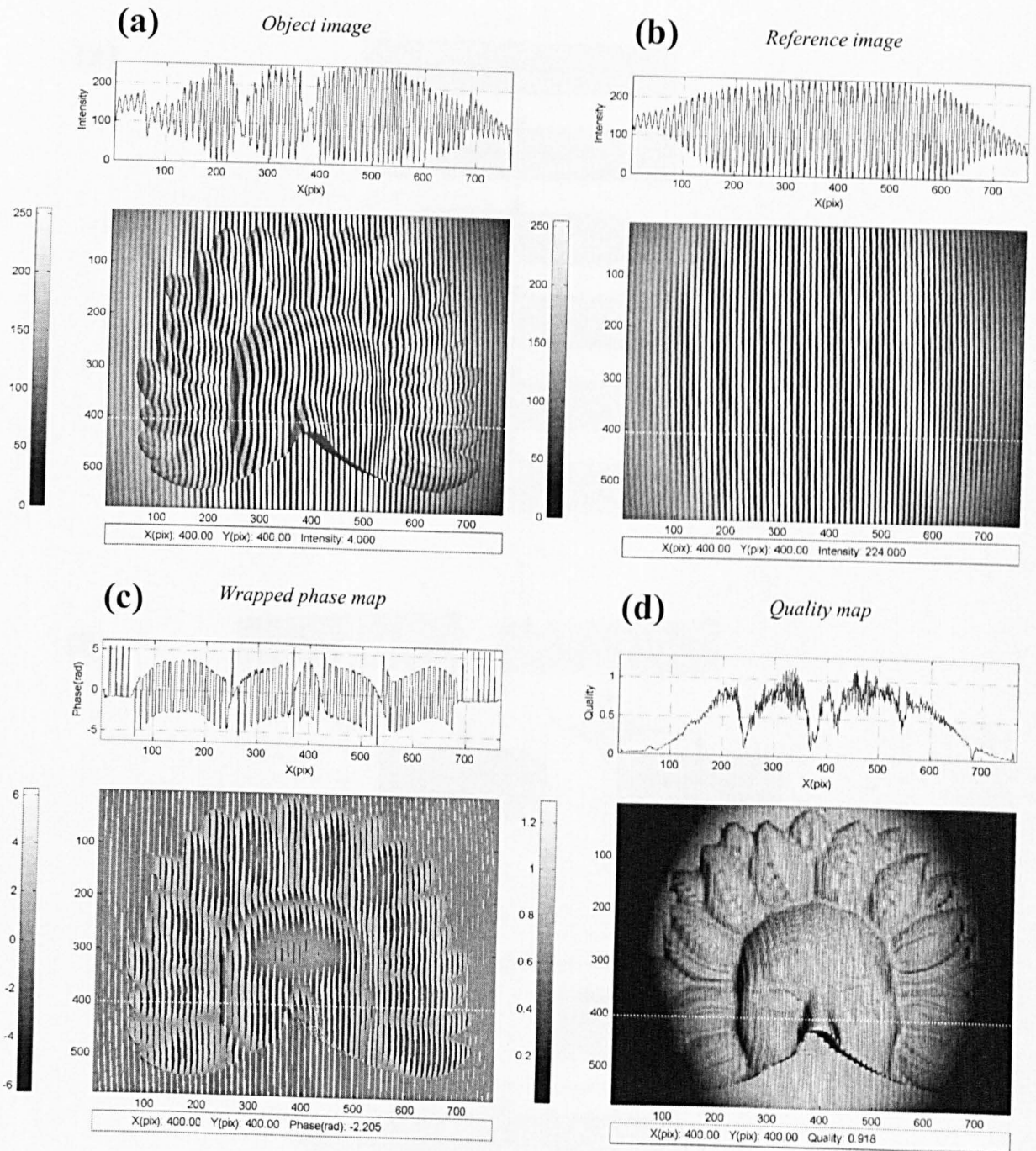


Figure 4.4: Typical set of data including (a) the object image, and (b) the reference image of a flat plate, collected using the same configuration of the optical elements. (c) Wrapped phase map resulting from the application of the five-step spatial algorithm to the reference and object images shown in (b) and (a). (d) Quality map used to guide the unwrapping of (c).

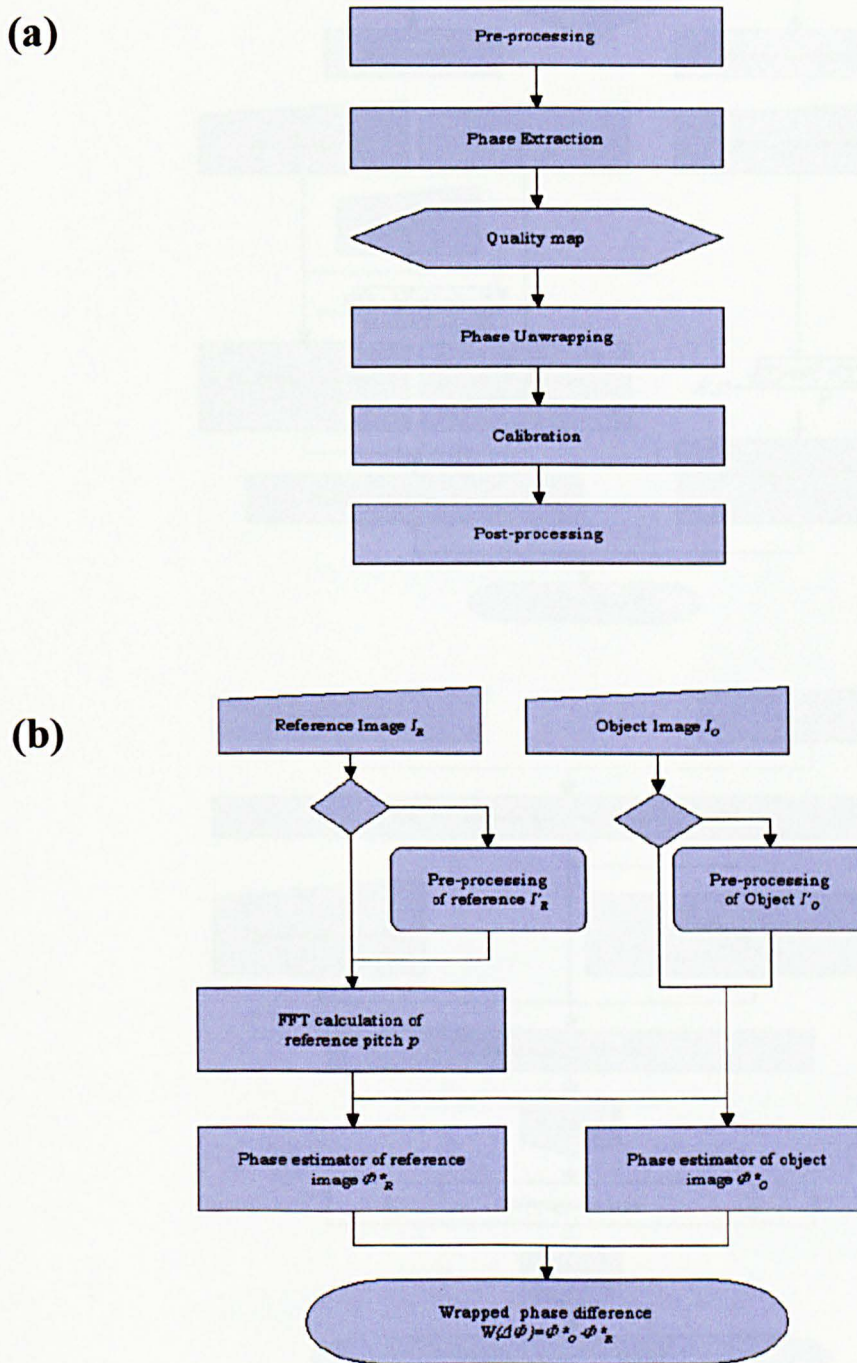


Figure 4.5: (a) Flowchart of the main steps of the processing algorithm. (b) Flowchart of the phase extraction algorithm.

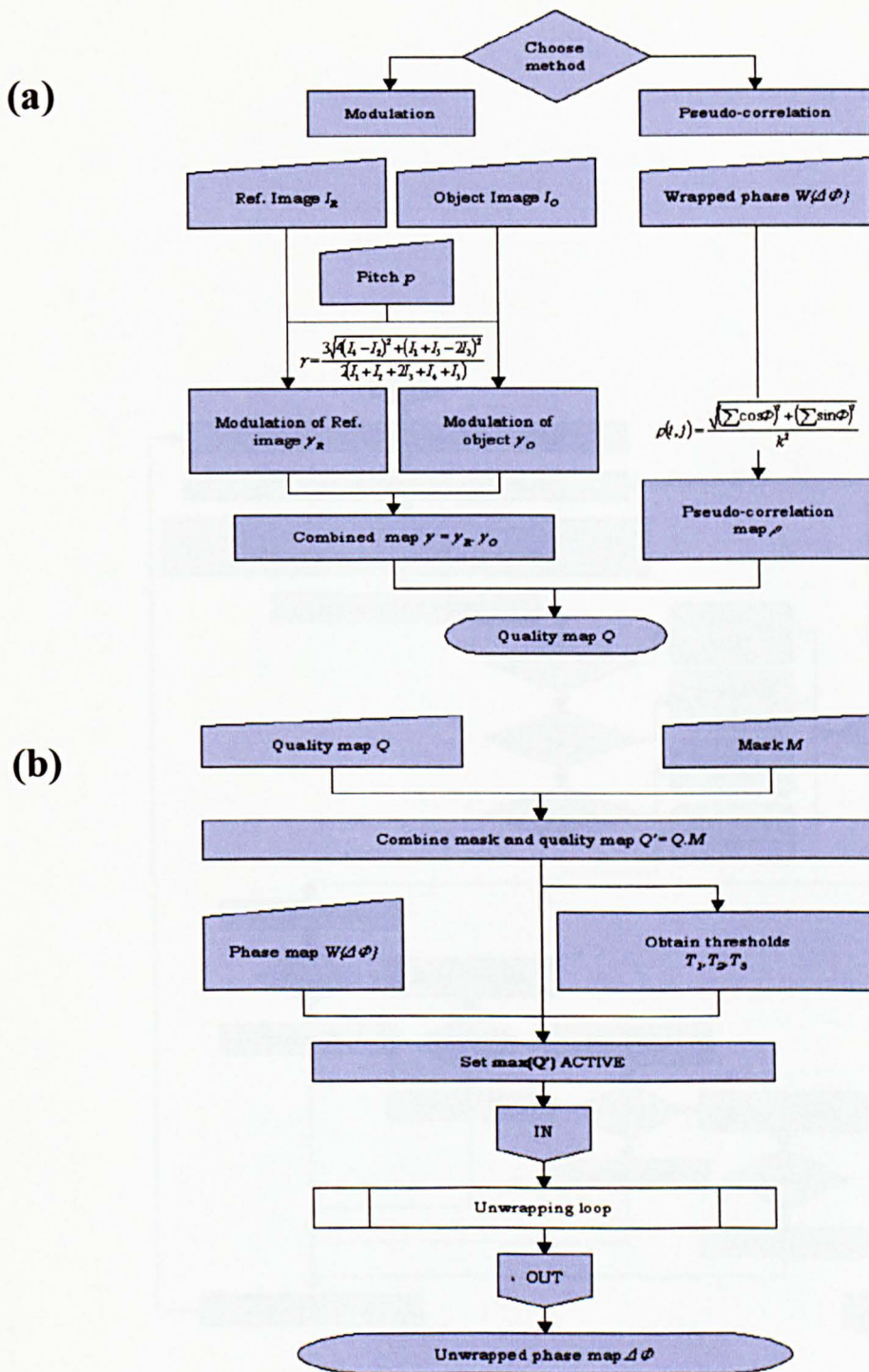


Figure 4.6: (a) Flowchart of the quality algorithms. (b) Flowchart of the unwrapping algorithm.



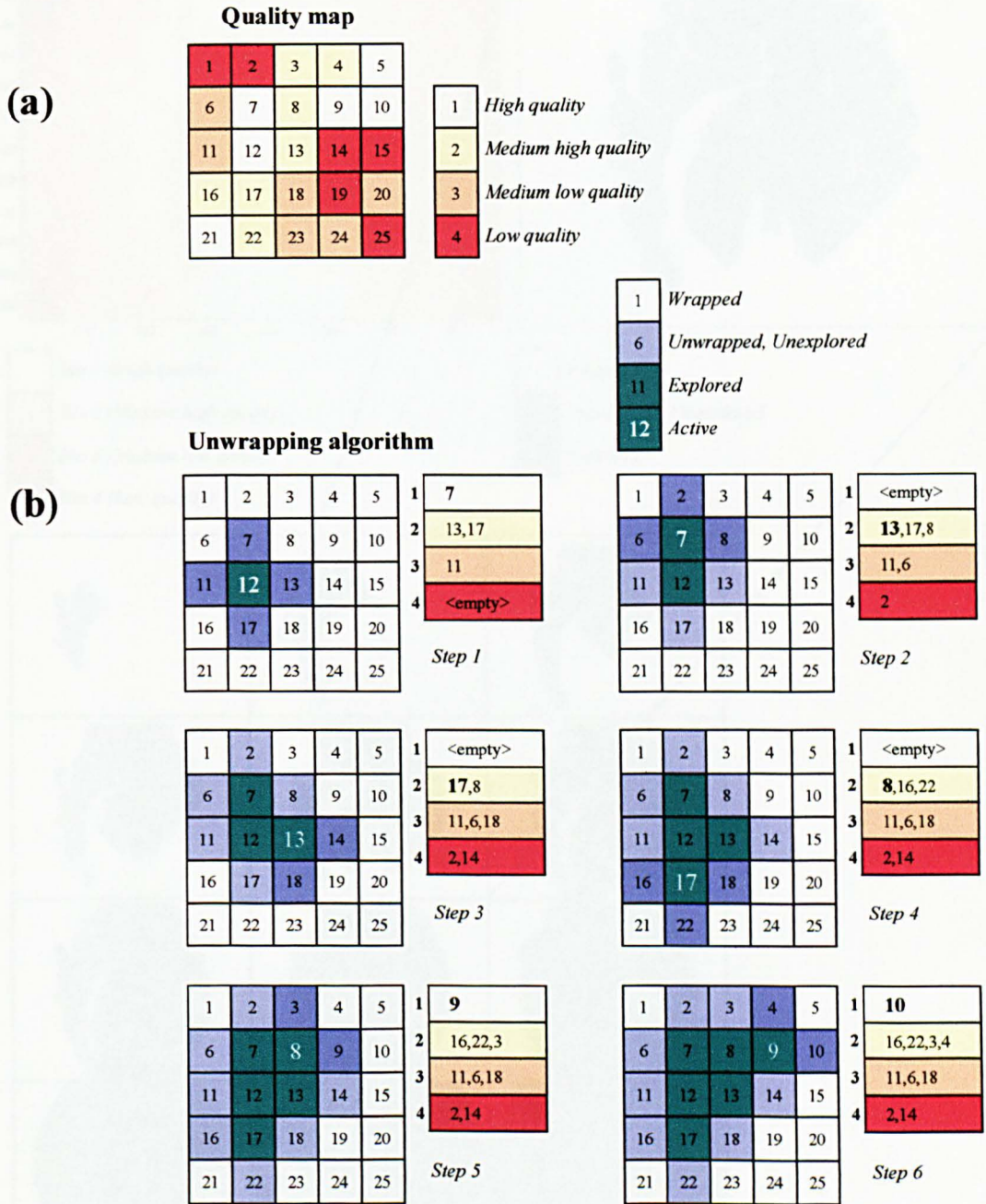


Figure 4.8: The operation of the quality bins unwrapping algorithm is illustrated using a simple 5x5 image. (a) Quality map of the image, where each pixel has been assigned to a quality bin (b) The first six iterations of the algorithm

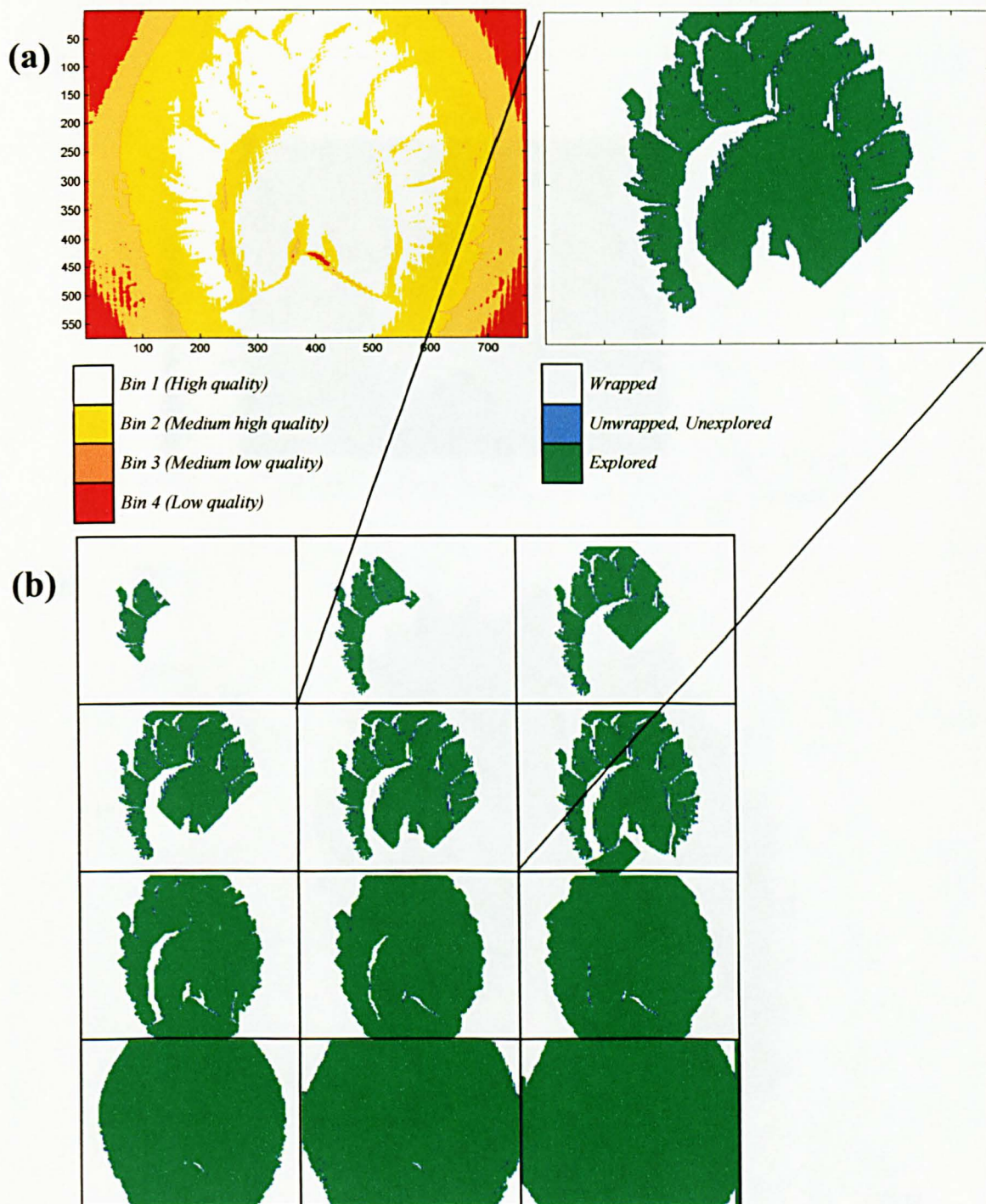


Figure 4.9: Unwrapping of a real example. (a) A histogram of the quality map in fig. 4.4(d) was analysed to select thresholds that separate the pixels into four groups according to their quality level, to define the four quality bins shown in the colour-coded figure. (b) Unwrapping of the phase map shown in fig. 4.4(c) using the quality bins in (a). The sequence of twelve snapshots reveal that the unwrapped region, shaded green, fills first the regions of the image containing high quality pixels, i.e. the white areas in the quality map in (a), then progressively spreads towards the lower quality regions, i.e. the yellow, the orange and finally the red areas in the quality map. A detail of step 5 in the sequence is also shown in the image.

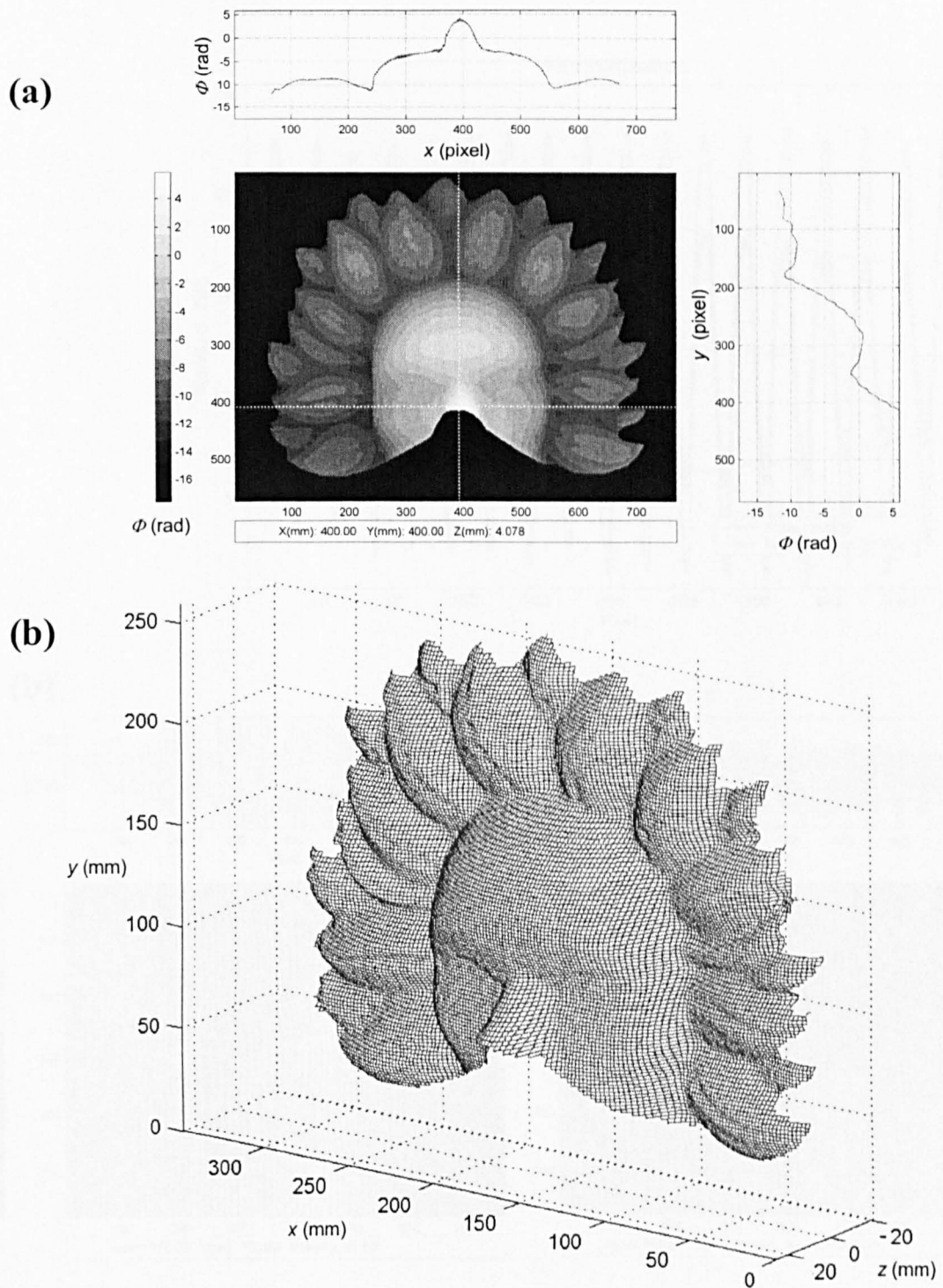
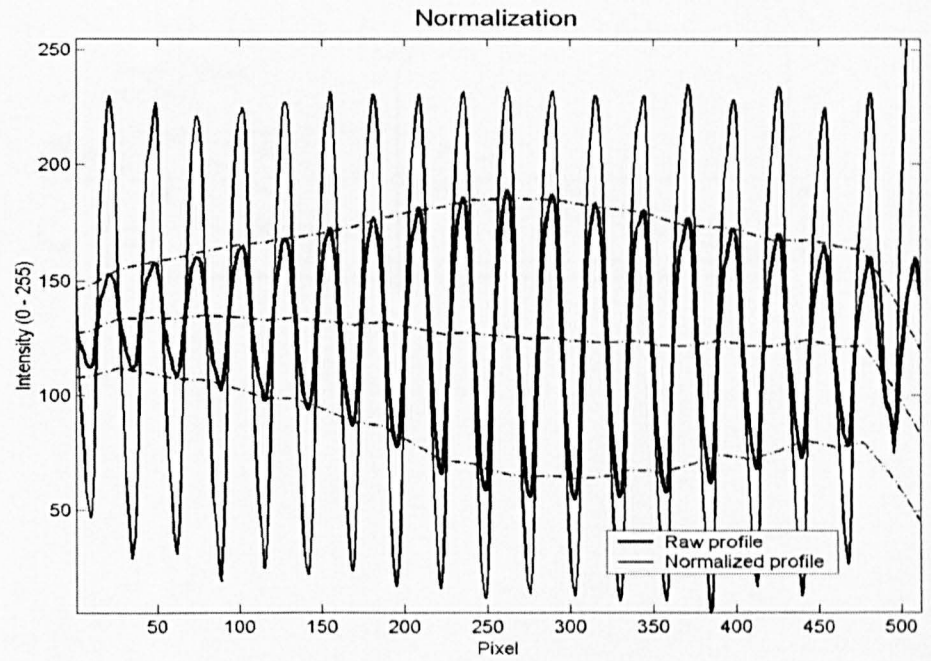


Figure 4.10: (a) Map of unwrapped phase resulting from the application of the quality-guided algorithm as described in fig. 4.9. (b) Three-dimensional plot of the surface, obtained from the phase map shown in (a). In this case, the height information was calculated using the zero-order approximation.

(a)



(b)

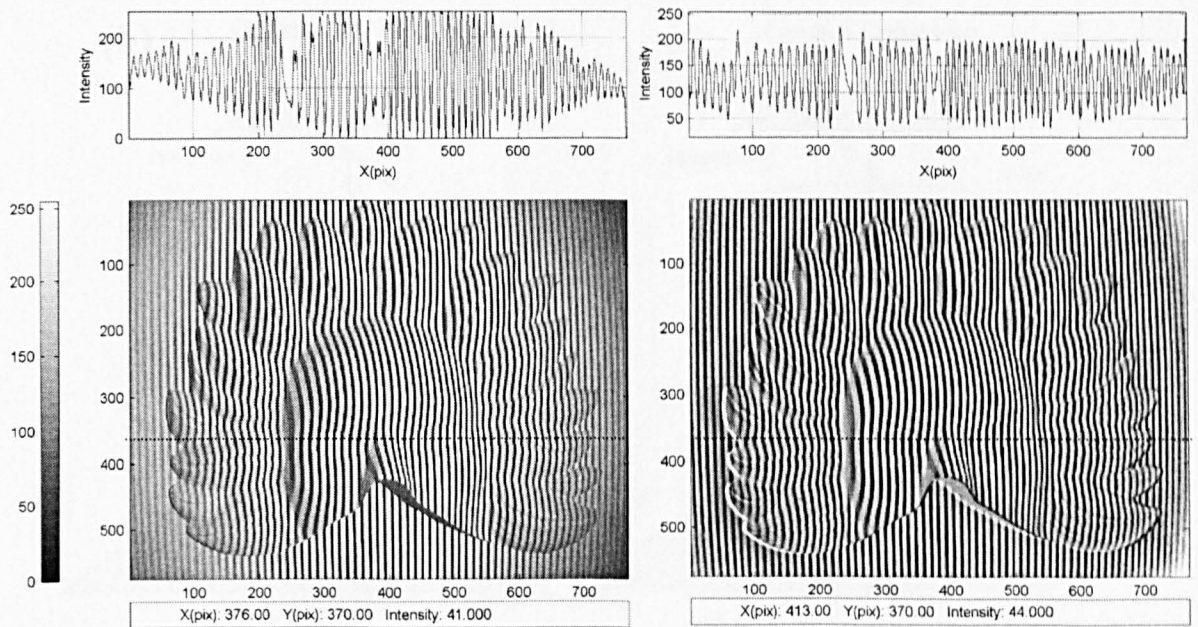


Figure 4.11: Normalisation algorithm. (a) Intensity profile along a horizontal line of the reference image. The thick continuous line represents the raw intensity profile. The dotted lines represent the background and amplitude terms calculated by the normalization algorithm. The thin line represents the normalized image, after removing these terms. (b) Normalization of the object image in the mask example. The plots are intensity profiles along the highlighted row in the images.

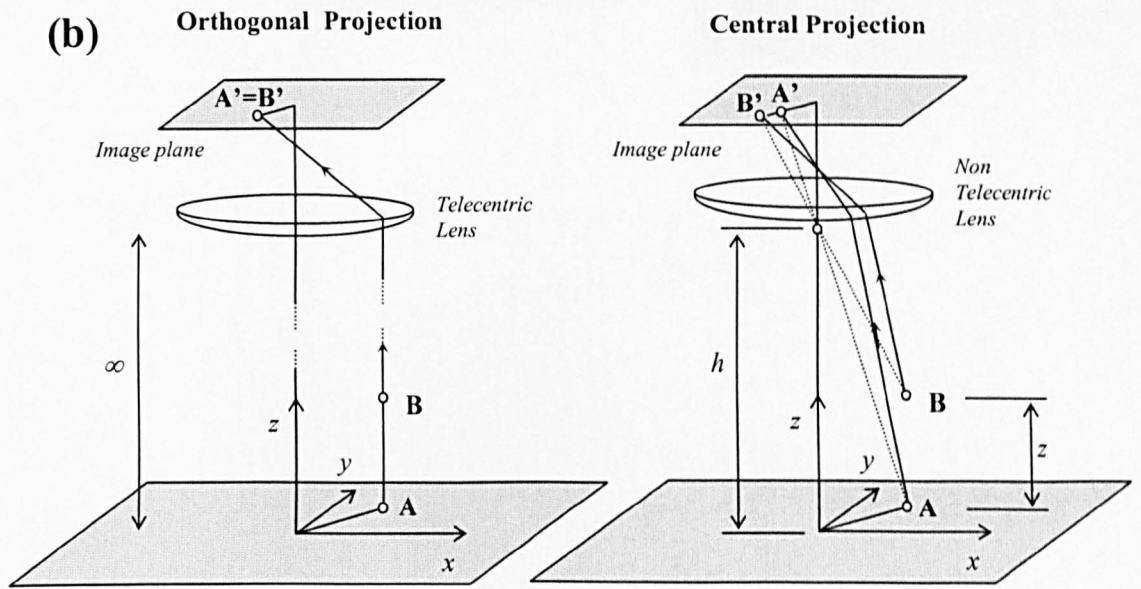
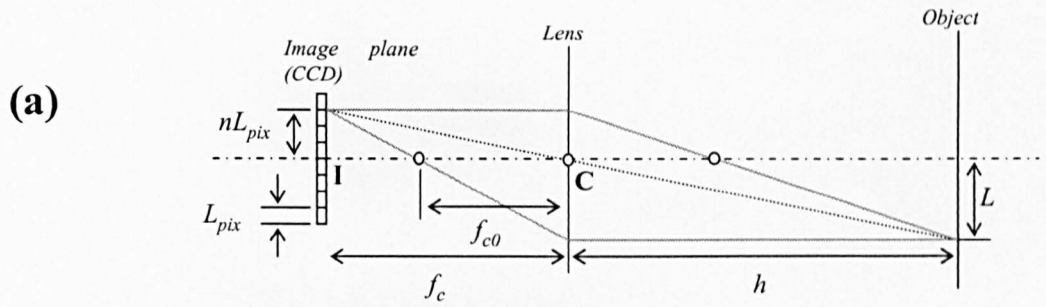


Figure 4.12: (a) Magnification (b) Correction of perspective error in non-telecentric optics.

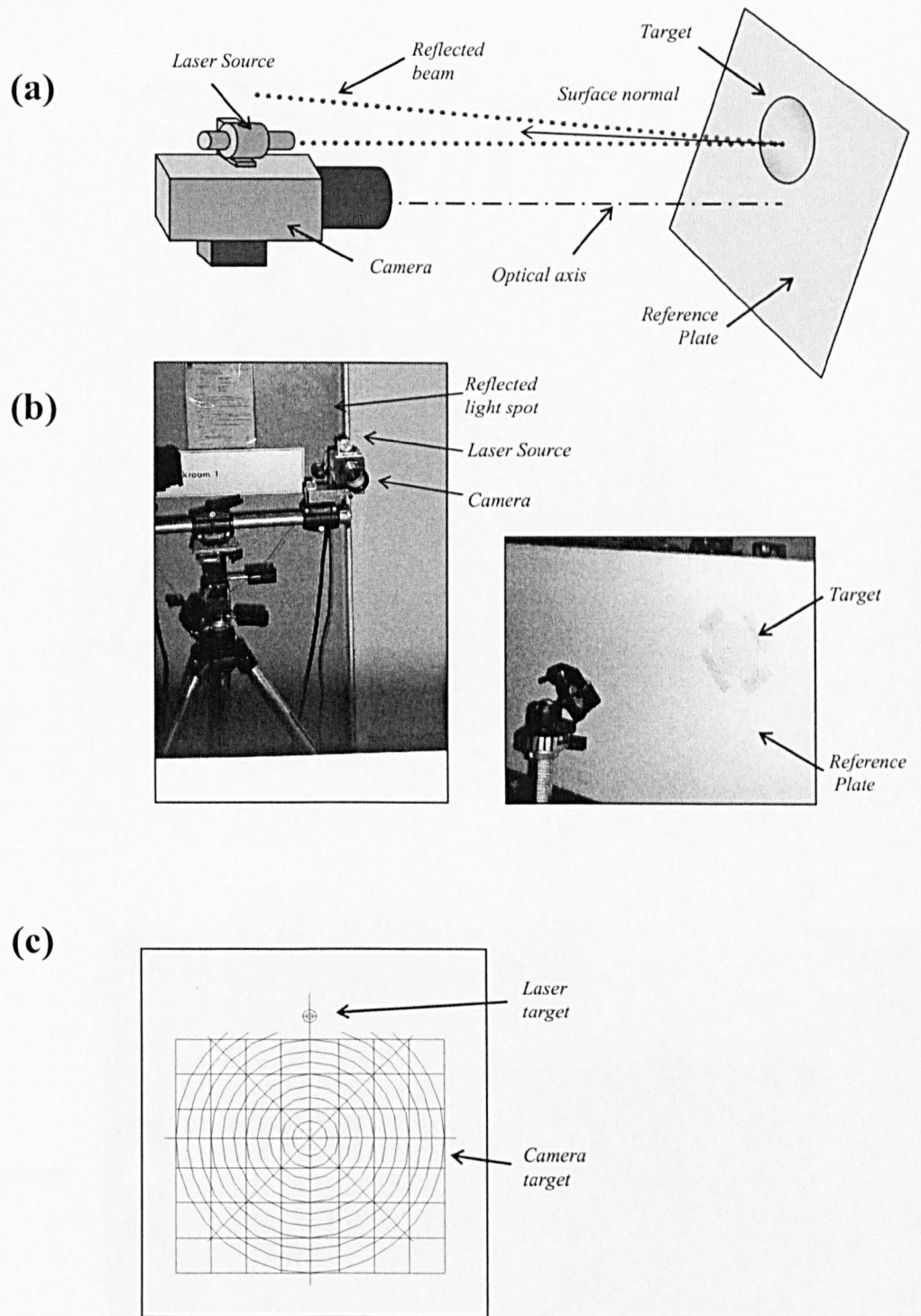


Figure 4.13: (a) Schematic diagram of the alignment procedure (b) View of alignment laser and the target attached to the reference plate during alignment. (c) Target used for the alignment of the laser beam with the camera axis.

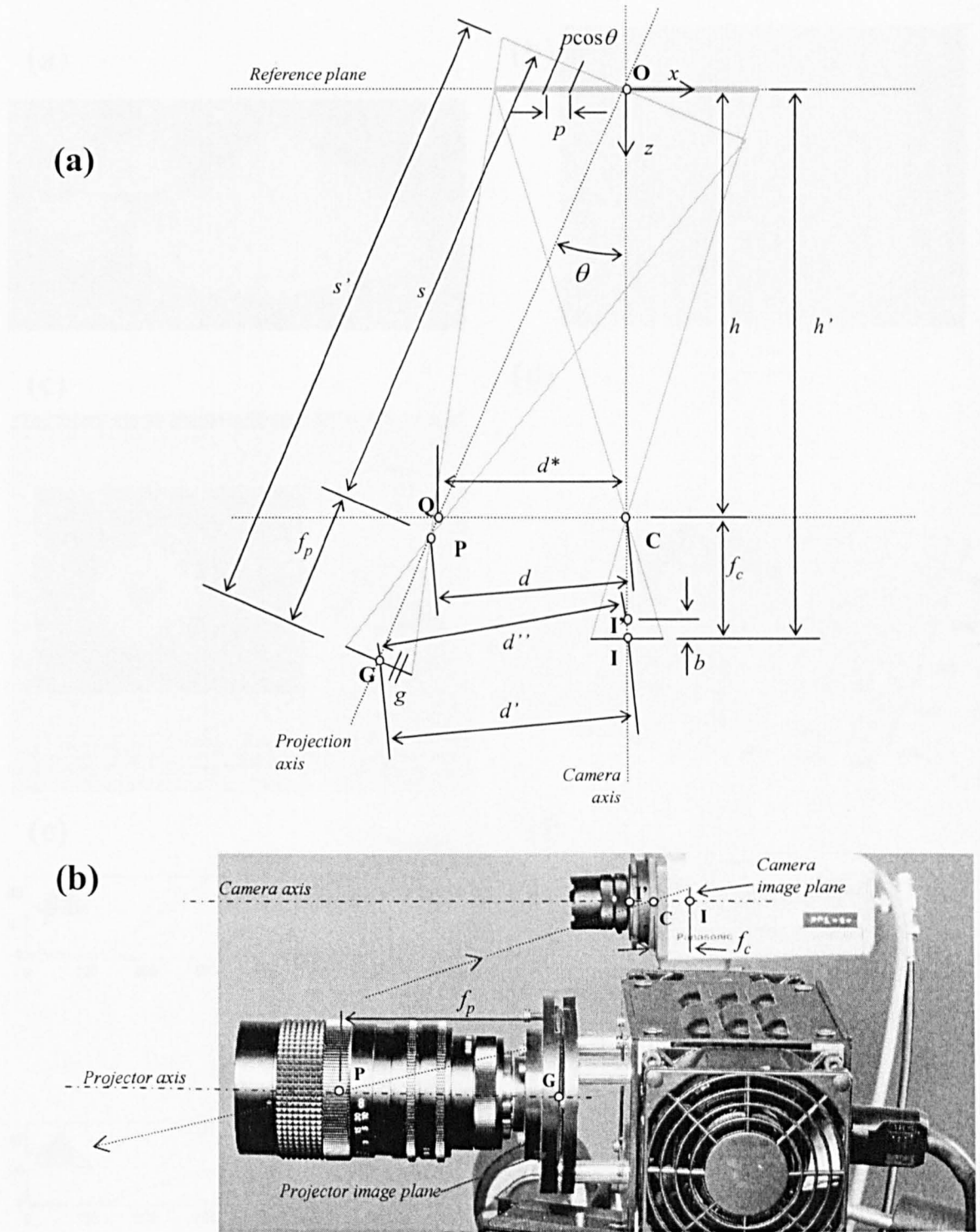


Figure 4.14: Manual calibration of the system. (a) Detailed diagram of the configuration of the fringe projection system. (b) Detail of the location of points  $C$ ,  $I'$  and  $I$  in the camera and points  $P$  and  $C$  in the projector.

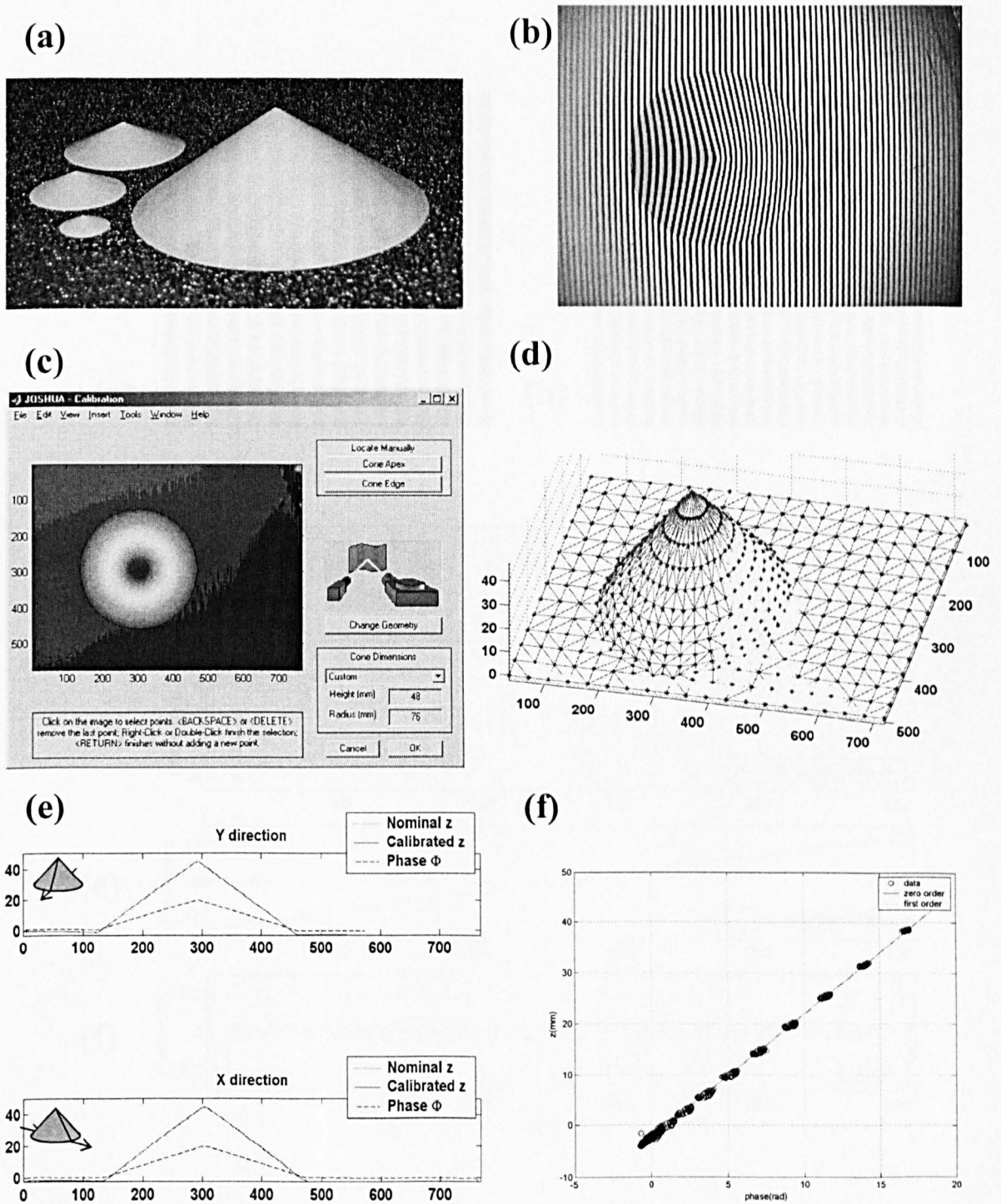


Figure 4.15: Automatic calibration of the method (a) Set of calibration cones. (b) Calibration image (c) JOSHUA calibration screen showing the automatic detection of apex and edges of the cone in the phase map. (d) Least squares fit of a reduced set of data points \* to an artificially generated cone, represented in the figure by the grid. (e) Profiles across vertical and horizontal lines containing the cone apex in the original phase map, the nominal  $z$  and the  $z$  map resulting from the calibration (f) This graph of height vs. phase revealed a strong linear trend, suggesting that the telecentric approximation was adequate in this example.

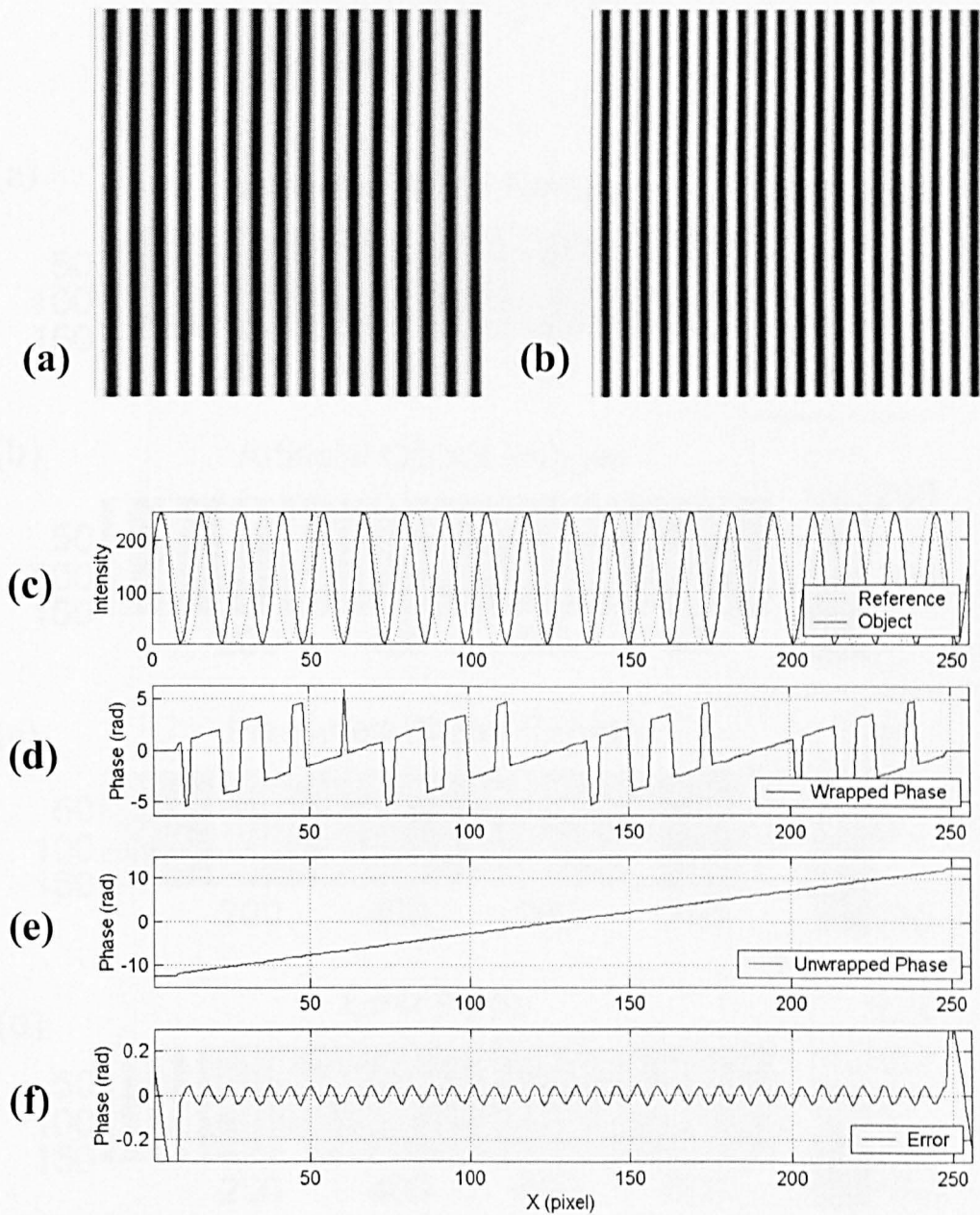


Figure 4.16: The phase measurement process is demonstrated in this numerical example (a) Reference image generated artificially with a phase carrier of pitch 16 pixels (b) Artificial object image corresponding to a 10% phase ramp (c) Intensity profiles of the object and reference images (d) Profile of wrapped phase map measured with the five step spatial phase carrier algorithm (e) Unwrapped phase map (f) Profile of the error inherent in the algorithm, calculated by subtracting the original phase ramp from the measured profile shown in (e). The large errors near the edges affect a band 8 pixels wide (i.e. the one half the pitch of the reference). The rest of the image presents sinusoidal error of frequency double that of the object.

$$\begin{cases} I = 128 + 128 \cos\left(\frac{2\pi}{p} x + \Phi\right) \\ \Phi = mx \end{cases}$$

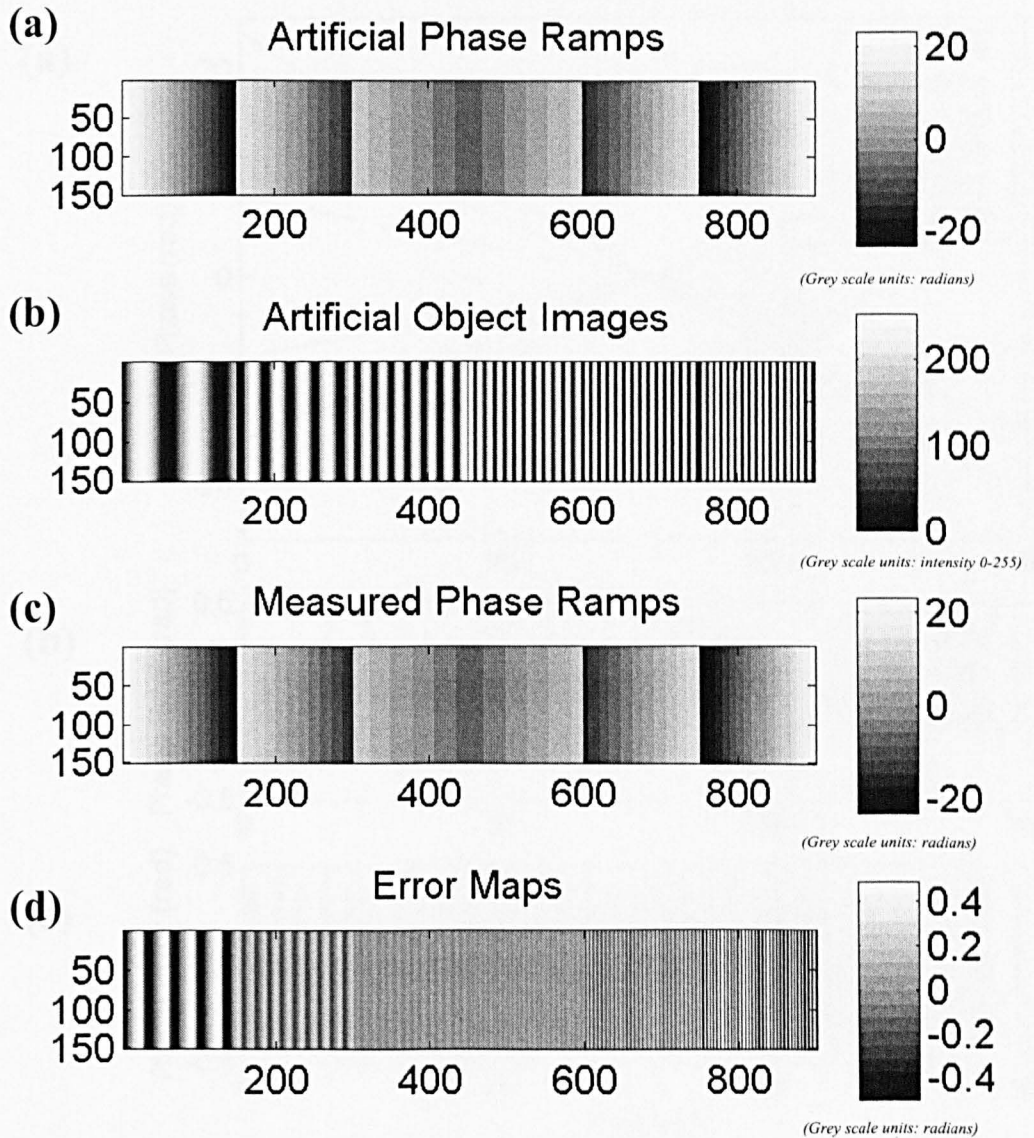


Figure 4.17: Numerical evaluation of the phase measurement algorithm. (a) A set of phase ramps with slopes  $m = -0.3, -0.2, -0.1, 0.1, 0.2$  and  $0.3$  (b) Fringe patterns generated artificially from the equation shown, with a pitch  $p = 16$  pixels. The images were  $256 \times 256$  pixels in size. (c) The object images were combined with the reference image in fig. 4.16(a) using the five-step spatial algorithm to yield this set of measured phase maps. (d) error maps resulting from subtracting the original phase ramps in (a) from the measured maps in (c). Note that the error maps are periodic functions with frequency double that of the corresponding object images

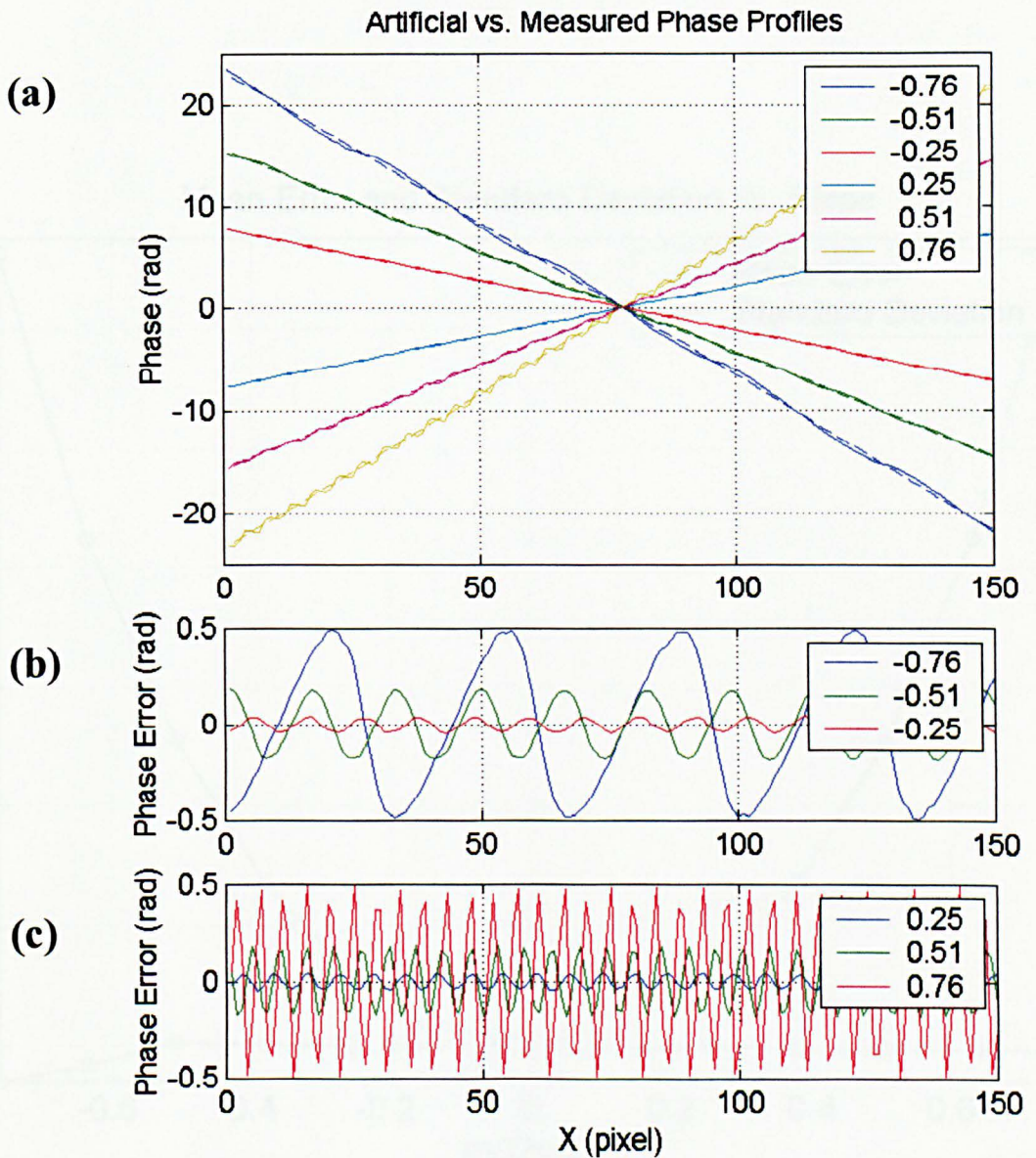


Figure 4.18: A set of profiles along a horizontal line of the measured phase ramps is shown in (a) superimposed to the values of the original phase ramps (dotted lines). Note the legend indicates the values of slope normalised with the maximum value, i.e.  $m/(2\pi/p)$ . Profiles of the error calculated subtracting the original phase ramp from the measured value are shown in (b) for negative slopes and in (c) for positive slopes. The figure shows that the amplitude of the error function increases with the slope but the mean error remains very nearly zero.

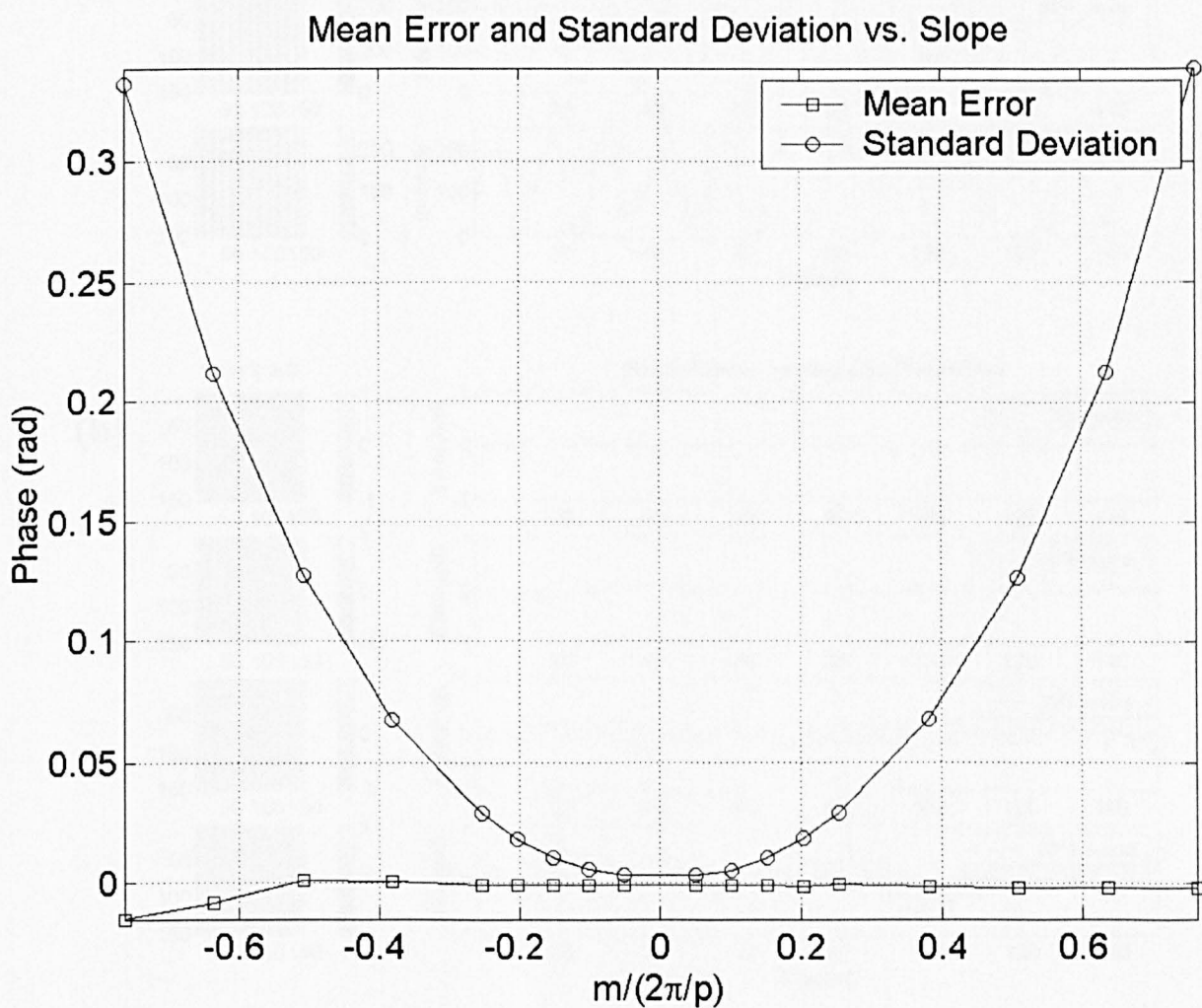


Figure 4.19: Numerical evaluation of the phase measurement algorithm. This plot summarizes the results of the numerical tests showing plots of the mean error and standard deviation versus the slope of the phase ramp normalised with the maximum value of  $2\pi/p$ .

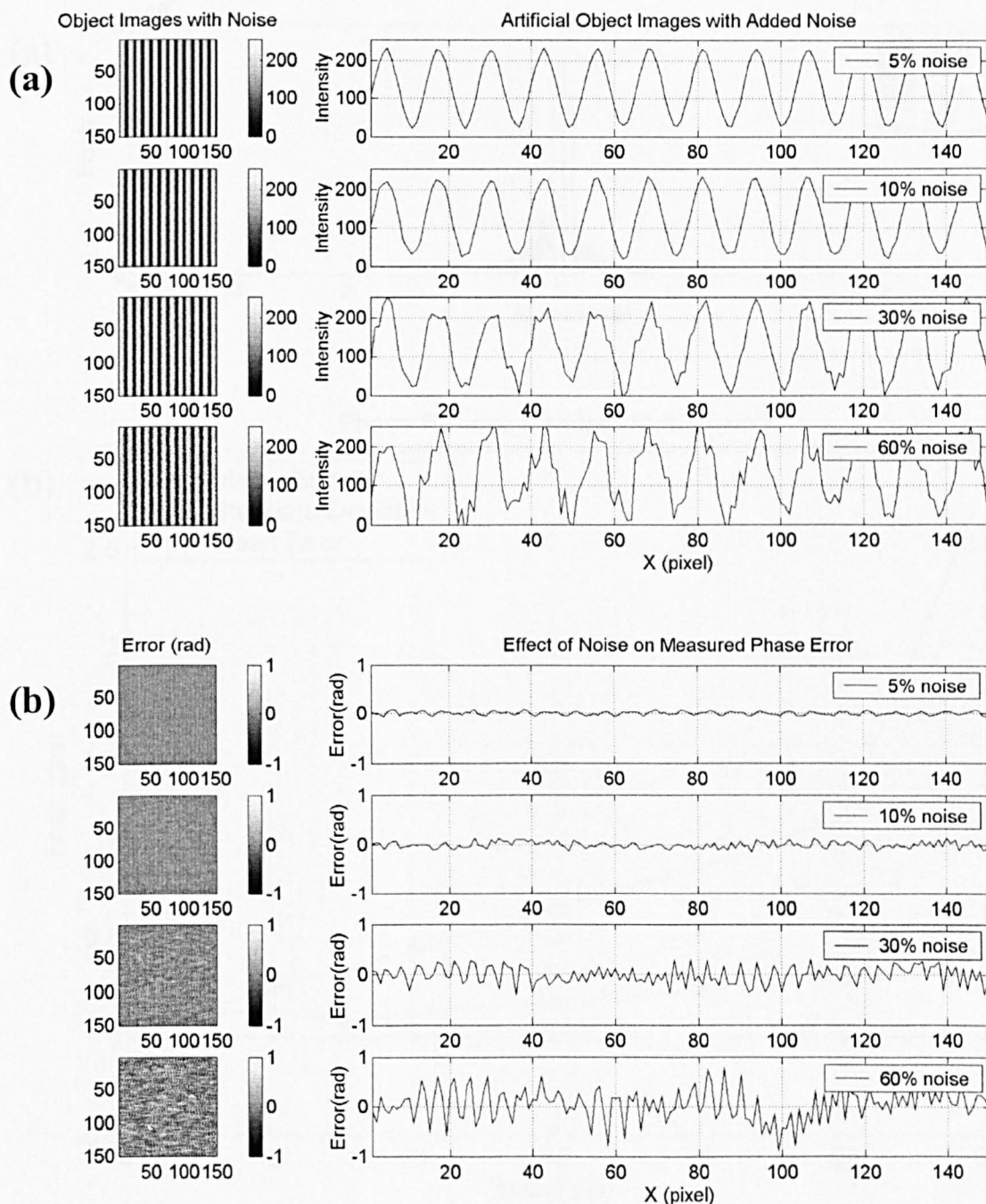


Figure 4.20: Numerical tests to study the influence of random noise. (a) Four artificial images generated by adding increasing levels of random noise to the object image shown in fig. 4.16(b). The reference images were obtained in the same way from the image in fig. 4.16(a) (b) Error maps obtained by processing each pair of images with added noise and subtracting the original phase ramp from the resulting measurement of phase.

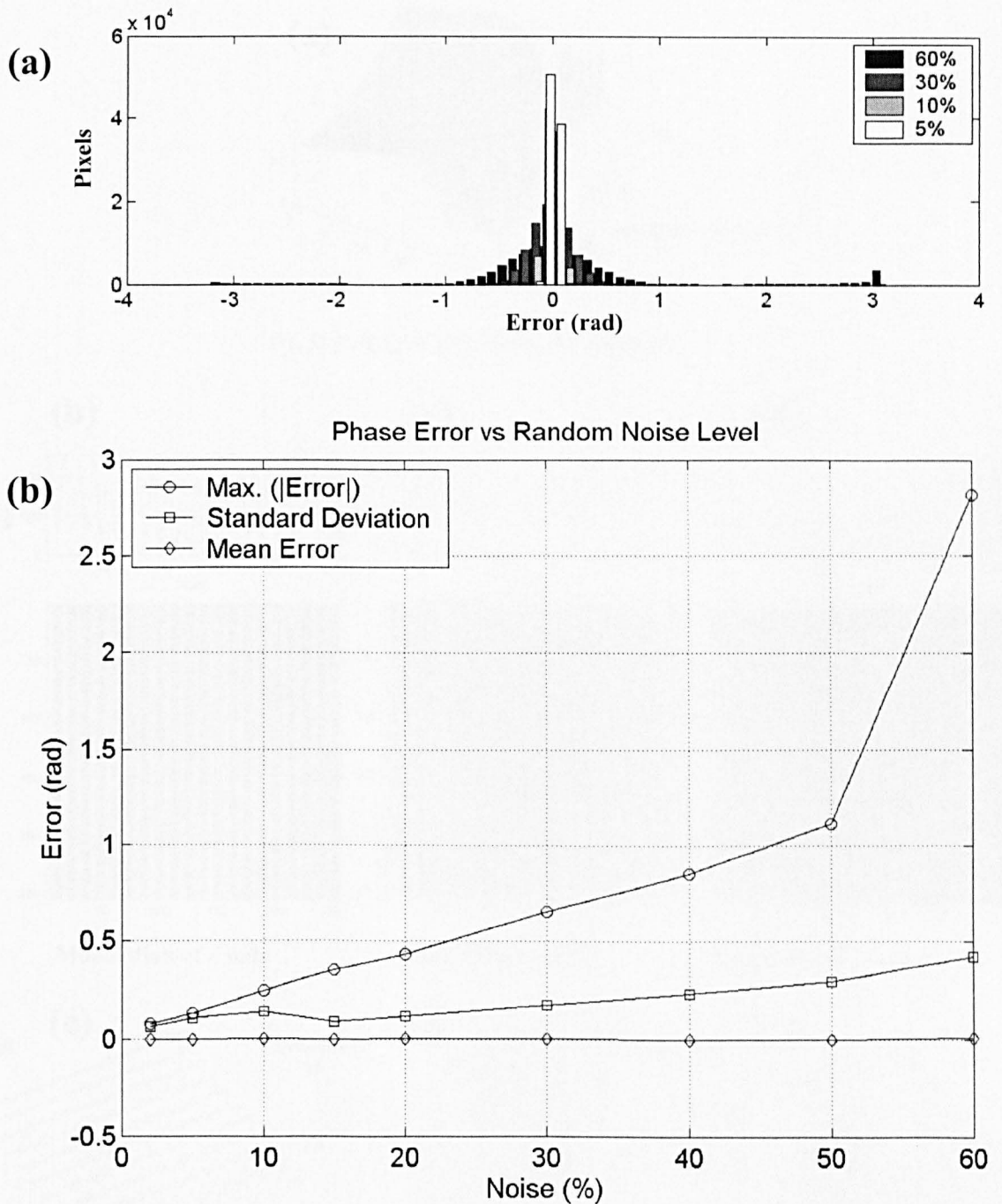


Figure 4.21: Phase error in artificial images with random added noise. (a) Histogram plots of the error distribution maps in the measured phase for 5%, 10%, 30% and 60% added noise showing an increase in the dispersion of the calculated values. The peaks in  $\pm\pi$  for the 60% case represents areas where the unwrapping procedure failed. (b) Plot of the maximum error, the standard deviation and the mean error versus the percentage of random noise added. The abrupt increase in the maximum error to values near  $\pi$  when the noise level increases above 50% corresponds to failures in the unwrapping algorithm.

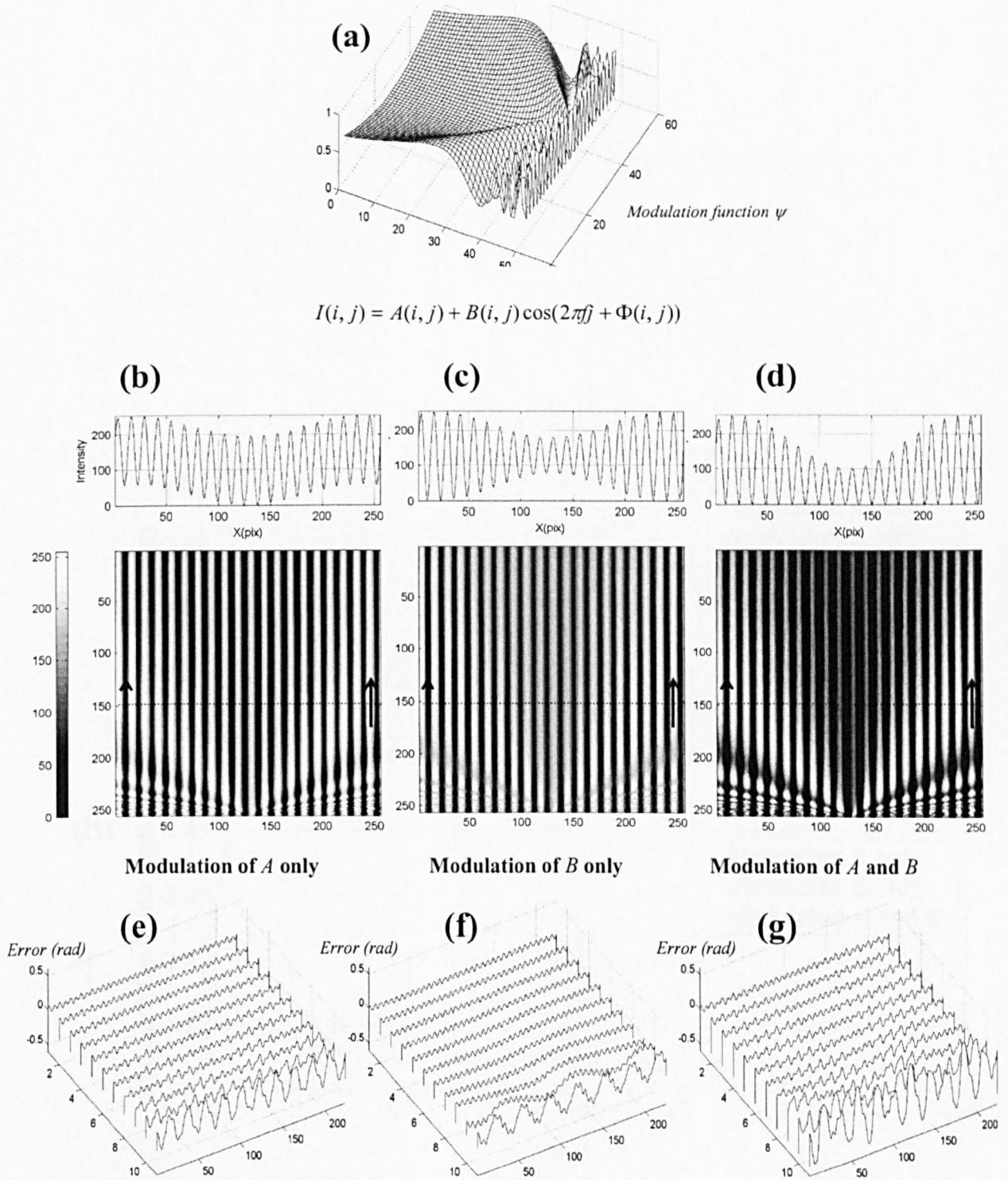


Figure 4.22: Numerical evaluation of the errors associated with non-uniformities in the background and amplitude of the fringe pattern. The modulation function shown in (a) was applied: (b) to the background term  $A$  only, (c) to the amplitude term  $B$  only, and (d) to both terms simultaneously. The modulated image and an intensity profile along a horizontal line are shown in each case. Figures (e) (f) and (g) show the error profiles along a set of horizontal lines in the phase maps which result respectively from processing the images in (b) (c) and (d).

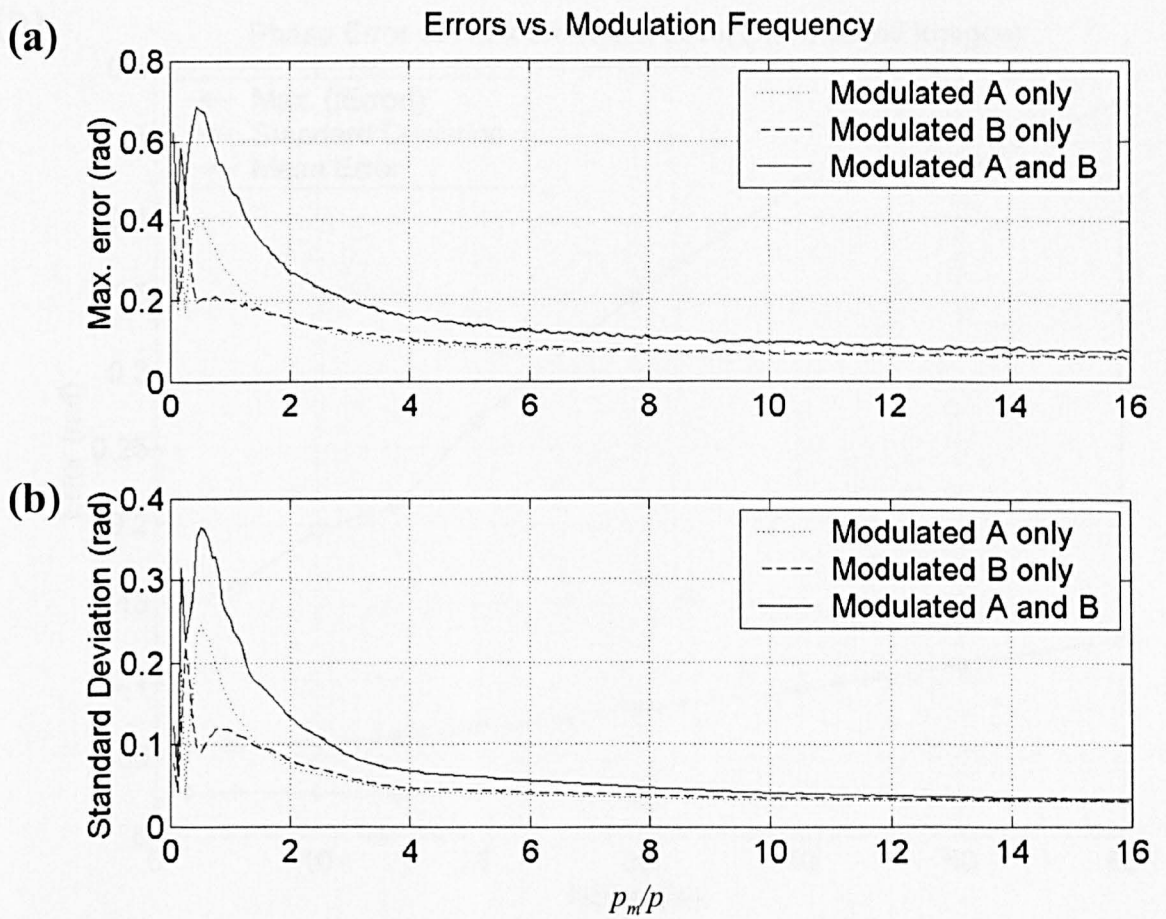


Figure 4.23: Effect of the modulation frequency on the error. Summary of the results obtained in numerical tests (a) Plot of maximum phase error versus the modulation pitch normalized with the pitch  $p$  of the fringes in the reference image. (b) Plot of standard deviation versus normalized modulation pitch. Note that  $p_m/p = f/f_m$

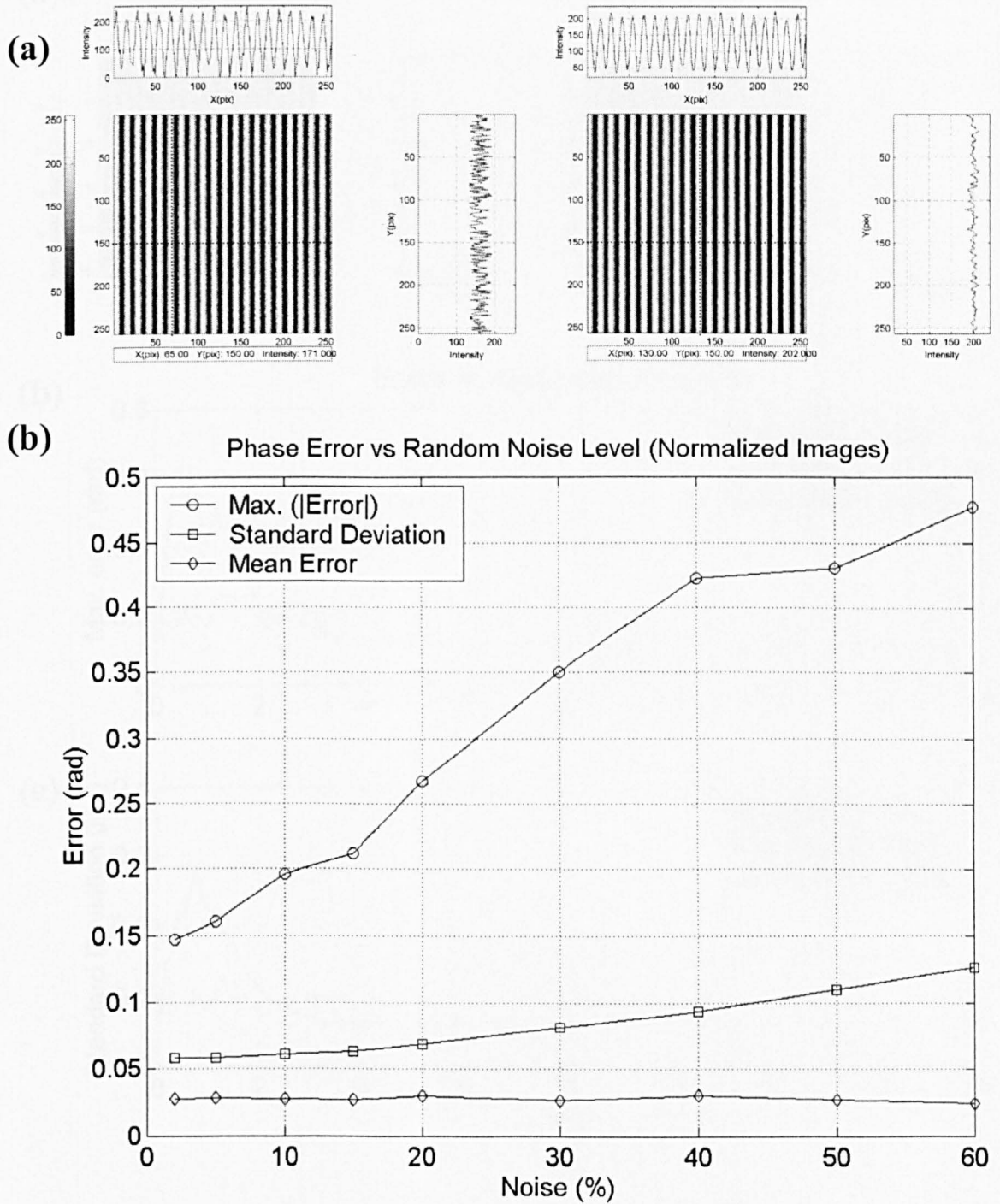


Figure 4.24: Effect of normalization in the errors due to random noise. (a) Normalization of an image with 60% random noise added (b) Plot of the maximum error, the standard deviation and the mean error versus the percentage of random noise added. This results represent a significant improvement when compared to fig. 4.21(a)

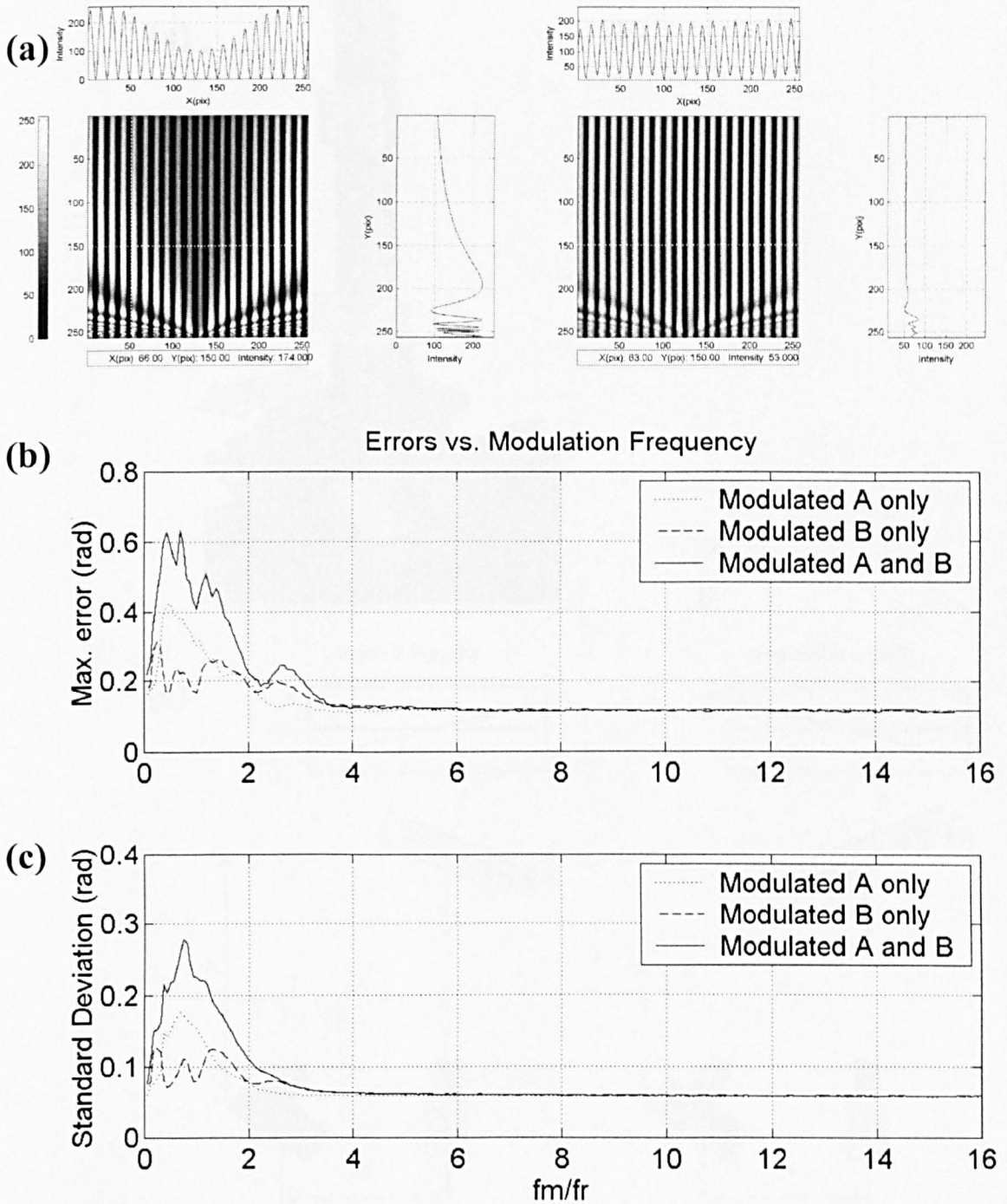


Figure 4.25: Effect of normalization in the errors due to modulation of the background and amplitude of the fringe pattern. (a) normalization of an image with modulated  $A$  and  $B$  terms (b) Maximum phase error versus normalized modulation frequency (c) Standard deviation versus normalized modulation frequency. Compare (b) and (c) with the graphs in fig. 4.23.

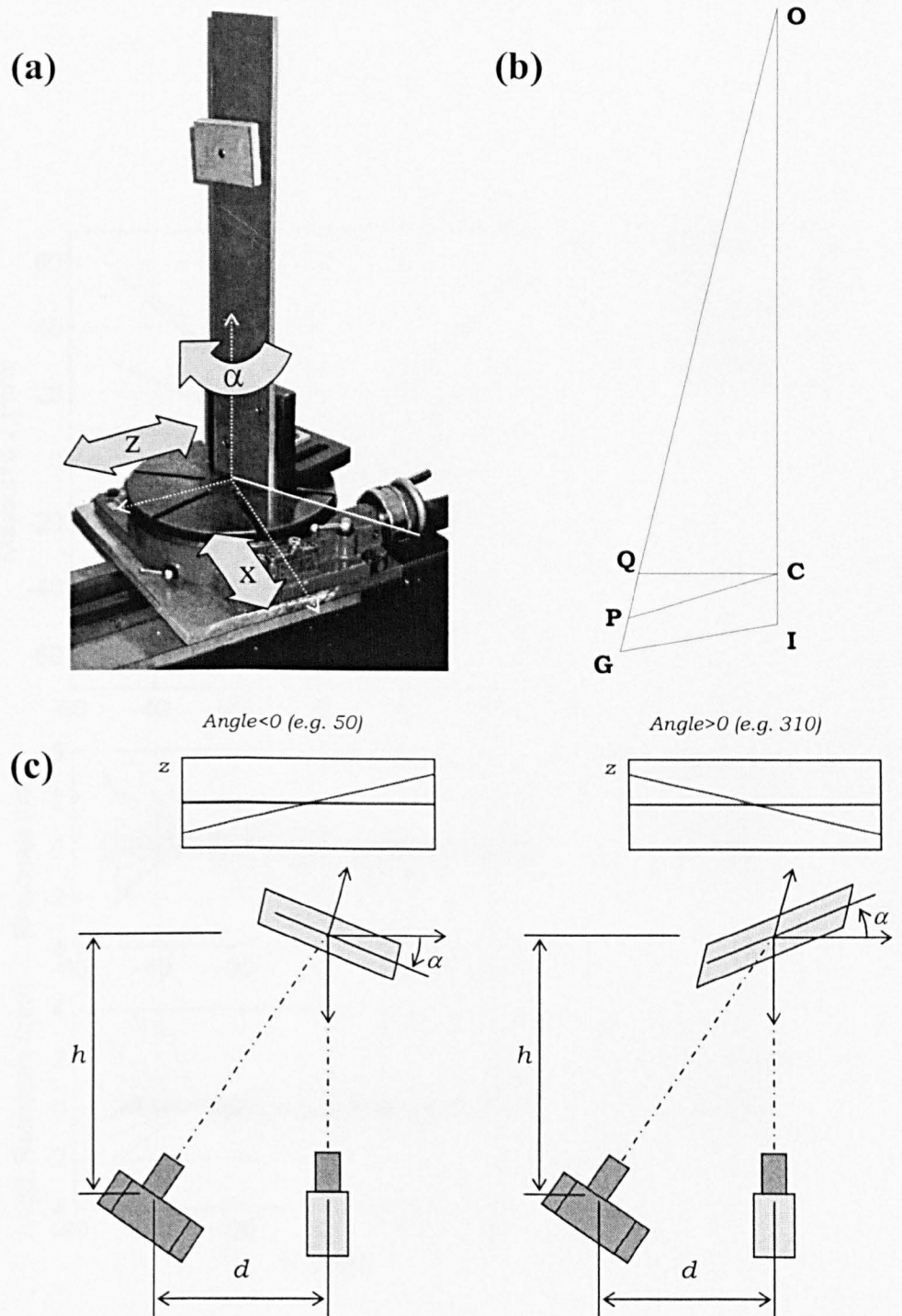


Figure 4.26: Experimental error analysis. A set of experimental tests was carried out with a flat plate rotated at different angles with respect to the camera for the evaluation of the method. (a) Rotation table and mounting bracket used to attach the samples, which allows  $x$  and  $z$  displacement and rotation about the  $y$ -axis. (b) Scaled representation of the optical configuration of the elements. (c) Sign convention defined for the angle of the rotating plate.

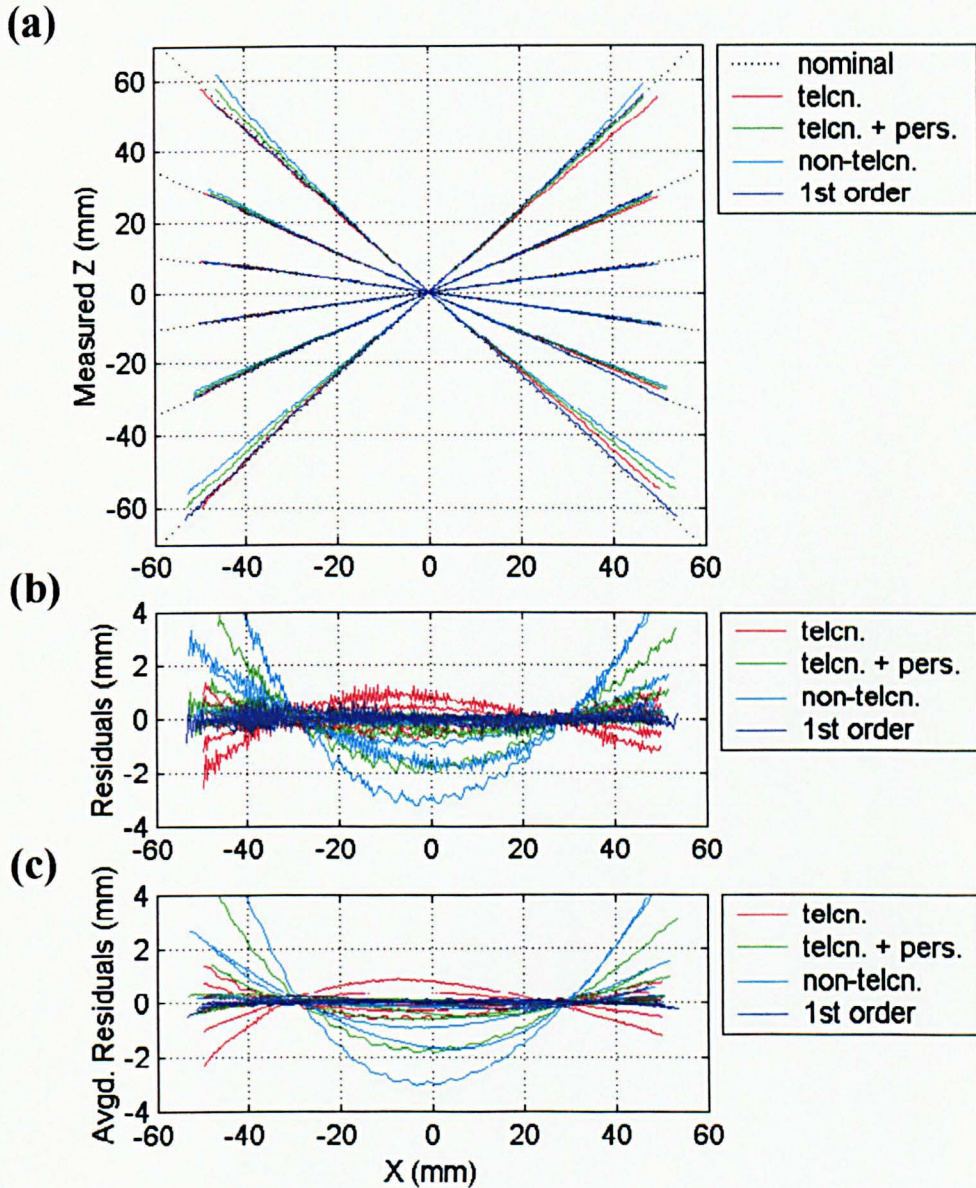


Figure 4.27: Tests with a flat plate rotated at different angles for experimental error analysis: manual calibration (measurement of  $\theta$ ). (a) Profiles of the height map along the horizontal middle line for the plate rotated at  $\pm 10$ ,  $\pm 30$  and  $\pm 50$  degrees. The graph compares the nominal position (dotted line) and the measured shape. Four calibration expressions were considered: telecentric, telecentric with perspective correction, non-telecentric, and first order. (b) Residuals along the middle line, calculated as the difference between the measured and the nominal profile in each case. (c) Averaged residuals along the  $y$ -direction to isolate systematic errors. Two effects can be observed: a smooth curvature due to finite optics, and a ripple due to estimation errors of the phase extraction algorithm.

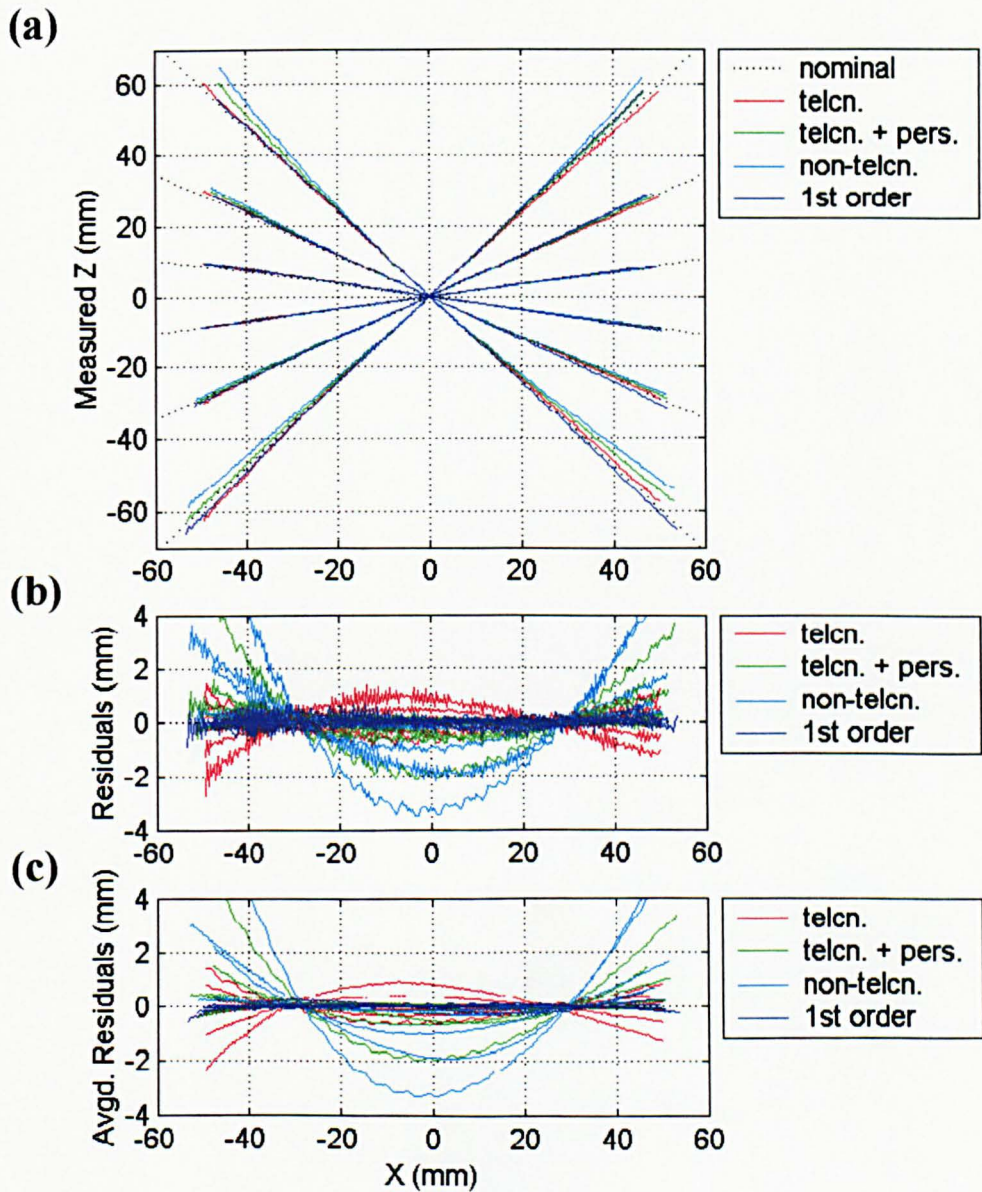


Figure 4.28: Tests with a flat plate rotated at different angles for experimental error analysis: manual calibration (measurement of  $d$ ). (a) Profiles of the height map along the horizontal middle line for the plate rotated at  $\pm 10$ ,  $\pm 30$  and  $\pm 50$  degrees. The graph compares the nominal position (dotted line) and the measured shape. Four calibration expressions were considered: telecentric, telecentric with perspective correction, non-telecentric, and first order. (b) Residuals along the middle line, calculated as the difference between the measured and the nominal profile in each case. (c) Averaged residuals along the  $y$ -direction to isolate systematic errors. Two effects can be observed: a smooth curvature due to finite optics, and a ripple due to estimation errors of the phase extraction algorithm.

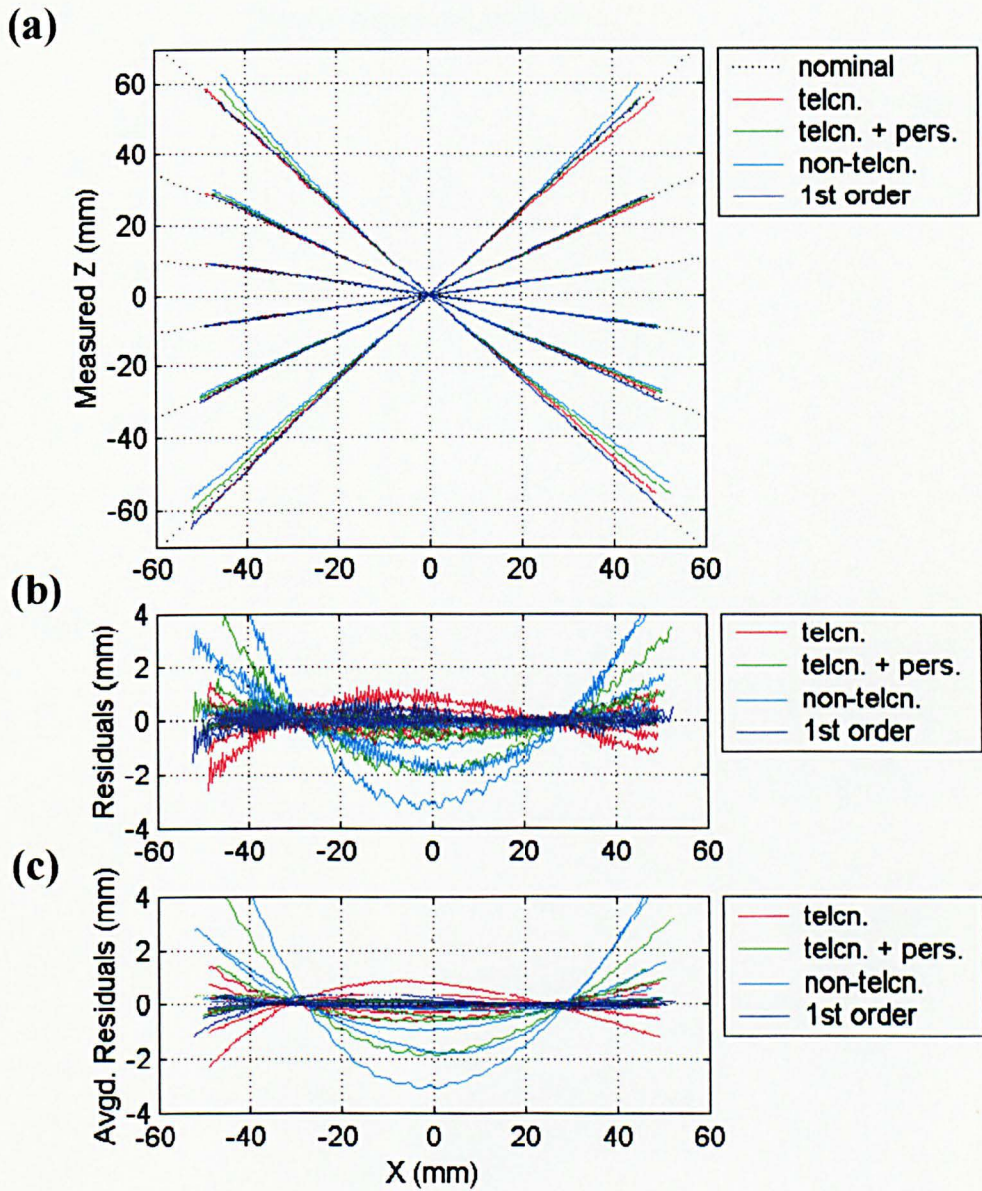


Figure 4.29: Tests with a flat plate rotated at different angles for experimental error analysis: automatic calibration (calib1). (a) Profiles of the height map along the horizontal middle line for the plate rotated at  $\pm 10$ ,  $\pm 30$  and  $\pm 50$  degrees. The graph compares the nominal position (dotted line) and the measured shape. Four calibration expressions were considered: telecentric, telecentric with perspective correction, non-telecentric, and first order. (b) Residuals along the middle line, calculated as the difference between the measured and the nominal profile in each case. (c) Averaged residuals along the  $y$ -direction to isolate systematic errors. Two effects can be observed: a smooth curvature due to finite optics, and a ripple due to estimation errors of the phase extraction algorithm.

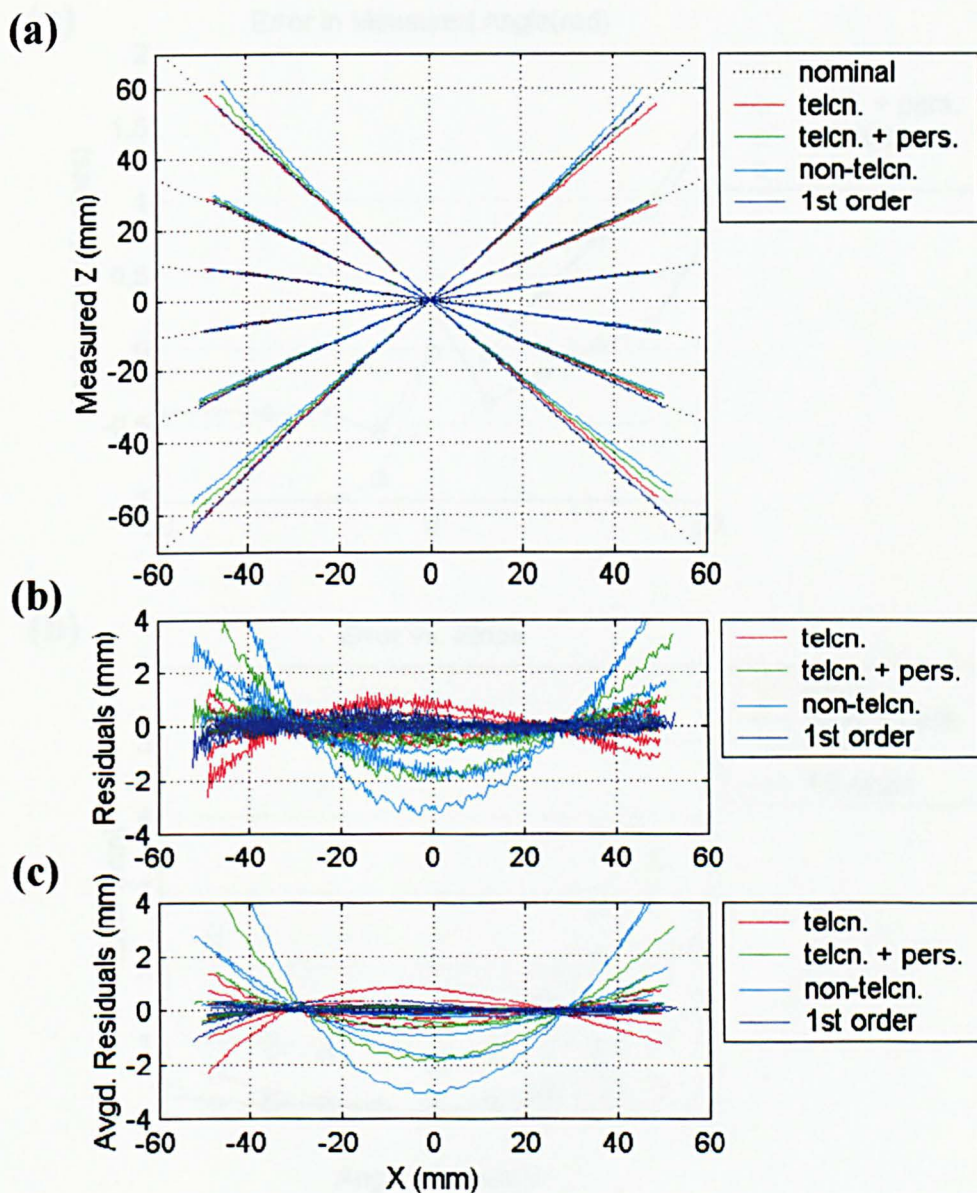


Figure 4.30: Tests with a flat plate rotated at different angles for experimental error analysis: automatic calibration (calib2). (a) Profiles of the height map along the horizontal middle line for the plate rotated at  $\pm 10$ ,  $\pm 30$  and  $\pm 50$  degrees. The graph compares the nominal position (dotted line) and the measured shape. Four calibration expressions were considered: telecentric, telecentric with perspective correction, non-telecentric, and first order. (b) Residuals along the middle line, calculated as the difference between the measured and the nominal profile in each case. (c) Averaged residuals along the y-direction to isolate systematic errors. Two effects can be observed: a smooth curvature due to finite optics, and a ripple due to estimation errors of the phase extraction algorithm.

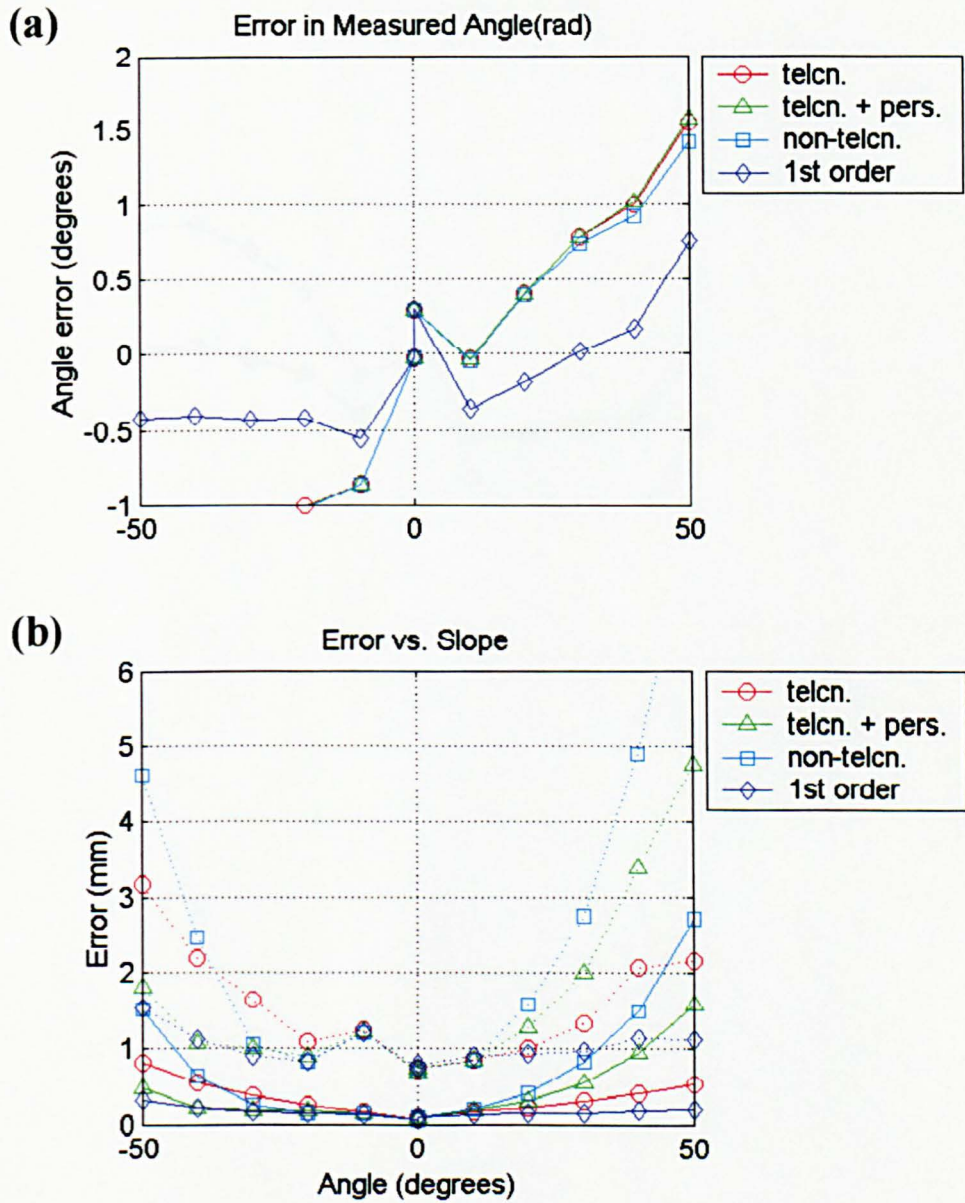


Figure 4.31: Error versus angle: results with manual calibration (measurement of  $\theta$ ). (a) Error in the measured angle with respect to the reading in the scale of the rotation table, for each of the four calibration expressions. (b) Plots of maximum error (dotted line) and standard deviation (solid line) versus the angle for each of the four calibration expressions considered. The error increases with the inclination of the surface, except for the first order expression, which corrects perspective and finite optics effects.

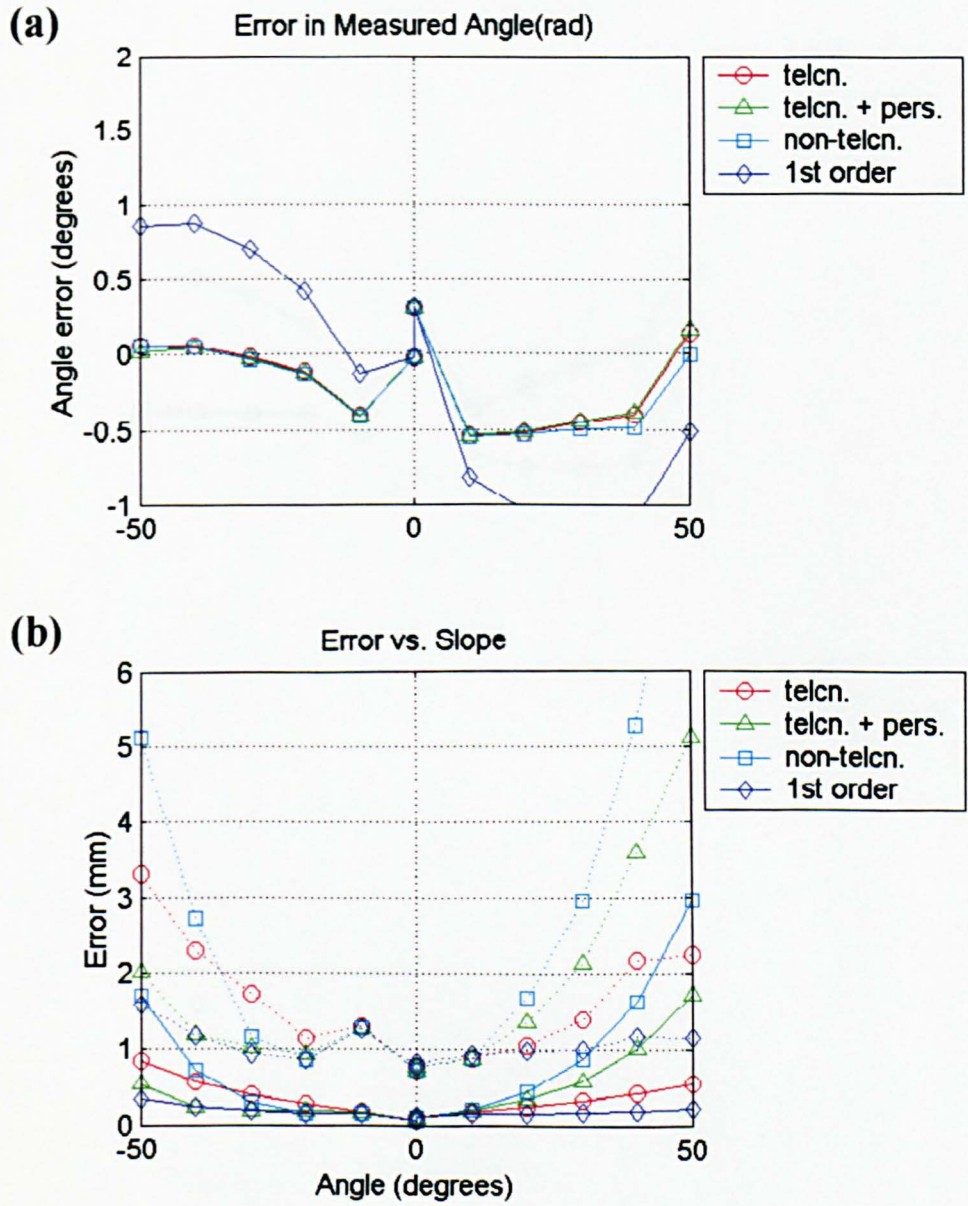


Figure 4.32: Error versus angle: results with manual calibration (measurement of  $d$ ). (a) Error in the measured angle with respect to the reading in the scale of the rotation table, for each of the four calibration expressions. (b) Plots of maximum error (dotted line) and standard deviation (solid line) versus the angle for each of the four calibration expressions considered. The error increases with the inclination of the surface, except for the first order expression, which corrects perspective and finite optics effects.

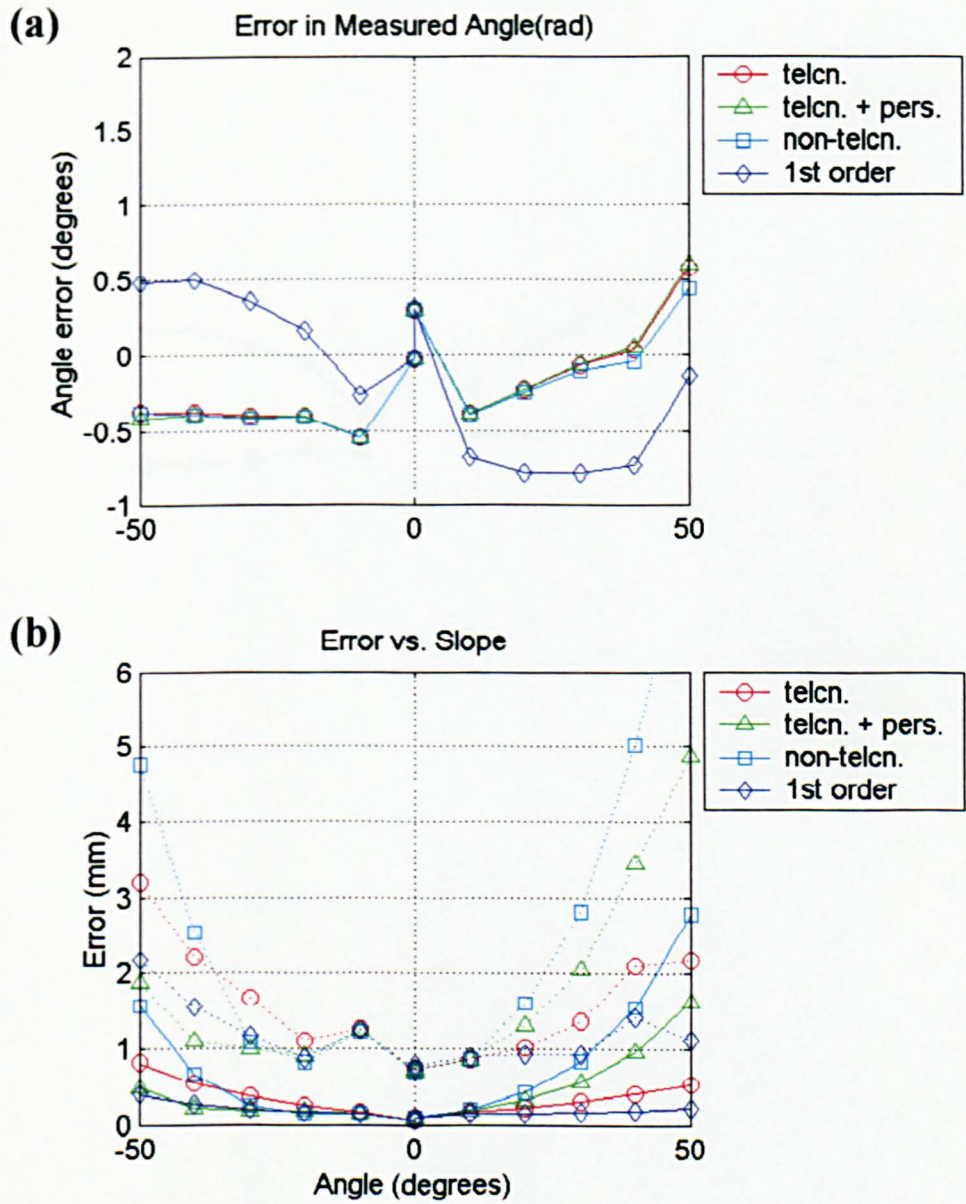


Figure 4.33: Error versus angle: results with automatic calibration (calib1). (a) Error in the measured angle with respect to the reading in the scale of the rotation table, for each of the four calibration expressions. (b) Plots of maximum error (dotted line) and standard deviation (solid line) versus the angle for each of the four calibration expressions considered. The error increases with the inclination of the surface, except for the first order expression, which corrects perspective and finite optics effects.

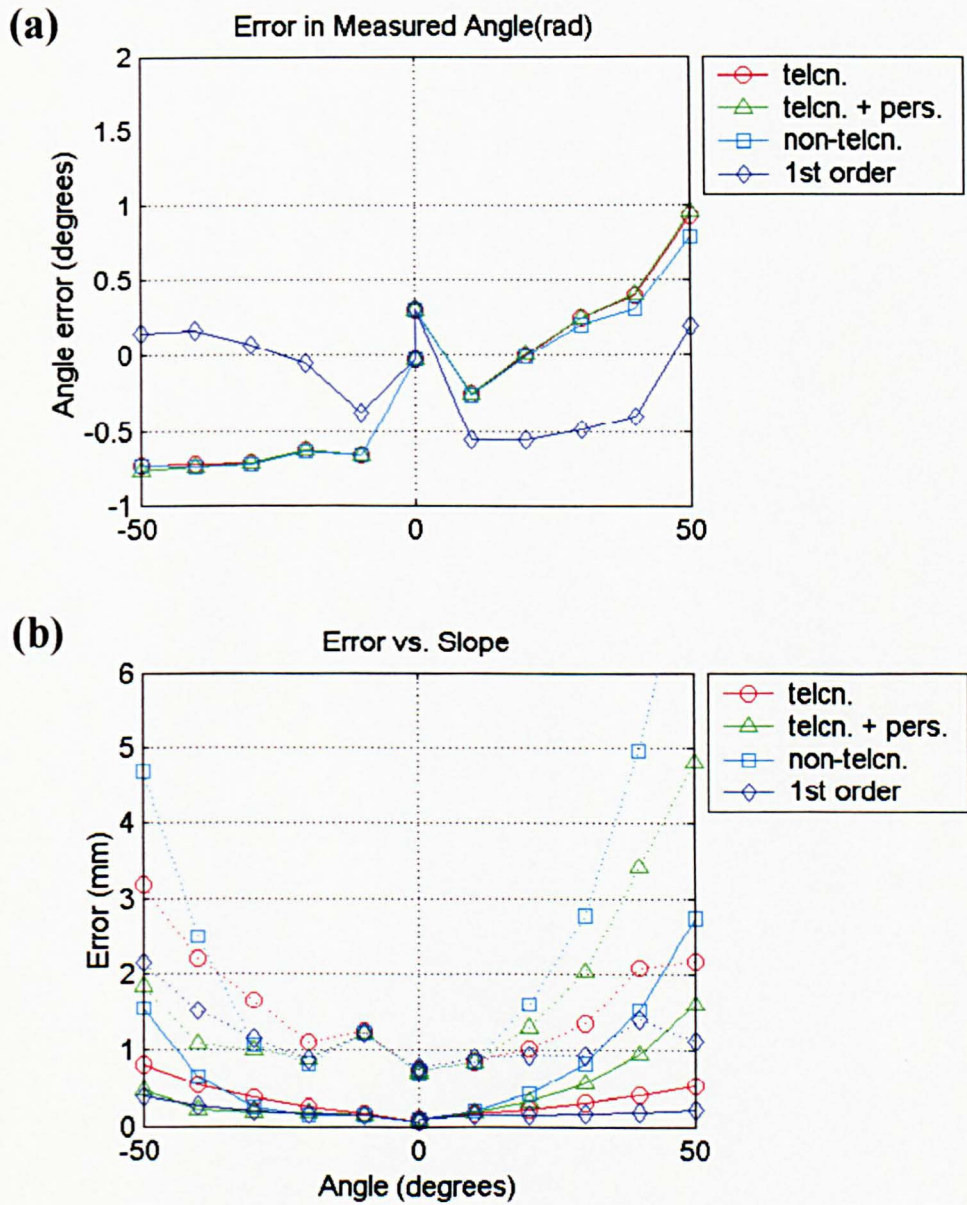


Figure 4.34: Error versus angle: results with automatic calibration (calib2). (a) Error in the measured angle with respect to the reading in the scale of the rotation table, for each of the four calibration expressions. (b) Plots of maximum error (dotted line) and standard deviation (solid line) versus the angle for each of the four calibration expressions considered. The error increases with the inclination of the surface, except for the first order expression, which corrects perspective and finite optics effects.